Fall 12-2020

Synthesis, Characterization, and Kinetics Studies of New Cobalt Complexes for the Production of H_2 in Acidic Media

Michael John Celestine
Old Dominion University, michaeljc2003@hotmail.com

Synthesis, characterization, and kinetics studies of new cobalt complexes for the production of H_2 in acidic media

by

Michael John Celestine
B.S., May 2012, University of the Virgin Islands
M.S., December 2015, Old Dominion University

A Thesis Submitted to the Faculty of
Old Dominion University in Partial Fulfillment of the
Requirements for the Degree of

DOCTARATE OF PHILOSOPHY

CHEMISTRY

OLD DOMINION UNIVERSITY

December 2020

Approved by:

Alvin A. Holder (Director)
Craig A. Bayse (Member)
John B. Cooper (Member)
Sandeep Kumar (Member)

ABSTRACT

Synthesis, characterization, and kinetics studies of new cobalt complexes for the production of H_2 in acidic media

Michael John Celestine

Old Dominion University, 2020

Director: Dr. Alvin A. Holder

The kinetics and mechanism of the oxidation of $[Co(dmgBF_2)_2(OH_2)_2]$ (where $dmgBF_2$ = difluoroboryldimethylglyoximato) by sodium hypochlorite (NaOCl), sodium bromate ($NaBrO_3$), and bromine (Br_2) was investigated by stopped-flow spectrophotometry at 450 nm over a wide temperature range. The pK_{a1} value for $[Co(dmgBF_2)_2(OH_2)_2]$ was calculated as 5.27 ± 0.14 at I = 0.60 (NaCl). From the variation in pH studies, the activation parameters were derived from the proposed mechanisms for NaOCl, $\Delta H_1^{\neq}$, $\Delta H_2^{\neq}$, $\Delta S_1^{\neq}$, and $\Delta S_2^{\neq}$ were calculated as 58 ± 7 kJ mol^{-1}, 47 ± 0.1 kJ mol^{-1}, 29 ± 2 J mol^{-1} K^{-1}, and -9 ± 0.4 J mol^{-1} K^{-1}, respectively. The reaction with Br_2 also had two sets of activation parameters for the two reacting species in solution which were Br_2Cl^- and OBr^- where, $\Delta H_1^{\neq}$, $\Delta H_2^{\neq}$, $\Delta S_1^{\neq}$, and $\Delta S_2^{\neq}$ were calculated as 26 ± 0.1 kJ mol^{-1}, 71 ± 2 kJ mol^{-1}, -52 ± 0.2 J mol^{-1} K^{-1}, and 105 ± 0.6 J mol^{-1} K^{-1}, respectively. Finally with $NaBrO_3$ there was only one reacting oxidant which was the bromate which gave the following activation parameters: $\Delta H^{\neq}$ and $\Delta S^{\neq}$ which were calculated as 57 ± 1 kJ mol^{-1} and 34 ± 4 J mol^{-1} K^{-1}, respectively.

In the interaction study of Et_3N with $[Co(dmgBF_2)_2(OH_2)_2]$ the isolated product was characterized as $[Co(dmgBF_2)_2(OH_2)(N(CH{=}CH_2)_3)]\bullet 5.25H_2O\bullet 0.25C_6H_9N$ via NMR and mass spectroscopy and elemental analysis. In the UV-visible studies, various changes were observed with the most dramatic being between 500 and 900 nm with the appearance of two new λ_{max} at 554 and 680 nm. In the HFEPR studies the isolated product anisotropic characteristics was observed to be rhombic in nature with the observed g-values for the g_x, g_y, and g_z were 2.25, 2.15, and 2.01, respectively. However, the reaction mixture produced a spectrum that where the anisotropic characteristic was axial with g-values of $g_{\|}$ = 2.19 and $g_{\perp}$ = 2.00.

The complexes $[Co(bpy)_2(PCA\text{-}(CF_3)_2)](PF_6)_2 \cdot H_2O$ **3**, $[Co(phen)_2(PCA\text{-}(CF_3)_2)](PF_6)_2 \cdot 1.25H_2O$ **4**, and $[Co(tpy)(phen)Cl](PF_6)_2 \cdot 0.25CH_3CN$ **7** (where PCA-$(CF_3)_2$ = *N*-(3,5-bis(trifluoromethyl)phenyl)pyridine-2-carbothioamide, tpy = 2,2';6',2''-terpyridine, bpy = 2,2'-bipyridine and phen = 1,10-phenanthroline) were synthesized, characterized, and tested for their overall effectiveness as a hydrogen evolution catalyst. Complexes **3** and **4** demonstrated catalytic HER in the presence of *p*-cyanoanilinium tetrafluoroborate in CH_3CN, with overpotentials for the HER of 730 and 630 mV for complexes **3** and **4**, respectively. The reduction potentials suggest that the HER was most likely facilitated by a homolytic pathway. Under photocatalytic conditions in the presence of $[Ru(bpy)_3](PF_6)_2$ as a photosensitizer and triethanolamine as a sacrificial reductant in DMF, complexes **3**, **4**, and **7** attained turnover numbers of 91, 140, and 79, respectively, when compared to the standard complex $[Co(dmgH)_2(py)Cl]$ (where dmgH = *dimethylglyoximato).*

This thesis is dedicated to Veronica and Joachim Celestine

ACKNOWLEDGMENTS

I would like to thank my family (mom, dad, Mary, Hilda, Catherine, Theresa, Deo, Lincoln, Davis, Correen, and Janice) for all their love and support. I would like to thank Dr. A. A. Holder my mentor, who gave me a chance to further my education. I would like to also thank my fellow lab mates; Mark A.W. Lawrence (former), Raj Gurung, Chriszcele Tano, Elizabeth A. Tonsel-White, Khadija Faye, Duaa Alajroush, Jimmie L. Bullock (former), Edward T. Artis, Deisy L. Esquivel, Lorne S. Joseph, Brianne Nunez, Jennifer E. Mejia, Emily Marquez, Chekeyl Harold, the other undergraduate students, and Professor Chee-Hun Kwak, who offered guidance and support. I would also like to thank the chemistry administrative staff for all their help. I would also like to thank Dr. Jurek Krzystek who assisted me in acquiring the HFEPR measurements at the National High Field Magnetic Laboratory in Tallahassee, Fl. Thanks to Professor Garry S. Hannan and his graduate students Olivier Schott and Vincent Picard who helped with gathering the photocatalytic hydrogen production. Dr. Colin D. McMillen for solving the crystal structures and Professor Craig A. Bayse for the DFT calculations.

I would like to thank the NSF for an NSF CAREER Award (awarded to Dr. Alvin A. Holder), which allowed the successful execution of the completion of this thesis, as this material is based upon work supported by the National Science Foundation under CHE-1431172 (formerly CHE – 1151832). I would also like to thank Old Dominion University for the help and support in completion of this work. I would also like to thank the faculty and staff at the University of the Virgin Islands for their guidance especially during my time as a RISE scholar and MARC trainee. I am also thankful to the staff at the National High Field Magnetic Laboratory in Tallahassee, Fl

for sponsoring my trip to acquire my HFEPR spectra. Also this research was supported partially by an appointment to the Student Research Participation Program at the U.S. Army Engineer Research and Development Center, Construction Engineering Research Laboratory, administered by the Oak Ridge Institute for Science and Education through an interagency agreement between the U.S. Department of Energy and ERDC-CERL. This work was also partially supported by the Center Directed Research Program at the U.S. Army Corps of Engineers.

TABLE OF CONTENTS

LIST OF TABLES

LIST OF FIGURES

Chapter 1: Introduction

1.0 Fossil fuels and global warming

It is common knowledge that the amount of fossil fuels that exist is finite and limited, alternative fuel sources will be seen to be the key players in the future of energy. With the energy consumption of the planet being filled by the burning of fossil fuels for which is causing major environmental problems such as the alteration of the global climate by the release of greenhouse gasses.[1-2] Figure 1 shows the energy consumption of both the world and North America. The major energy consumption comes from the use of the fossil fuels oil, gas, and coal. What should be noted in the figure is how much of the energy we use comes from fossil fuels, and with burning of those energy sources releases gases such as CO_2, CO, N_2O, and more which instinctively behave as a blanket.[3]

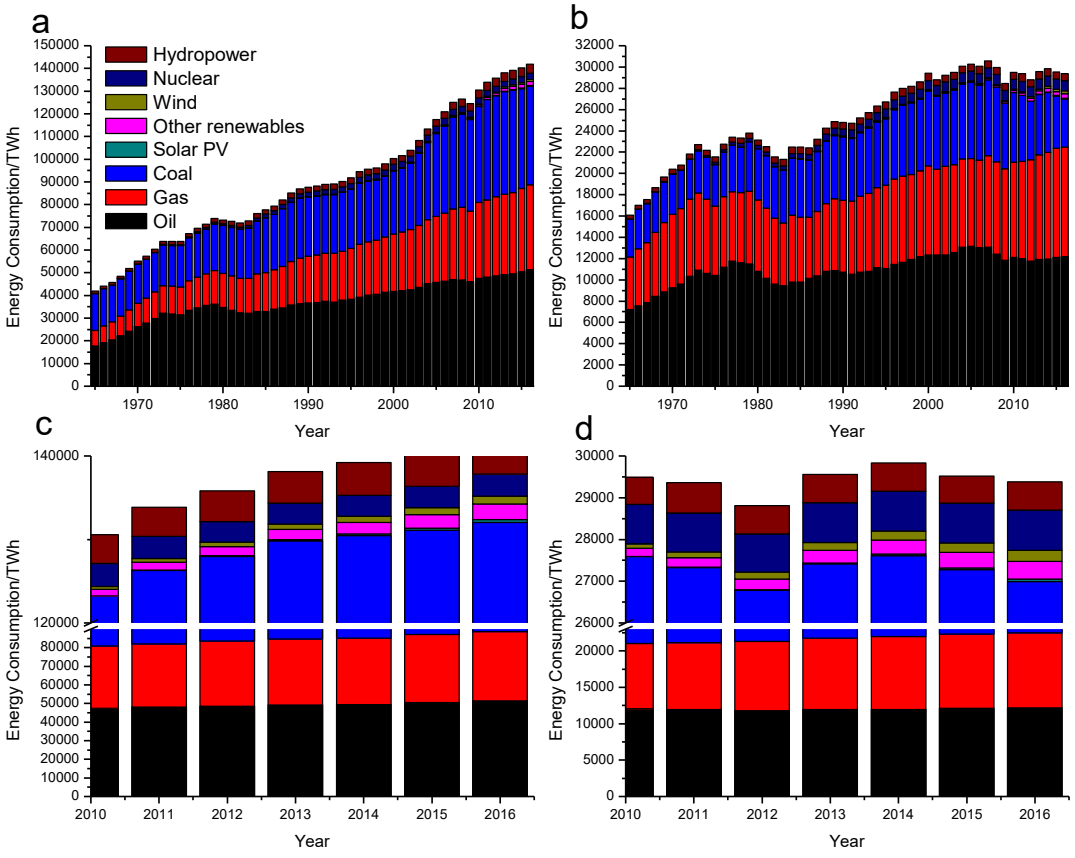

Figure 1. Energy consumption of different energy sources for the World (a and c) and North America (b and d).[4]

This blanket allows sunlight to reach the surface, but the light that is converted to heat as well as the naturally produced heat from the planet is no longer able to radiate out into space but

is directed back to the surface of the planet. This leads to an increase in the mean temperature which is often termed "global warming." Many studies have been conducted on how these different gasses affect the global climate, where it was observed that within the past 200 years there has been an 31% increase in CO_2 concentrations, with an increase in mean global surface temperature of about 0.4 – 0.8 °C in the past 100 years, 1-2 mm rise in the mean sea level, and thinning of about 40% of artic sea ice.[3, 5] It is observed in Figure 2 that between these changes exists a direct correlation between the increasing CO_2 levels and the change in average temperature. Thus, a growth into cleaner energy sources must overcome that of fossil fuels.

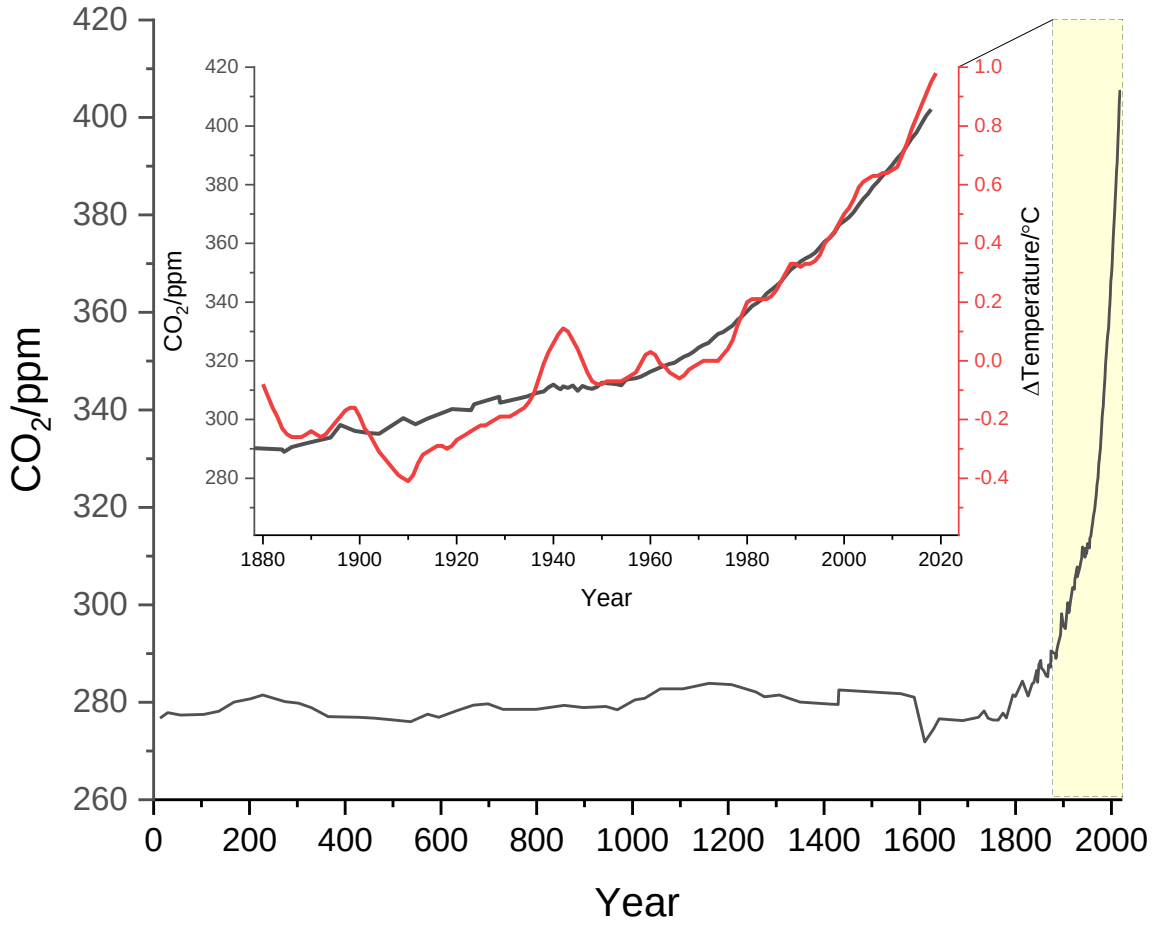

Figure 2. CO_2 concentration and temperature changes over time.[6-7]

Though it is hard to observe in Figure 1, the use of other renewable sources, wind, and solar photovoltaic began making somewhat of an impact in the percentage of energy consumed circa 1965, 1989, and 1999, respectively. Though they have grown significantly since then, there are still many obstacles that needs to be addressed as the world proceeds towards a clear planet. The cost of producing energy from renewable sources have become more feasible especially within

the last decade especially when it comes to solar energy, as illustrated in Figure 3. In the year 2010 the cost of producing energy via solar photovoltaic cells would cost about 350 USD/MWh when compared to 2016 would cost less than 140 USD/MWh. Which may not seem as much of a significant change, but when compared to the price of producing the same amount of energy from fossil fuels seems a lot more comparable. This leads towards the direction that we are trying to move towards with one of the main focuses being the conversion of solar energy into chemical energy.

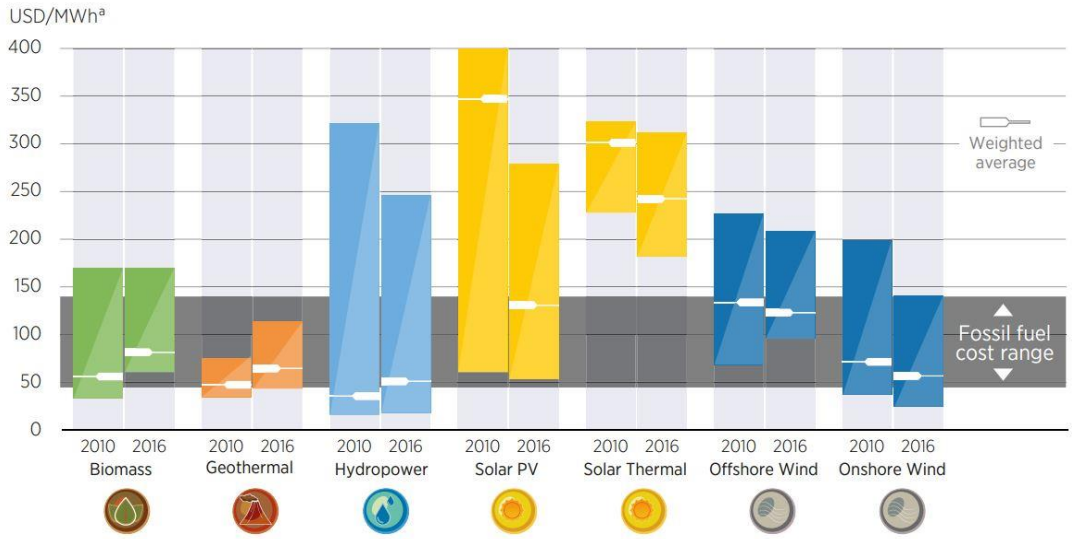

Figure 3. Levelized cost of electricity between 2010 and 2016. Note: (a) MWh: megawatt-hour; and (b) All costs are in 2016 USD. Weighted Average Cost of Capital is 7.5% for OECD and China and 10% for Rest of World.[4]

The conversion of solar energy to chemical energy is ever growing, with hydrogen being a clean renewable source of energy that is carbon-free.[8-13] Hydrogen production through the reduction of water appears to be a convenient solution for long-term storage of renewable energy. Some platinum catalyst has been observed to be able to reduce water to hydrogen with rates that close to thermodynamic equilibrium.[14-15] However, due to the high cost of noble metals such as Pt, Rh, Ir, *etc*., there is a search for viable hydrogen production catalysts based on cheap and abundant first-row transition metals, for instance, Fe, Co, and Ni.[16-17] There has been a growth in the use of photocatalytic systems involving first row transition elements for the production of cleaner energy.[18-26] We can look at biological systems which have enzymes that are capable of producing hydrogen. One such system is hydrogenase, which is categorized by the active site such as [FeFe]-H_2ases and [FeNi] -H_2ases.[27-29] In many cases, the sheer robustness of the hydrogenase have been observe to be minimal due to its sensitivity to catalytic poisons such as oxygen.[28-29]

Widespread research in light-driven production of hydrogen has been done on heterogeneous photocatalysis compared to homogeneous photocatalysis which began to grow after the year 2000.[30-34] There has been a growth in the research of the use of photocatalytic properties of first row transition elements.[18-26]

1.1 Clean energy sources

In 1984, Kuhn[35] wrote the following:

> *"What is it that most us would wish for from the research laboratories around the world? A cure for cancer? The synthesis of a convincing meat substitute from soya? Or perhaps a Fifth Generation computer! A moment's reflection will remind us that however desirable such breakthroughs might be, without a continuing supply of energy, in the right form, in the right place and at the right price, civilisation as we know it today would collapse and the very tiny fraction of the human race to survive would revert to a medieval existence. The supreme importance of energy conversion and power sources as intrinsic requirements of an advanced civilisation call for no further justification, and mastery of Energy Technology demands the highest of all research priorities."*

With those words in mind from 40+ years ago, if we take into consideration the finite nature of fossil fuels and its harmful byproducts when burned, cleaner energy sources are a must. There are many alternative sources of energy such as nuclear, geothermal, and hydroelectrical, but all of these have major drawbacks. With nuclear toxic waste is produced with no real means of containment, and geothermal and hydroelectrical energy sources are location based. There is another alternative, one which harnesses the power of the sun and directing it split water and store that energy in the form of hydrogen.

1.2 Chemistry of Cobalt

Cobalt is the 32nd most abundant element found on Earth in the form of minerals such as cobaltite.[36-37] Cobalt like many transition have variable oxidation states, with the most commonly observed oxidation states of +2 and +3, though higher oxidation states such as the +4 and +5 states do exist they are unstable and are easily reduced (see Figure 4 for examples).[36, 38] One of the first

people to note the oxidation of a cobalt(II) salt was B. M. Tasaert in 1798 [39] who noted that when aqueous ammonia was added to the salt that solution would turn brown, and red/maroon when boiled.[39] It wasn't until later when Frémy proved that the oxidation state of the cobalt metal center went from +2 to +3, and the complex was associated with six NH_3 molecules.[39] However, it wasn't until Alfred Werner who decoded the mystery of interaction between the cobalt(III) metal center and the NH_3 molecules, and with test utilizing $AgNO_3$ proved that the chloride ions were in fact counterions.[39] With $AgNO_3$ test, Werner was able to determine $[Co(NH_3)_5Cl]Cl_2$ (purple) had two chloride counterions whereas $[Co(NH_3)_6]Cl_3$ (orangish-yellow) having three through gravimetric analysis of the resulting AgCl that was formed, and he would later theorize the existence of the cis/trans isomerization of $[Co(NH_3)_4Cl_2]Cl$.[40]

It is noted that the cobalt(III) complexes are incredibly kinetically inert [38] and undergoes ligand-exchange reactions very slowly.[37] The cobalt(III) metal center is also observed to have an high affinity for nitrogen donors, halides, and water, with its most common geometry being that of octahedral.[37] These complexes also tend to be low spin except when the fluoride anion is coordinated to the metal center.[39] Cobalt(II) complexes come in many geometries with the common being octahedral and tetrahedral, and some have been reported to have a square planar configuration.[37] The octahedral geometry is favored over that of the tetrahedral because of the d^7 metal centers ligand field stabilization energies.[37] Tetrahedral Co(II) complexes generally formed with two monodentate anions and two neutral ligands, and in rare cases tetrahedral complexes with bidentate monoanions have been reported.[37] Figure 4 shows selected cobalt complexes with their common geometries.

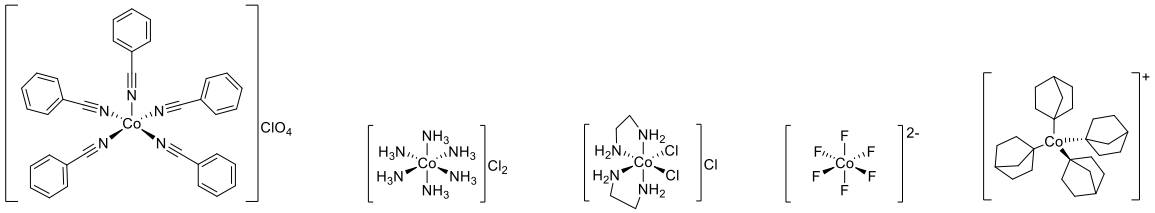

Figure 4. Cobalt complexes with various oxidation states.[37]

Within mammals and many other types of animals, cobalt is usually observed as cobalamins, Figure 5A, which has one of the most intricate structures of all vitamins.[41] The cobalt metal center of cobalamins have been observed to range from the Co(III) species to the Co(I) species, with the Co(I) species being needed for the formation of Co(III) organo-cobalamins.[41]

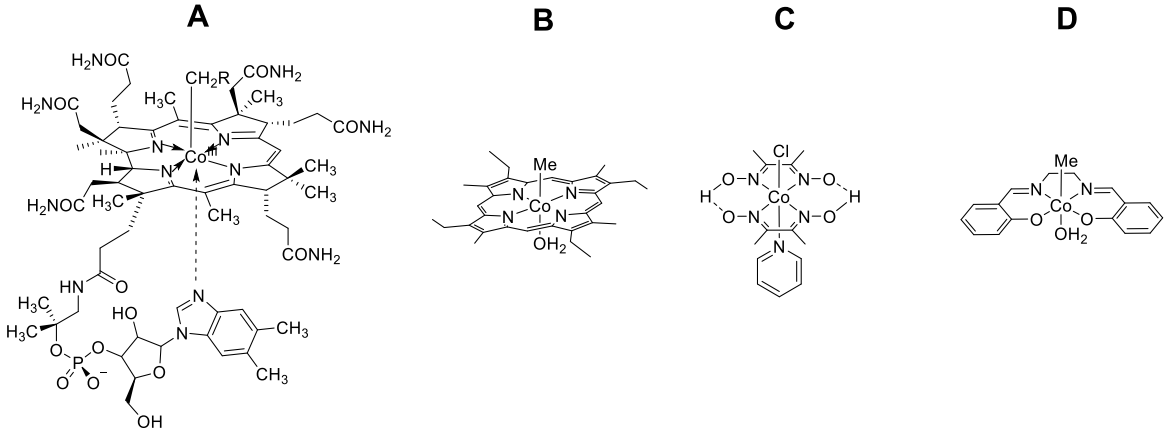

Figure 5. Structure of vitamin B_{12} and some model complexes.

1.3 Chemistry of Ruthenium

Ruthenium is the 80th most abundant element found on Earth and are among one of the rarest, with a natural occurrence of 10^{-7}% within the Earth's crust.[36, 42] Ruthenium exists with multiple oxidation states ranging from +2 to +8, with the +2 to +4 states being the most common.[36-37, 42] It is also known that ruthenium-containing complexes have the ability to be oxidized or reduced without any structural changes.[37] Ruthenium(II) complexes, Figure 6, are known for their stability and are almost always octahedral in structure.[43] These complexes are all low-spin thus are also all diamagnetic as well.[43-44]

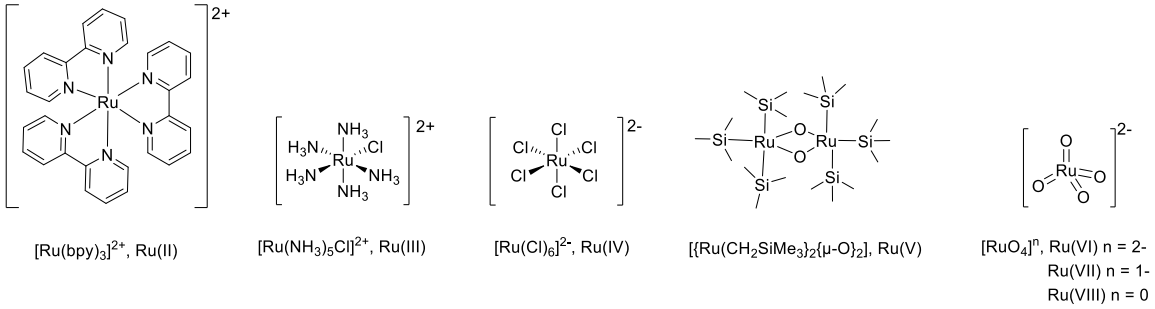

Figure 6. Ruthenium complexes with various oxidation states.[37]

Upon coordination of polypyridyl ligands to a ruthenium metal center many ruthenium(II) complexes have shown extraordinary properties such as photoinduced energy migration and charge transfer which produces the long lived triplet state excited ion, with the most famous being $[Ru(bpy)_3]^{2+}$.[37, 42] This excited ion is produced when an electron from the t_{2g} orbital is transferred to a π^* of the polypyridyl ligand producing Ru^{III}-$L^{\bullet -}$ which would decay back to Ru^{II}-L or could

transfer or receive an electron from the quencher.[37, 44] When L is a polypyridyl ligand such as bpy, the radical anion that is formed becomes a powerful reducing agent while the resulting Ru(III) species acting as a powerful oxidizing agent.[42] This is very evident in Figure 8, where the difference in potential between the different oxidation states of the ruthenium differ on average by about 1.26 V.[45] Upon coordination of polypyridyl ligands many ruthenium(II) complexes have shown extraordinary properties such as photoinduced energy migration and charge transfer which produces the long lived triplet state excited ion, with the most famous being $[Ru(bpy)_3]^{2+}$.[37, 42]

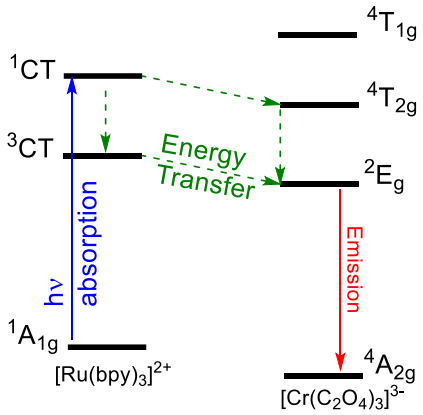

Figure 7. Energy diagram of the photoexcitation of $[Ru(bpy)_3]^{2+}$ and subsequent energy transfer to $[Cr(C_2O_4)_3]^{3-}$ .Reprinted with permission.[46]

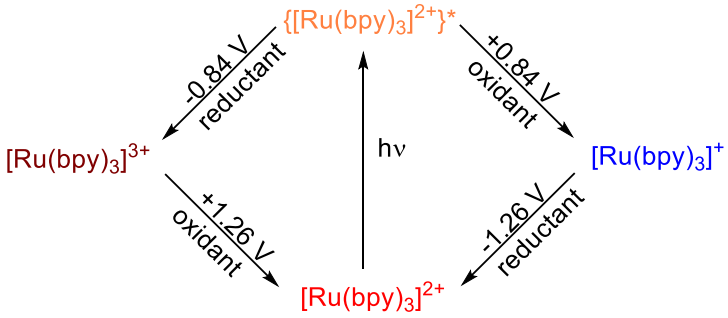

Figure 8. Redox and photo-chemistry of $[Ru(bpy)_3]^{2+}$.[45]

1.4 Artificial photosynthesis

Water-splitting consists of the hydrogen evolution reaction (HER) and the oxygen evolution reaction (OER). These two half reactions (the oxidation and reduction of water) are depicted below. [47]

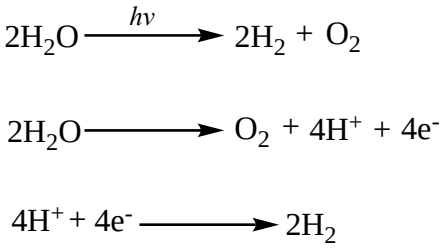

Figure 9. Half reactions for the production of molecular hydrogen and oxygen.[48]

Typically, photocatalytic systems that produce H_2 consist of a photosensitizer, an electron relay, a sacrificial electron donor, and a heterogeneous or homogeneous catalyst.[49] Wang *et. al.*[50] summarizes some of the progress for metal-based catalyst used in hydrogen evolution in homogeneous systems. Homogeneous systems have not been researched as much as heterogeneous catalytic systems for hydrogen production. Homogeneous systems are an attractive alternative because they can be covalently bound to photosensitizer (such as a ruthenium complex). This allows for more efficient electron transfer. Photosensitizer (light harvesting units such as $[Ru(bpy)_3]^{2+}$) have effectively harvested light in hydrogen production techniques. A key detail to note is the direct electron transfer from the excited photosensitizer to the catalyst must be favorable. Intermolecular electron transfer must be efficient for the catalytic proton reduction (production of hydrogen). [50] This a reoccurring theme in many research studies. Fihri *et al.* also stressed the importance of a molecular connection between the photosensitizer and the hydrogen evolving catalyst. This was made evident with their $[Ir(ppy)_2(L\text{-}pyr)Co(dmgBF_2)_2(OH_2)]PF_6$ complex (where ppy = 2-phenylpyridine and L-pyr = (4-pyridine)oxazolo[4,5-f]phenanthroline) (Figure 10) being able to produce more H_2 over the tested time of 15 hours when compared to its individual components.[51] Structural modifications of the bridging ligands should allow more efficient electron transfer between the light harvesting unit and the catalytic metal center. The photocatalytic activity can increase in efficiency if this is taken into consideration.

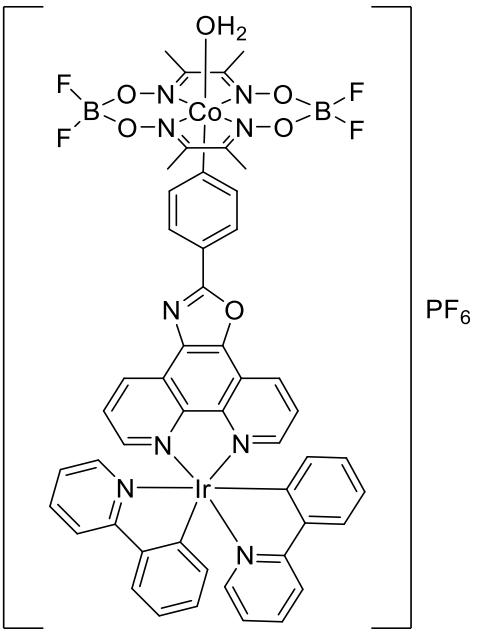

Figure 10. Structure of $[Ir(ppy)_2(L\text{-}pyr)Co(dmgBF_2)_2(OH_2)]PF_6$.[51]

Intrigued by photosynthesis like Lubitz and co-workers, we are curious about the natural catalyst that is created called photosystem II.[52] Water-splitting is the most common convention used to reproduce this process. However, the process of mimicking photosynthesis contains many variables that need to be considered. For instance, the catalyst's environment also determines the potential efficiency of the catalyst activity.[53] In comparison to aqueous environments, organic solvents are favored due to greater stability and different electrocatalytic behavior.[53] The photosynthesizer harvests the sun's energy and offers electron transfer through the bridging ligands to the catalytic metal center where the hydrogen evolution reaction takes place. Photosynthesis includes multistep electron transfer, which are common in many biological systems, and allow controlled kinetics of redox systems. [54]

One of the more well-known tandem artificial photosystems known is the artificial leaf designed by D. Nocera.[55] The artificial leaf has the ability to split water while producing oxygen, and is able to transfer the electrons internally to the opposite side of the leaf were the protons that it produces are reduced to form hydrogen, Figure 11. What should also be noted is the use of non-noble metals as the catalysts. The process begins at the cobalt cuboidal catalyst, which behaves like the manganese cuboidal structure found in photosystem II, where H_2O is oxidized to produce O_2. As it was noted by Nocera,[55] due to their catalyst being able to operate at a pH circa 7 they

were easily able to use the non-noble or in his words “nonprecious” metals nickel, molybdenum, and zinc which were electroplated on the surface of the leaf.

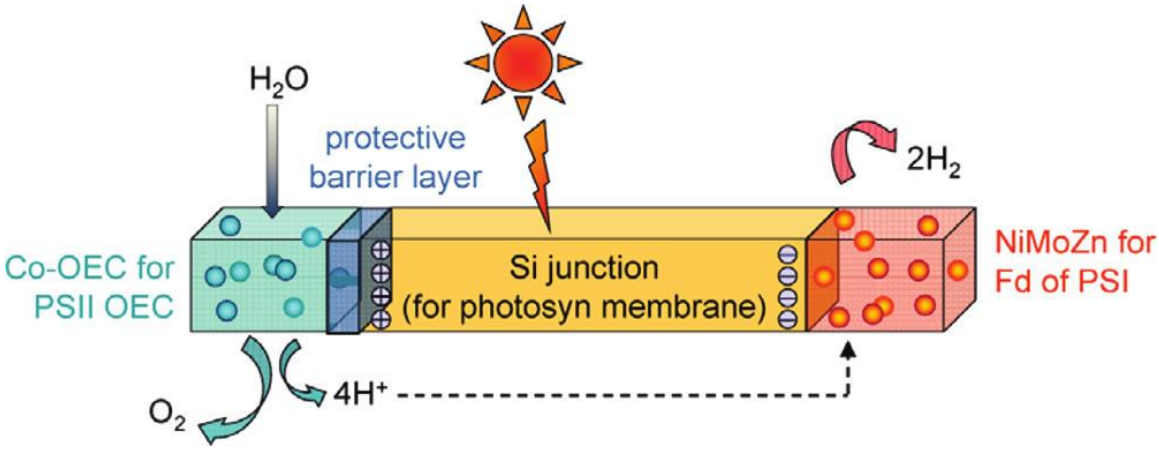

Figure 11. The artificial leaf with a Co-OEC water oxidation catalyst and a NiMoZn hydrogen evolution catalyst. Reprinted (adapted) with permission from (Nocera, D. G. *Acc. Chem. Res.* **2012,** *45* (5), 767-776.). Copyright (2020) American Chemical Society.[55]

Now if we take the simple design of the artificial leaf into consideration, we can then begin to design systems that use a similar motif all while keeping the hydrogen and oxygen separate. One example of this would be the work carried out by Mase *et al.*,[56] where in the presence of light their [$BiVO_4$/FeO(OH)] catalyst splits water to form oxygen. The electrons are then transferred to the next chamber via a wire while the protons would migrate to the other chamber by passing through a Nafion membrane. A similar system was also used by Sherman *et al.*,[57] where a binuclear Ru(II)-Ru(II) catalyst was used for the splitting of the water and a Pt electrode for the production of hydrogen. Their Ru(II)-Ru(II) catalyst is made up of a ruthenium(II) photosensitizer bridged to the ruthenium(II) oxygen evolution catalyst. Their complex was immobilized on the surface of an electrode, which allowed for the removal of the electrons from the system. The protons were then allowed to migrate from the chamber where they were produced to the chamber where they were ultimately reduced by a Pt electrode via a Nafion membrane.

The evolution of photocatalytic production has led to the advancement of technology for solar energy conversion and storage, especially when it comes to the individual production of H_2 and O_2.[58] Though, in many cases the back reactions and back electron transfers hinder the effectiveness of what photocatalytic production of these important gasses.[58-59] In the work of Miseki *et al.*,[58] they used a novel VO_2^{+}/VO^{2+} redox mediator which allowed them to photocatalytically produce O_2 and H_2 on the surface of their Fe−H−Cs−WO_3 and Ru/$SrTiO_3$:Rh

photocatalyst, respectively. When compared to conventional redox reagents such as Fe^{2+} and I^-, the hydrogen evolution rate that was observed for $Ru/SrTiO_3$:Rh using VO^{2+} redox was 2-fold higher.[58] The Z-scheme of water splitting, Figure 12, by the (Ru/ $SrTiO_3$:Rh)−(Fe−H−Cs−WO_3)−(VO_2^+/VO^{2+}) system was able to not only demonstrated both in the stepwise operation and in the conventional one pot operation; with the stepwise operation to produce H_2 and O_2 separately have exhibited enhanced performance when it is compared to the conventional one-pot operation.[58], with the efficiency of the system in the presence of simulated sunlight was estimated to be 0.06%. The importance of the Z-scheme lies in the fact that it models what occurs in nature with photosystems I and II.

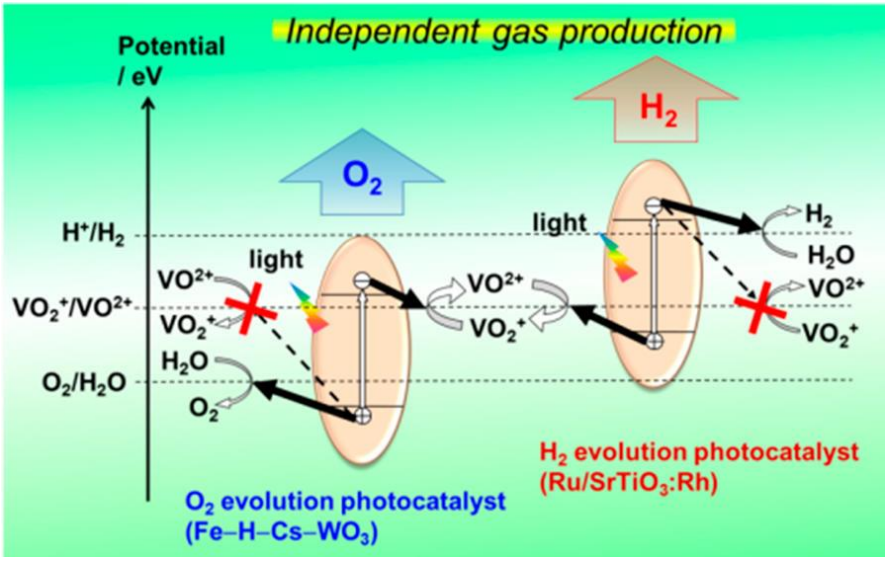

Figure 12. The Z-scheme of independent gas production of two-step water splitting system. Reprinted (adapted) with permission from (Miseki, Y.; Fujiyoshi, S.; Gunji, T.; Sayama, K. *J. Phys. Chem. C* **2017,** *121* (18), 9691-9697). Copyright (2020) American Chemical Society.[58]

1.5 Transition metal complexes that produce H_2

As early as 1972, the duo of Fujishima and Honda,[60-61] was able to photocatalytically produce H_2 using a TiO_2 photocatalytic electrode. It should also be known that the potential difference between two electrodes needed for electrolysis of water is greater than 1.23 V, and with a direct conversion of this value, a system powered by a 1000 nm light should drive this reaction forward.[60] Thus, the use of visible light would provide much more energy to drive this process of hydrogen production.[60] They even came up with three conditions for hydrogen production, where it was stated that this could happen even if no electrical potential is applied; (i) O_2 evolution must

occur at a potential more negative than H_2 evolution, (ii) H_2 evolution must occur at a potential more positive than O_2 evolution, and (iii) O_2 evolution must be more negative than H_2 evolution is positive.[60] There is only one problem, with TiO_2 because it has wide band gaps, they are not responsive to visible light which makes up about 43 % of the solar energy, but are responsive to UV light which makes up about 4 %.[61] Though the wide band gap can be changed via doping with material like recently with sulfide based catalyst.[61]

As mentioned above, the sacrificial electron donor is necessary for replacing the electrons that are used up in the production of H_2. Wang *et al*.[61] did a study with $Zn_{0.5}Cd_{0.5}S$, g-C_3N_4, and TiO_2 with various sacrificial donors. They studied four types of donors (pH), they being carboxylic acids (~2), alcohols (~6), amines (~11), and inorganic reactants (~13). Upon testing they observed that the Na_2S/Na_2SO_3 worked best with $Zn_{0.5}Cd_{0.5}S$, methanol with TiO_2, and triethanolamine with g-C_3N_4. But this shows how important it is to select the correct sacrificial electron donor which will help maximize the amount of H_2 that is produced. The concluded that for the organic donors, if they have lower oxidation potential and high permittivity are related to enhanced H_2 production when compared with the same catalyst.[61]

In 2016 Troppmann *et al*.,[62] reported on a hydrogenase Self-assembled vesicles where the ruthenium photosensitizer was either embedded or absorbed into/onto the membrane which was further functionalized by the adsorption of an [FeFe]-hydrogenase subunit mimic; this is observed in Figure 13. This study was conducted in water under acidic conditions, with one of the main takeaways being that when the membrane was present there was an observed increase in the amount of hydrogen that was produced ranging between a six- to twelvefold increase.[62] This is attributed to the close nature of the membrane keeping the hydrogenase close to the photosensitizer.[62] This type of system could also translate to the combination of both hydrophilic and hydrophobic catalytic complexes for light-driven proton reduction in acidic water which would provide a flexible method for membrane functionalization.[62]

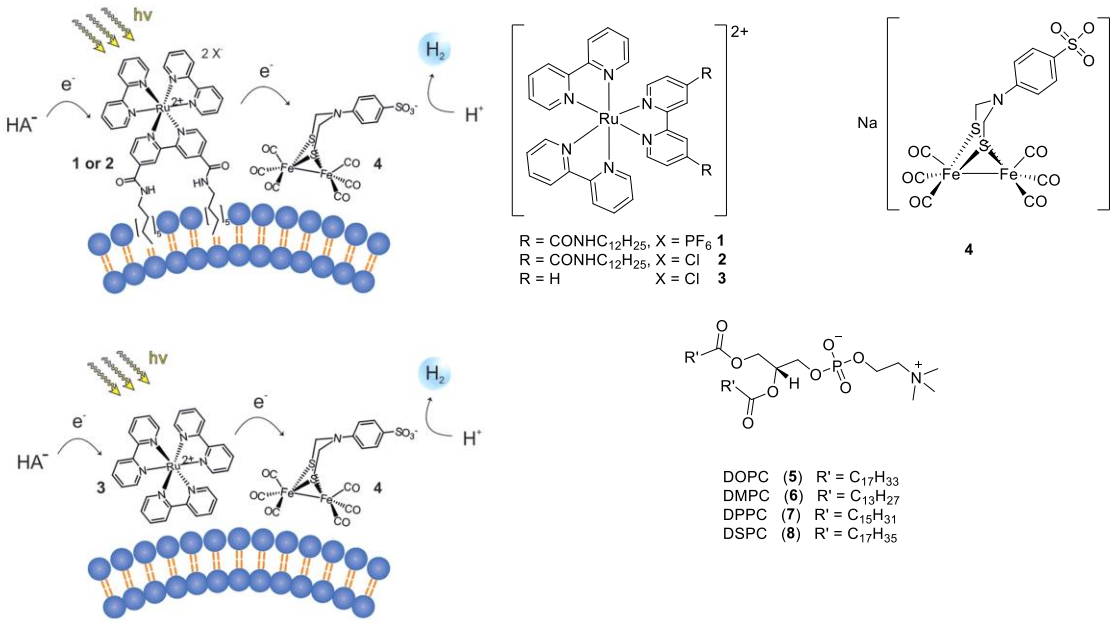

Figure 13. Ruthenium(II) photosensitizers (**1** – **3**), [FeFe]-H_2ase subunit mimic (**4**), and phospholipids (**5** – **8**) used for photocatalytic production of hydrogen on a phospholipid membrane.[62]

Hartley *et al.*,[63] conducted studies using iron(III) polypyridyl complexes, Fe-1 to Fe-3, which were observed to produce hydrogen in a mixture of EtOH:H_2O. For their complexes they were observed to have an optimal pH of 12.5, but the high pH is more attributed to triethylamine's preferred pH of operation. Complexes Fe-1, Fe-2, and Fe-3 were observed to have TON at 1132, 421, 545, respectively, with the sulfito ligand observed in Fe-2 forming a larger chelating ring when compared to the other two complexes which may contribute to the lower stability observed.

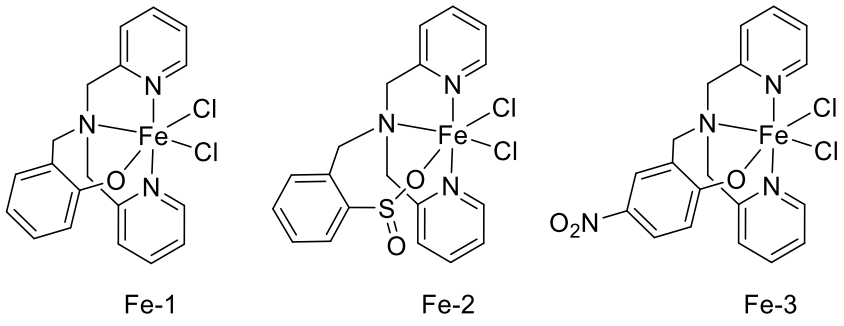

Figure 14. Structures of Iron(III) polypyridyl complexes.[63]

Nickel thiolate complexes have been shown great interests due to the sulfur-ligated complexes ability to mimic the [Fe-Ni]-hydrogenase active site, also, dimeric metal complexes

based on nickel hydrides have demonstrated significant catalytic activity.[64] Hydrogenases are special because they allow for bio-enzymes to catalyze protons and electrons into molecular hydrogen at a low overpotential that is close to the thermodynamic potential.[65] However, hyrdogenases of Fe, Ni, and Han and co-workers are specifically interested developing further knowledge about nickel(II) complexes containing pyridine-2-thiolate ligands. It was reported that great catalytic activity for hydrogen production came from the complex $[Ni(pyS)_3]$ with Fluorescein (Fl) being the photosensitizer and triethylamine (TEA) as the sacrificial electron donor.[65] Photolysis was used to monitor how much hydrogen gas was produced.

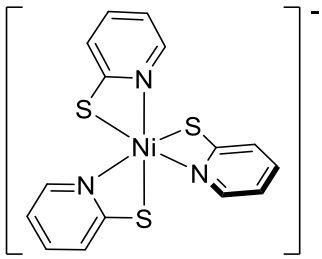

Figure 15. Nickel(II) complex containing pyridine-2-thiolate ligands.[65]

The structure above depicts a nickel(II) complex containing pyridine-2-thiolate ligands. For over two decades, nickel(II) containing complexes with pyridine-2-thiolate ligands has not been studied for its catalytic activity. However, Han and co-workers have decided to discover and analyze pyridine-2-thiolate for its catalytic activity. Recently, pyridine-2-thiolate has exemplified exceptional catalytic activity. It is now believed to demonstrate the same in photocatalytic production of H_2.

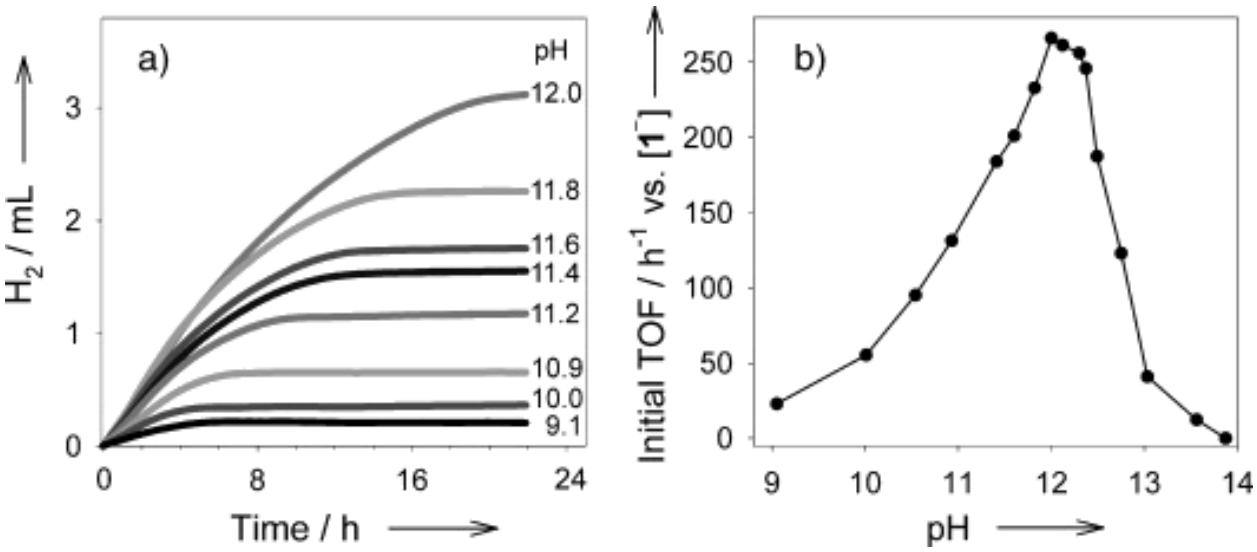

Figure 16. Graph (a) shows the amount of hydrogen gas produced from systems containing pyridine-2-thiolate. The systems were exposed to light at different pH levels. Graph (b) shows the effect of the pH on the original rate of hydrogen. Reprinted with permission.[64]

It was shown that $[Ni(pyS)_3]$ highly generated H_2 at the basic pH of 12.0 to 12.4. At the higher pH values there was a dramatic decrease in the hydrogen production rate.[64] This is probably due to the lower proton concentration in solution and the fact that H_2 generation becomes more thermodynamically unfavorable with increasing pH values. In contrast, lowering the pH value from 12.0 to 9.0 led to both a lower initial rate of H_2 production and shorter system longevity. [64]

Lv and co-workers[47] have found a Ni_4P_2 to be a robust catalyst via photocatalytic production due to its ability to perform efficiently under various conditions. Specifically, a tetra-nickel containing polyoxotungstate $Na_6K_4[Ni(H_2O)_2\ (PW_9O_{34})_2]\cdot 32H_2O$ (Na_6K–Ni_4P_2) was the complex that was synthesized. An iridium complex, $[Ir(ppy)_2(dtbbpy)]^+$ was used as a photosensitizer, and triethanolamine (TEOA) was used as a sacrificial electron donor. Typically, Ru(II) complexes are used a photosensitizer, but $[Ir(ppy)_2(dtbbpy)]^+$ was found to have better intramolecular electron transfer. Overall, polyoxometallates (POMS) are favorable as catalysts because they can be manipulated extensively and can maintain stability during hydrolysis in water or hydrogenation under reducing conditions.[47] Their ability to be manipulated extensively allows them to respond to reaction requirements.[66] Ensafi and co-workers found POMS to a promising class of hydrogen evolution catalysts.[66] Favorably, polyoxometallates are also soluble in water and are sometimes considered to be "the smallest nanoparticles" which have extra-large "surface area" to contact water.[67] POMS also have the properties of super-acidity and a good proton conductivity; this allows them to positively impact the kinetics of a hydrogen evolution reaction.[66]

Many polyoxometallates properties compare with metal oxide semiconductors;[66] this increases their favorability rating as a catalysts for H_2 production. It was reported by Lv and co-workers that Ni_4P_2 has the highest value for a noble-metal-free polyoxometallates catalyzed H_2 evolution system due to its ability to maintain stability and performance for a week with a turnover rate of 6500.[66] However, there are only a few reports that show polyoxometallates as water-reducing catalysts being successful at operating under the visible light spectrum, most studies show them working with UV light irradiation.[11] Knowing this, researchers believe that polyoxometallates could be more effective under the influence of visible light when organic dye is used to make them more sensitive to the light source.[67]

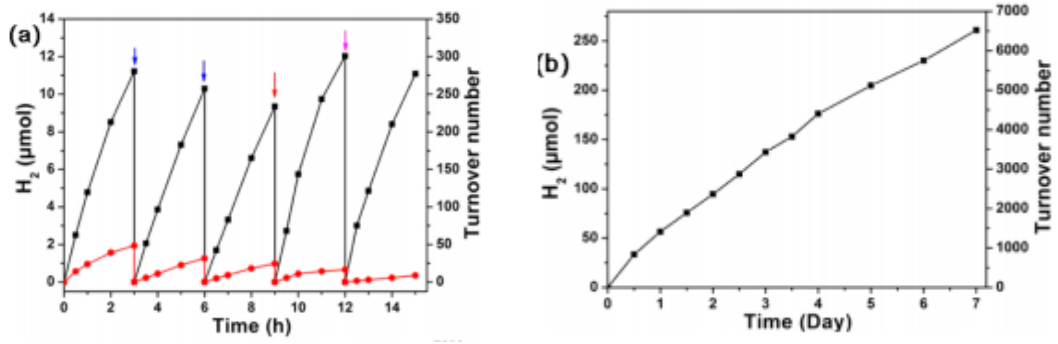

Figure 17. Graph a) depicts photocatalytic H_2 production using molar amounts of the catalyst Ni_4P_2 (black curve), and molar amounts of $NiCl_2$ (red curve). Also, graph a) was under the influence of LED light, the photosynthesizer, TEOA, and CH_3CN/DMF, and deaerated with Ar. Graph b) depicts a long-term version of H_2 reduction. In addition, graph b) consists of the same material as graph a) but at different amounts. [68]

The use of cobalt-containing catalysts for the production of hydrogen have been studied for many years.[69] Most of the cobalt catalyst are seen to be catalytically active systems when they have a square-planar macrocyclic or pseudo macrocyclic ligand.[70] The process of direct light-to-chemical energy conversion mastered by photosynthetic organisms like plants, requires the efficient coupling of an hydrogen evolution catalyst to a photosensitizer via a bridging ligand.[71] In many past studies, tandem ruthenium(II)-cobalt(II) complexes (Figure 18) were observed to have increased catalytic yields when compared to if the metal complexes were mixed as two separate complexes.[20] In 2008, Fihri *et al.*,[72] synthesized mixed metal ruthenium(II)/iridium(III)-cobalt(II) complexes where the metal centers were bridged to via (4-pyridine)oxazo[4,5-f]phenanthroline which had maximum turn over numbers (TON = $\frac{mol\ H_2}{mol\ cat.}$) of 165 and 210 for their ruthenium(II) and iridium(III) complexes, respectively. Later Cropek *et al.*,[73] synthesized repeated the same synthesis with the ruthenium(II) complex, but instead of using 2,2'-bipyridine as the

terminal ligands either 1,10-phenanthroline (phen) or 2-(2'-pyridyl)benzothiazole (pbt). With volumes of H_2 that they reported, the calculated TON were about 4658 and 14256 for phen and pbt, respectively, which were much higher than its predecessor. However, these are not the only instances of multinuclear mixed metal complexes. There are others such as Rau,[74] Sakai,[75], and Elvington[26] who have dedicated many years into the development of mixed metal complexes that were able to produce hydrogen in the presence of simulated sunlight.

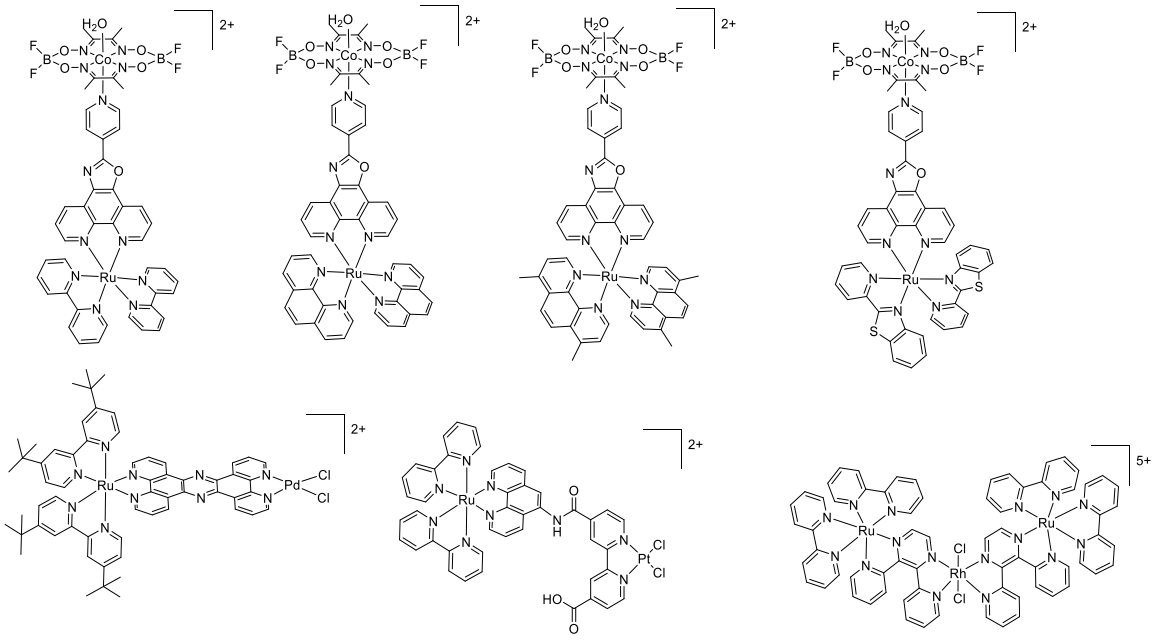

Figure 18. Multinuclear mixed-metal complexes that have been reported to produce H_2 with simulated sunlight. [26, 72-75]

1.5.1 Chemistry of cobalt and its use as a H_2 evolution catalyst

Cobalt which is normally found in nature with nickel and arsenic in the form of the minerals smaltite ($CoAs_2$), cobaltite (CoAsS), and linnaeite (Co_3S_4)[37, 76], has many properties of interest, especially when it comes to the production of hydrogen. The +2 and +3 oxidation states are the most common oxidation states with the +3 oxidation state being known to be kinetically inert.[76]

The use of cobalt containing catalysts for the production of hydrogen have been studied for many years.[69] Many cobalt catalyst have been observed to be catalytically active when they have a square-planar macrocyclic or pseudo macrocyclic ligand (Figure 5B-D).[70] The process of direct light-to-chemical energy conversion mastered by photosynthetic organisms like plants, requires

the efficient coupling of an hydrogen evolution catalyst to a photosensitizer via a bridging ligand.[71] In many past studies, tandem ruthenium(II)-cobalt(II) complexes were observed to have increased catalytic yields when compared to if the metal complexes were mixed as two separate complexes.[20]

For the last three decades there have been many studies that was carried out on both heterogeneous and homogeneous catalyst where the photosensitizer is covalently bonded or not, respectively, that when irradiated are able to produce hydrogen from protons from water.[71] $[Ru(bpy)_3]^{2+}$ in the presence of $[Co(bpy)_3]^{2+}$ has been observed to produce H_2 in aqueous media, but the best results was seen in a solution with 50% MeCN.[77]

The use of cobalt(III)-containing such as $[Co(phen)_2(phendione)](PF_6)_3$ (where phendione = 1,10-phenanthroline-5,6-dione) or $[Co(phen)_3]^{3+}$ have been observed to have the ability to produce hydrogen in the presence of a photosensitizer (e.g. eosin Y or $[Ru(bpy)_3]^{2+}$) and a sacrificial electron donor (triethylamine or *L*-ascorbic acid).[22, 78] Unlike with the cobaloximes, when the complexes are reduced to form the cobalt(I) species, there is not decrease in the coordination number thus all six coordination sites remain occupied by the N-N ligands as observed in Figure 19.[79] This is different from what was observed with Sutin and coworkers,[34, 80-81] where when $[Co(bpy)_3]^{n+}$ is reduced to the cobalt(I) species when the solvent is bombarded with electrons which causes the loss of one of the bpy ligands which were observed in many cases as $Hbpy^+$. The loss of one of the ligands could contribute to decomposition of the complex which would also lead to low turnover numbers which have been noticed with complexes of this nature, especially when compared to catalyst based off cobaloximes.

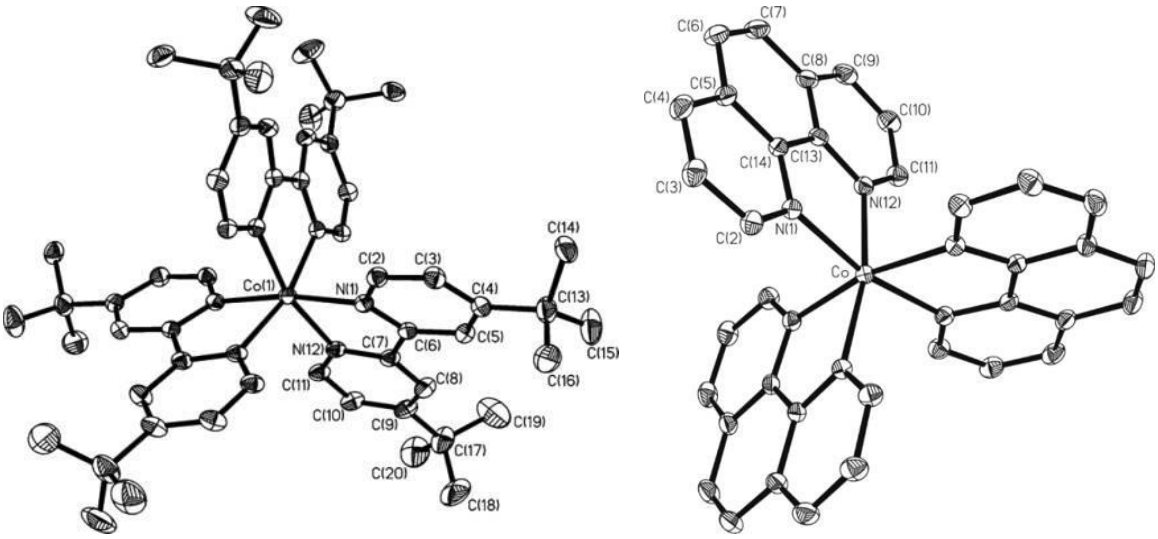

Figure 19. Crystal structures of monocation $[Co^I(^tbpy^0)_3]^+$ and $[Co^I(^tphen^0)_3]^+$.

Not only can these type of complexes act as hydrogen evolution catalyst, they could also act as electron mediators as seen in Figure 20.[82]

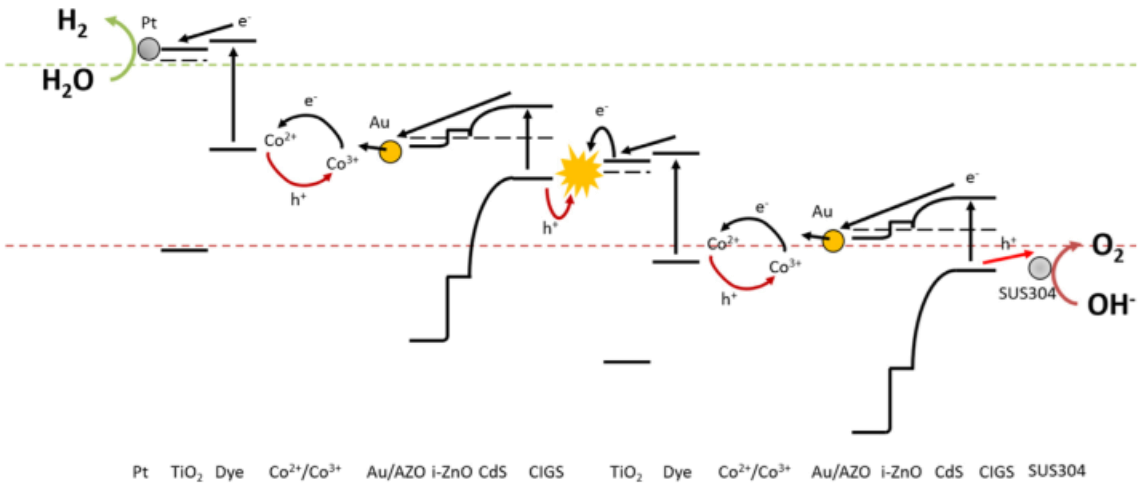

Figure 20. Schematic charge flow within the proposed PV electrolysis cell equipped with two DSSC/CIGS tandem solar cells, a Pt cathode, and a SUS304 anode for photoelectrochemical water splitting.[82]

1.6 Photosensitizers

Many times, the process of electron transfer from the ruthenium photosensitizer to the hydrogen evolution catalyst (HEC) is not investigated, but it has been observed on many occasions that the ruthenium photosensitizer can utilize two distinct pathways, Figure 21. The two pathways are dependent on the type of electron process that occurs when the photosensitizer is in its excited state. With the oxidative mechanism, the most commonly stated mechanism, the photosensitizer first transfers its excited electron to the HEC before it is replenished by the sacrificial electron donor.[83] On the other hand the reductive mechanism proceeds with an electron transfer from the sacrificial electron donor to the excited photosensitizer before reduction of the HEC.[83] The preferred mechanism for either pathway can be identified through photophysical quenching studies in which by the early 1980s there was a vast ocean of amounts of information on photoinduced electron transfer involving $[Ru(N\text{-}N)_3]^{2+}$ (where N-N = bpy or phen).[83-84] From calculations it was observed that the excited state redox potentials that were calculated from the ground state as well

as the excited state showed that the photoexcited $[Ru^*(bpy)_3]^{2+}$ is not only a strong reductant but also a good oxidant as well.[85]

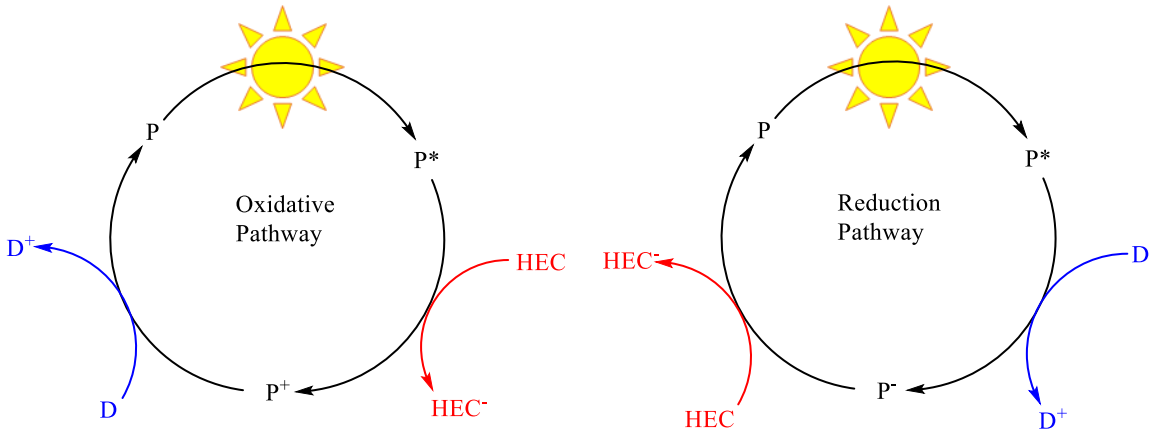

Figure 21. Possible photochemical mechanisms for catalyst reduction in a homogeneous system for hydrogen production involving a HEC.[83, 86-87]

1.6.1 Organic dyes

Traditional photosensitizers used in homogeneous photocatalytic systems, are most commonly made up of expensive transition metal complexes such as ruthenium(II) or iridium(III).[88] However, there is also are many examples of organic dyes also being utilized for this process such as bodipy and eosin Y (Figure 22). There was a study conducted on the use of the organic dye triazatriangulenium (TATA+) which was utilized as a photosensitizer that was able to facilitate in the production of H_2 in acidic water. With their dye, tris(ethoxyethanol)triazatriangulenium, cobalt catalyst and ascorbic acid the as sacrificial electron donor, they were able to produce H_2 with their best results observed at pH 4.5 when it was irradiated with visible light. Under the same conditions they observed that their dye was out preforming $[Ru(bpy)_3]^{2+}$ which was attributed to the stability of $TATA^{\bullet}$ when compared to $[Ru(bpy)_2(bpy^{\bullet-})]^{+}$. Under the conditions used the $TATA^{\bullet}$ was observed under nanosecond transient experiments to form when the singlet excited state of $TATA^{+}$ was quenched by the sacrificial electron donor. The $TATA^{\bullet}$ would then transfer the electron to the cobalt catalyst which then were able to monitor through the formation of the Co(I) species.

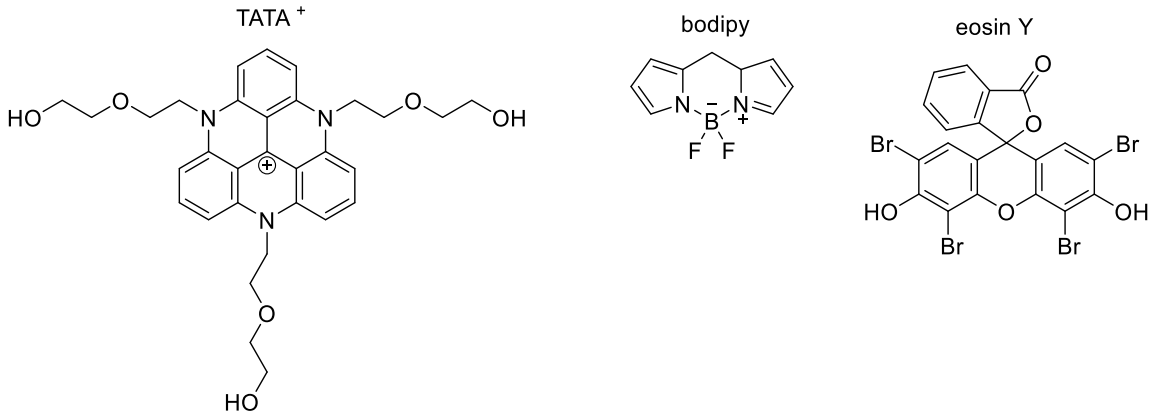

Figure 22. Selected organic photosensitizers.[49, 88-89]

1.6.2 Ruthenium and iridium-based complexes

As was stated above with the organic dyes, there is a fundamental problem with the traditional ruthenium(II) photosensitizers which are rooted in their instability during the catalytic production of hydrogen. Photophysical studies are typically done to observe which pathway is more favorable. In the figure below, Figure 23, the quenching of the excited $[Ru(bpy)_3]Cl_2$ is monitored through the decay of its fluorescence signal. On its own the excited ruthenium(II) complex will naturally go back to its ground state, but when either the complex or ascorbic acid is added the observed rate for the quenching of the ruthenium is observed to increase. When comparing the two quenching rates the ascorbic acid quenches the excited ruthenium faster than the complexes, thus it is safe to say that this system follows that of the reductive pathway.

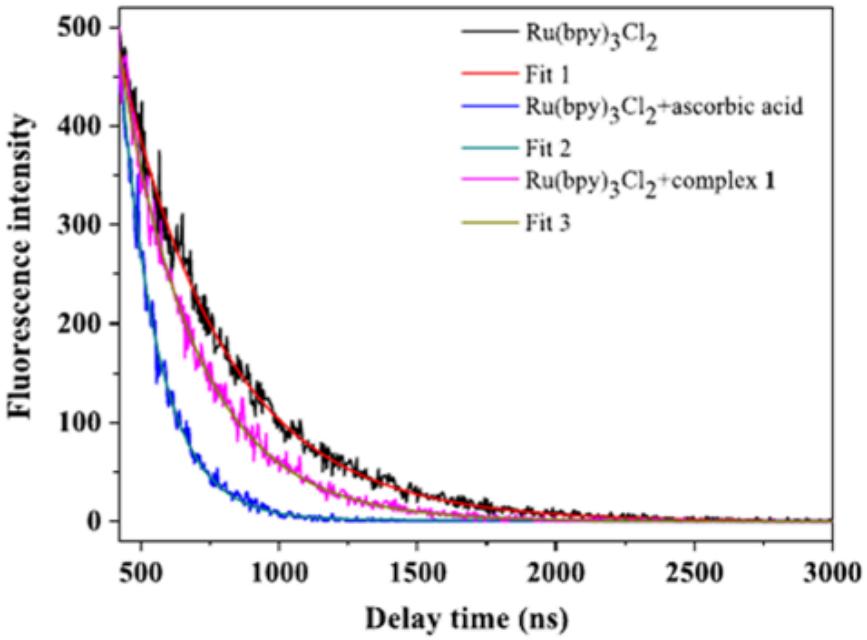

Figure 23. Fluorescence quenching of $[Ru(bpy)_3]Cl_2$ in aqueous buffer solutions at pH 5.5 after the sequential additions of $[Co(phen)_2(CN)_2]ClO_4$ (complex 1) or *L*-ascorbic acid.[90]

$[Ru(bpy)_3]^{2+}$ (where bpy = 2,2′-bipyridine, Ru-1) again is the go to photosensitizer in many photocatalytic studies.[91] This is due largely to the ^{3}MLCT state (metal-to-ligand charge transfer, $\pi_M \rightarrow \pi_L^*$).[91] Yet, it is plagued with a photostability and excited state lifetime (<1 μs), but in the study conducted by Guo *et al.*,[91] they were able to increase the stability of the photosensitizer by modification of one of the terminal ligands. Their two complexes used in the study were $[Ru(bpy)_2$(3-pyrenyl-1,10-phenanthroline)$]^{2+}$ (Ru-3) and $[Ru(bpy)_2$(3-pyrenyl ethynylene-1,10-phenanthroline)$]^{2+}$(Ru-4) that through testing was observed to have a ^{3}IL/^{3}MLCT equilibrated state and ^{3}IL state (intra-ligand charge transfer, $\pi_L \rightarrow \pi_L^*$) as lowest excited state, respectively. In the case of Ru-4 which had the best performance of the four photosensitizers used, the ^{3}IL state was observed to be long-lived lasting up to 120 μs with no significant photobleaching over 13 hours, when compared to Ru-1 and $[Ru(bpy)_2$(1,10-phenanthroline)$]^{2+}$ (Ru-2) which photobleaching was observed within the first 30 minutes. The photocatalytic reactions were carried out with the ruthenium(II) photosensitizers, $[Co(dmgH)_2pyCl]$ as a HEC, and N, N-dimethyl-p-toluidine (DMT) as an electron donor. The longer-lived Ru-3 and Ru-4 had significant enhancements to their catalytic performance when compared to Ru-1 and Ru-2, with Ru-4 having a TON of 9140 with a TOF of 6.3 min^{-1}. The reductive quenching mechanism was observed to be the more dominant mechanism from their study with the subsequent electron transfer to the catalyst having

similar orders of magnitude. A possible explanation for the enhancement observed lies within the pyrene moiety which can not only increase charge separation which allows for the resulting hole to combine with an electron from the sacrificial donor and the effective delocalization of the excited electron before it is transferred to the HEC.

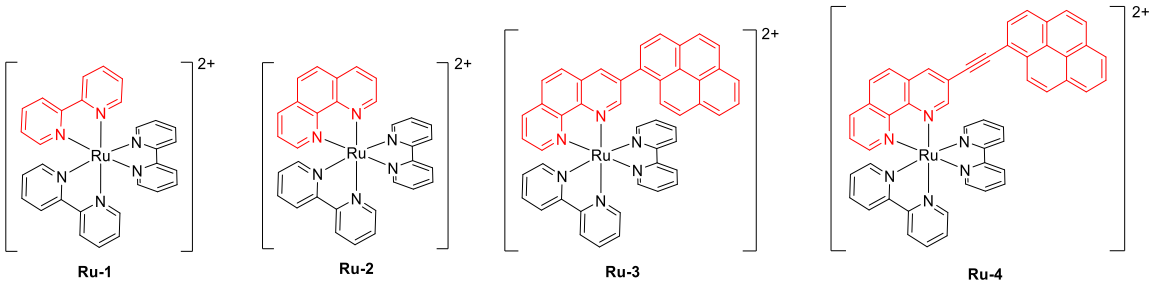

1.7 Sacrificial electron donors used in the photocatalytic production of hydrogen

In 2017, M. Natali,[92] reported on the use of *L*-ascorbic acid as a sacrificial electron donor photosensitizer in the presence of a Ru photosensitizer and a cobaloxime. In his study he investigated the effects that pH has on the production of hydrogen using a cobalt HEC, which was modeled after a study conducted by Reynal *et al*.[93] where they used a Ni (Dubois) catalyst for the same process. In Natali's study, it was observed that with ascorbic acid there was a preference for reductive quenching at a pH between 3-5.5 and the Co(I) protonation favoring a pH between 5-8. In his study, there was a case where an overlap of both processes gave way to highest turnover number.

When producing hydrogen in many studies an extra source of electrons is used to drive the reaction forward. These sacrificial electron donors all vary in structure. In the majority of photocatalytic experiments carried out where hydrogen is produced, the use of a sacrificial electron donor is seen as a must,[20-21, 94] though the main goal is for the electrons to be supplied by the medium water.

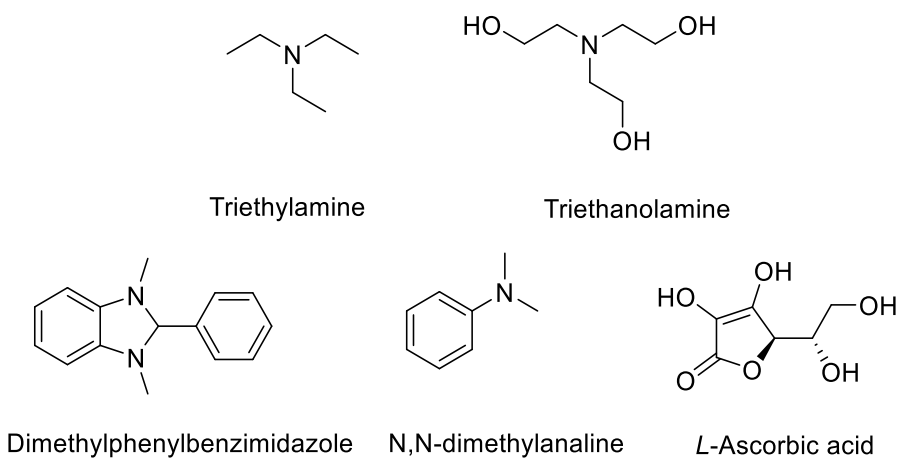

Figure 24. Commonly used sacrificial electron donors.[95]

Though the sacrificial electron donor supplies the system with the electrons needed, it can also be proven problematic if back electron transfers were to occur. In Scheme 1, the typical mechanism for the formation of the cobalt(I) species by the reductive pathway. When choosing a sacrificial electron donor it is important to pick one that will transfer its electron to the photosensitizer and the radical cation that is formed would decompose in solution. In the paper by Rodenberg *et al*.,[59] they postulated based on their data that the radical cation that is formed after the electron is transferred can react with the reduced photosensitizer and the cobalt(I) species, as well as three pathways where the radical is deactivated.

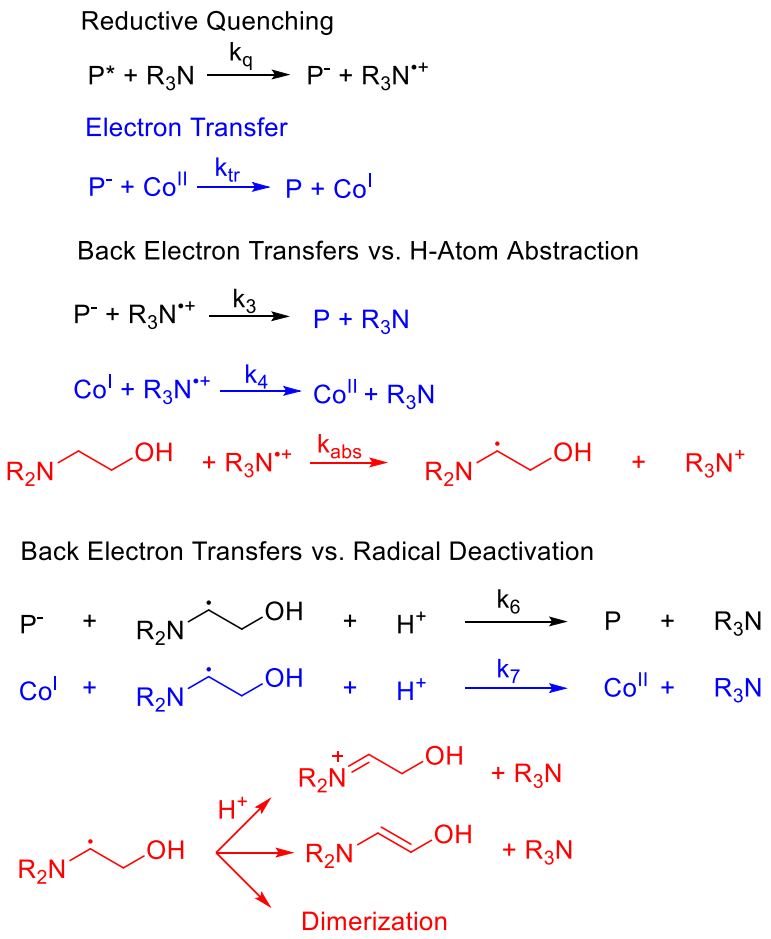

Scheme 1. Mechanism for the electron transfer and formation of the Co(I) species.[59]

1.8 Reactions of alkylated amines with transition metals

In the 50's to the 70's the York group and others studied the reaction between amines and transition metals, with a majority of them focusing on copper.[96-102] It is observed that the oxidizability of amines tends to increase with the more aliphatic groups on the amine as illustrated by the following, $R_3N > R_2NH > RNH_2 > NH_3$.[96] However, this is the opposite when it comes to coordination with the tertiary aliphatic amines tending to coordinate the least to the metal center, as seen in the table below with metal halides.[103]

Table 1. Interaction between metals and aliphatic ethylamines.[103]

Metal/amine	Et_3N	Et_2NH	$EtNH_2$
Ca	NR	NR	2:1 (4:1)
Zn	NR	2:1	2:1 (5:1)
Co(II)	1:1	2:1	2:1 (6:1)
Ratios given are amine:metal, and values in parentheses are the maximum recorded.			

Yoke and company,[103] conducted several studies with copper halides. In their study with copper(I), it was observed that the only observable interaction between the metal center and triethylamine was that they coordinated in a 1:1 fashion, which was a stark difference to what was observed with the zinc halide.[103] When compared to copper(II) study where it was observed that the ratio of coordination between the copper(II) metal center to triethylamine was 1:2.[103] As well as when copper(II) chloride suspended in chlorobenzene was treated with triethylamine and was worked up with water, released what was characterized as copper(I) as well as the release of the volatile acetaldehyde leaving behind a tarry product, illustrated in Scheme 2.[103] The formation of the acetaldehyde indicated that the triethylamine was oxidized to at least diethylvinylamine. It was noted that in their reaction with of one mole of copper(II) chloride reacting with 2 moles of triethylamine, only about $\frac{1}{6}$ moles of the triethylamine was oxidized which leads to the notion that trivinylamine was produced since 1.84 moles of the triethylamine was recovered.[98] The final product tarry product was then noted to be the result of an eneamine polymerization reaction which can be compared to an aldol condensation.[98]

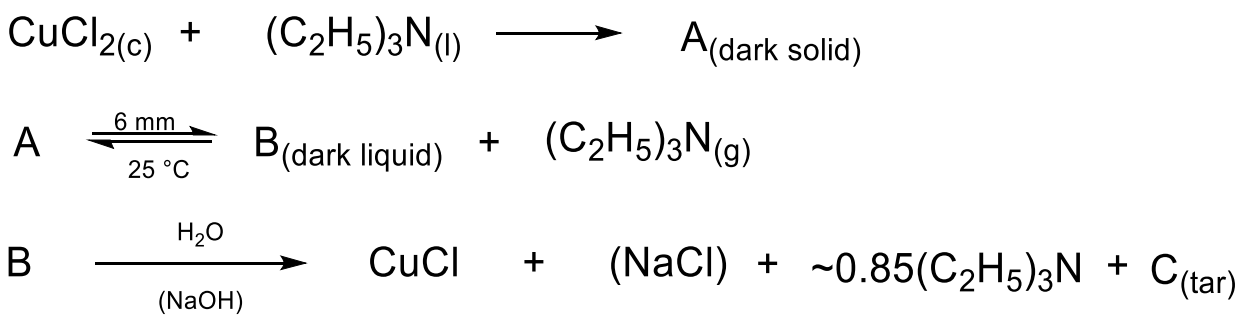

Scheme 2. Reaction with $CuCl_2$ with Et_3N.[103 1964]

1.9 Chemistry of NaOX, $NaXO_3$, and X_2 as oxidants, X = Cl or Br

In terms of stability hypohalites tend to be unstable especially when concentrated and even when it is diluted and the temperature is above room temperature.[104] With decomposition occurring over a wide pH range (4.8 – 13.5) and has a second order rate; with the decomposition occurring between the hypohalites.[104]

In terms of stability hypohalites tend to be unstable especially when concentrated and even when it is diluted and the temperature is above room temperature.[104] With decomposition occurring over a wide pH range (4.8 – 13.5) and has a second order rate; with the decomposition occurring between the hypohalites.[104]

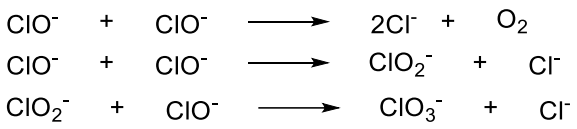

Scheme 3. Decomposition of hypochlorite.[104]

Metal oxides have been utilized to decompose hypohalites especially hypochlorite and hypobromite. In 1977 Gray *et al*.,[105] studied the mechanism for decomposition both hypochlorite and hypobromite in the presence of copper(II) hydroxide.[105] studied the mechanism for decomposition both hypochlorite and hypobromite in the presence of copper(II) hydroxide. [105] studied the mechanism for decomposition both hypochlorite and hypobromite in the presence of copper(II) hydroxide. In their study the two electron oxidant reacted with a binuclear copper(II) species that was formed *in situ* under very basic conditions. The hypohalite then coordinates and bridges the two copper(II) metal centers which allows for an inner-sphere electron from each metal center to the hypobromite.[105]

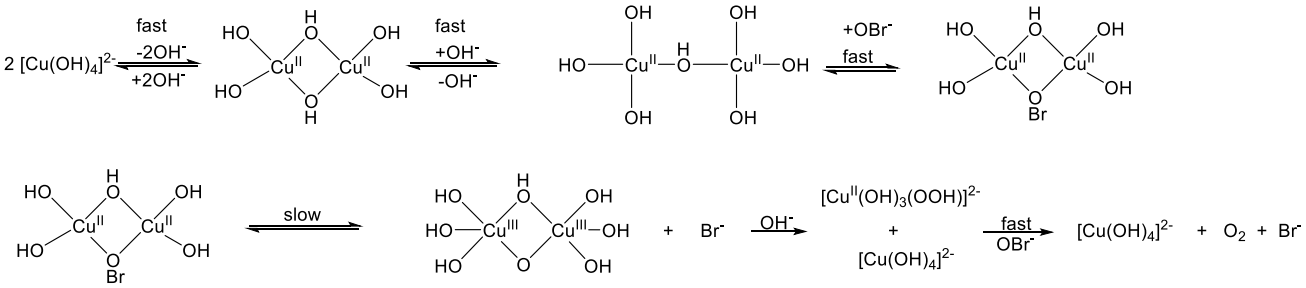

Scheme 4. Mechanism of decomposition of hypobromite in the presence of copper(II) hydroxide.[105]. Mechanism of decomposition of hypobromite in the presence of copper(II) hydroxide.[105]. Mechanism of decomposition of hypobromite in the presence of copper(II) hydroxide.[105]

1.10 High field electron magnetic resonance

As energy and magnetic fields have a perpendicular but proportional relationship, it is easy to see that when one is changed an induced response is observed by the other. For electron magnetic resonance (EMR) measurements the energy added to the system is represented by its frequency which ranges from 1 – 1000 GHz.[106] These frequencies can be broken up with some obtaining special names such as L-, S-, X-, K-, Q-, and W-band, which represents specific frequencies circa 1, 3, 9, 24, 35, and 94 GHz, respectively.[107] The X-, Q-, and W-band frequencies are typically used for commercial instruments, with instruments utilizing radiation frequencies above 70 GHz being labeled as high field instruments.[108]

Within electron paramagnetic resonance (EPR) measurements the molecule/compound/complex that is being analyzed must have at least one unpaired electron and the signal that is produced is unique to that analyte. As it is common knowledge, electrons spin and their spin states that are either ±½, which in the presence of a magnetic field aligns itself to the poles. In EPR measurements, the energy added to the system is held constant while the magnetic field is changed or vice versa, and when the conditions are optimal the electron will flip, and this is represented by the following simplified equation: $\Delta E = g|\mu_B|B_0$, where ΔE is the change in energy, μ_B is the atomic unit of the magnetic moment, and B_0 is the magnetic field.[108] When analyzing an EPR spectrum the resonating/absorbance peak is not an identifier for the compound cause it can shift positions based on the radiation frequency used, but the g-factor which is independent of the radiating frequency is.[107] This is illustrated in Figure 25, in which as the radiating energy is increased, so does the position of the absorbance peak. However, if radiation energy used and the magnetic field at the peak of the absorbance is inputted into equation above, in all three instances the value for the g-factor for that specific absorbance will be the same. Due to the g-factor being independent of the radiation frequency, another effect is also observed in terms of spectral resolution. Again in Figure 25, as the radiating frequency is increased from acquisition 1 to acquisition 3 a significant improvement in the resolution is observed, which is due to a separation in the spin Hamiltonian of the field-dependent interactions from the field-independent ones.[109]

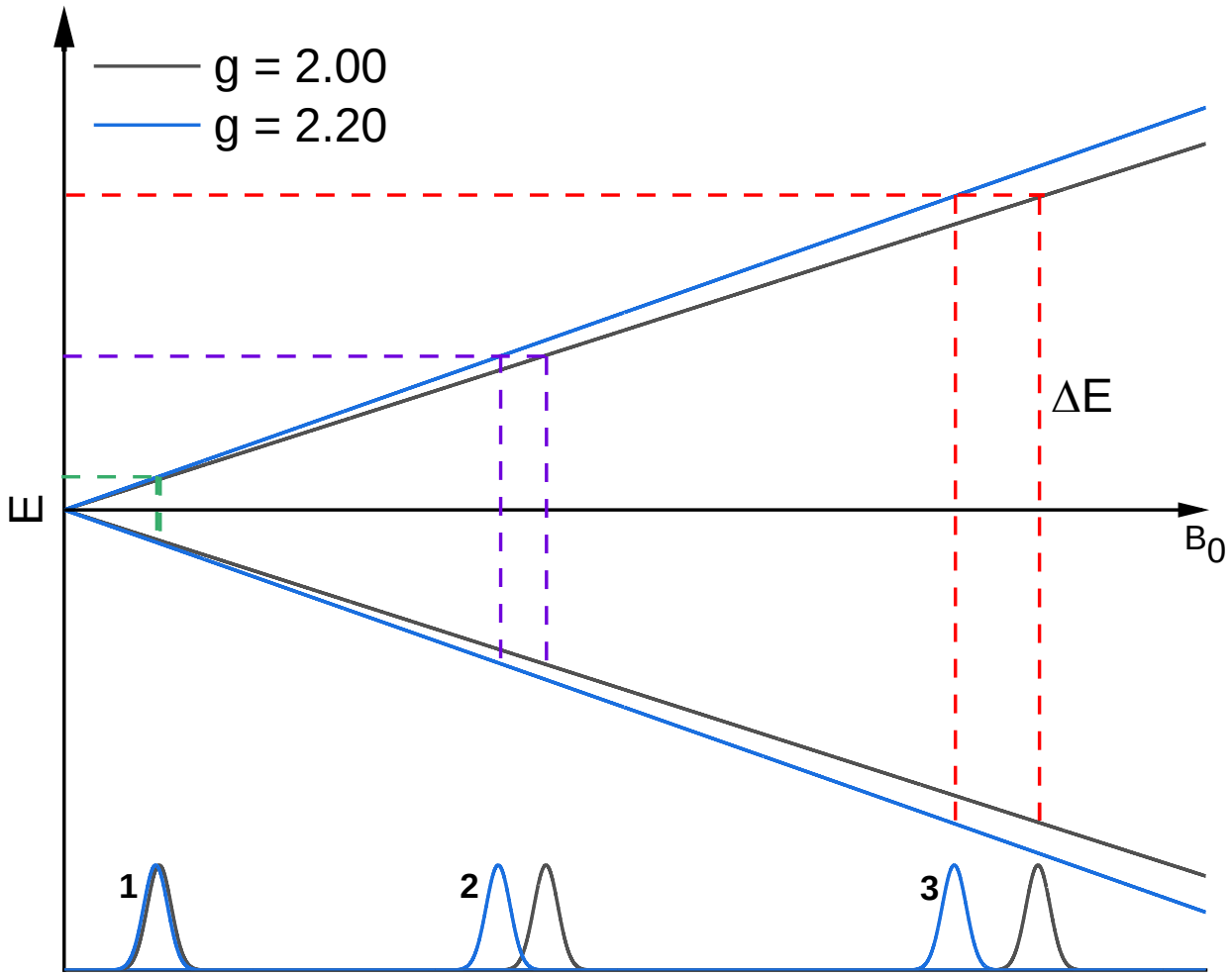

Figure 25. Enhanced spectral resolution with increasing magnetic field.

With high spin cobalt(II) complexes there is a stark difference between the tetrahedral geometry compared to if it was in the octahedral configuration. The Zeeman energy split for octahedral high spin cobalt(II) complexes are typically large (D = 100 cm^{-1}) while tetrahedral high spin cobalt(II) complexes are small.[110] Due to this, it make HFEPR measurements preferred over conventional EPR measurements especially when complexes have such large zero-field splitting (zfs) energies like high spin octahedral cobalt(II) complexes. With cobalt(I) complexes due to their reactive nature it is hard to isolate the complex that is air stable, however, there have been some cases such as with the [$CoX(PPh_3)_3$] (where X = Cl, Br, or I) complexes which showed activity at liquid helium temperatures.[111] It should be noted that the Co(I) species is isoelectronic to Ni(II) complexes. From their studies they were able to calculate the ZFS (D) as +4.46, +5.52, and +8.04 cm^{-1} for [$CoCl(PPh_3)_3$,[111] which is very similar to that of tetrahedral cobalt(II) complexes.

In a study with various vanadium(IV) complexes with dipicolinic acid analogues, the spectra produced by the X-band measurements occurred between 3100 to 4100 G with the classical hyperfine splitting observed for vanadium.[112] The HFEPR spectrum at 224 GHz of one of the complexes, $[V(dipic)(Hdipic)(OH_2)]\bullet 3H_2O$, the first noticeable difference was the disappearance of the hyperfine signals and in the simulations when the zfs energies was larger and smaller than zero showed no change when compared to the acquired spectrum. This was due to the complex only having one unpaired electron as the zfs energy only affects paramagnetic species with more than one unpaired electron.

1.11 Project Aim

For many years, my mentor has been interested in the development of transition metal complexes that contain at least one cobalt metal center,[73, 113-119] and also inorganic reaction mechanisms that involve electron transfer processes.[113-114, 120-121] The current aim of this study is to synthesize various cobalt(III)-containing complexes for the purpose of producing hydrogen either photocatalytically or electrochemically. The main focus of the project is the synthesis of trinuclear mixed-metal complexes whose ability to produce H_2 will be tested.

The process of producing H_2 involves electron transfer processes, thus we studied the oxidation of the cobalt(II) metal center of $[Co(dmgBF_2)_2(OH_2)_2]$. Though this is moving in the opposite direction that we are interested in, the information gained is beneficial in the understanding of the overall electron transfer process. This process was monitored via stopped-flow spectroscopy using the oxidants NaOCl, $NaBrO_3$, and Br_2 where we observed the kinetics related to the cobalt(II) metal center going to the cobalt(III) oxidation state.

We also investigated the interaction of $[Co(dmgBF_2)_2(OH_2)_2]$ with the commonly used sacrificial electron donor Et_3N. When mixed together the color of the solution and the resulting UV-visible spectrum changes to resemble that of the cobalt(I) species but persists in the presence of air.

Chapter 2: Oxidation of $[Co(dmgBF_2)_2(OH_2)_2]$ with various oxidants *

2.0 Materials and methods

2.0.1 Materials

Analytical or reagent grade chemicals obtained from commercial sources were used as received throughout this study. Microanalyses (C, H, and N) were performed by Intertek Pharmaceutical Services (291 RT 22 East; PO Box 470; Whitehouse, NJ 08888). All sodium hypochlorite solutions were made up using Alfa Aesar sodium hypochlorite (14.5% available chlorine), which was standardized against $Na_2S_2O_3 \bullet 5H_2O$. The secondary standard, $Na_2S_2O_3 \bullet 5H_2O$, was standardized against the primary standard, KIO_3 using a the standard literature procedure [122].The secondary standard, $Na_2S_2O_3 \bullet 5H_2O$, was standardized against the primary standard, KIO_3 using a the standard literature procedure [122].The secondary standard, $Na_2S_2O_3 \bullet 5H_2O$, was standardized against the primary standard, KIO_3 using a the standard literature procedure [122]. Bromine and sodium bromate was used without the need for standardization.

2.0.2 Physical measurements

All ^{59}Co NMR spectra were acquired on a Bruker 400 MHz NMR spectrometer using the Bruker "cpmg1d" pulse sequence for up to 450,000 transients, and referenced to $K_3[Co(CN)_6]$ in DMSO-d_6 (δ = 289 ppm) [123]. All NMR spectra were processed using ACD/NMR Processor Academic Edition Version 12.01.All ^{59}Co NMR spectra were acquired on a Bruker 400 MHz NMR spectrometer using the Bruker "cpmg1d" pulse sequence for up to 450,000 transients, and referenced to $K_3[Co(CN)_6]$ in DMSO-d_6 (δ = 289 ppm) [123]. All NMR spectra were processed using ACD/NMR Processor Academic Edition Version 12.01.All ^{59}Co NMR spectra were acquired on a Bruker 400 MHz NMR spectrometer using the Bruker "cpmg1d" pulse sequence for up to 450,000 transients, and referenced to $K_3[Co(CN)_6]$ in DMSO-d_6 (δ = 289 ppm) [123]. All NMR spectra were processed using ACD/NMR Processor Academic Edition Version 12.01.

---

*Reproduced with permission from Celestine, M. J.; Joseph, L. S.; Holder, A. A., Kinetics and mechanism of the oxidation of a cobaloxime by sodium hypochlorite in aqueous solution: Is it an outer-sphere mechanism?, Inorg. Chim. Acta 2017, 454, 254-265.; and Tonsel-White, E. A.; Celestine, M. J.; Tano, C. M.; Nunez, B. S.; Kumar, S.; Holder, A. A., Biochar and kinetics studies on the reduction of sodium bromate by a cobaloxime in an aqueous media: How we can remove a toxic substance from our environment, *Inorg. Chim. Acta* **2020**, 119697.

All electrochemical data were acquired on a BASi® Epsilon C3 under an argon atmosphere in aqueous solution, which was thoroughly purged with Ar before any acquisition at room temperature. A standard three electrode configuration was employed consisting of a glassy carbon working electrode (diameter = 3 mm), Pt wire auxiliary electrode, and a Ag/AgCl (BASi, 3.0 M NaCl which was separated from the analytical solution by a Vicor® frit) reference electrode in aqueous media. The scan rate used within this study was 100 mV s^{-1}. The total ionic strength was maintained with 0.60 M NaCl.

2.0.3 UV-visible and kinetic studies

All UV-visible spectra were acquired on an Agilent® 8453A diode array spectrophotometer. All kinetic measurements were acquired using a Hi-Tech SF-61SX2 stopped-flow spectrophotometer interfaced with a computer. The spectrophotometer syringes were immersed in a water-bath linked to a thermostat system (Haake AC 150/A10) capable of maintaining temperatures within ± 0.01 °C. For the electron transfer reaction involving sodium hypochorite and $[Co(dmgBF_2)_2(OH_2)_2]$, the following was carried out: A solution of the complex of known concentration was prepared in a volumetric flask (50 ml). The ionic strength of the solution was adjusted to the required value with appropriate amounts of NaCl; then the flask was thermostatted for 10 minutes before introducing the solutions into the syringes of the stopped-flow spectrophotometer. The apparatus was equilibrated to the reaction temperature for at least one hour prior to use, and the complex solution with no buffer was kept in one of the thermostatted drive syringes for five minutes before each acquisition. By having no buffer in the complex's solution, this was to ensure that the pH jump method was utilized as we found that both buffers can react slowly with the complex, but not on the stopped-flow time scale.

The other thermostatted syringe contained either the sodium hypochlorite or bromine, with the phosphate buffer ($NaH_2PO_4 \bullet H_2O/Na_2HPO_4 \bullet 2H_2O$), and the supporting electrolyte (NaCl); or sodium bromate with HCl and NaCl. This syringe with its contents was also prethermostatted at the desired temperature. Both reactants were then mixed in the stopped-flow spectrophotometer after triggering. An excess of the oxidant was used in all cases to ensure pseudo-first order conditions. The kinetic data were collected and processed using TgK Scientific Kinetic Studio software suite V 4.0.1.27092. The pseudo-first order rate constants (k_{obs}) were determined by a non-linear least squares regression to fit the curve of the photomultiplier voltage versus time. The

reported rate constants are an average of at least three kinetic runs. The standard deviation for each k_{obs} values is ±10%. The pH of each solution was measured with a Fisher Scientific Accument® XL150 pH/mV analyzer, fitted with a VWR sympHony probe.

2.0.4 Stoichiometric studies

The redox stoichiometry [oxidant: complex] was determined by measuring the absorbance at 450 nm ($[Co(dmgBF_2)_2(OH_2)_2]$) of buffered solutions containing the complex at a fixed concentration while varying the concentration of sodium hypochlorite; then determining the break point of the plot of absorbance versus the ratio, [oxidant]: [complex].

2.0.5 Determination of the pK_{a1} value of $[Co(dmgBF_2)_2(OH_2)_2]$

The pK_{a1} value of $[Co(dmgBF_2)_2(OH_2)_2]$ was determined by measuring the largest absorbance change at 265 nm as the pH value was varied. Two buffers were employed for this study; for the pH values ranging from 3.50 to 5.50, a sodium acetate/acetic acid buffer was used, but the phosphate buffer was used in the pH range of 5.25 to 8.00.

2.0.6 Preparation of the complexes

$[Co(dmgBF_2)_2(OH_2)_2]$ [124], $[Co(NH_3)_5Br]Br_2$ [125], $[Co(NH_3)_5Cl]Cl_2$ [125], $Co(NH_3)_5OH_2](ClO_4)_3$ [115], and $K[Co(EDTA)]\bullet 2H_2O$ [126] were prepared by the literature procedures.

2.0.7 Synthesis of $[Co(dmgBF_2)_2(OH_2)(OH)]\bullet 1.75NaOCl$

NaOCl (1.13 ml, 1.77 M stock concentration) was added to H_2O (450 ml) in a 500 ml beak; then the pH was adjusted to 8.04 with HCl. $[Co(dmgBF_2)_2(OH_2)_2]$ (0.1008 g, 0.24 mmol) was dissolved in the resulting solution, and the mixture was stirred at room temperature for 44 hours during which time a green solid precipitated out of solution. The mixture was then filtered, and the precipitate was washed with deionized water, air dried, and collected. Yield = 0.0171g (13%) Calc. for $C_8H_{15}B_2Cl_{1.75}CoF_4N_4Na_{1.75}O_{7.75}$: C, 17.41; H, 2.65; N, 10.15%. Found: C, 17.87; H, 2.31; N, 9.70%. FTIR (ν/cm^{-1}): 826.9 (vs) (B-F), 941.9 (s) (B-F), 986.6 (vs) (O-B), 1101.0 (vs) (N-O), 1131.5 (s) (Co-OH), 1175.7 (vs) (B-F), 1215.5 (s) (N-O), 1635.2 (s) (C=N), and 3554.8 (vs) (O-H). δ_H (DMSO-d_6) = 1.90, 6.47, and 11.32 ppm; δ_{Co} (DMSO-d_6) = 3077 ppm.

2.1. Results and discussion

2.1.1 Oxidation of [Co(dmgBF$_2$)$_2$(OH$_2$)$_2$] by NaOCl

2.1.1.1 Synthesis and characterization of [Co(dmgBF$_2$)$_2$(OH$_2$)(OH)]•1.75NaOCl

It is interesting to note that sodium hypochlorite can react with [Co(dmgBF$_2$)$_2$(OH$_2$)$_2$]. When [Co(dmgBF$_2$)$_2$(OH$_2$)$_2$] was reacted with a sodium hypochlorite at a pH of 7.82 (phosphate buffer), the golden color of the solution went colorless almost immediately, but when the solutions were unbuffered and the ionic strength was not controlled, it was observed that a green solid precipitated out of an aqueous solution. Due to this observation, we preformed the reaction on a larger scale and a green product isolated with a 13% yield (see Scheme 5). Elemental analysis (C, H, and N) was carried out on the green product, which was formulated as [Co(dmgBF$_2$)$_2$(OH$_2$)(OH)]•1.75NaOCl. The complex was very insoluble in water and in acetonitrile but had a solubility that is less than 1.0 mM in DMSO.

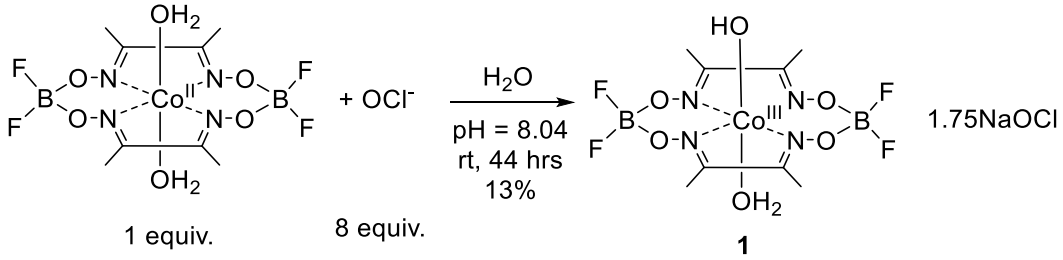

Scheme 5. Synthesis of [Co(dmgBF$_2$)$_2$(OH$_2$)(OH)]•1.75NaOCl

An FTIR spectrum which was acquired of the product isolated from the reaction revealed some interesting features (see Figure 26). The FT IR spectrum that was acquired for [Co(dmgBF$_2$)$_2$(OH$_2$)(OH)]•1.75NaOCl has ν(B-F) stretching frequencies at 826.9 cm^{-1} and 941.9 cm^{-1}, as well as the ν(O-B) stretching frequency at 986.6 cm^{-1} [73]. The ν(B-F) stretching frequency which was originally observed at 1158.5 cm^{-1} in [Co(dmgBF$_2$)$_2$(OH$_2$)$_2$] was blue shifted to 1175.7 cm^{-1} in the product. Similarly, the ν(C=N) stretching frequency for [Co(dmgBF$_2$)$_2$(OH$_2$)$_2$] which is observed at 1618.2 cm^{-1} was shifted 1638.4 cm^{-1}. In [Co(dmgBF$_2$)$_2$(OH$_2$)$_2$], the antisymmetric and symmetric ν(OH) stretching frequencies are observed at 3529.4 and 3601.6 cm^{-1} as well as the HOH bending at 1548.4 cm^{-1} [127]. When compared to the product the only stretching frequency from the water that was observed was the ν(OH) stretching frequency which was apparent at 3554.8 cm^{-1}; while the peak corresponding to the bending frequency for the cobalt-hydroxo bond, ν(Co-OH), was observed at 1131.5 cm^{-1} [127]. Any peak that would correspond to the OCl$^-$ species

appears to be masked the stretching frequency of the complex [128]. Such as the bending stretching frequency that should appear between 900 to 1240 cm^{-1} as well as the very weak O-Cl stretching frequency at 739 cm^{-1}. [128] Such as the bending stretching frequency that should appear between 900 to 1240 cm^{-1} as well as the very weak O-Cl stretching frequency at 739 cm^{-1}. [128]

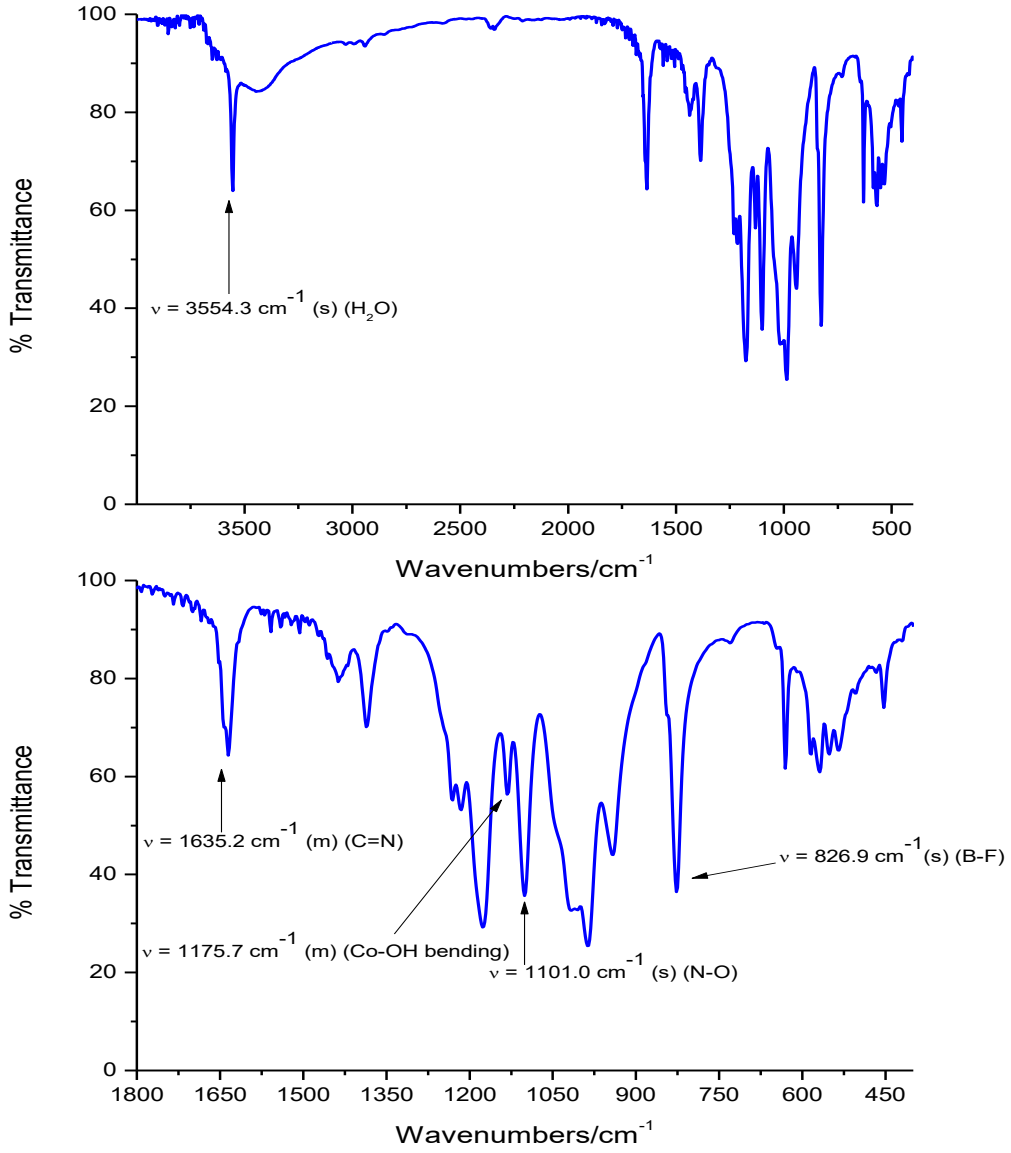

Figure 26. The FTIR spectra of $[Co(dmgBF_2)_2(OH_2)(OH)]\bullet 1.75NaOCl$.

Initially when the complex was added to DMSO only a small amount of the complex dissolved into the solution which was observed as a pale green color, but as time progressed the solution's color changed to a dark brown as more and more of the complex dissolved into solution.

Figure 27 shows a plot of the molar extinction coefficient versus wavelength of $[Co(dmgBF_2)_2(OH_2)_2]$ and $[Co(dmgBF_2)_2(OH_2)(OH)]\bullet 1.75NaOCl$ (red) in DMSO, where for the latter, there is a peak at 451 nm with a molar extinction coefficient of 2.2×10^3 M^{-1} cm^{-1}. The appearance of this peak signifies the possibility that DMSO is reacting with the complex to produce a species that is very soluble in DMSO.

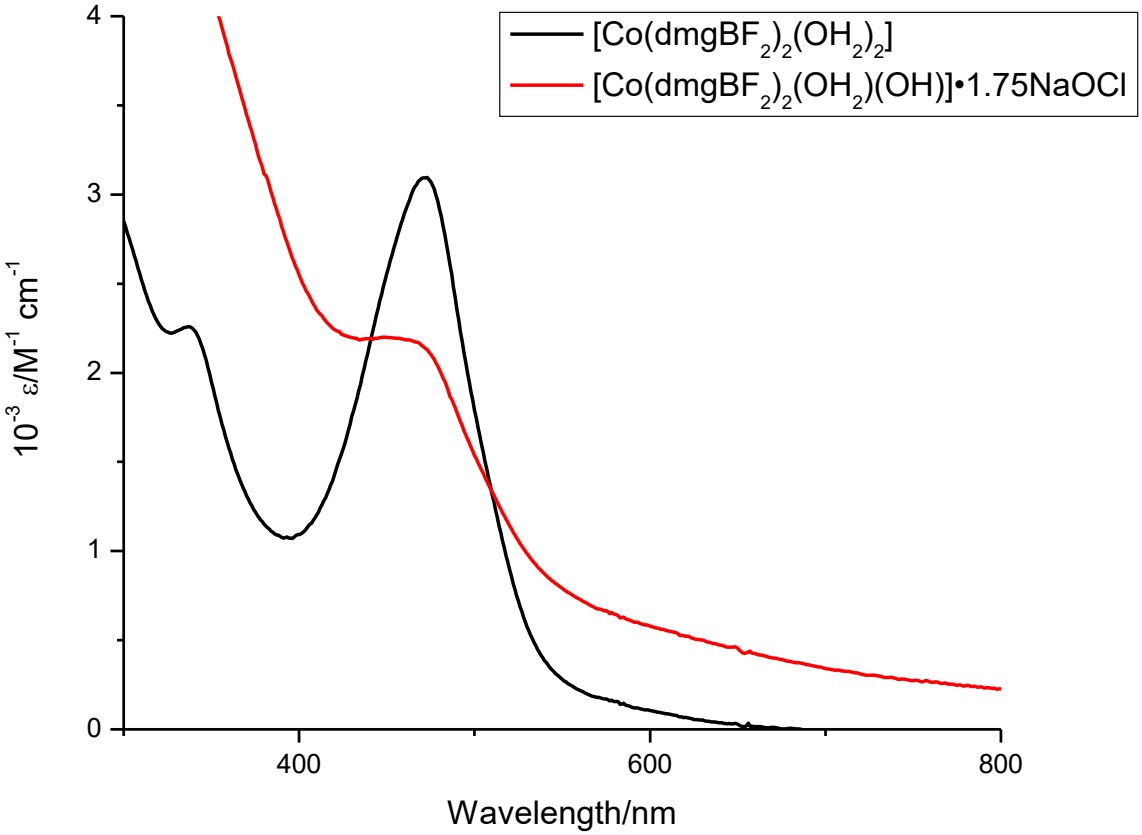

Figure 27. A plot of the molar extinction coefficient versus wavelength of $[Co(dmgBF_2)_2(OH_2)_2]$ (black) and $[Co(dmgBF_2)_2(OH_2)(OH)]\bullet 1.75NaOCl$ (red) in DMSO.

The ^1H NMR spectrum of $[Co(dmgBF_2)_2(OH_2)(OH)]\bullet 1.75NaOCl$ in DMSO (Figure 28) also reveals evidence that the DMSO is reacting with $[Co(dmgBF_2)_2(OH_2)(OH)]\bullet 1.75NaOCl$ to form a Co(II) species. This is evident in the broad nature of the peak in the ^1H NMR spectrum as the cobalt(II) species would be paramagnetic in nature. The methyl groups on the complex appears at $\delta = 1.90$ ppm with the appearance of two other peak appearing at $\delta = 6.47$ ppm and $\delta = 11.32$ ppm which corresponds to the DMSO and hydroxo ligands, respectively. When compared to $[Co(dmgBF_2)_2(OH_2)_2]$, the methyl peak from $[Co(dmgBF_2)_2(OH_2)(OH)]\bullet 1.75NaOCl$ appears upfield in the ^1H NMR spectrum. However, when compared to dimethylglyoxime (dmg), the

chemical shifts for the methyl peaks are observed to similar chemical shift as well as the peak circa 11.32 ppm, which in the dimethylglyoxime case belongs to the oxime (C=N-OH).

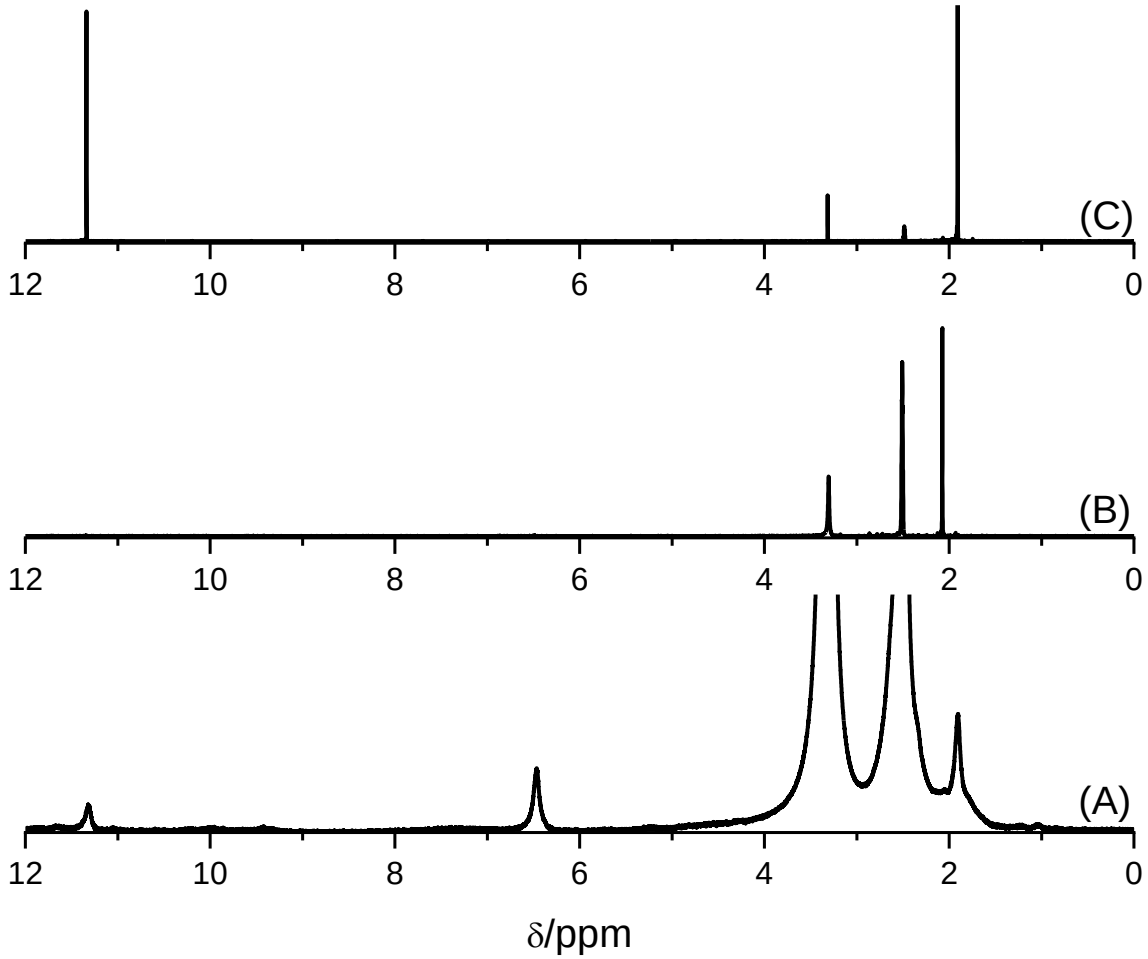

Figure 28. ^{1}H NMR spectra of [Co(dmgBF$_2$)$_2$(OH$_2$)(OH)]•1.75NaOCl (**A**), [Co(dmgBF$_2$)$_2$(OH$_2$)$_2$] (**B**), and dmg (**C**) in DMSO-d$_6$.

On acquisition of the ^{59}Co NMR spectrum of the product arising from a the dissolved complex, [Co(dmgBF$_2$)$_2$(OH$_2$)(OH)]•1.75NaOCl in DMSO-d$_6$ (Figure 29), a chemical shift was observed at δ = 3077 ppm. In comparison, Cropek *et al*. [73] observed a chemical shift of 5652 ppm in DMSO-d$_6$ for [Co(dmgBF$_2$)$_2$(OH$_2$)$_2$]. When we compare the chemical shifts of [Co(dmgBF$_2$)$_2$(OH$_2$)$_2$] and the product that was formed from the reaction between [Co(dmgBF$_2$)$_2$(OH$_2$)(OH)]•1.75NaOCl and DMSO-d$_6$, the former appeared downfield to the latter. It must be stressed that detailed EPR spectroscopic studies will be carried out on the product that is formed in DMSO.

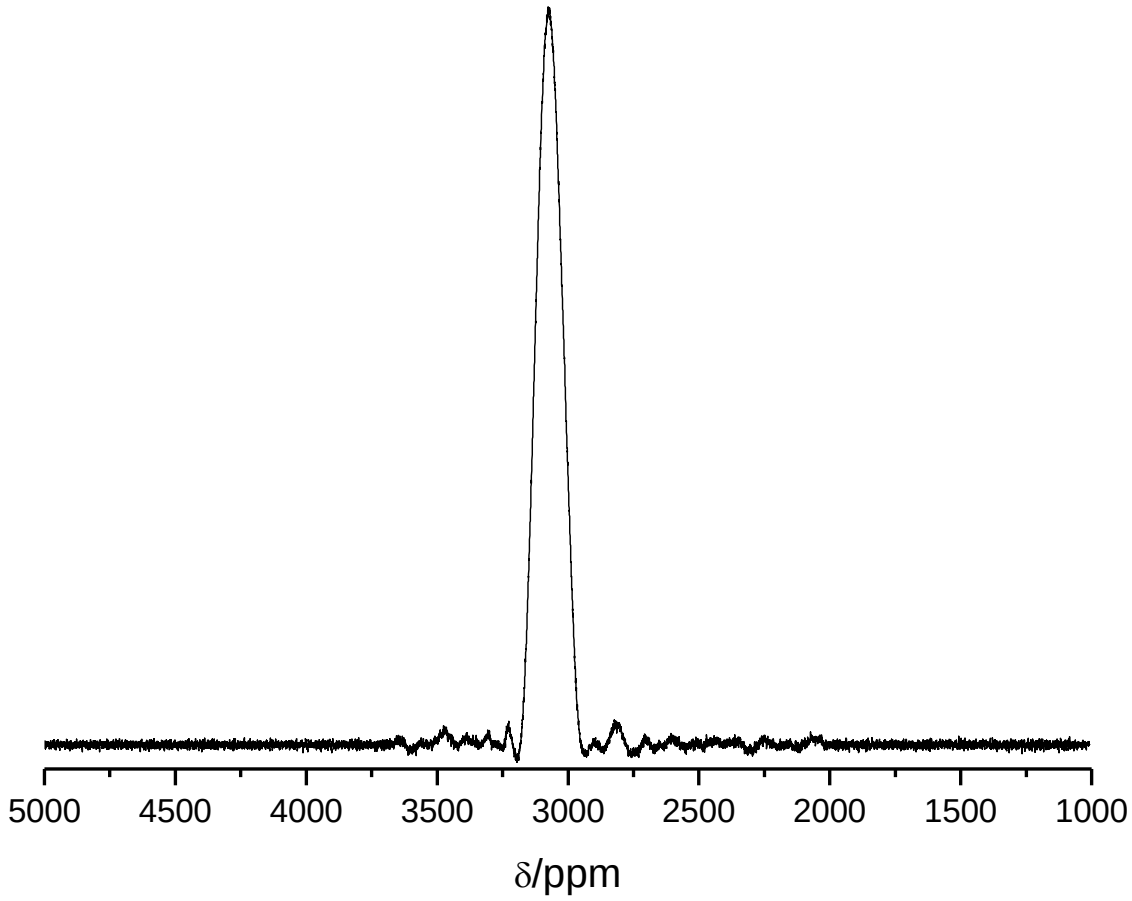

Figure 29. ^{59}Co NMR spectrum of $[Co(dmgBF_2)_2(OH_2)(OH)]\bullet 1.75NaOCl$ in DMSO-d_6.

Dimethyl sulfoxide can act as an oxidant, whereby it is reduced to form dimethyl sulfide under mild conditions (aerobic and anaerobic).[129-131] It has also been reported that DMSO can act as a reducing agent under certain conditions, yielding its fully oxidized form, dimethyl sulfone ($DMSO_2$), as the product.[132-133] In our case, we believe that DMSO has reacted with $[Co(dmgBF_2)_2(OH_2)(OH)]\bullet 1.75NaOCl$ and reduced the Co(III) metal center to a Co(II) metal center. The Co(II)-containing product is believed to have DMSO coordinated as a ligand (see proposed structure 2).

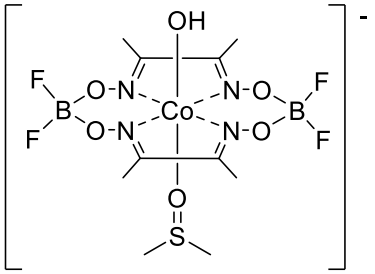

2

2.1.1.2 A brief spectroscopic study between $[Co(dmgBF_2)_2(OH_2)_2]$ and five Co(III) complexes as a reason why we chose sodium hypochlorite as an oxidant

Bakac *et al.* [124] have reported that the UV-visible spectrum of $[Co(dmgBF_2)_2(OH_2)_2]$ is characterized by absorption maxima at 456, 328, and 260 nm with molar extinction coefficients of 4.06 x 10^3, 1.92 x 10^3, and 5.82 x 10^3 M^{-1} cm^{-1}, respectively. The peak at 456 nm is particularly characteristic and, owing to its position and intensity, is most often of use in kinetics studies. In contrast, the cobalt(III) complex, $[Co(dmgBF_2)_2(OH_2)_2]^+$, as reported by Bakac *et al.* [124], has a relatively weak and featureless visible spectrum, with an intensity that rises into the UV region toward the general cobaloxime-type absorption at ca. 260 nm [124]. Bakac *et al.* [124] have reported that the UV-visible spectrum of $[Co(dmgBF_2)_2(OH_2)_2]$ is characterized by absorption maxima at 456, 328, and 260 nm with molar extinction coefficients of 4.06 x 10^3, 1.92 x 10^3, and 5.82 x 10^3 M^{-1} cm^{-1}, respectively. The peak at 456 nm is particularly characteristic and, owing to its position and intensity, is most often of use in kinetics studies. In contrast, the cobalt(III) complex, $[Co(dmgBF_2)_2(OH_2)_2]^+$, as reported by Bakac *et al.* [124], has a relatively weak and featureless visible spectrum, with an intensity that rises into the UV region toward the general cobaloxime-type absorption at ca. 260 nm [124]. Bakac *et al.* [124] have reported that the UV-visible spectrum of $[Co(dmgBF_2)_2(OH_2)_2]$ is characterized by absorption maxima at 456, 328, and 260 nm with molar extinction coefficients of 4.06 x 10^3, 1.92 x 10^3, and 5.82 x 10^3 M^{-1} cm^{-1}, respectively. The peak at 456 nm is particularly characteristic and, owing to its position and intensity, is most often of use in kinetics studies. In contrast, the cobalt(III) complex, $[Co(dmgBF_2)_2(OH_2)_2]^+$, as reported by Bakac *et al.* [124], has a relatively weak and featureless visible spectrum, with an intensity that rises into the UV region toward the general cobaloxime-type absorption at ca. 260 nm [124].

We carried out a UV-visible study between $[Co(dmgBF_2)_2(OH_2)_2]$ and five Co(III) complexes in water. Figure 30 shows the UV-visible spectra for all five Co(III) complexes, each at a concentration of 1.0 mM when compared to 0.10 mM for $[Co(dmgBF_2)_2(OH_2)_2]$. We expect that at 20 times the concentration of $[Co(dmgBF_2)_2(OH_2)_2]$ or more, the peak at 450 nm will be completely masked by the absorbance of the Co(III) oxidants. When two equivalents of sodium hypochlorite are reacted with one equivalent of $[Co(dmgBF_2)_2(OH_2)_2]$, there was a decrease in absorbance at 450 nm and an increase in absorbance at 250 nm (see Figure 31), which is indicative of the formation of $[Co(dmgBF_2)_2(OH_2)_2]^+$. As there is no absorbance of sodium hypochlorite at 450 nm, we have elected to use an oxidizing agent that does not absorb at the λ_{max} of $[Co(dmgBF_2)_2(OH_2)_2]$. This would enable us to determine the pseudo-first order rate constants when we carry out kinetics studies with $[Co(dmgBF_2)_2(OH_2)_2]$ and sodium hypochlorite at 450 nm (where the largest absorbance change of $[Co(dmgBF_2)_2(OH_2)_2]$ is expected to occur).

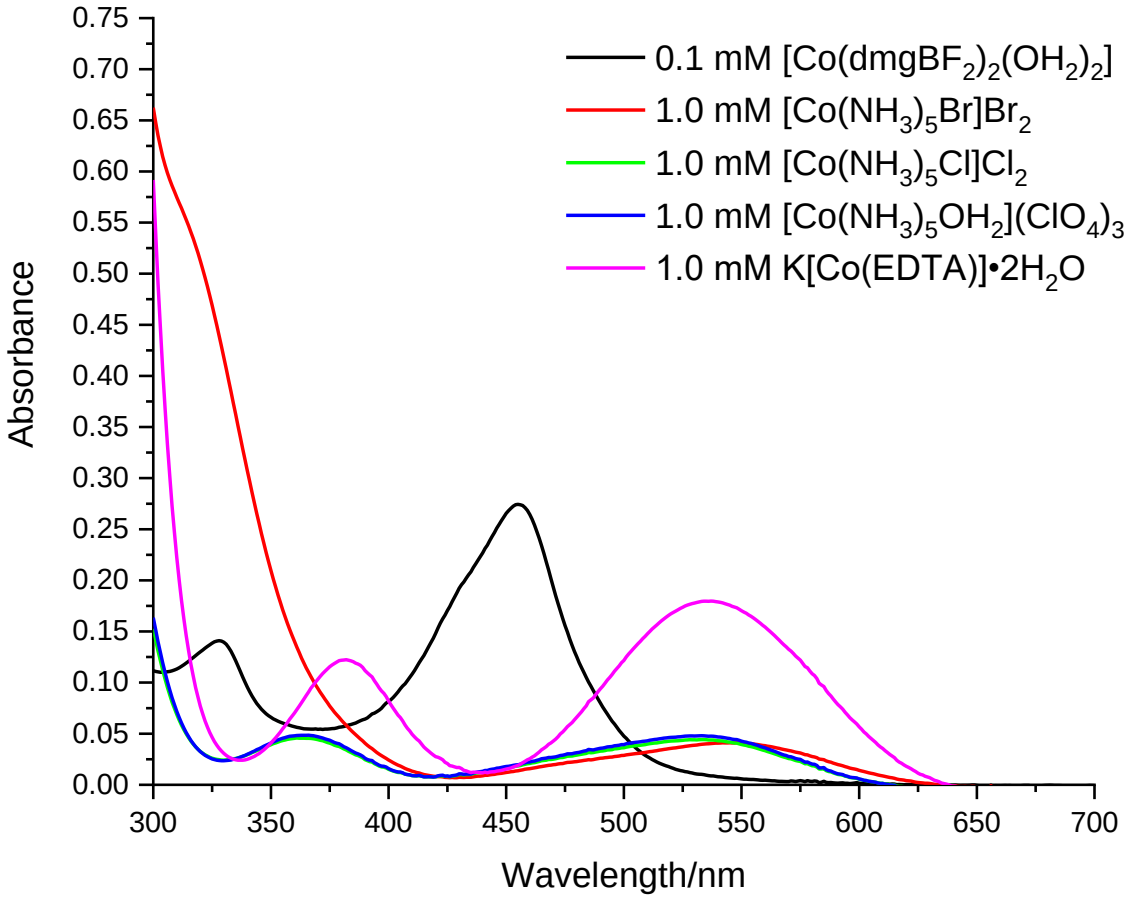

Figure 30. A plot of absorbance versus wavelength comparing 0.1 mM $[Co(dmgBF_2)_2(OH_2)_2]$ in water to the respective 1.0 mM Co(III) complex.

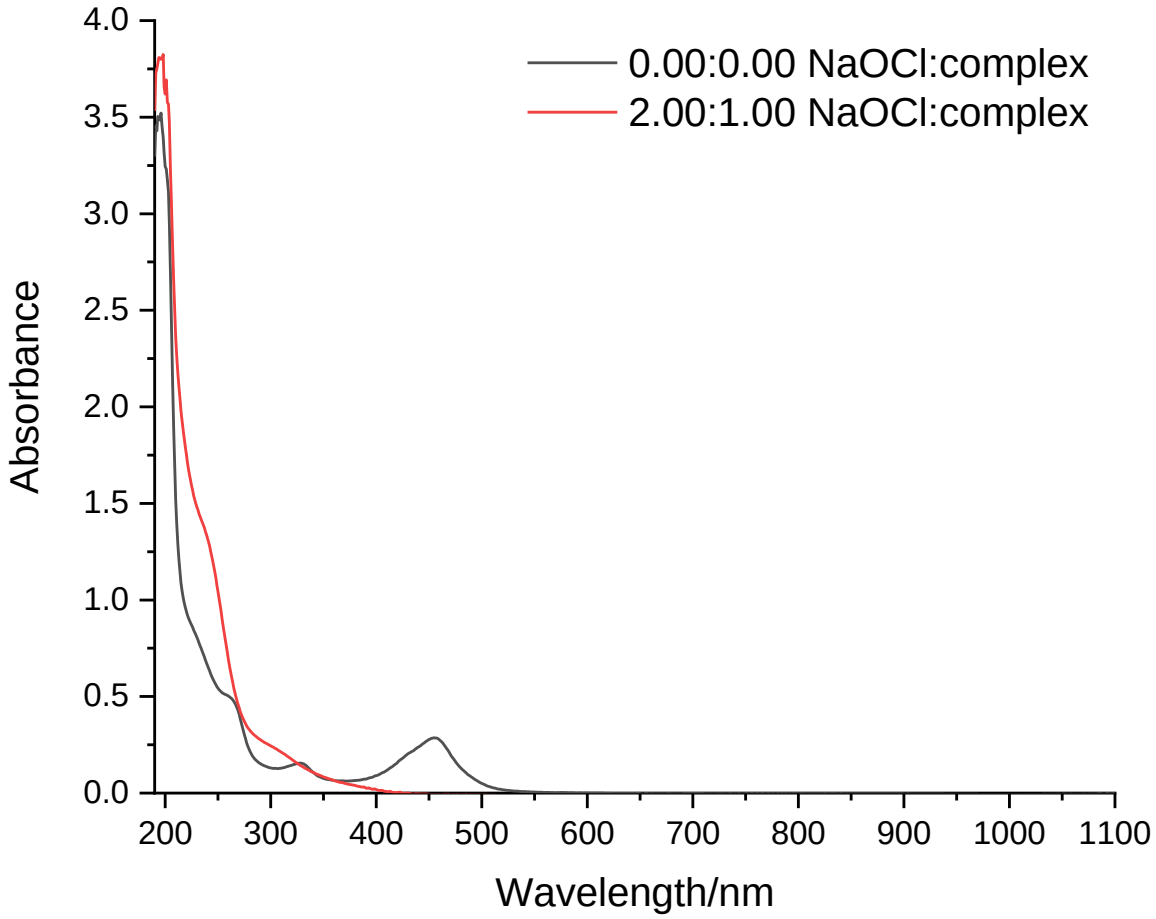

Figure 31. A plot of absorbance versus wavelength for the reaction between 0.10 mM $[Co(dmgBF_2)_2(OH_2)_2]$ and 0.20 mM NaOCl (I = 0.60 M (NaCl), buffer = phosphate buffer, and pH = 7.33 ± 0.02) (B).

2.1.1.3 Determination of the pKa value for [Co(dmgBF2)2(OH2)2]

The pK_{a1} value for the first dissociation of a proton from $[Co(dmgBF_2)_2(OH_2)_2]$ was obtained via a variation in pH at a constant concentration of complex, where the larges absorbance change at 265 nm occurred (see Figure 32). A non-linear regressional analysis was used to determine a pK_{a1} value of 5.27 ± 0.14 (I = 0.60 M (NaCl)). The pKa_1 value of 5.27 ± 0.14 for

$[Co(dmgBF_2)_2(OH_2)_2]$ can be compared to $pKa_1 = 4.40 \pm 0.03$ (I = 0.10 M ($LiClO_4$)) for $[Co(dmgBF_2)_2(OH_2)_2]^+$ as reported by Wang and Jordan [134]

$$[Co(dmgBF_2)_2(OH_2)_2] \overset{K_{a1}}{\rightleftharpoons} [Co(dmgBF_2)_2(OH_2)(OH)]^- + H^+ \quad (1)$$

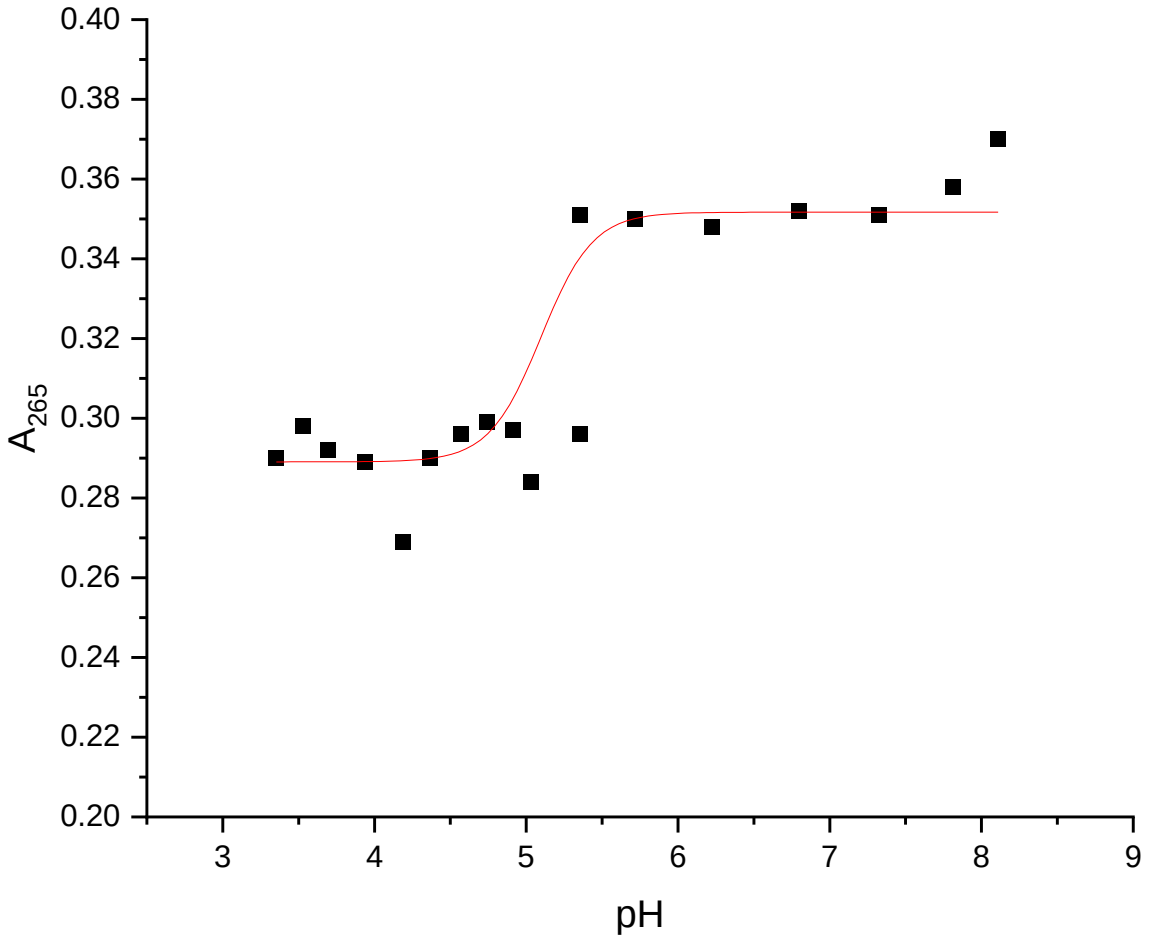

Figure 32 A plot of absorbance versus pH at room temperature. [Complex] = 0.10 mM, I = 0.60 M (NaCl), λ = 265 nm, acetate buffer (3.50 ≤ pH ≤ 5.50), and phosphate buffer (5.25 ≤ pH ≤ 8.00).

2.1.1.4 Nature of the reaction and the stoichiometry of the reaction

Sodium hypochlorite is known for its oxidizing ability; and in the literature, sodium hypochlorite and its protonated form hypochlorous acid are two electron acceptors. [135] Thus, one mole of sodium hypochlorite should react with two moles of $[Co(dmgBF_2)_2(OH_2)_2]$ in aqueous solution. The stoichiometry was obtained via spectrophotometric titration at 450 nm, where the disappearance of $[Co(dmgBF_2)_2(OH_2)_2]$ was monitored (see Figure 33 and

Table 2). Due to the fact that hypochlorite is a two electron oxidant the stoichiometry that was observed was 0.5:1.0 ([NaOCl]:[complex]).

Table 2. Stoichiometry of the reaction between [[Co(dmgBF$_2$)$_2$(H$_2$O)$_2$] and sodium hypochlorite, pH = 7.33 ± 0.02 (phosphate buffer), I =0.60 M (NaCl), [complex] = 0.10 mM, λ = 450 nm, and cuvette path length = 1.00 cm.

[NaOCl]$_T$/[complex]	**Absorbance**
0.000	0.28
0.125	0.24
0.250	0.13
0.500[a]	0.00
0.750	0.00
1.000	0.00
1.250	0.00
1.500	0.00
1.750	0.00
2.000	0.00

[a] Break point occurs at [NaOCl]$_T$/[complex] = 0.50.

As such, the stoichiometric data in Table 1 and Figure 33 are consistent with the reaction summarized in the following equation:

$$OCl^- + 2[Co(dmgBF_2)_2(OH_2)(OH)]^- + H_2O \rightarrow 2[Co(dmgBF_2)_2(OH_2)(OH)] + Cl^- + 2OH^- \quad (2)$$

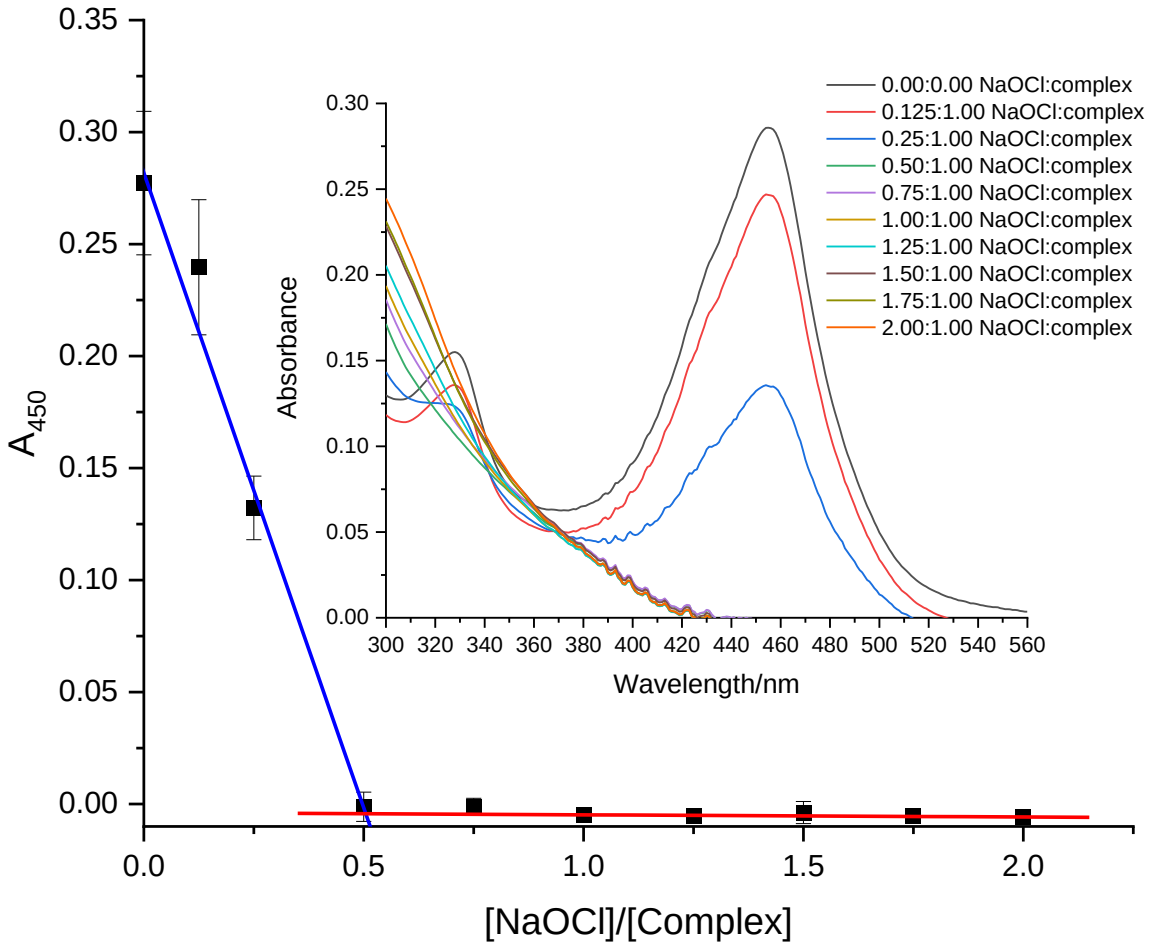

Figure 33. A plot of absorbance versus the ratio of [NaOCl]/[Complex] for the oxidation of $[Co(dmgBF_2)_2(OH_2)_2]$ by NaOCl. Inset = a plot of Absorbance versus wavelength for the oxidation of $[Co(dmgBF_2)_2(OH_2)_2]$ by NaOCl. [Complex] = 0.10 mM, λ = 450 nm, I = 0.60 M (NaCl), buffer = phosphate buffer, and pH = 7.33 ± 0.02.

2.1.1.5 Sodium hypochlorite concentration, ionic strength, temperature, and pH dependence of the reaction

Kinetic studies were carried out over the ranges of 1.00 mM ≤ [NaOCl] ≤ 10.0 mM, 5.34 ≤ pH ≤ 7.78 and 10.3 °C ≤ θ ≤ 25.3 °C ranges, at a constant ionic strength of 0.60 M (NaCl). The reactions were observed at stopped-flow times in a uniphasic fashion where the pseudo-first order rate constants (k_{obs}) were determined. For the kinetic runs where the total concentration of sodium hypochlorite was varied, it was observed that as the concentration increased, the k_{obs} values also increased (Table 3 and Figure *34*). The plot in figure 9 shows a positive slope as well as a non-zero intercept, where the intercept was given the term k'_1 and the slope as k'_2. A linear plot gave values for k'_1 and k'_2 as 7.56 s^{-1} and 2.26 x 10^4 M^{-1} s^{-1}, respectively. The non-zero intercept can be interpreted as there is a step that is dependent on the solvent and not on the oxidant, or that there

is some type of equilibrium that may exist. If the latter is the case, then the data can be interpreted as the reaction favoring the formation of the intermediate and subsequent oxidation. The following equation was used for the plot:

$$k_{obs} = k'_1 + k'_2 [NaOCl] \quad (3)$$

Table 3. Pseudo-first order rate constants for the oxidation of $[Co(dmgBF_2)_2(OH_2)_2]$ by NaOCl. Variation in NaOCl concentration. [Complex] = 0.10 mM, λ = 450 nm, I = 0.60 M (NaCl), θ = 10.1 °C, buffer = phosphate buffer, and pH = 7.45 ± 0.08.

[NaOCl]/mM	**10^{-2} k_{obs}/s^{-1}**
1.00	0.27
2.00	0.53
3.00	0.76
4.00	0.99
5.00	1.20
6.00	1.43
7.00	1.67
8.00	1.88
9.00	2.14
10.0	2.29

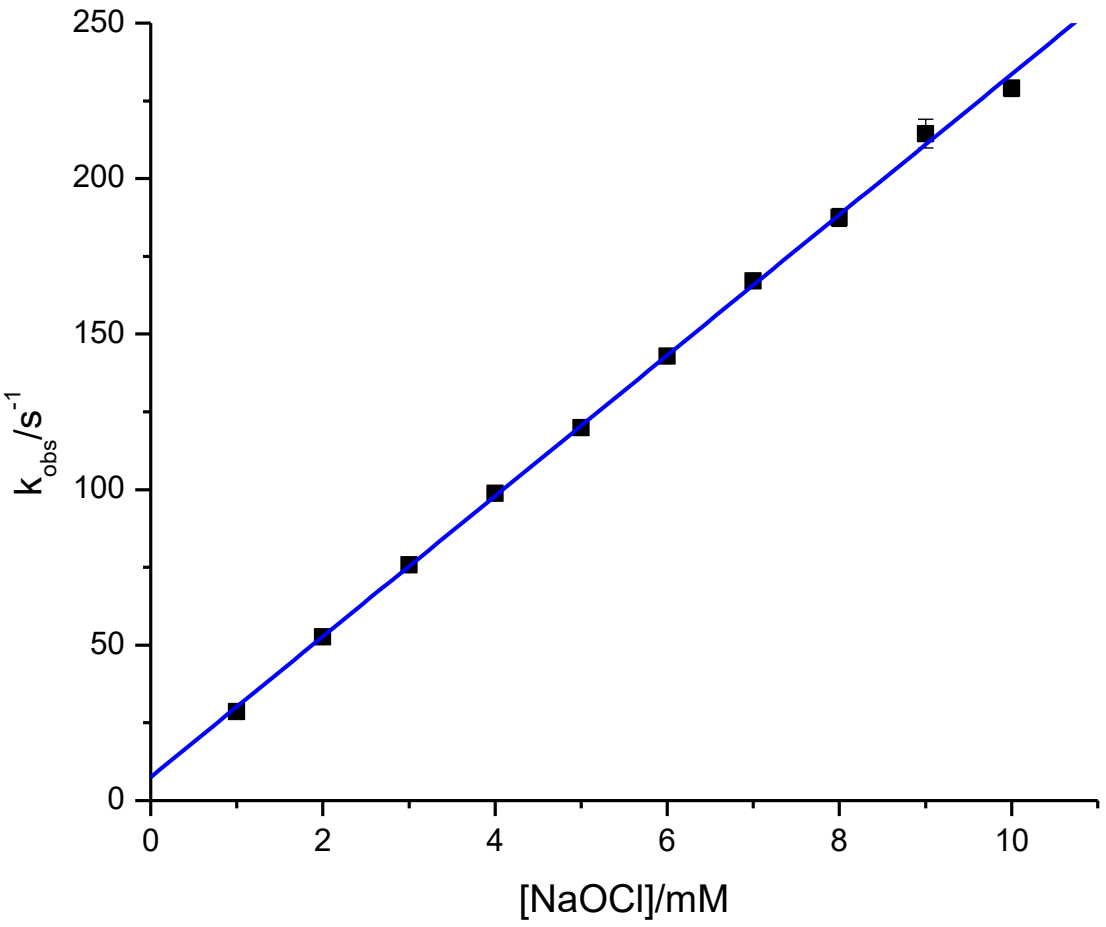

Figure 34. A plot of k_{obs} versus the concentration of NaOCl. [Complex] = 0.10 mM, λ = 450 nm, I = 0.60 M (NaCl), θ = 10.1 °C, buffer = phosphate buffer, and pH = 7.82 ± 0.08

The ionic strength has been recognized for its effects on the rates of ionic reactions [136-137]. When the reacting species have similar charges, the rate of reaction is observed to increase, whereas when the reacting species have opposite charges, the rate of reaction is observed to decrease [136-137]. Upon varying the ionic strength as shown by in our kinetic data in table 3, as the ionic strength is increased, the k_{obs} value is increased. By applying the Brönsted-Bjerrum equation [138],The ionic strength has been recognized for its effects on the rates of ionic reactions [136-137]. When the reacting species have similar charges, the rate of reaction is observed to increase, whereas when the reacting species have opposite charges, the rate of reaction is observed to decrease [136-137]. Upon varying the ionic strength as shown by in our kinetic data in table 3, as the ionic strength is increased, the k_{obs} value is increased. By applying the Brönsted-Bjerrum equation [138],The ionic strength has been recognized for its effects on the rates of ionic reactions [136-137]. When the reacting species have similar charges, the rate of reaction is observed to increase,

whereas when the reacting species have opposite charges, the rate of reaction is observed to decrease [136-137]. Upon varying the ionic strength as shown by in our kinetic data in table 3, as the ionic strength is increased, the k_{obs} value is increased. By applying the Brönsted-Bjerrum equation [138],

$$\log k_{obs} = \log k^{o}_{obs} + (2Az_1z_2\sqrt{I})/(1+\sqrt{I}) \quad (4)$$

where k^{o}_{obs} is the rate constant at infinite dilution, z_1 and z_2 are the ionic charges of the reactants, and A is the Debye-Hückel constant (A = 0.4961 $M^{-1/2}$ at 10 °C) [138].is the rate constant at infinite dilution, z_1 and z_2 are the ionic charges of the reactants, and A is the Debye-Hückel constant (A = 0.4961 $M^{-1/2}$ at 10 °C) [138].is the rate constant at infinite dilution, z_1 and z_2 are the ionic charges of the reactants, and A is the Debye-Hückel constant (A = 0.4961 $M^{-1/2}$ at 10 °C) [138]. By carrying out a linear regressional analysis on equation 4 with the data from Table 4, z_1z_2 was calculated as +1.04 and k^{o}_{obs} as 1.65 x 10^1 s^{-1}. From the value of z_1z_2, it can be inferred that the reacting species have charges of z_1 = -1 and z_2 = -1, which signifies that the reacting species in solution are $[Co(dmgBF_2)_2(OH_2)(OH)]^-$ and OCl^- at pH 5.49.

Table 4. Pseudo-first order rate constants for the oxidation of $[Co(dmgBF_2)_2(OH_2)_2]$ by NaOCl at various ionic strengths. [Complex] = 0.05 mM, [NaOCl] = 3.00 mM, λ = 450 nm, θ = 10.1 °C, buffer = phosphate buffer, and pH = 5.49 ± 0.11.

I/M	k_{obs}/s^{-1}
0.24	36.06 ± 0.01
0.30	38.45 ± 1.16
0.40	42.30 ± 3.15
0.50	43.48 ± 4.48
0.60	47.15 ± 4.41

Under the pseudo-first order conditions, it was observed that the k_{obs} values first began to decrease slightly, then increase as the pH was increased (see Figure 35). Based on the data in Table 5, this reaction is pH dependent. The pK_a value of HOCl was reported as 7.4 [139-140]. At pH 7.4, we would expect 50% HOCl and 50% OCl^- to be in existence. From the pK_a value of 5.27 for $[Co(dmgBF_2)_2(OH_2)_2]$, it can be deduced that the predominant species would be the aqua hydroxo

species, $[Co(dmgBF_2)_2(OH_2)(OH)]^-$ over the pH range (5.34 to 7.42) used in this study as shown in table 5 and figure 10.

Table 5. Pseudo-first order rate constants for the oxidation of $[Co(dmgBF_2)_2(OH_2)_2]$ by NaOCl by varying the pH. [Complex] = 0.05 mM, [NaOCl] = 3.00 mM, λ = 450 nm, I = 0.60 M (NaCl), and buffer = Phosphate buffer.

θ = 10.3 °C		**θ = 15.2 °C**		**θ = 20.0 °C**		**θ = 25.3 °C**	
pH	k_{obs}/s^{-1}	pH	k_{obs}/s^{-1}	pH	k_{obs}/s^{-1}	pH	k_{obs}/s^{-1}
5.50	27.0	5.42	35.8	5.35	44.3	5.34	76.3
5.77	27.6	5.63	35.3	5.63	41.2	5.64	74.0
6.12	26.3	6.02	34.5	6.01	39.1	5.98	72.2
6.50	24.5	6.43	31.5	6.44	38.0	6.44	76.2
6.96	28.9	6.85	36.7	6.85	46.4	6.88	92.3
7.42	33.6	7.23	44.0	7.26	54.2	7.27	113.8
7.62	36.5	7.53	48.2	7.78	59.3	7.51	128.7

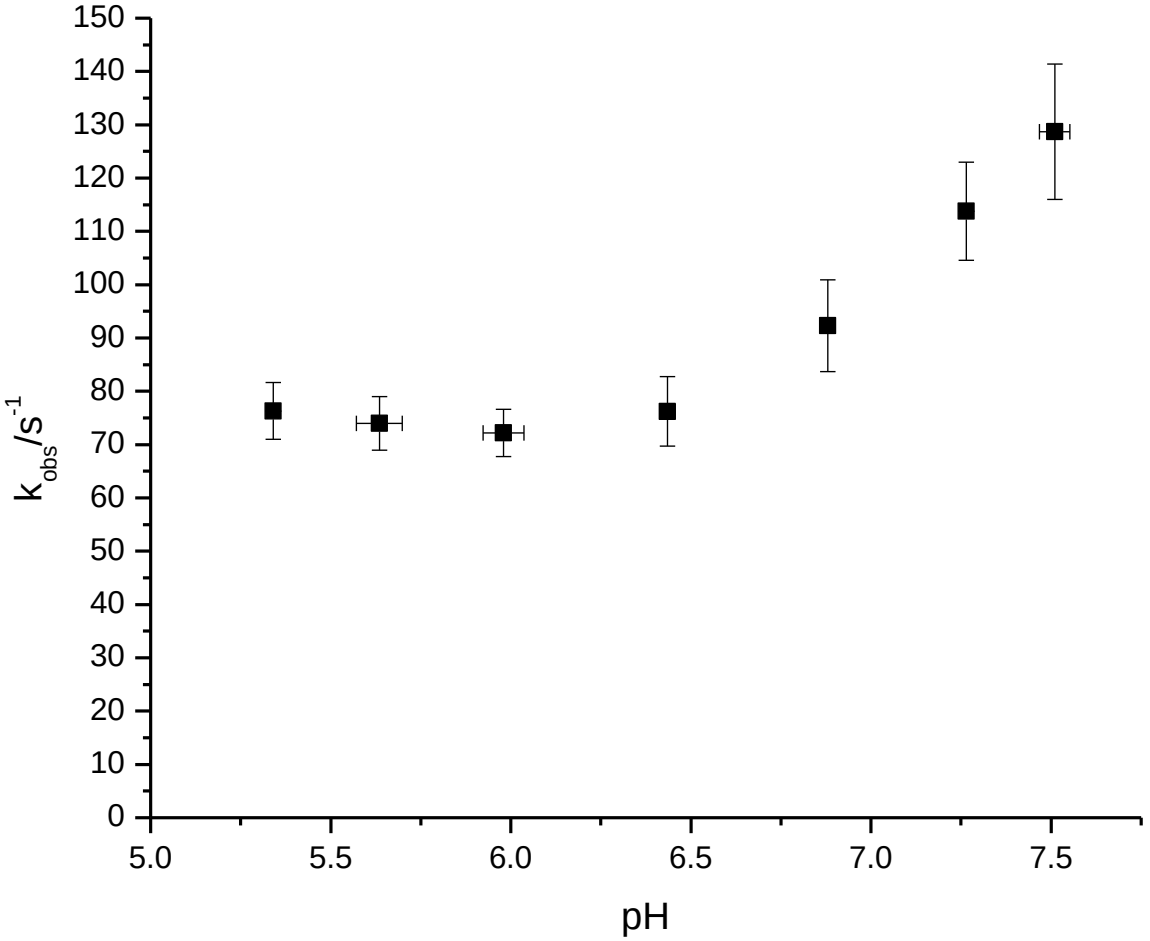

Figure 35. A plot of k_{obs} versus pH. [Complex] = 0.05 mM, [NaOCl] = 3.00 mM, λ = 450 nm, I = 0.60 M (NaCl), θ = 25.3 °C, and buffer = phosphate buffer.

The data in Table 3Table 4-Table 5 can be satisfactorily explained in terms of the proposed mechanism shown in Scheme 6.

$$[Co(dmgBF_2)_2(OH_2)(OH)]^- + OCl^- \xrightarrow{k_1} \text{Products}$$

$$\rightleftharpoons \; K_a$$

$$[Co(dmgBF_2)_2(OH_2)(OH)]^- + HOCl \xrightarrow{k_2} \text{Products}$$

Scheme 6. Mechanism for the oxidation of $[Co(dmgBF_2)_2(OH_2)_2]$ by sodium hypochlorite.

The expression for such a mechanism would then lead to equation 5:

$$k_{obs} = ((k_2[H^+] + k_1K_a)/([H^+] + K_a))[OCl^-]_T \qquad (5)$$

where $[OCl^-]_T$ is the total hypochlorite concentration. Since the concentration of OCl^- is increasing as the pH is increased and the fact that there is an increase in the k_{obs} value, k_1 should be the main contributing path over the pH range, and equation 5 can be rearranged to give:

$$(k_{obs}([H^+] + K_a))/[OCl^-]_T = k_2[H^+] + k_1K_a \quad (6)$$

A plot of the left-hand side of the equation 6 versus $[H^+]$ is linear over the range $5.34 \leq pH \leq 7.42$, with the slope being k_2 and an intercept being k_1K_a. A plot at 10.3 °C is shown in Figure 36. A linear regressional analysis was performed and the second-order rate constants k_1 and k_2 were calculated for each temperature. The k_1 and k_2 values are shown in Table 6, along with the corresponding enthalpy and entropy of activation calculated using the Eyring's equation. The negative entropy of activation in Table 6 is indicative of an associative mechanism or could implicate the solvent as playing a dominant role.

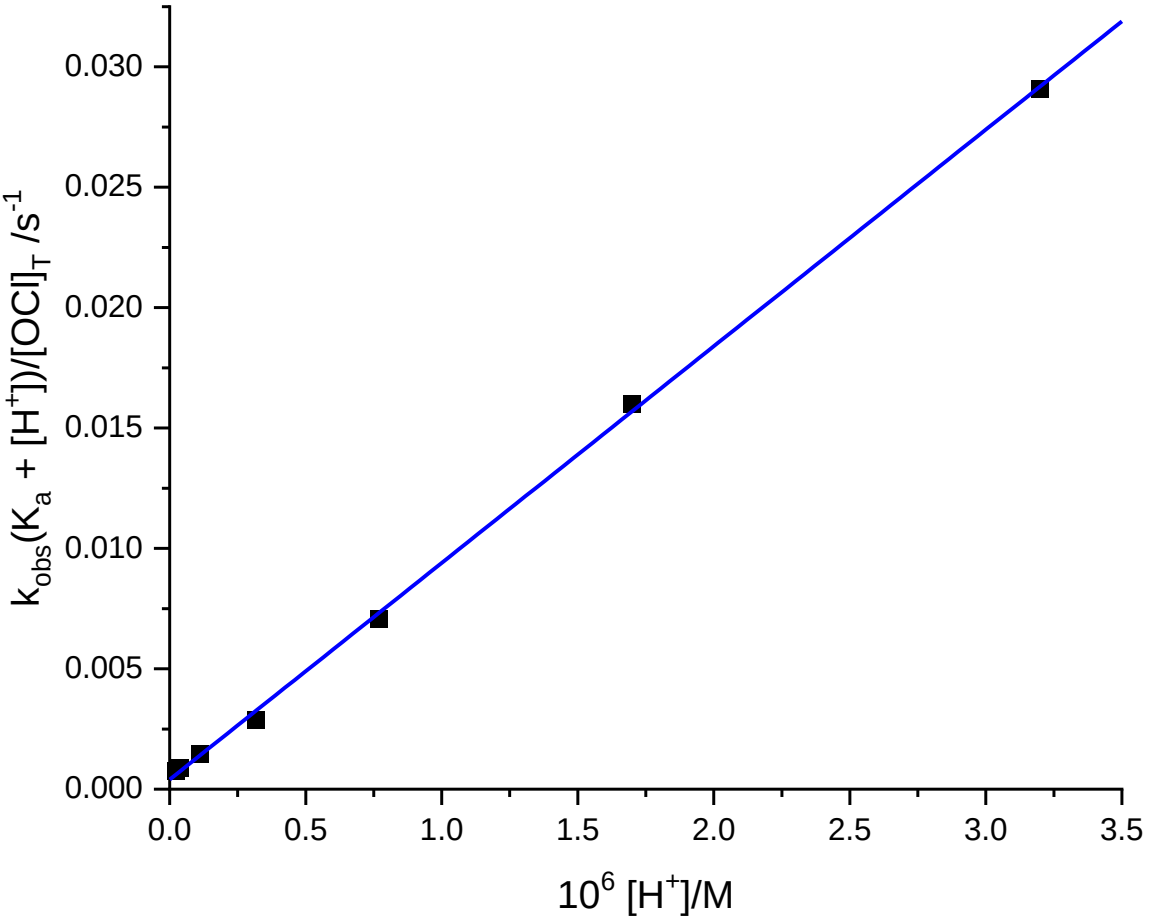

Figure 36. A plot of $k_{obs}(K_a + [H^+])/[OCl]_T$ versus $[H^+]$ for the oxidation of $[Co(dmgBF_2)_2(OH_2)_2]$ by 3 mM NaOCl. [Complex] = 0.05 mM, λ = 450 nm, I = 0.60 M (NaCl), θ = 10.3 °C, and buffer = phosphate buffer.

Table 6. Rate parameters values and the activation parameters for the reaction between $[Co(dmgBF_2)_2(OH_2)_2]$ and sodium hypochlorite.

θ/°C	10^{-4} k_1/M^{-1} s^{-1}	10^{-4} k_2/M^{-1} s^{-1}
10.3	0.99	0.90
15.2	1.05	1.25
20.0	1.63	1.80
25.3	3.54	2.51
	$\Delta H_1^{\ddagger}$ = 58 ± 7 kJ mol^{-1}	$\Delta H_2^{\ddagger}$ = 46.9 ± 0.1 kJ mol^{-1}
	$\Delta S_1^{\ddagger}$ = 29 ± 2 J mol^{-1} K^{-1}	$\Delta S_2^{\ddagger}$ = -8.8 ± 0.4 J mol^{-1} K^{-1}

Table 7 shows a few oxidants that have been studied in conjunction with $[Co(dmgBF_2)_2(OH_2)_2]$ for developing mechanisms for the electron transfer process, where the mechanism for many of these reactions are known.

Table 7. Table of rate constants and activation parameters for the oxidation of $[Co(dmgBF_2)_2(OH_2)_2]$ by various oxidants.

Oxidant	I/M	θ/°C	k/M^{-1} s^{-1}	$\Delta H^{\ddagger}$/kJ mol^{-1}	$\Delta S^{\ddagger}$/J mol^{-1} K^{-1}	Ref.
NaOCl	0.6[a]	5.3	3.54 x 10^3	46.9	-8.8	This work
$[Co(NH_3)_5Br]^{2+}$	0.1[b]	5	50	-	-	[134]
$[Co(NH_3)_5Cl]^{2+}$	0.1[b]	25	2.90	-	-	[134]
$[Co(NH_3)_5N_3]^{2+}$	0.1[b]	25	5.90	-	-	[134]
$[Fe(bpy)_3]^{3+}$	0.04[c]	25	1.59 x 10^6	9.3	-95.0	[141]
$[Co(OH_2)_5(OH)]^{2+}$	1.0[b]	25	1.00 x 10^5	75.8	66.1	[142]
$[Fe(OH_2)_6]^{3+}$	0.5[b]	25	2.90 x 10^2	--	--	[142]
$[Fe(OH_2)_5(OH)]^{2+}$	0.5[b]	25	6.20 x 10^4	--	--	[142]
[a] NaCl						
[b] $LiClO_4$						
[c] $HNO_3/NaNO_3$						

If we take the $[Co(NH_3)_5X]^{2+}$ (where X = Cl^-, Br^-, or N_3^-) series, all the oxidants used in Table 7 were observed to react via an inner-sphere mechanism. In the studies conducted on $[Co(OH_2)_5(OH)]^{2+}$, $[Fe(OH_2)_6]^{3+}$, and $[Fe(OH_2)_5(OH)]^{2+}$ it was stated that the electron transfer

occurred through an inner-sphere mechanism, which occurs via a hydroxide-bridged intermediate [124, 142]. In the case of $[Fe(bpy)_3]^{3+}$, since the bpy ligands cannot form a bridge to the cobaloxime, it was deemed that this reaction proceeded via an outer-sphere mechanism [141].[141].[141]. When we compare the oxidants, $[Fe(bpy)_3]^{3+}$ and NaOCl, there is a definite trend in $\Delta S^{\ddagger}$, with the value being less negative as the charge of the oxidant decreases from +3 to -1, indicating that the higher charged transition state gives more loss of entropy. This may be expected if solvent molecules become more restricted around a more highly charged activated complex.

2.1.1.6 Electrochemical studies and the Marcus cross relationship

The Marcus cross relationship is often used in determining whether or not a reaction proceeds via an outer-sphere electron transfer.[143-145] The Marcus theory predicts the second-order rate constant (k_{12}) for heteronuclear outer-sphere redox reactions from the electron self-exchange rate constants (k_{11} and k_{22}) of the respective oxidant and reductant. In order to apply the Marcus theory, the redox potentials for both reactants are needed to calculate the overall equilibrium constant (K_{12}). Before applying the Marcus equation, it is important to acquire the cyclic voltammogram for $[Co(dmgBF_2)_2(H_2O)_2]$ in order to determine the $Co^{II/III}$ redox couple. As such, the cyclic voltammogram of $[Co(dmgBF_2)_2(H_2O)_2]$ was acquired in water with NaCl as the supporting electrolyte (see Figure 37). The redox couples in Figure 37 (versus NHE) were obtained by adding +0.206 V to each $E_{½}$ value (versus Ag/AgCl) for the $Co^{II/III}$ and $Co^{II/I}$ redox couples. Thus, the couples of $E_{½}$ ($Co^{II/III}$) = +0.36 V and $E_{½}$ ($Co^{II/I}$) = -0.61 V (both versus Ag/AgCl) were converted to give redox couples of $E_{½}$ ($Co^{II/III}$) = +0.57 V and $E_{½}$ ($Co^{II/I}$) =-0.40 V (both versus NHE), respectively.

In the cyclic voltammogram (Figure 37), the $Co^{II/III}$ redox couple calculated as +0.57 V (versus NHE) at I = 0.60 M (NaCl) in aqueous media is more cathodic in value than the values obtained by Lawrence *et al*. ($E_{½}$ ($Co^{II/III}$) = +0.69 V (versus NHE) at I = 0.10 M ($NaClO_4$)) [146], Bakac *et al.*, ($E_{½}$ ($Co^{II/III}$) = +0.68 V (versus NHE) at I = 0.10 M ($LiClO_4$)) [124], and Wang and Jordan ($E_{½}$ ($Co^{II/III}$) = +0.65 V (versus NHE) at I = 0.10 M) [134].), the $Co^{II/III}$ redox couple calculated as +0.57 V (versus NHE) at I = 0.60 M (NaCl) in aqueous media is more cathodic in value than the values obtained by Lawrence *et al*. ($E_{½}$ ($Co^{II/III}$) = +0.69 V (versus NHE) at I = 0.10 M ($NaClO_4$)) [146], Bakac *et al.*, ($E_{½}$ ($Co^{II/III}$) = +0.68 V (versus NHE) at I = 0.10 M ($LiClO_4$)) [124], and Wang and Jordan ($E_{½}$ ($Co^{II/III}$) = +0.65 V (versus NHE) at I = 0.10 M) [134].), the $Co^{II/III}$ redox

couple calculated as +0.57 V (versus NHE) at I = 0.60 M (NaCl) in aqueous media is more cathodic in value than the values obtained by Lawrence *et al*. ($E_{½}(Co^{II/III})$ = +0.69 V (versus NHE) at I = 0.10 M ($NaClO_4$)) [146], Bakac *et al.*, ($E_{½}(Co^{II/III})$ = +0.68 V (versus NHE) at I = 0.10 M ($LiClO_4$)) [124], and Wang and Jordan ($E_{½}(Co^{II/III})$ = +0.65 V (versus NHE) at I = 0.10 M) [134].

When we compare the $Co^{II/III}$ redox couple in acetonitrile [146-148], it is generally observed to be quasi-reversible at $E_{½}(Co^{II/III})$ = +0.70 V (versus a Ag wire) at I = 0.10 M ($[^nBu_4N]ClO_4$) [146], where the redox couple tends to appear more anodic when compared to our value of $E_{½}(Co^{II/III})$ = +0.36 V (versus Ag/AgCl) at I = 0.6 M (NaCl).

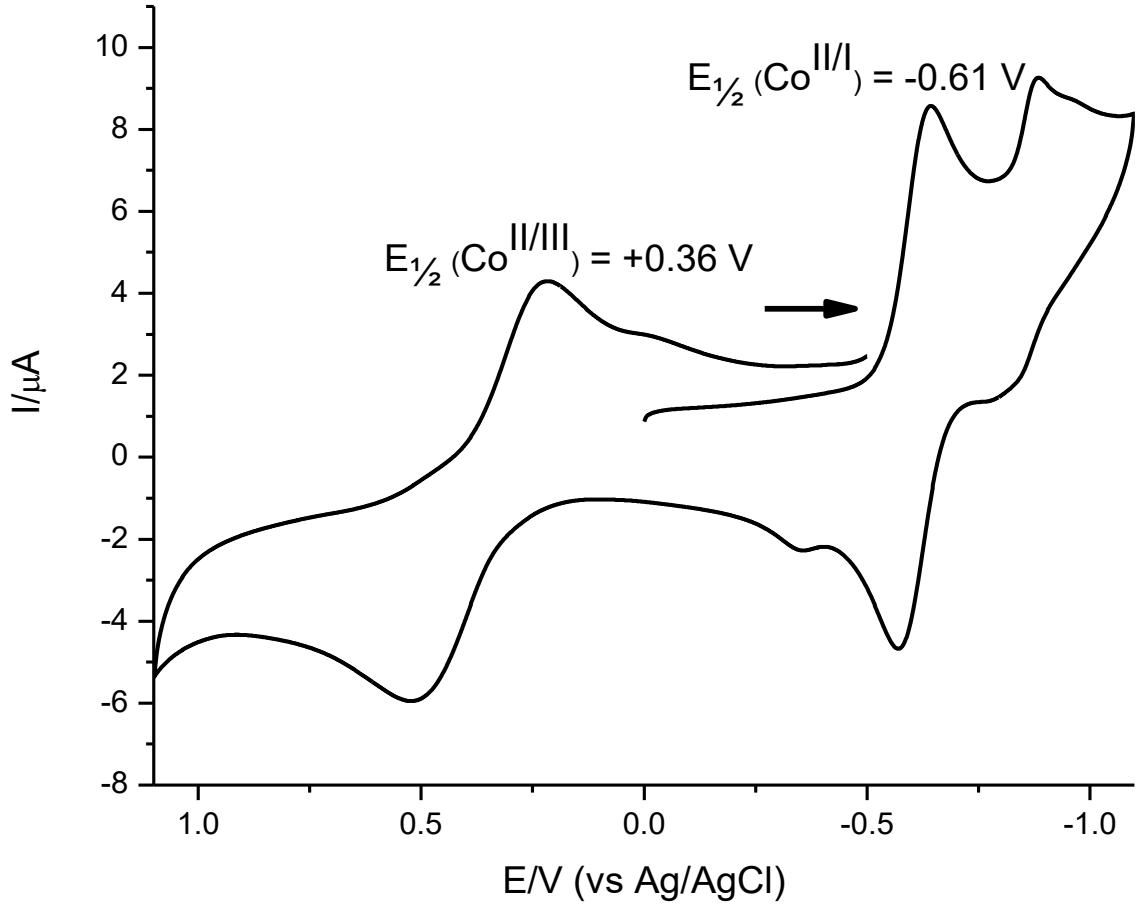

Figure 37. A cyclic voltammogram of $[Co(dmgBF_2)_2(OH_2)_2]$ in water. Working electrode = glassy carbon electrode, auxiliary electrode = Pt wire, reference electrode = Ag/AgCl, supporting electrolyte = 0.6 M (NaCl), [complex] = 1.0 mM, and scan rate = 100 mV s^{-1}.

If we were to assume that the electron transfer process between $[Co(dmgBF_2)_2(H_2O)_2]$ and NaOCl is outer-sphere, then we have to apply the Marcus theory. The equations used in the Marcus theory are as follows [143-145]:The equations used in the Marcus theory are as follows [143-145]:The equations used in the Marcus theory are as follows [143-145]:

$$k_{12} = \sqrt{k_{11}k_{22}K_{12}f_{12}} \quad (7)$$

$$\log f_{12} = ((\log K_{12})^2)/(4\log((k_{11}k_{22})/10^{22})) \quad (8)$$

$$\ln K_{12} = (nF(E^{\circ}_{11} - E^{\circ}_{22}))/(RT) \quad (9)$$

where k_{11} and k_{22} are the self-exchange rate constants for OCl^- and $[Co(dmgBF_2)_2(OH_2)_2]$, respectively. In calculating the self-exchange rate constant, k_{22}, for the complex at I = 0.60 M (NaCl), the points that were used as follows: 8.7 x 10^{-3} [141], 5.7 x 10^{-3} [134], and 1.7 x 10^{-4} M^{-1} s^{-1} [142], for the ionic strengths of 0.04 M ($NaNO_3$), 0.1 M ($LiClO_4$), and 1.0 M ($LiClO_4$), respectively. It is assumed that the k_{22} value is independent on the type of supporting electrolyte, but it is noted that k_{22} is dependent upon the variation of ionic strength. The self-exchange rate constant for $[Co(dmgBF_2)_2(OH_2)_2]$, k_{22} = 3.1 x 10^{-4} M^{-1} s^{-1}, was calculated from Figure 38where k_{11} and k_{22} are the self-exchange rate constants for OCl^- and $[Co(dmgBF_2)_2(OH_2)_2]$, respectively. In calculating the self-exchange rate constant, k_{22}, for the complex at I = 0.60 M (NaCl), the points that were used as follows: 8.7 x 10^{-3} [141], 5.7 x 10^{-3} [134], and 1.7 x 10^{-4} M^{-1} s^{-1} [142], for the ionic strengths of 0.04 M ($NaNO_3$), 0.1 M ($LiClO_4$), and 1.0 M ($LiClO_4$), respectively. It is assumed that the k_{22} value is independent on the type of supporting electrolyte, but it is noted that k_{22} is dependent upon the variation of ionic strength. The self-exchange rate constant for $[Co(dmgBF_2)_2(OH_2)_2]$, k_{22} = 3.1 x 10^{-4} M^{-1} s^{-1}, was calculated from where k_{11} and k_{22} are the self-exchange rate constants for OCl^- and $[Co(dmgBF_2)_2(OH_2)_2]$, respectively. In calculating the self-exchange rate constant, k_{22}, for the complex at I = 0.60 M (NaCl), the points that were used as follows: 8.7 x 10^{-3} [141], 5.7 x 10^{-3} [134], and 1.7 x 10^{-4} M^{-1} s^{-1} [142], for the ionic strengths of 0.04 M ($NaNO_3$), 0.1 M ($LiClO_4$), and 1.0 M ($LiClO_4$), respectively. It is assumed that the k_{22} value is independent on the type of supporting electrolyte, but it is noted that k_{22} is dependent upon the variation of ionic strength. The self-exchange rate constant for $[Co(dmgBF_2)_2(OH_2)_2]$, k_{22} = 3.1 x 10^{-4} M^{-1} s^{-1}, was calculated from Figure 38 at an ionic strength of 0.60 M. From the Marcus cross equation, $E°_{11}$ (OCl^-/Cl^-) = +0.89 V [149], $E°_{22}$ ($Co^{III/II}$) = +0.57 V, K_{12} = 6.59 x 10^{10}, and k_{12} = 3.5 x 10^4 M^{-1} s^{-1} (from the OCl^- pathway in scheme 2). From the Marcus cross equation, $E°_{11}$ (OCl^-/Cl^-) = +0.89 V [149], $E°_{22}$ ($Co^{III/II}$) = +0.57 V, K_{12} = 6.59 x 10^{10}, and k_{12} = 3.5 x 10^4 M^{-1} s^{-1} (from the OCl^- pathway in scheme 2). From the Marcus cross equation, $E°_{11}$ (OCl^-/Cl^-) = +0.89 V [149], $E°_{22}$ ($Co^{III/II}$) = +0.57 V, K_{12} = 6.59 x 10^{10}, and k_{12} = 3.5 x 10^4 M^{-1} s^{-1} (from the OCl^- pathway in scheme 2). Since the self-exchange rate constant for OCl^- has not been reported in the literature, and the reaction is assumed to be an outer-

sphere electron transfer process; then the self-exchange rate constant (k_{11}) for OCl^- is calculated as 1.2 x 10^3 M^{-1} s^{-1} at 25.3 °C.

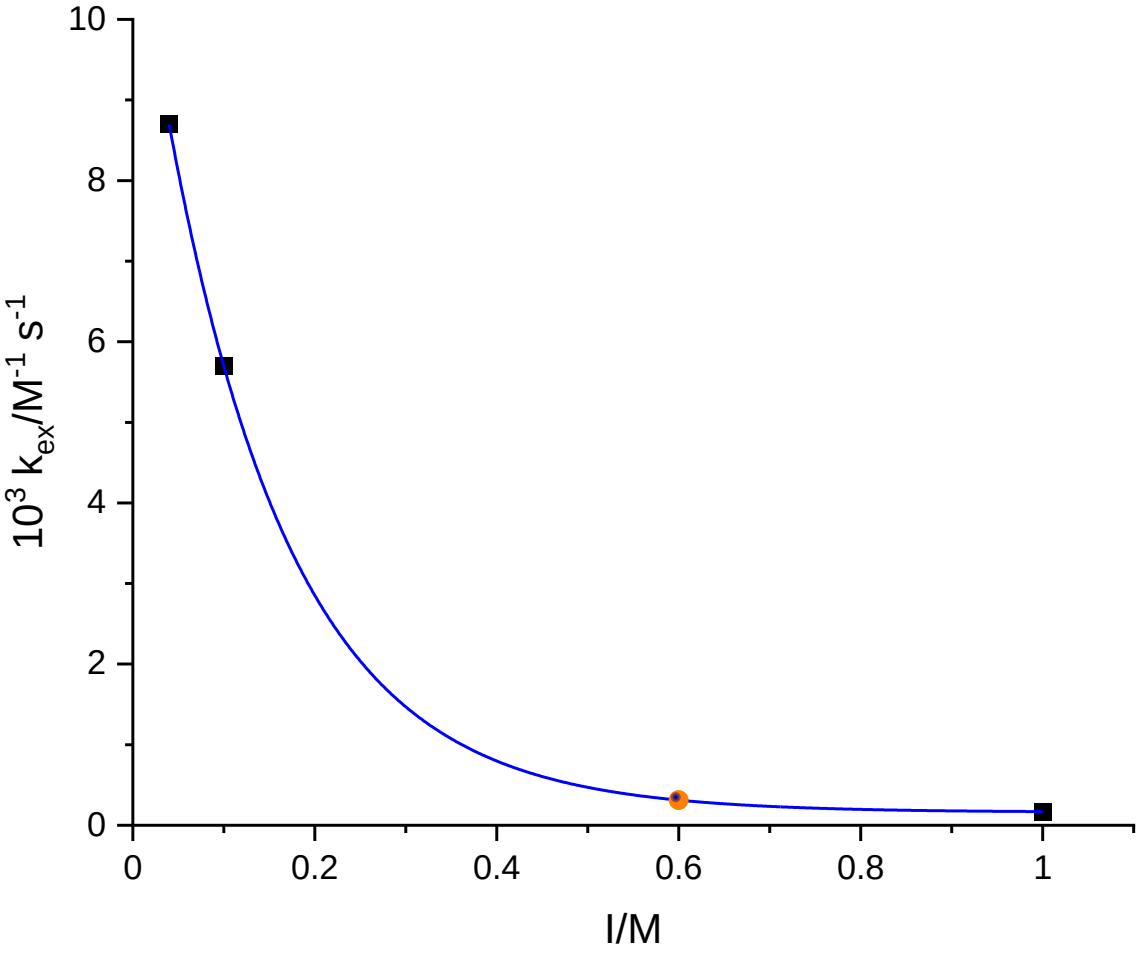

Figure 38. A plot of k_{ex} versus ionic strength for $[Co(dmgBF_2)_2(OH_2)_2]$ in water.

Table 8 shows the self-exchange rate constants calculated by the Marcus relationship for electron transfer processes that involve $[Co(dmgBF_2)_2(OH_2)_2]$ and several oxidants. If we compare the k_{22} values of the reactions that are known to proceed via an outer-sphere mechanism, we observe those values to be relatively small. When we compare those values to the values from the studies involving the hexaaquairon(III) cation, the k_{22} values are much larger and could be attributed to the inner-sphere electron transfer. We found that the k_{12} value for the $[Co(dmgBF_2)_2(H_2O)_2]/OCl^-$ couple is smaller than the $[Co(dmgBF_2)_2(H_2O)_2]/[Fe(bpy)_3]^{3+}$ couple, but the k_{11} value is nearly 10 times larger for the former.

Table 8. Self-exchange rate constants calculated by the Marcus relationship [142].

Couple	log K_{12}	$k_{12}/M^{-1}\ s^{-1}$	$k_{22}/M^{-1}\ s^{-1}$	f_{12}	$k_{11}/M^{-1}\ s^{-1}$
$[Co(dmgBF_2)_2(H_2O)_2] + [Co(OH_2)_5(OH)]^{2+}$ [a]	13.53	1.0×10^5	1.7×10^{-4}	1.2×10^{-2}	1.6×10^2
$[Co(dmgBF_2)_2(H_2O)_2] + [Fe(bpy)_3]^{3+}$ [b]	7.27	1.6×10^6	8.7×10^{-3}	1.7×10^{-1}	8.0×10^6
$[Co(dmgBF_2)_2(H_2O)_2]^{+} + [Co(sep)_3]^{2+}$ [c]	10.49	5.5×10^3	(2.0×10^{-3})[d]	5.8×10^{-2}	3.5
$[Co(dmgBF_2)_2(H_2O)_2]^{+} + [Co(sep)_3]^{2+}$ [c]	15.05	1.5×10^5	(6.6×10^{-4})[d]	3.5×10^{-3}	3.5
$[Co(dmgBF_2)_2(H_2O)_2] + [Fe(OH_2)_6]^{3+}$ [e]	1.69	2.9×10^2	1.3×10^2	9.3×10^{-1}	4.2[f]
$[Co(dmgBF_2)_2(H_2O)_2] + [Fe(OH_2)_6]^{3+}$ [e]	1.69	2.9×10^2	9.4×10^4	9.3×10^{-1}	(6.2×10^{-3})[g]
$[Co(dmgBF_2)_2(H_2O)_2] + [Fe(OH_2)_5(OH)]^{2+}$ [e]	-4.75	6.2×10^4	4.1×10^{11}	1.3×10^{-1}	3.0×10^3
$[Co(dmgBF_2)_2(H_2O)_2] + OCl^-$ [h]	10.82	3.5×10^4	3.1×10^{-4}	5.0×10^{-2}	1.2×10^3

[a] At 25 °C with I = 1.0 M ($LiClO_4$) [142].[a] At 25 °C with I = 1.0 M ($LiClO_4$) [142].[a] At 25 °C with I = 1.0 M ($LiClO_4$) [142].

[b] Reference [141].[b] Reference [141].[b] Reference [141].

[c] Reference [134].[c] Reference [134].[c] Reference [134].

[d] The k_{22} for $[Co(dmgBF_2)_2(H_2O)_2]^{+/0}$ and $[Co(dmgH)_2(H_2O)_2]^{+/0}$ recalculated from [134].[d] The k_{22} for $[Co(dmgBF_2)_2(H_2O)_2]^{+/0}$ and $[Co(dmgH)_2(H_2O)_2]^{+/0}$ recalculated from [134].[d] The k_{22} for $[Co(dmgBF_2)_2(H_2O)_2]^{+/0}$ and $[Co(dmgH)_2(H_2O)_2]^{+/0}$ recalculated from [134].

[e] At 25 °C with I = 0.5 M ($LiClO_4$).

[f] Reference [150].[f] Reference [150].[f] Reference [150].

[g] Determined from a least-squares fit to $k_{12} = \sqrt{k_{11}k_{22}K_{12}f_{12}}W_{12}$ with Z = 1.9 x 10^{10} M^{-1} cm^{-1}.[151] with Z = 1.9 x 10^{10} M^{-1} cm^{-1}.[151] with Z = 1.9 x 10^{10} M^{-1} cm^{-1}.[151]

[h] Our work: I = 0.60 M (NaCl) at 25.3 °C.

2.1.2 Oxidation of $[Co(dmgBF_2)_2(OH_2)_2]$ by $NaBrO_3$

2.1.2.1 Stoichiometry

The bromate ion is a known oxidant, and is reported to be a five-electron acceptor under acidic conditions, and a six-electron acceptor under neutral conditions [37]. When $[Co(dmgBF_2)_2(OH_2)_2]$ was reacted with $NaBrO_3$ in acidified aqueous media (see Figure 39), the absorbance circa 450 nm was observed to decrease when the concentration of the bromate was increased. When the absorbance at 450 nm is plotted, a 1:5 ratio of bromate to the complex (see Figure 39) is observed. The stoichiometric data in Figure 39 are consistent with the reaction summarized in equation 10. This result is consistent with the literature, where under acidic

conditions, the bromate anion is reduced by the reductant via the transfer of five electrons to the oxidant [37, 152-153]. Based on the gravimetric study above, we believe that $[Co(dmgBF_2)_2(OH_2)_2]$ can also be oxidized by the bromine byproduct formed in equation 10 to form $[Co(dmgBF_2)_2(OH_2)_2]^+$, with the eventual formation of the Br^- anion. The formation of the Br^- anion was proven in the gravimetric study as shown above.

$$5\,[Co(dmgBF_2)_2(OH_2)_2] + BrO_3^- + 6\,H^+ \rightarrow 5\,[Co(dmgBF_2)_2(OH_2)_2]^+ + 0.5\,Br_2 + 3\,H_2O \qquad (10)$$

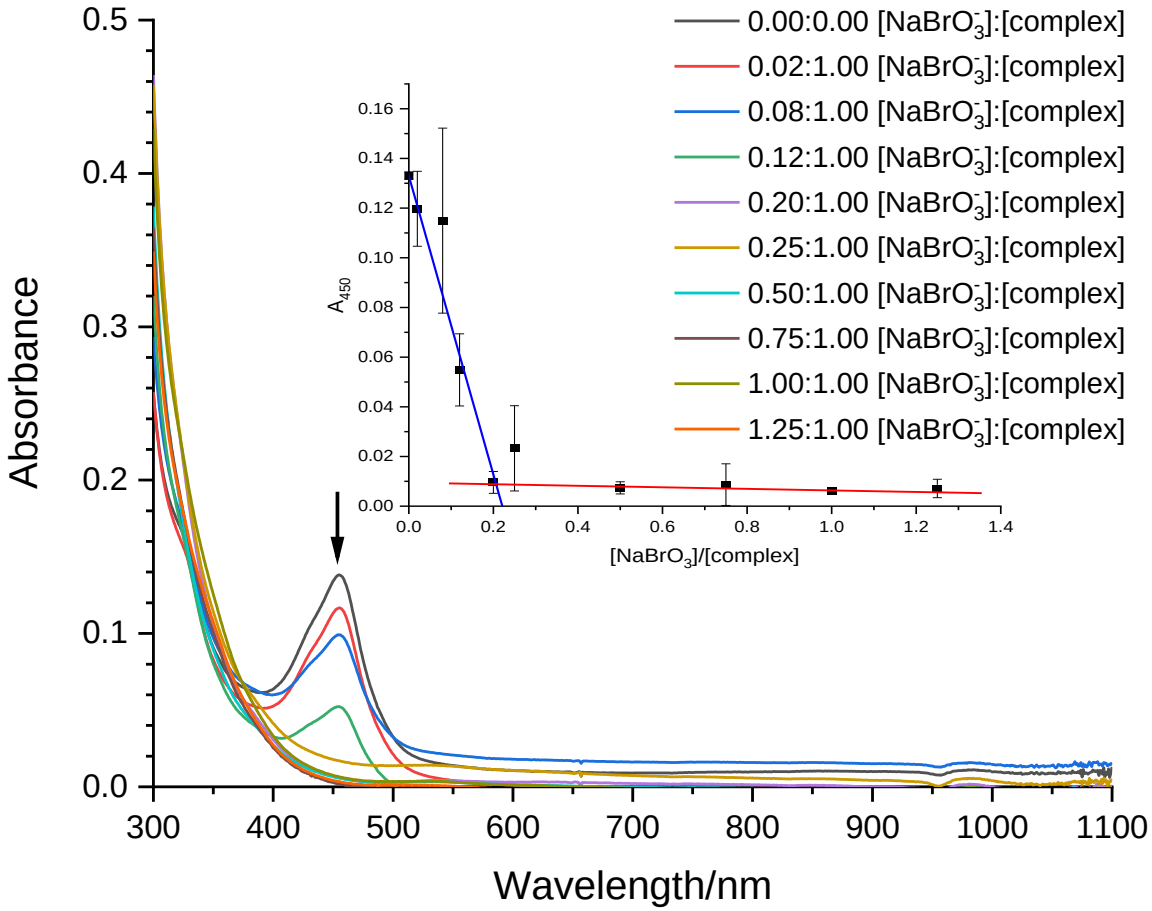

Figure 39. UV-visible spectral change for the oxidation of $[Co(dmgBF_2)_2(OH_2)_2]$ by $NaBrO_3$. Inset: A plot of absorbance versus the $[NaBrO_3]$/[complex] ratio for the oxidation of $[Co(dmgBF_2)_2(OH_2)_2]$ by $NaBrO_3$. [complex] = 0.10 mM, [HCl] =14.0 mM, λ = 450 nm, I = 0.60 M (NaCl), and at room temperature.

2.1.2.2 Variation in concentration of sodium bromate

The pseudo-first order rate constants or the variations in bromate concentration, acid concentration, ionic strength, and temperature are shown in Table 9 -Table 11. The k_{obs} value was found to increase with an increase in thee sodium bromate concentration. A plot of k_{obs} versus [sodium bromate] is shown in Figure 40. There is a zero intercept, which implies that the rate is first-order with respect to sodium bromate.

Table 9. Pseudo-first order rate constants for the oxidation of $[Co(dmgBF_2)_2(OH_2)_2]$ by $NaBrO_3$. [complex] = 0.1 mM, [HCl] = 7.0 mM, I = 0.6 M (NaCl), λ = 450 nm, and θ = 25.1 °C.

$[NaBrO_3]$/mM	$10^3\ k_{obs}/s^{-1}$
1	3.2
2	6.3
3	9.0
4	11.9
5	14.7
6	18.1
7	20.8
8	23.5
9	25.8
10	29.3

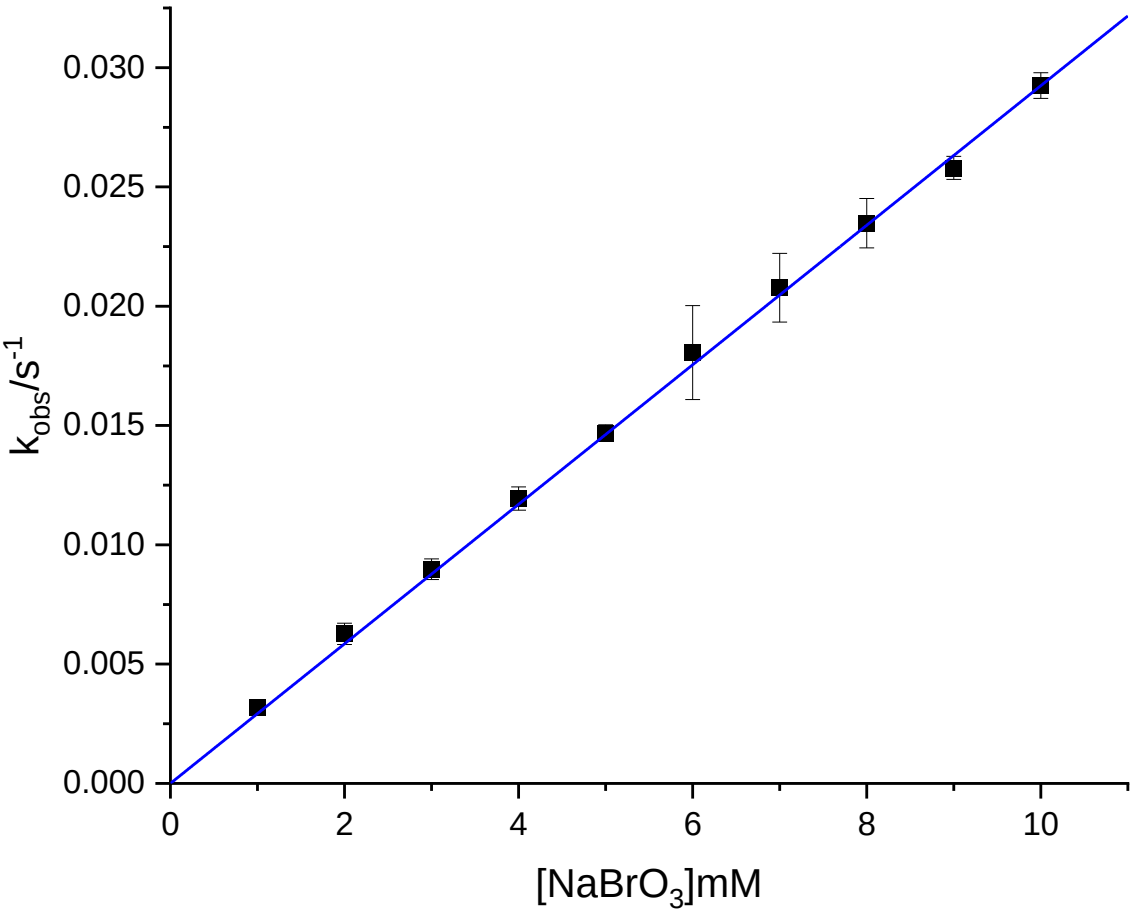

Figure 40. A plot of k_{obs} versus the concentration of $NaBrO_3$ for the oxidation of $[Co(dmgBF_2)_2(OH_2)_2]$ by $NaBrO_3$. [complex] = 0.1 mM, [HCl] = 7.0 mM, I = 0.6 M (NaCl), λ = 450 nm, and θ = 25.1 °C.

2.1.2.3 Variation in ionic strength

When the ionic strength was varied (see Table 10) the resulting data showed that the observed rate did not change within the margin of error. It is widely recognized that the ionic strength can play an important role in the rate of a reaction, where if the two reactants have similar charges then the rate should increase when the ionic strength is increased and decrease if the charges are different [136-137]. This lack of change in the observed rate as the ionic strength was varied is indicative of at least one of the reacting species being neutral, and that would be $[Co(dmgBF_2)_2(OH_2)_2]$.) the resulting data showed that the observed rate did not change within the margin of error. It is widely recognized that the ionic strength can play an important role in the rate of a reaction, where if the two reactants have similar charges then the rate should increase when the ionic strength is increased and decrease if the charges are different [136-137]. This lack of change in the observed rate as the ionic strength was varied is indicative of at least one of the reacting species being neutral, and that would be $[Co(dmgBF_2)_2(OH_2)_2]$.) the resulting data showed that the observed rate did not change within the margin of error. It is widely recognized that the ionic strength can play an important role in the rate of a reaction, where if the two reactants have similar charges then the rate should increase when the ionic strength is increased and decrease if the charges are different [136-137]. This lack of change in the observed rate as the ionic strength was varied is indicative of at least one of the reacting species being neutral, and that would be $[Co(dmgBF_2)_2(OH_2)_2]$.

Table 10. A table of pseudo-first order rate constants for the variation in ionic strength for the oxidation of $[Co(dmgBF_2)_2(OH_2)_2]$ by $NaBrO_3$. [complex] = 0.1 mM, $[NaBrO_3]$ = 10.0 mM, [HCl] = 7.0 mM, λ = 450 nm, and θ = 25.0 °C.

I/M	**10^2 k_{obs}/s^{-1}**

0.1	3.0 ± 0.0
0.2	3.0 ± 0.1
0.3	3.0 ± 0.1
0.4	3.0 ± 0.2
0.5	3.0 ± 0.1
0.6	3.0 ± 0.3

2.1.2.4 Variation in concentration of HCl and temperature

The kinetic studies were carried out over the ranges of 1.00 mM ≤ [HCl] ≤ 11.00 mM and 25.1 °C ≤ θ ≤ 40.2 °C; while keeping the ionic strength constant at 0.60 M (NaCl). When the concentration of HCl was varied (see Table 11) at the lower acid concentrations, the rate of reaction was rather slow. An increase in the k_{obs} values is observed when the acid concentration is increased. This implies that $HBrO_3$ is the predominant reacting species versus the BrO_3^- anion.

Table 11. Tabulated k_{obs} values at various HCl concentrations and temperatures for the oxidation of $[Co(dmgBF_2)_2(OH_2)_2]$ by $NaBrO_3$. [Complex] = 0.1 mM, $[NaBrO_3]$ = 10.0 mM, λ = 450 nm, and I = 0.6 M (NaCl).

	10^2 k_{obs} /s^{-1}					
[HCl]/mM	25.1 °C	27.0 °C	30.0 °C	35.4 °C	37.0 °C	40.2 °C
1.00	0.37	0.47	0.56	0.83	1.04	1.32
2.00	0.80	0.85	1.12	1.69	1.99	2.66
3.00	1.17	1.35	1.63	2.56	2.97	3.90

4.00	1.57	1.87	2.29	3.54	3.86	5.10
5.00	1.97	2.35	3.03	4.35	5.19	6.53
6.00	2.36	2.80	3.46	5.32	6.02	8.14
7.00	2.81	3.20	4.15	6.22	7.29	9.44
8.00	3.31	3.76	4.99	7.28	8.31	10.86
9.00	3.72	4.37	5.84	8.19	9.41	12.45
10.00	4.23	5.07	6.64	9.17	10.39	14.09
11.00	5.06	5.85	7.41	10.22	11.41	14.85

The data in Table 9 -Table 11 can be satisfactorily explained in terms of the proposed mechanism shown in Scheme 7.

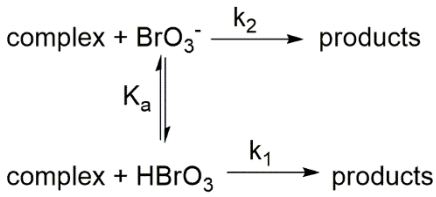

Scheme 7. Proposed mechanism for the oxidation of $[Co(dmgBF_2)_2(OH_2)_2]$ by $NaBrO_3$.

The expression for such a mechanism would then lead to Equation 11:

$$k_{obs} = \frac{(k_2K_a + k_1[H^+])[BrO_3^-]_T}{[H^+] + K_a} \qquad (11)$$

where $[BrO_3^-]_T$ is the total sodium bromate concentration and the pK_a of bromic acid = -2 [154]. Here, we assume that the pK_a value is independent on temperature. Since there is an increase in k_{obs} with an increase in acid concentration, k_1 will be the main contributing path with the predominant reacting species being the oxidant, $HBrO_3$. As such, the following expression is applied: where $[BrO_3^-]_T$ is the total sodium bromate concentration and the pK_a of bromic acid = -2 [154]. Here, we assume that the pK_a value is independent on temperature. Since there is an increase in k_{obs} with an increase in acid concentration, k_1 will be the main contributing path with the predominant reacting species being the oxidant, $HBrO_3$. As such, the following expression is applied:where $[BrO_3^-]_T$ is the total sodium bromate concentration and the pK_a of bromic acid = -2 [154]. Here, we assume that the pK_a value is independent on temperature. Since there is an increase in k_{obs} with an increase in acid concentration, k_1 will be the main contributing path with the

predominant reacting species being the oxidant, $HBrO_3$. As such, the following expression is applied:

$$k_{obs} = \frac{k_1[H^+][BrO_3^-]_T}{[H^+] + K_a} \quad (12)$$

The expression can be rearranged to give the following equation:

$$\frac{k_{obs}([H^+] + K_a)}{[BrO_3^-]_T} = k_1[H^+] \quad (13)$$

Using equation 13, Figure 41 was plotted and the k_1 values were calculated. Using the Eyring equation, the activation parameters were calculated from the k_1 values. From Figure 42, the $\Delta H^{\ddagger}$ and $\Delta S^{\ddagger}$ values were calculated as 57 ± 1 kJ mol^{-1} and 34 ± 4 J mol^{-1} K^{-1}, respectively (see Table 12). The positive $\Delta S^{\ddagger}$ value implies a D mechanism for the redox reaction.

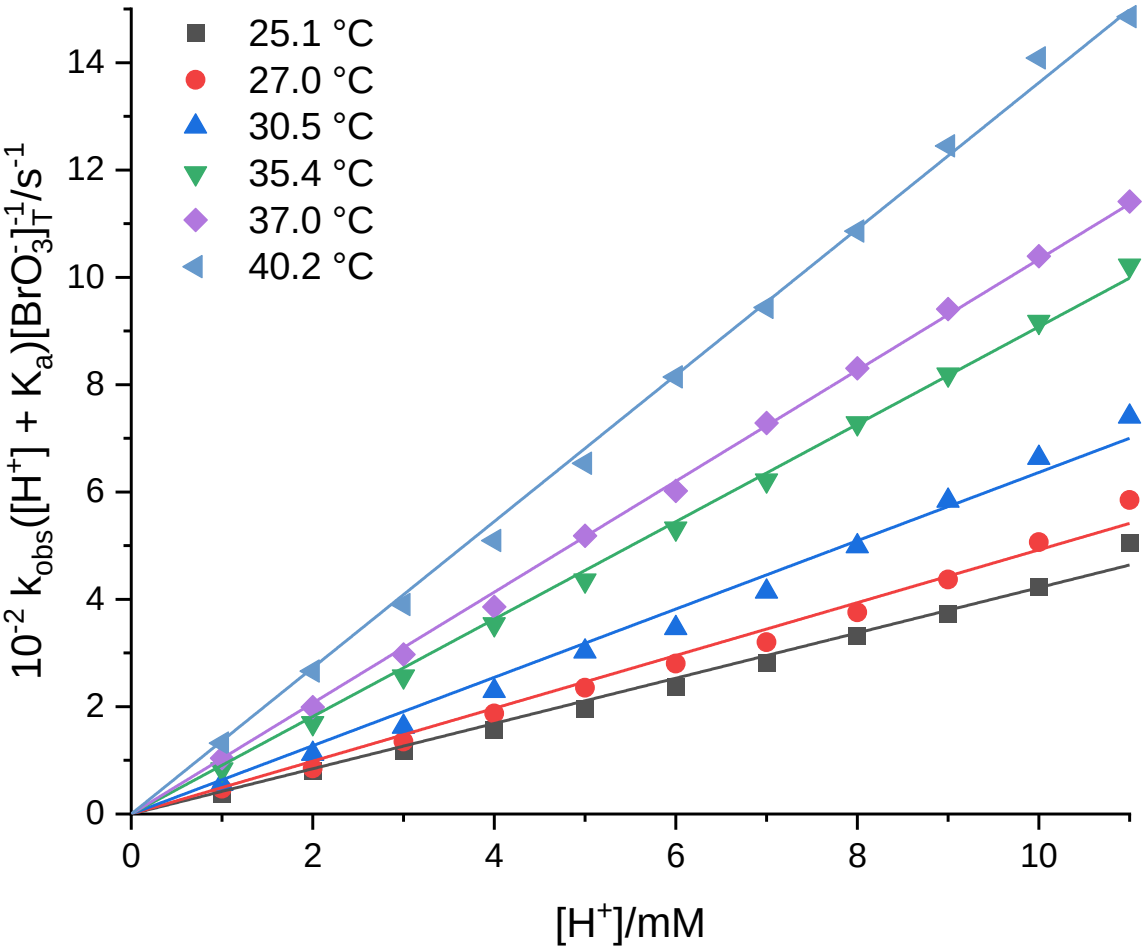

Figure 41. Plots of $k_{obs}([H^+] + K_a)[NaBrO_3]_T^{-1}$ versus the concentration of HCl for the oxidation of $[Co(dmgBF_2)_2(OH_2)_2]$ by $NaBrO_3$ at various temperatures. [complex] = 0.1 mM, [$NaBrO_3$] = 10.0 mM, λ = 450 nm, and I = 0.6 M (NaCl).

Table 12. Rate and activation parameters for the oxidation of $[Co(dmgBF_2)_2(OH_2)_2]$ by $NaBrO_3$.

θ/°C	**$10^{-4}\ k_1/M^{-1}\ s^{-1}$**
25.1	4.22
27.0	4.92
30.0	6.36
35.4	9.08
37.0	10.3
40.2	13.6
$\Delta H^{\ddagger} = 57 \pm 1$ kJ mol^{-1}	
$\Delta S^{\ddagger} = 34 \pm 4$ J mol^{-1} K^{-1}	

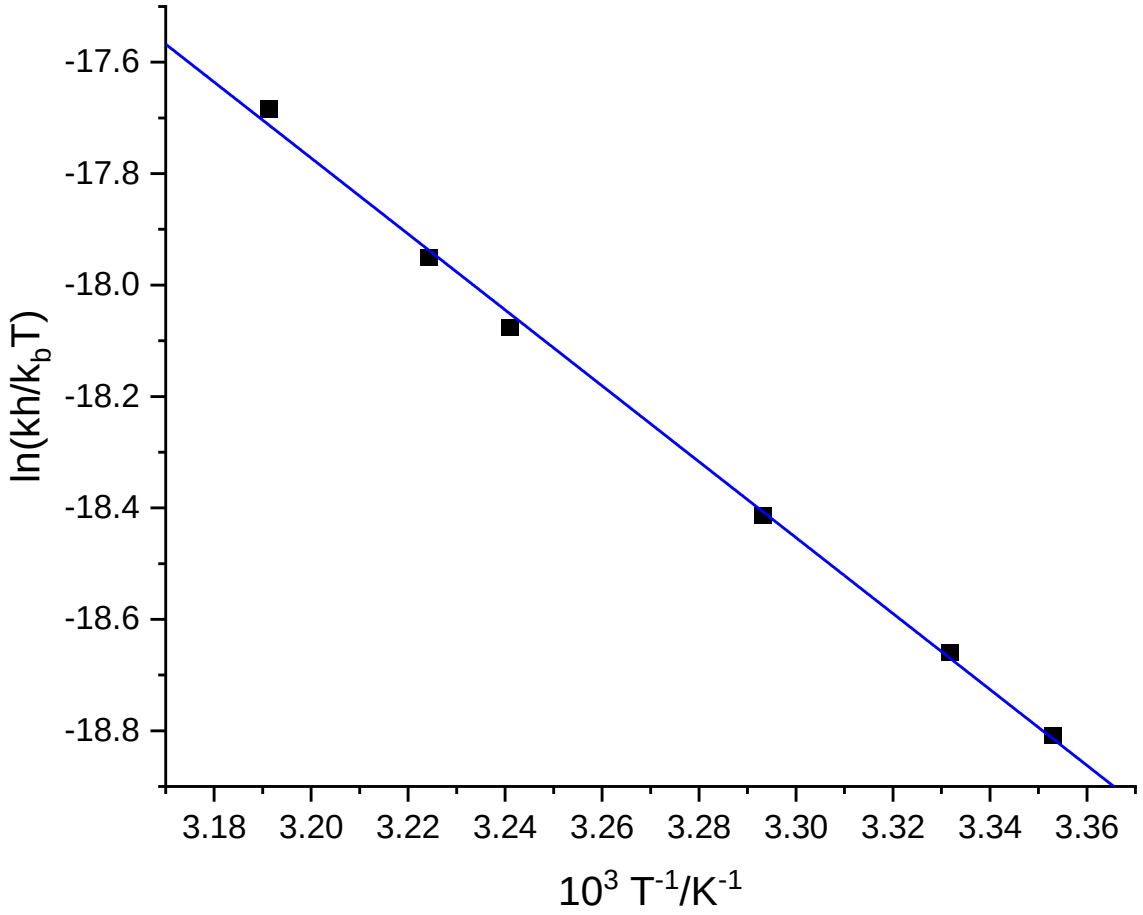

Figure 42. An Eyring plot for the reduction of the bromate anion by the cobaloxime.

Pujari and Banerjee, [152] and Summer *et al*. [155] both saw similar effects of when the proton concentration is increased so does the rate of the reaction. This is due to a dependence the protonation of the bromate anion and the resulting bromic acid oxidizing either the cobalt(II) or the iron(II) species as reported by Pujari and Banerjee [152] and Summer *et al*. [155], respectively. With Summer and coworker's work, [155] the observed rates had similar magnitudes, with their reactions being faster with a lower concentration of protons. An example would be at 25 °C, where the pseudo-first order rate constant was 9.52 x 10^{-2} s^{-1} with 0.1 mM [H^+], 4 mM BrO_3^-, and 0.1 mM $[Fe(bpy)_3]^{2+}$. In the case of Iyun and company [156], the rate constant at 25 °C for the reaction between the bromate anion and the binuclear ruthenium(II) complex ($[\{Ru(OH_2)(bpy)_2\}_2\{\mu\text{-}O\}]^{4+}$) was (6.50 ± 0.10) x 10^{-2} M^{-1} s^{-1}, which is a hundred times what was observed in our studies. Iyun and company [156] also noted that the reaction had two parallel reactions, one which was acid dependent and the other being acid independent. However, when we compare our study with the

study as reported by Pujari and Banerjee [152], our redox reaction was about a hundred times faster than theirs. Pujari and Banerjee, [152] and Summer *et al*. [155] both saw similar effects of when the proton concentration is increased so does the rate of the reaction. This is due to a dependence the protonation of the bromate anion and the resulting bromic acid oxidizing either the cobalt(II) or the iron(II) species as reported by Pujari and Banerjee [152] and Summer *et al*. [155], respectively. With Summer and coworker's work, [155] the observed rates had similar magnitudes, with their reactions being faster with a lower concentration of protons. An example would be at 25 °C, where the pseudo-first order rate constant was 9.52×10^{-2} s^{-1} with 0.1 mM $[H^+]$, 4 mM BrO_3^-, and 0.1 mM $[Fe(bpy)_3]^{2+}$. In the case of Iyun and company [156], the rate constant at 25 °C for the reaction between the bromate anion and the binuclear ruthenium(II) complex ($[\{Ru(OH_2)(bpy)_2\}_2\{\mu\text{-}O\}]^{4+}$) was $(6.50 \pm 0.10) \times 10^{-2}$ M^{-1} s^{-1}, which is a hundred times what was observed in our studies. Iyun and company [156] also noted that the reaction had two parallel reactions, one which was acid dependent and the other being acid independent. However, when we compare our study with the study as reported by Pujari and Banerjee [152], our redox reaction was about a hundred times faster than theirs. Pujari and Banerjee, [152] and Summer *et al*. [155] both saw similar effects of when the proton concentration is increased so does the rate of the reaction. This is due to a dependence the protonation of the bromate anion and the resulting bromic acid oxidizing either the cobalt(II) or the iron(II) species as reported by Pujari and Banerjee [152] and Summer *et al*. [155], respectively. With Summer and coworker's work, [155] the observed rates had similar magnitudes, with their reactions being faster with a lower concentration of protons. An example would be at 25 °C, where the pseudo-first order rate constant was 9.52×10^{-2} s^{-1} with 0.1 mM $[H^+]$, 4 mM BrO_3^-, and 0.1 mM $[Fe(bpy)_3]^{2+}$. In the case of Iyun and company [156], the rate constant at 25 °C for the reaction between the bromate anion and the binuclear ruthenium(II) complex ($[\{Ru(OH_2)(bpy)_2\}_2\{\mu\text{-}O\}]^{4+}$) was $(6.50 \pm 0.10) \times 10^{-2}$ M^{-1} s^{-1}, which is a hundred times what was observed in our studies. Iyun and company [156] also noted that the reaction had two parallel reactions, one which was acid dependent and the other being acid independent. However, when we compare our study with the study as reported by Pujari and Banerjee [152], our redox reaction was about a hundred times faster than theirs.

In the literature where the bromate is used as an oxidant, it is noted that when the first two (2) electrons are transferred, the resulting bromine-containing species that is formed is the BrO_2^- anion [157-159]. This is reported to be a more powerful oxidant than BrO_3^- [157-159]. Note that in studies

as reported by Pujari and Banerjee [152], the complex is only able to undergo a single electron oxidation, that leads to the formation of the $Br^{IV}O_2$ which would be highly reactive and would be quickly reduced in solution to produce the BrO_2^- anion. In the literature where the bromate is used as an oxidant, it is noted that when the first two (2) electrons are transferred, the resulting bromine-containing species that is formed is the BrO_2^- anion [157-159]. This is reported to be a more powerful oxidant than BrO_3^- [157-159]. Note that in studies as reported by Pujari and Banerjee [152], the complex is only able to undergo a single electron oxidation, that leads to the formation of the $Br^{IV}O_2$ which would be highly reactive and would be quickly reduced in solution to produce the BrO_2^- anion. In the literature where the bromate is used as an oxidant, it is noted that when the first two (2) electrons are transferred, the resulting bromine-containing species that is formed is the BrO_2^- anion [157-159]. This is reported to be a more powerful oxidant than BrO_3^- [157-159]. Note that in studies as reported by Pujari and Banerjee [152], the complex is only able to undergo a single electron oxidation, that leads to the formation of the $Br^{IV}O_2$ which would be highly reactive and would be quickly reduced in solution to produce the BrO_2^- anion.

2.1.3 Oxidation of $[Co(dmgBF_2)_2(OH_2)_2]$ by Br_2

2.1.3.1 Determination of the bromine species

Taking into consideration the speciation that may occur in the presence of NaCl, a UV-visible spectroscopy study was carried out on bromine in the buffer at various pH, as well as in the presence of salt and no salt. In *Figure 43* a clear difference between bromine with and without NaCl produce two distinct spectra. Without NaCl, two peaks are observed at 260 and 393 nm which corresponds to HOBr and Br_2, respectively. This is expected as it is well documented in literature. When NaCl is added, it is observed that peak at 260 nm is no longer visible, and the peak that once appeared at 393 nm is now blue shifted to 381 nm. The peak at 381 nm is indicative of the Br_2Cl^- species being present in solution. Upon acquisition of the bromine solutions at various pH as what was conducted in the kinetic experiments, it is observed that at the more acidic pH the predominant species present in solution is Br_2Cl^-, which slowly fades as the pH is made more basic. At the highest pH measured it was observed that the bromine species that are present are HOBr and OBr^-.

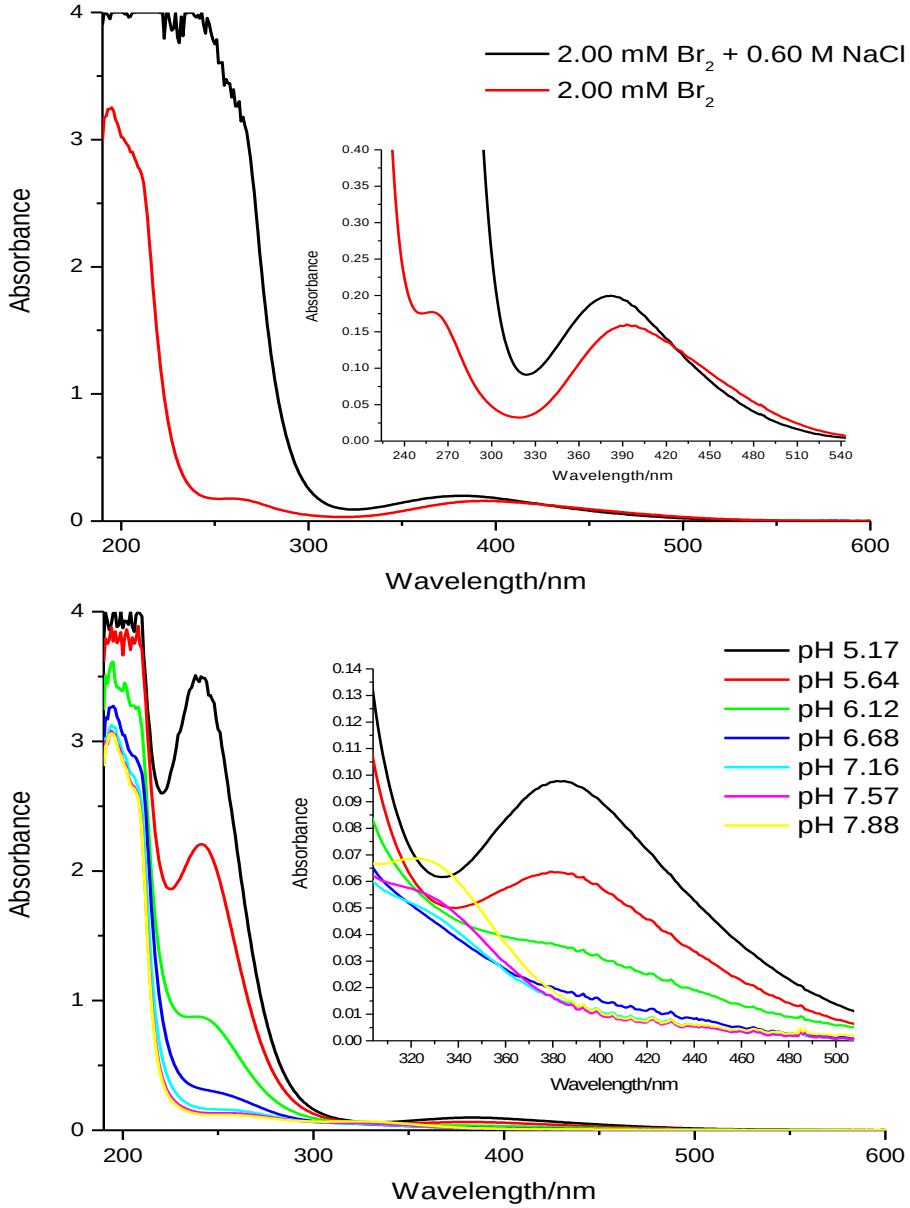

Figure 43. A plot of absorbance versus wavelength of (top) 2.00 mM bromine with and without NaCl, (bottom) 2.00 mM bromine at various pH with constant ionic strength of 0.60 M (NaCl).

2.1.3.2 Stoichiometry of the reaction

From the stoichiometric data in Figure 44, it was observed that for every three moles of bromine that is reduced, four moles of $[Co(dmgBF_2)_2(OH_2)_2]$ is oxidized at a near neutral pH. This is very different from what is expected as the bromine species within the solution should all be two electron oxidants like what was observed with NaOCl. A possible explanation to what is being observed could be linked back to the relative reactivity of the halogens with Br_2 being a weaker

oxidant when compared to Cl_2 and the relative reactivity of the radicals they produce.[37] Thus, if this does occur after the its first reduction the resulting bromine radical could either oxidize another $[Co(dmgBF_2)_2(OH_2)_2]$ or participate in radical propagation.

$$Br_2Cl^- \overset{[Cl^-]}{\longleftrightarrow} Br_2 \xrightarrow{H_2O,\ pH>7} BrO^- + Br^-$$

$$4\,[Co(dmgBF_2)_2(OH_2)_2] + 3\,Br_2 \rightarrow\ 4\,[Co(dmgBF_2)_2(OH_2)_2]^+ + Br_2\ byproducts$$

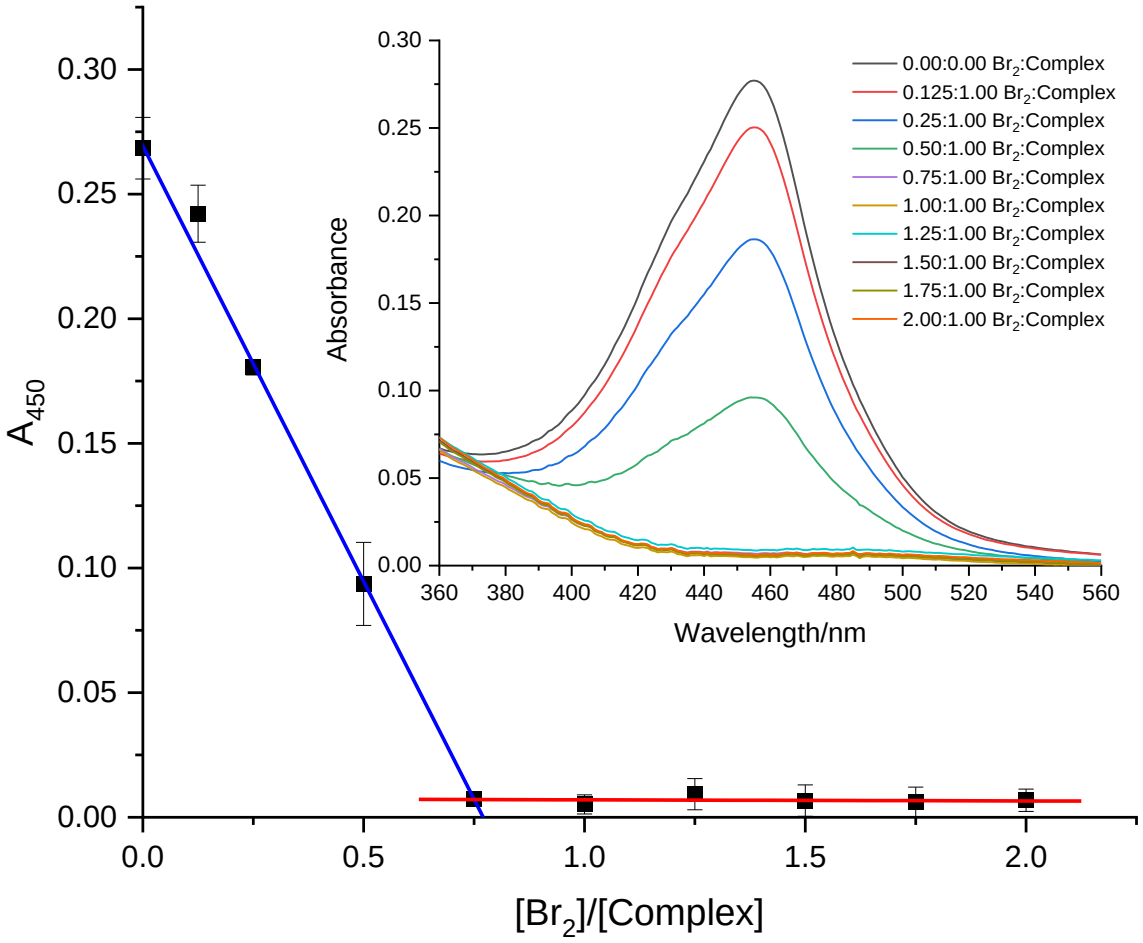

Figure 44. A plot of absorbance change versus the ratio of $[Br_2]$/[complex] for the oxidation of $[Co(dmgBF_2)_2(OH_2)_2]$ by Br_2 in water. Inset = A plot of absorbance versus wavelength for the oxidation of $[Co(dmgBF2)_2(OH2)_2]$ by Br_2 in water. [Complex] = 0.10 mM, λ = 450 nm, I = 0.60 M (NaCl), θ = room temperature, and buffer = phosphate buffer, pH = 7.30 ± 0.06.

2.1.3.3 Aqueous bromide solution, concentration, ionic strength, temperature and pH dependence of the reaction

Kinetic studies carried out over the ranges of 0.50 mM ≤ [Br_2] ≤ 4.00 mM, 5.13 ≤ pH ≤ 7.52 and 10.1 °C ≤ θ ≤ 25.0 °C, all while holding the ionic strength constant at 0.60 M with NaCl. For the kinetic runs where the total concentration of bromine was varied, it was observed that as the concentration increased a saturation effect was observed, as seen in Figure *45*. This type of behavior is indicative of the existence of an equilibrium and the possibility pairing between both reactants as seen in Scheme 8, where equilibriums that possibly exist are between $[Co(dmgBF_2)_2(OH_2)(OH_2)]^-$ and either Br_2Cl^- and OBr^-.

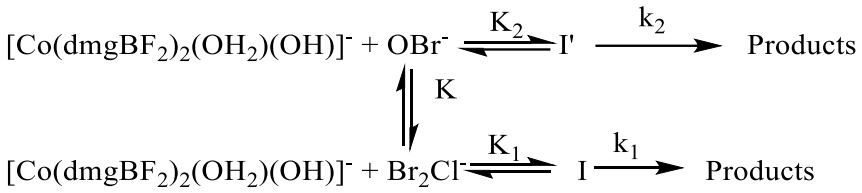

Scheme 8.Proposed mechanism for the oxidation of $[Co(dmgBF_2)_2(OH_2)_2]$ by bromine at various pH values in the presence of Cl^-.

Table 13. Pseudo-first order rate constants for the oxidation of $[Co(dmgBF_2)_2(OH_2)_2]$ by Br_2 in water. [Complex] = 0.05 mM, λ = 450 nm, I = 0.60 M (NaCl), θ = 10.1 °C, and buffer = phosphate buffer, pH = 7.45 ± 0.08.

$[Br_2]$/mM	**10^{-2} k_{obs}/s^{-1}**
0.50	0.97

1.00	1.71
1.50	2.36
2.00	2.90
2.50	3.17
3.00	3.29
3.50	3.44
4.00	3.51

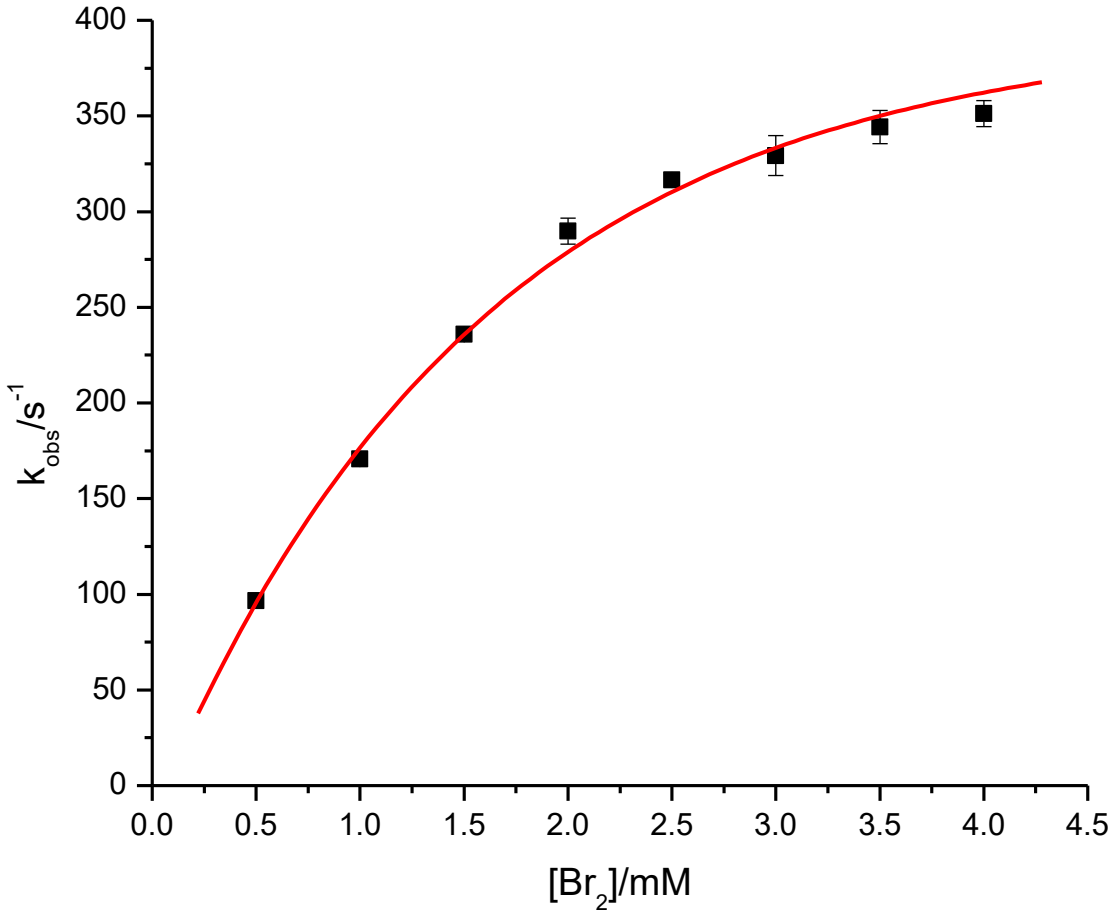

Figure 45. A plot of k_{obs} vs the concentration of bromine in water. [complex] = 0.05 mM, λ = 450 nm, I = 0.60 M (NaCl), θ = 10.1 °C, and buffer = phosphate buffer, pH = 7.45 ± 0.08.

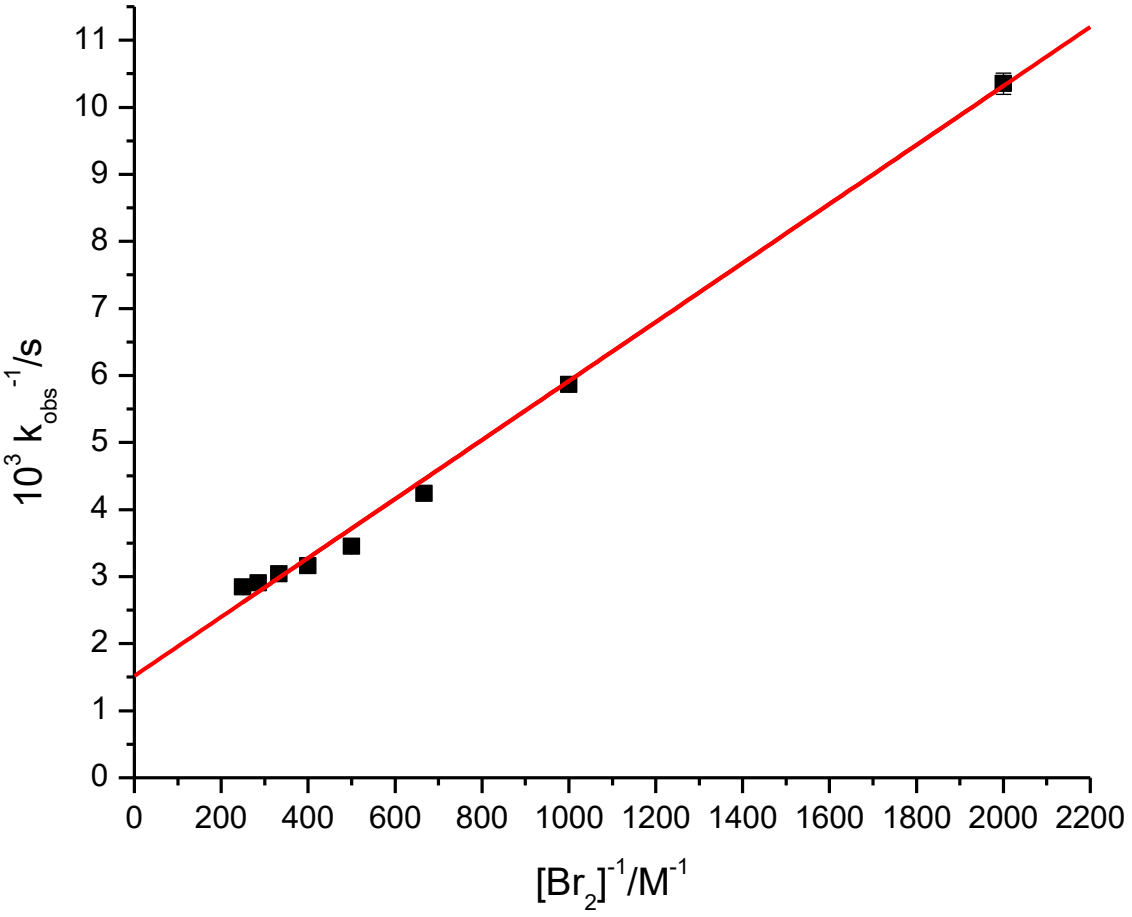

Figure 46. A plot of k_{obs}^{-1} vs the inverse concentration of bromine in water. [complex] = 0.05 mM, λ = 450 nm, I = 0.60 M (NaCl), θ = 10.1 °C, and buffer = phosphate buffer, pH = 7.45 ± 0.08.

Upon varying the ionic strength of the solution, t was observed that as the ionic strength was increased, so did the observed rate of oxidation. By applying the Brönsted-Bjerrum equation,[138] Upon varying the ionic strength of the solution, t was observed that as the ionic strength was increased, so did the observed rate of oxidation. By applying the Brönsted-Bjerrum equation,[138] Upon varying the ionic strength of the solution, t was observed that as the ionic strength was increased, so did the observed rate of oxidation. By applying the Brönsted-Bjerrum equation,[138]

In Figure 47, a plot of log k_{obs} versus $I^{1/2}/(1 + I^{1/2})$ results in slope of 1.66 resulting in a z_1z_2 of 1.67 and from the intercept, $k°_{obs}$ of 9.78 x 10^1. From z_1z_2 it can be inferred that the reacting species have charges of $z_1 = -1$ and $z_2 = -2$.

Table 14. A table of pseudo-first order rate constants for the variation in ionic strength for the oxidation of $[Co(dmgBF_2)_2(OH_2)_2]$ by Br_2. [complex] = 0.1 mM, $[Br_2]$ = 10.0 mM, pH = 5.31 ± 0.14, λ = 450 nm, and θ = 25.0 °C.

I/M	**k_{obs}/s^{-1}**
0.24	338.64 ± 30.5
0.3	380.51 ± 12.6
0.4	445.02 ± 10.1
0.5	468.21 ± 13.7
0.6	516.54 ± 7.3

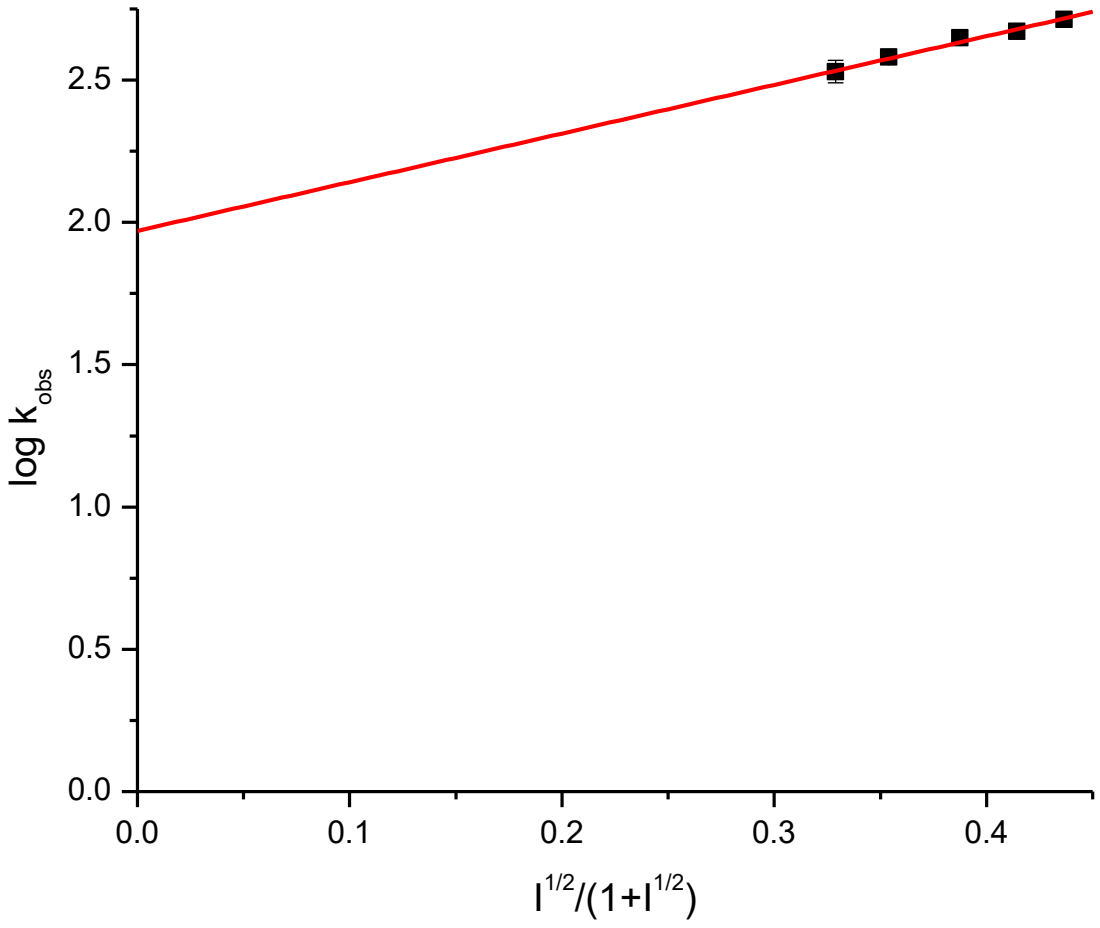

Figure 47. A plot of log k_{obs} versus $I^{1/2}/(1 + I^{1/2})$ in water at various ionic strengths. [Complex] = 0.05 mM, $[Br_2]$ = 2.00 mM, λ = 450 nm, θ = 10°C, and buffer = phosphate buffer, pH = 5.31 ± 0.14.

Following the variation of ionic strength, the pH was varied while keeping both reactants and ionic strength constant. It was observed that as the pH is increased that there is a change in the complex with an equilibrium that varies with temperature, see Table 15 and Figure 48. This change can be interpreted as one of the aqua ligands being deprotonated from $[Co(dmgBF_2)_2(OH_2)_2]$ to form $[Co(dmgBF_2)_2(OH_2)]^-$, with the former being more reactive than the latter in the presence of the bromine solution. Using the data from the pH study an expression for k_{obs} was derived by taking into consideration the proposed equilibrium that exist between the two reactants, and the K derived from what was observed through the change of pH. From *Scheme* 8 the following expression for k_{obs} was derived:

$$k_{obs} = \frac{k_1 K_1 [H^+] + k_2 K_2 K_a}{[H^+] + K_a} [Br_2]_T \qquad (14)$$

The expression can be rearranged to give:

$$\frac{k_{obs}([H^+] + K_a)}{[Br_2]_T} = k_1 K_1 [H^+] + k_2 K_2 K_a \qquad (15)$$

Table 15. Pseudo-first order rate constants for the oxidation of $[Co(dmgBF_2)_2(OH_2)_2]$ by Br_2 in water by varying the pH. [complex] = 0.05 mM, $[Br_2]$ = 2.00 mM, λ = 450 nm, I = 0.60 M (NaCl), and buffer = phosphate buffer.

θ = 10.1 °C		**θ = 15.1 °C**		**θ = 20.0 °C**		**θ = 25.0 °C**	
pH	10^{-2} k_{obs}/s^{-1}	pH	10^{-2} k_{obs}/s^{-1}	pH	10^{-2} k_{obs}/s^{-1}	pH	10^{-2} k_{obs}/s^{-1}
5.13	5.17	5.22	5.21	5.19	6.23	5.31	7.35
5.63	4.31	5.57	5.27	5.59	6.59	5.62	6.96
6.04	4.13	6.00	4.79	5.97	5.74	6.06	6.05
6.45	3.60	6.49	4.13	6.45	4.85	6.48	5.13
6.85	2.87	6.92	3.50	6.88	4.13	6.93	4.46
7.17	2.56	7.25	3.15	7.31	3.81	7.32	4.21
7.36	2.39	7.47	3.00	7.52	3.61	7.49	4.12

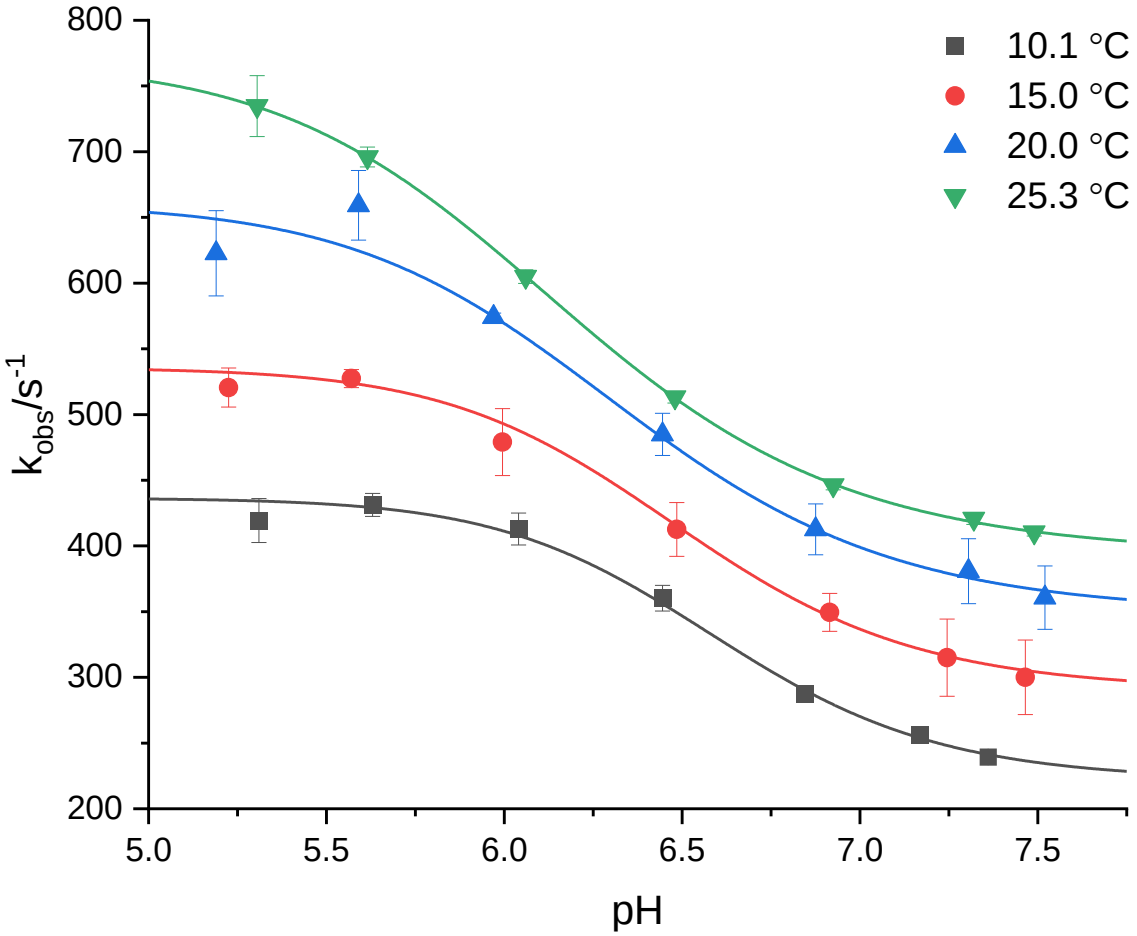

Figure 48. A plot of k_{obs} versus pH for the oxidation of $[Co(dmgBF_2)_2(OH_2)_2]$ by Br_2. [Complex] = 0.05 mM, $[Br_2]$ = 2.00 mM, λ = 450 nm, I = 0.60 M (NaCl), and buffer = phosphate buffer.

Table 16. Rate parameters, pK_a, and activation parameter values for the reaction between $[Co(dmgBF_2)_2(OH_2)_2]$ and aqueous bromine.

θ/°C	**10^{-5} k'$_1$/M^{-1} s^{-1}**	**10^{-5} k'$_2$/M^{-1} s^{-1}**	**10^7 K/M**
10.1	2.16	1.29	2.45
15.1	2.68	1.87	3.09
20.0	3.23	3.53	4.37
25.0	3.93	5.95	7.41
$\Delta H^{\ddagger}$/ kJ mol^{-1}	26 ± 0.1	71 ± 2	
$\Delta S^{\ddagger}$/J mol^{-1} K^{-1}	-52 ± 0.2	105 ± 1	

When the left-hand side of equation 15 is plotted versus $[H^+]$ gave a linear representation over the pH range, with the slope being k_1K_1 and an intercept being k_2K_2. The plot shown in Figure 49 shows the linearity over the pH range used. Upon analysis and interpretation of the data both k_1K_1 and k_2K_2 was obtained through linear regressional analysis, but due the inability to separate k_1K_1 into k_1 and K_1, and k_2K_2 into k_2 and K_2, they were combined to give k'_1 and k'_2, respectively. That data is summarized in

Table 16. From the rate parameters of the pH studies with Br_2, parallel reactions were monitored with Br_2 and their activation parameters were also calculated (k'$_1$: $\Delta H^{\neq}$ = 26 ± 0.1 kJ mol^{-1} and $\Delta S^{\neq}$ = -52 ± 0.2 J mol^{-1} K^{-1}, and k'$_2$: $\Delta H^{\neq}$ = 71 ± 2 kJ mol^{-1} and $\Delta S^{\neq}$ = 105 ± 0.6 J mol^{-1} K^{-1}). The $\Delta S^{\ddagger}$ value for k'$_1$ (-52 kJ mol^{-1}) indicates that the reaction for that portion of the reaction is proceeding through a associative type mechanism while the $\Delta S^{\ddagger}$ value for k'$_2$ (105 J mol^{-1}K^{-1}) it can be inferred that an dissociative type mechanism may be occurring.

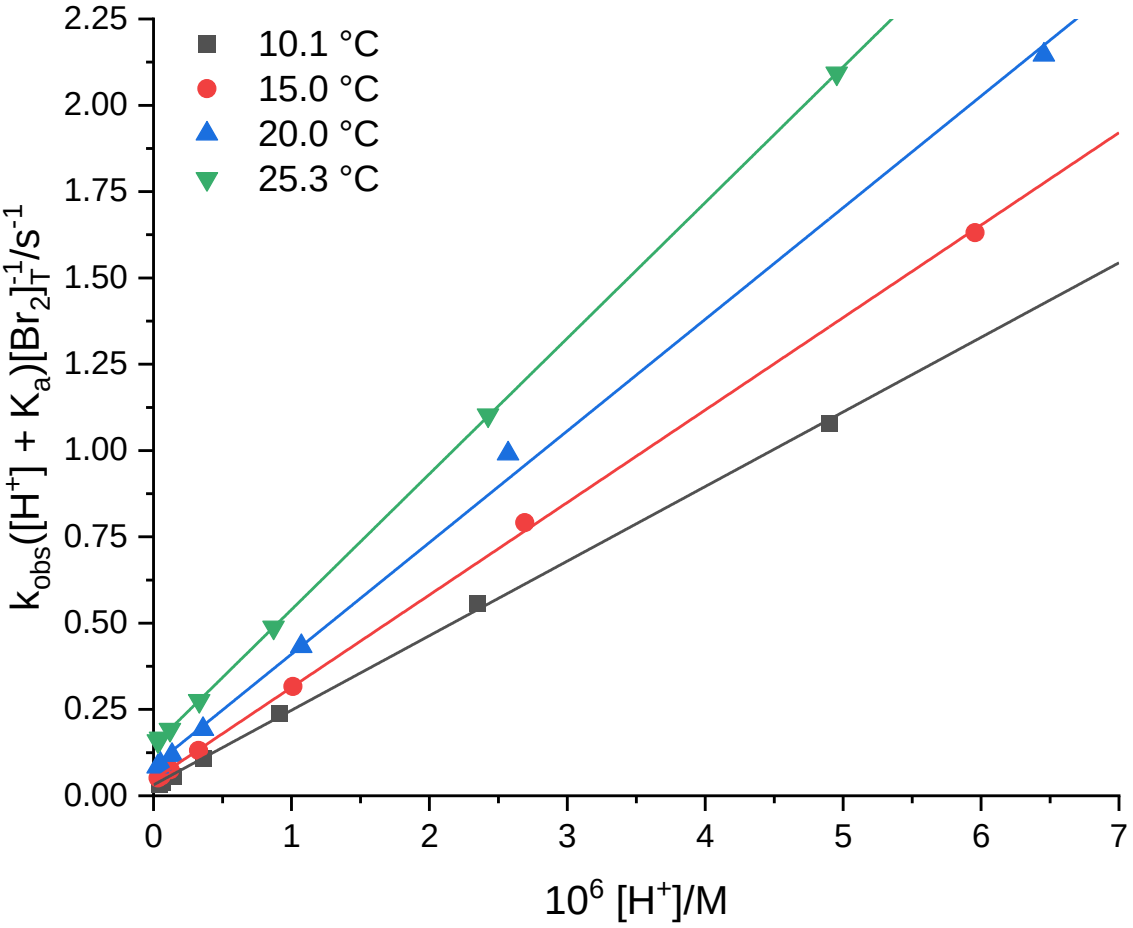

Figure 49. A plot of kobs([H$^+$] + Ka)/[Br_2]$_T$ vs [H$^+$] for the oxidation of [Co(dmgBF_2)$_2$(OH_2)$_2$] by 2 mM Br_2 in water. [complex] = 0.05 mM, λ = 450 nm, I = 0.60 M (NaCl), and buffer = phosphate buffer.

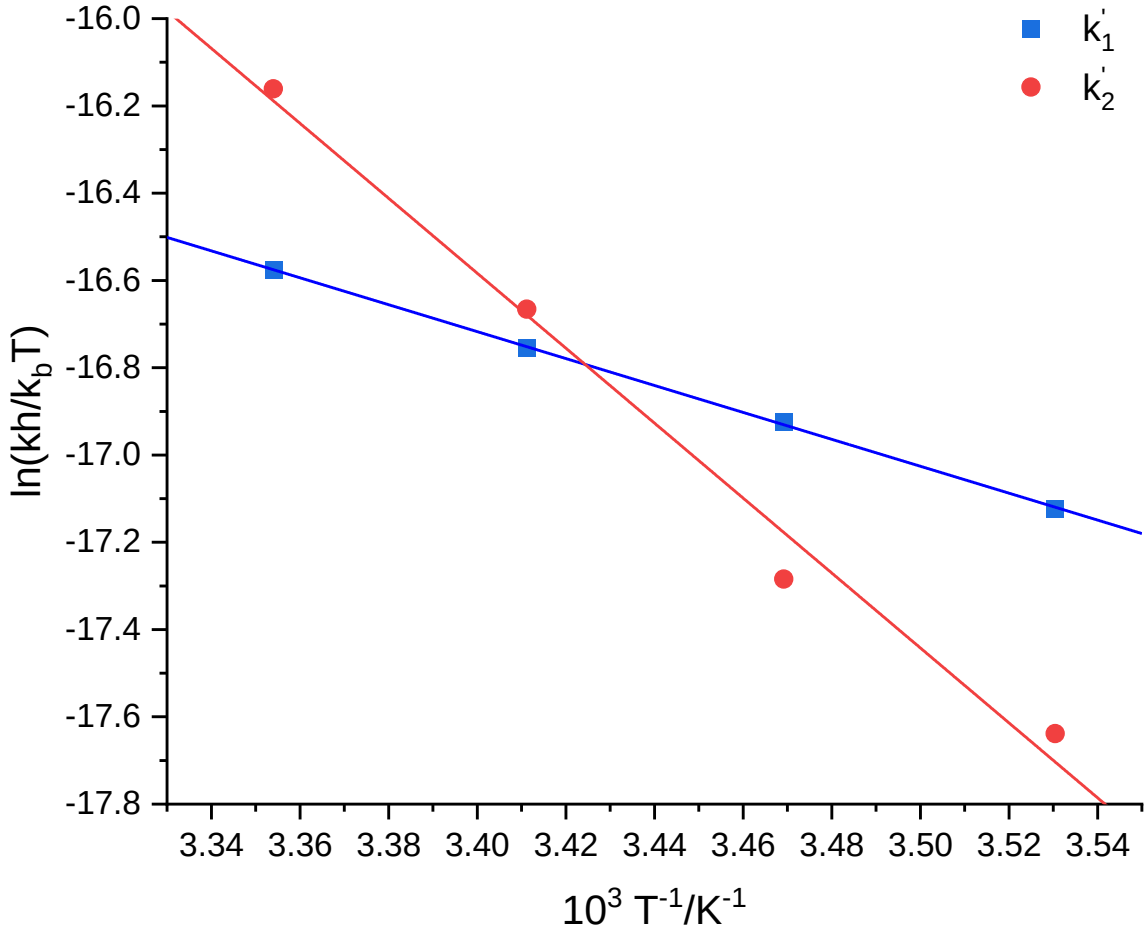

Figure 50. An Eyring plot for the reduction of the bromine by the cobaloxime.

2.1.4 Isokinetic data

The activation parameters from the NaOCl, $NaBrO_3$, and Br_2 studies are similar and thus, an isokinetic plot of $\Delta H^{\ddagger}$ and $\Delta S^{\ddagger}$ since:

$$\Delta H^{\neq} = \Delta G_0^{\neq} + \beta_0 \Delta S^{\neq} \quad (16)$$

Where $ß_0$ is the isokinetic temperature and $\Delta G_0^{\ddagger}$ is the intrinsic free energy of activation. The isokinetic plot is shown in Figure 51. Figure 51 contains the activation parameters that were acquired in these studies as well as the activation parameters from the same reaction with the oxidant $[Fe(bpy)_3](ClO_4)_3$.[141] It is concluded that there is a high likelihood that the reactions follow a similar mechanism, with $\Delta G_0^{\ddagger}$ = 45 ± 0.9 kJ mol^{-1} and $ß_0$ = 377 ± 9.5 K. From $ß_0$ it shows that if the temperature of the reaction is below 377 K, then the reactions would be controlled by $\Delta H^{\ddagger}$, and above this temperature by $\Delta S^{\ddagger}$.

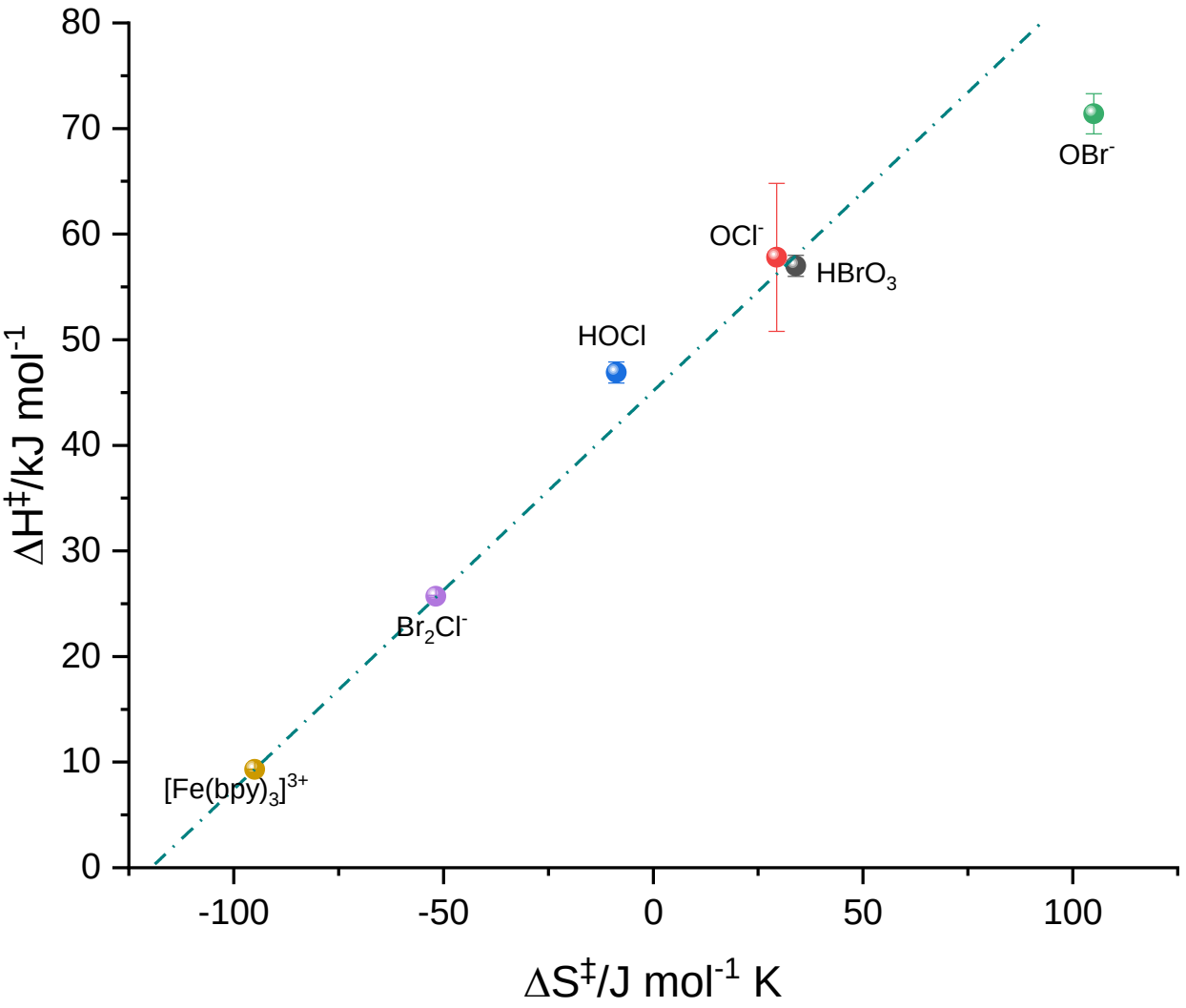

Figure 51. Isokinetic plot of the activation parameters from the oxidation of $[Co(dmgBF_2)_2(OH_2)_2]$.

2.2 Summary of the oxidation of $[Co(dmgBF_2)_2(OH)_2]$

In the beginning kinetic studies were attempted with various cobalt(III) complexes, but there was a problem with the complexes absorbing within the same region as the complex of interest. Thus, a change to oxidants who have an absorbance near zero within the region of interest was utilized.

In all three studies there a dependence on pH was observed, with studies that contains bromine in any form prefers the more acidic conditions whereas with the hypochlorite study the opposite, more basic solutions were preferred. In the end it was observed that all three oxidants used followed a similar electron transfer mechanism. In the study with NaOCl it was observed

that both HOCl and OCl^- both oxidized the complex with the fastest rate of oxidation being attributed to OCl^-. During the kinetic studies a solid was observed to form in solution overtime which was later identified as $[Co(dmgBF_2)_2(OH_2)(OH)]$.

The bromate study the reaction is observed to be the most straight forward of the three with only as the reaction was only dependent on one oxidant which was observed to be $HBrO_3$. When the bromate concentration was varied it was observed that the reaction was first-order with respect to bromate which was different from the hypochlorite study as there was a an pathway that was either dependent on the solvent or the existence of an equilibrium, which favors that latter form the mechanism that was developed.

Studies with bromine revealed through the variation in bromine concentration resulted in the saturation of the observed rates which meant that an equilibrium exists which from the proposed mechanism was observed to be Br_2Cl^- and OBr^-. The reacting species were identified via the UV-visible spectroscopic study and through the variation in pH study the equilibrium constant was observed to shift with temperature for the bromine species.

Chapter 3: Interaction of $[Co(dmgBF_2)_2(OH_2)_2]$ with Et_3N

3.0 Materials and physical measurements

3.0.1 Materials

Analytical or reagent grade chemicals obtained from commercial sources were used as received throughout this study.

3.0.2 Physical measurements

HFEPR spectra were recorded at the National High Magnetic Field Laboratory (NHMFL, Tallahassee, FL, USA). The spectrometer employs a Virginia Diodes (Charlottesville, VA, USA) source operating at a base frequency of 12 – 14 GHz and multiplied by a cascade of multipliers in conjunction with a 15/17 T super conducting magnet.[160] Detection was provided with an InSb hot-electron bolometer (QMC Ltd., Cardiff, UK). The magnetic field was modulated at 50 kHz. A Stanford Research Systems SR830 lock-in amplifier converted the modulated signal to DC voltage. Low temperature was provided by an Oxford Instruments (Oxford, UK) continuous flow cryostat with temperature controller.

All simulations were produced using Bruker's XSophe software.

ESI MS spectra were acquired via positive electrospray ionization on a Bruker 12 Tesla APEX –Qe FTICR-MS with an Apollo II ion source at the College of Sciences Major Instrument Cluster (COSMIC), Old Dominion University. Samples were dissolved in methanol before being introduced by direct injection using a syringe pump with a flow rate of 2 μL s^{-1}. The data was processed using Bruker Daltonics Data Analysis Version 3.4. ESI MS spectra were acquired via positive electrospray ionization on an ABSciex API2000 LC/MS/MS spectrometer. Samples were dissolved in acetonitrile, followed by direct injection using a syringe pump with a flow rate of 20 μL s-1.

3.1 Experimental

3.1.1 Reaction between $[Co(dmgBF_2)_2(OH_2)_2]$ and Et_3N

$[Co(dmgBF_2)_2(OH_2)_2]$ (0.21 g, 0.50 mmol) was dissolved in MeCN (80 ml) and Et_3N (0.48 g, 664 μl 4.76 mmol) was added to the solution. After 24 hours the reaction mixture was

rotovapped down to dryness and the resulting residue was sonicated in Et_2O and was filtered through a fine frit and was stored in the freezer. Yield: 0.25 g (100%) Calc for $C_{15.5}H_{35.75}B_2CoF_4N_{5.25}O_{10.25}$ calc. (found): C 33.40 (33.71), H 6.47 (6.14), and N 13.19 (12.82). High resolution ESI MS: mz/ = 498.1 (M^+) and 6.13.2 ($\{M+H_2O+C_6H_{11}N\}^+$)

3.1.2 High Field EPR sample preparation

Solid $[Co(dmgBF_2)_2(H_2O)_2]$ (16 mg) or $[Co(dmgBF_2)_2(OH_2)(N(C_2H_3)_3)]$ (83 mg) were mixed together with eicosane in a mortar and were gentle ground together. The mixture was then pressed into a pellet and was placed on top of the sample holder and held in place with Teflon tape.

The complex, $[Co(dmgBF_2)_2(H_2O)_2]$ (21 mg, 0.05 mmol), was dissolved in acetonitrile (1 ml) to produce a saturated solution for the neat cobalt(II) study. For all other solutions, $[Co(dmgBF_2)_2(H_2O)_2]$ (21 mg, 0.05 mmol) was dissolved with one or both of the following; $[Bu_4N]BH_4$ (0.0445 g, 0.5 mmol) and/or triethylamine (97.3 µl, 0.0708 g, 0.7 mmol), with the final volume adjusted to 1 ml of acetonitrile. Samples that contained triethylamine was then allowed to sit for 24 hours before their EPR spectra were acquired and samples with the borohydride were made in an glovebox under an inert atmosphere. Three hundred (300) microliters of sample in a plastic tube is then frozen in liquid nitrogen before it was placed in the sample holder and the temperature was brought down to 10 K.

3.2 Results and discussion

3.2.1 Reaction between $[Co(dmgBF_2)_2(OH_2)_2]$ and Et_3N

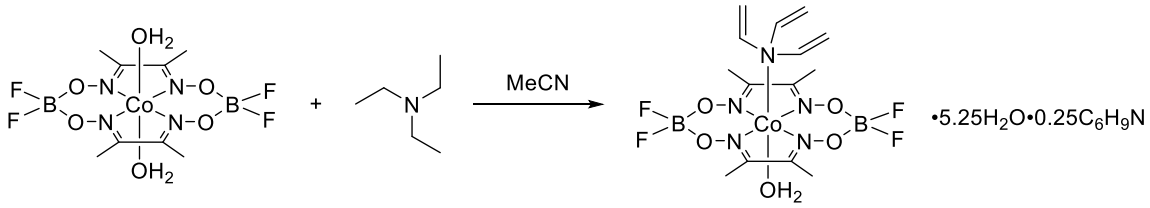

Scheme 9. Reaction between $[Co(dmgBF_2)_2(OH_2)_2]$ and Et_3N.

The interaction between cobaloximes and triethylamine is nothing new, in the 70's Schrauzer *et al.*,[161] investigated the interactions between a bromo(pyridine)cobaloxime reacting with ethyl vinyl ether in the presence of ethanol, dichloromethane, and triethylamine. They noted that though the system is very complicated, there is evidence that the cobalt(I) species is formed in solution and reacts with the dichloromethane to produce chloromethyl(pyridine)cobaloxime which is unstable under basic conditions. At the end of their reaction the product that was obtained

from the cobaloxime was pyridinecobaloxime(II). This study was done as a follow up to a study on another study by Silverman, in which Silverman had a rebuttal as it was stated that the product that was obtained had a cobalt(III) metal center with an alkyl ligand coordinated to the metal center.[162] The biggest takeaway from these studies This study was done as a follow up to a study on another study by Silverman, in which Silverman had a rebuttal as it was stated that the product that was obtained had a cobalt(III) metal center with an alkyl ligand coordinated to the metal center.[162] In another study conducted by Weiss[98] noted the coordination of NEt_3 to the copper(II) metal center resulting in the formation of $[CuCl_2(N(CH_2CH_3)_2]$, which is followed by the reduction of the copper(II) metal center and liberation of a triethylamine radical cation. They also note that the radical cation can participate in subsequent radical reactions resulting in the formation of diethylvinylamine which can also coordinate to the copper(II) metal center forming $[CuCl(N(CH_2CH_3)_2(CH{=}CH_3))]$. After the reaction was complete it was observed that after all the copper(II) was reduced to copper(I) and when the Et_3N was collected, it was noted only one sixth of the two moles of Et_3N had actually reacted with the one mole of copper(II) used.[98] It was noted that with subsequent oxidations the resulting trivinylamine which underwent polymerization resulting in the formation of a tarry product.[98]

3.2.2 Elemental analysis

From the elemental analysis of the product collected from the reaction it was observed to have the following percentages for the C, H, and N as 33.71%, 6.14%, and 12.82%, respectively. The structure and solvates that is the best match for what was observed from the elemental analysis data is where one of the waters in the axial position is replaced by triethylamine with all three ethyl groups oxidized to alkenes. This gave C, H, and N percentages as 33.35%, 6.47%, and 13.17%, respectively.

3.2.3 Mass spectroscopic analysis

The mass spectrum of the product that was collected from the reaction between the cobaloxime and Et_3N has a peak at a m/z = 498.1. This mirrors what was observed from the elemental analysis data with the complex having a calculated m/z of 498.12. The m/z that was observed at 613.2 is most likely the core complex with one water and triethylamine with two of the ethyl groups being oxidized to alkenes giving a m/z = 613.22.

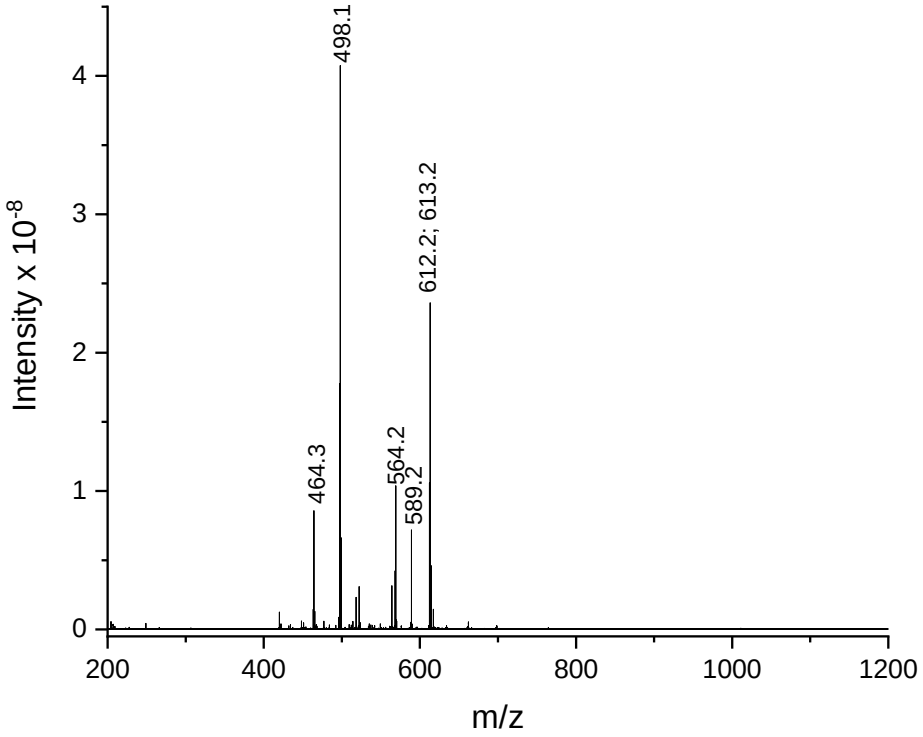

Figure 52. HR MS (positive mode) of $[Co(dmgBF_2)_2(OH_2)(N(C_2H_4)_3)]\bullet 5.25H_2O\bullet 0.25C_6H_9N$.

3.2.4 FTIR spectroscopic studies

After the reaction of the reaction of the complex with Et_3N an FTIR spectrum was acquired. Changes in the stretching frequencies associated with C=N, O-B, and one of the B-F is observed to shift to higher frequencies. This change is attributed to a change to the cobalt metal center of the complex caused when the Et_3N is coordinated. With the starting material there are several conformations that exist, when the Et_3N moiety coordinates to the metal center due to its larger size when compared to H_2O which previously occupied the axial position causes steric hinderance with the equatorial ligands which a push on the axial ligands.

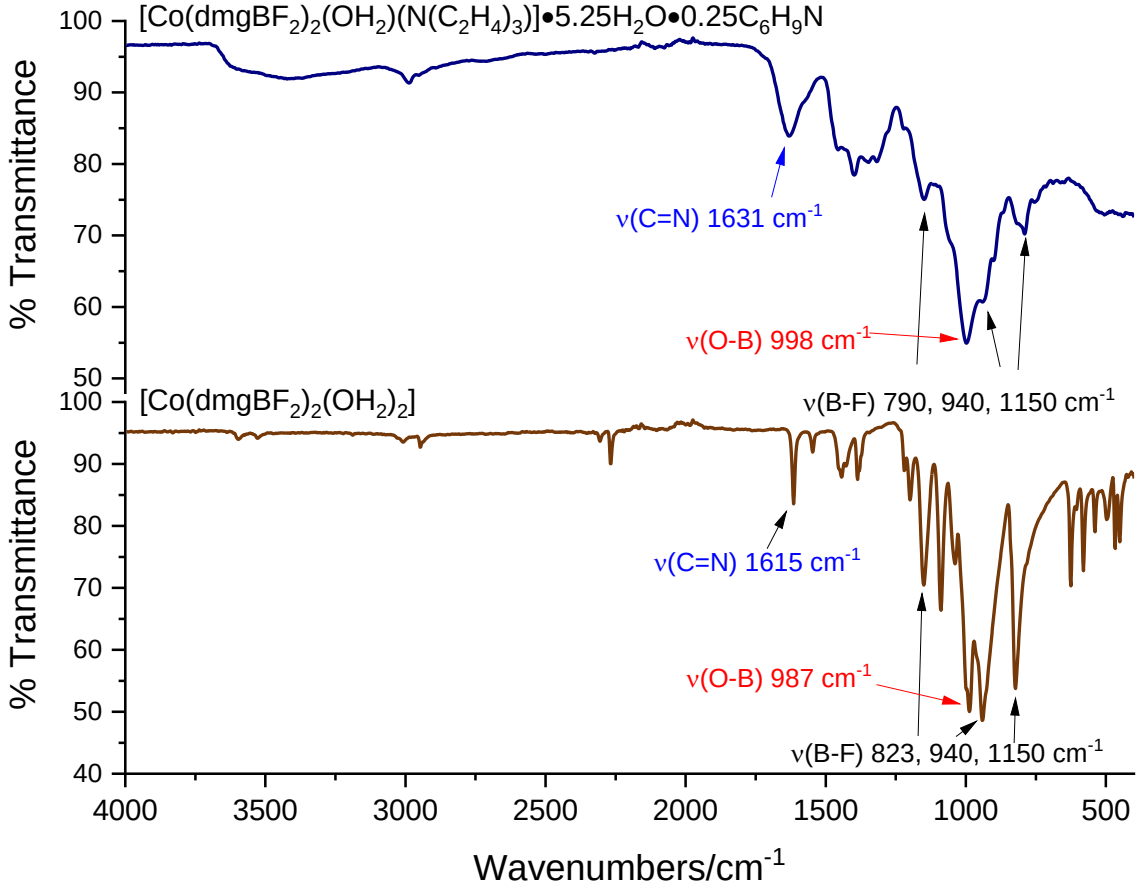

Figure 53. FTIR spectra of $[Co(dmgBF_2)_2(OH_2)_2]$ and $[Co(dmgBF_2)_2(OH_2)(N(C_2H_4)_3)]\bullet 5.25H_2O\bullet 0.25C_6H_9N$.

3.2.5 NMR spectroscopic studies

A time course NMR spectroscopic study conducted on a mixture of the complex and Et_3N. At zero hours the methyl groups of the complex are originally observed at 2.14 ppm which slowly shifts downfield to 2.19 ppm. Likewise, a downfield shift is also observed with the chemical shifts originating from Et_3N starting from 2.46 ppm to 2.475 ppm and 0.99 ppm to 1.00 ppm. It should be noted that due to the paramagnetic nature of the cobalt(II) metal center any chemical shift from a ligand would appear would be broader than it would normally appear if it was coordinated to a diamagnetic metal center or by itself in solution. With the methyl groups though they appear broad, the shift broadens even more as time progresses. An explanation of this could be an increase in the paramagnetic nature of the complex. In conjuncture with those peaks that were observed as moderately strong, very small peaks were also observed near the baseline of the spectra. These changes were observed between 8 ppm to 11 ppm (see Figure 114); with a very broad chemical

shift that was observed at 9.19 ppm which vanished by 2.5 hours and a chemical shift that was observed soon after at 9.72 ppm.

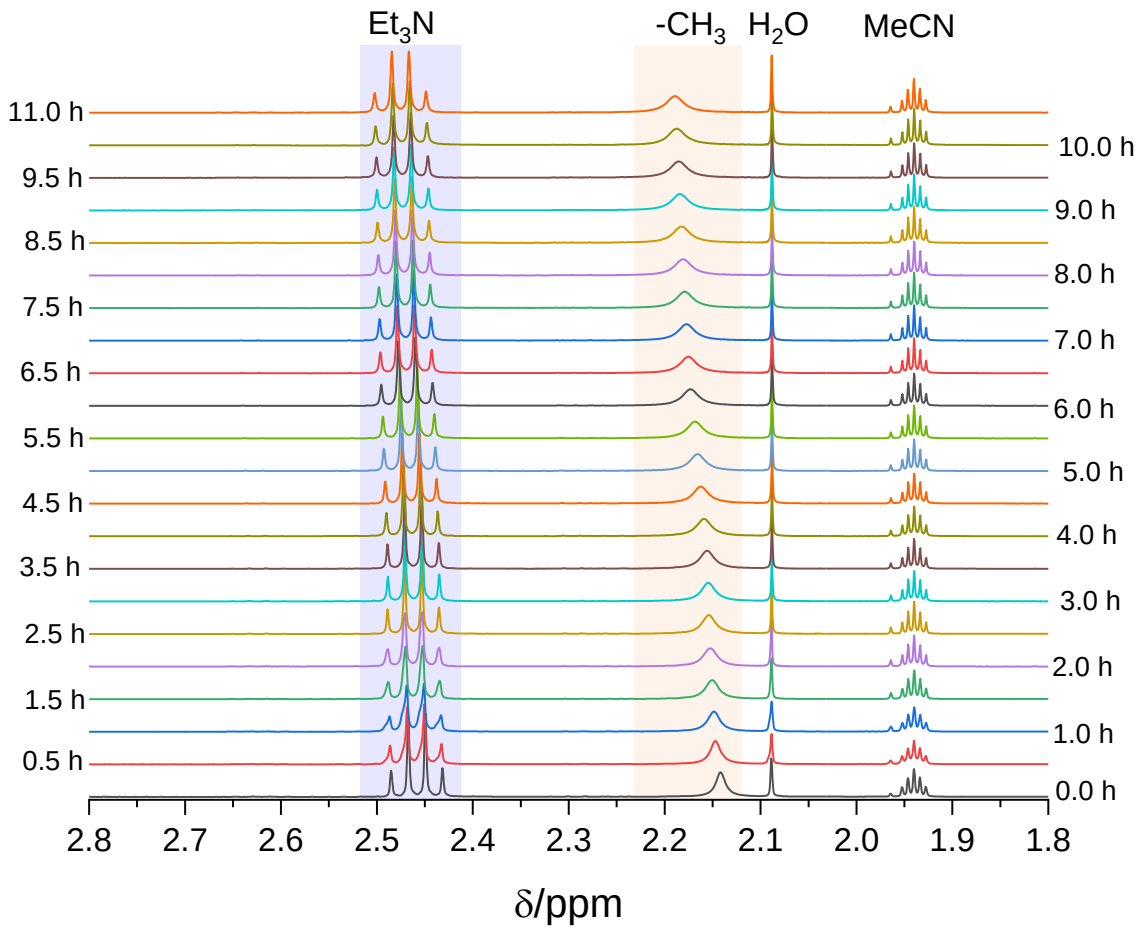

Figure 54. ^{1}H NMR spectra of $[Co(dmgBF_2)_2(OH_2)_2]$ with Et_3N in CD_3CN. $[Co(dmgBF_2)_2(OH_2)_2]$ = 2.38 mM and $[Et_3N]$ = 33.32 mM.

3.2.6 Mass spectroscopic study

Just like with the NMR spectroscopic study, a similar study was conducted using the mass spectrometer (Figure 55). The first thing that should be mentioned is that the axial ligands of cobaloximes tend to undergo an exchange with the they solvent used. Upon investigating the collected spectra, the first m/z of interest is observed at 525.5. This peak corresponds to the complex with one of the axial ligands being acetonitrile and the other being *N*,*N*-diethylethenamine. The appearance of this *N*,*N*-diethylethenamine was formed through the oxidation of triethylamine. A second peak of interest was also observed at a m/z = 266.8, which corresponds to the complex with acetonitrile and triethylamine occupying the axial positions. This

mass to charge ratio is directly related to the previous one observed as the oxidation state of this species is +1 that of the species observed at a m/z of 525.5. This means that complex is reduced resulting in the oxidation of the triethylamine. The oxidized triethylamine can then act as a radical and react with the solvent which gives rise to *N*,*N*-diethylethenamine. The final mass to charge ratio observed, m/z = 289.7, corresponds to the complex with two *N*,*N*-ethyldiethenamine in the axial position. In this case the oxidation state of the complex is very similar to that of the species with the unoxidized triethylamine.

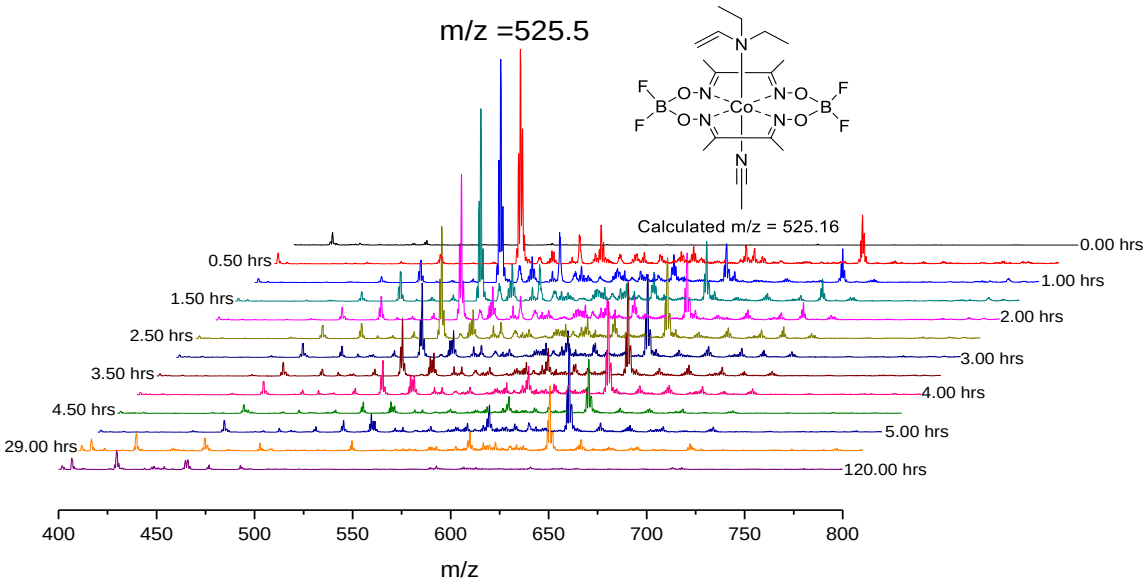

Figure 55. ESI MS of $[Co(dmgBF_2)_2(OH_2)_2]$ with Et_3N in acetonitrile. $[Co(dmgBF_2)_2(OH_2)_2]$ = 1.0 mM, $[Et_3N]$ = 30.0 mM, positive mode.

3.2.7 UV-visible spectroscopic studies

The spectrophotometric titration involving $[Co(dmgBF_2)_2(OH_2)_2]$ in the presence of triethylamine, Figure 56, was seen initially as no interaction between $[Co(dmgBF_2)_2(OH_2)_2]$ and triethylamine. Twenty-four hours a color change was apparent in the solutions containing the triethylamine. The solutions had changed from a translucent gold to a purple coloration. The color change was seen to be faster at higher concentrations when the near infrared region was observed. In Figure 57, two peaks at 550 and 660 nm were observed with their absorbance increasing as the concentration of triethylamine is increased. Upon investigation of the peak that appears at 1162 nm, Figure 58, the peak remains unchanged up to the addition of one equivalent of triethylamine.

At five and ten equivalence the peak is seen to have undergone a blue shift and the peaks broaden to shoulders. After 24 hours the peaks at 1162 nm and the blue shifted shoulders are no longer observed with the higher equivalence solutions (Figure 59).

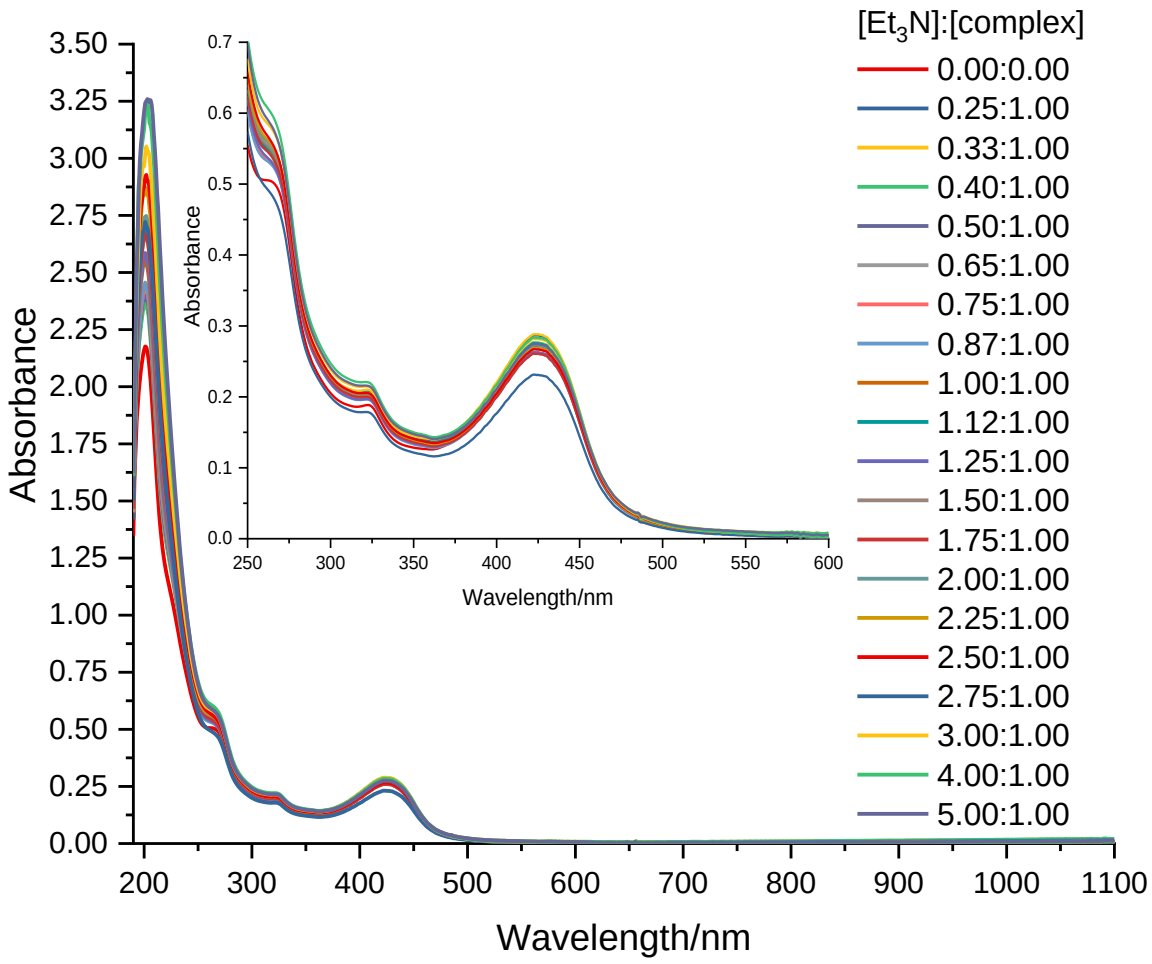

Figure 56. Spectrophotometric titration of Et_3N with $[Co(dmgBF_2)_2(OH_2)_2]$ in acetonitrile after 0 hours. $[Co(dmgBF_2)_2(OH_2)_2]$ = 0.1 mM

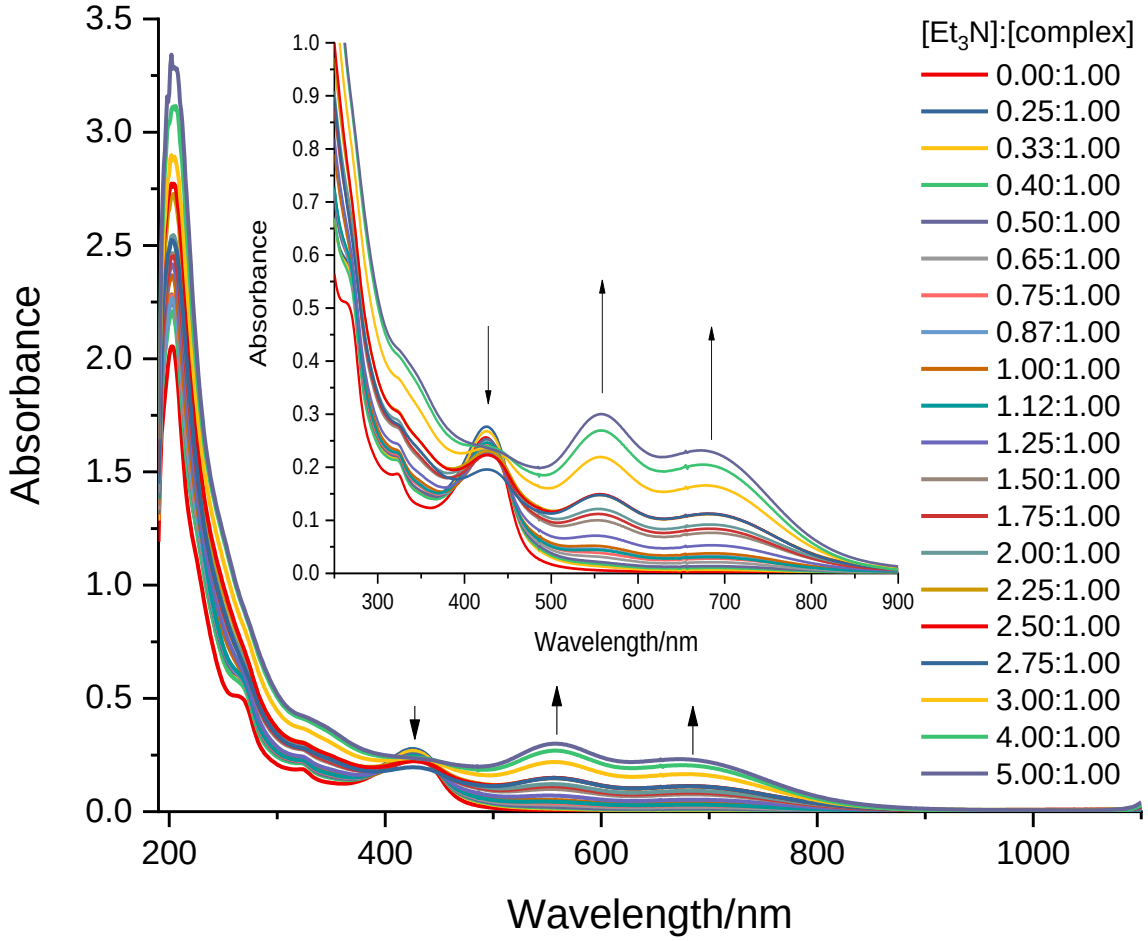

Figure 57. Spectrophotometric titration of Et_3N with $[Co(dmgBF_2)_2(OH_2)_2]$ in acetonitrile after 24 hours. $[Co(dmgBF_2)_2(OH_2)_2]$ = 0.1 mM

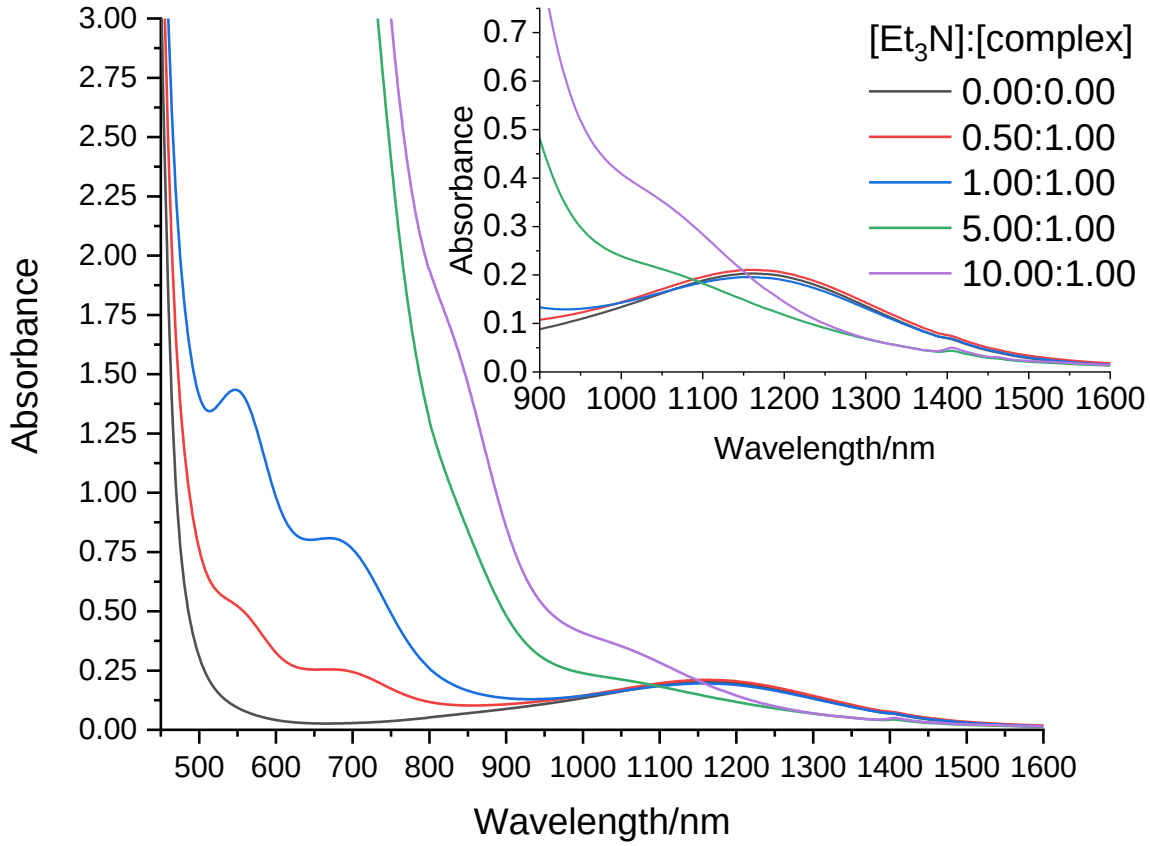

Figure 58. Spectrophotometric titration of Et_3N with $[Co(dmgBF_2)_2(OH_2)_2]$ in acetonitrile after 0 days. $[Co(dmgBF_2)_2(OH_2)_2]$ = 2.00 mM, $[Et_3N]$ = 0.00 < x < 20.0 mM.

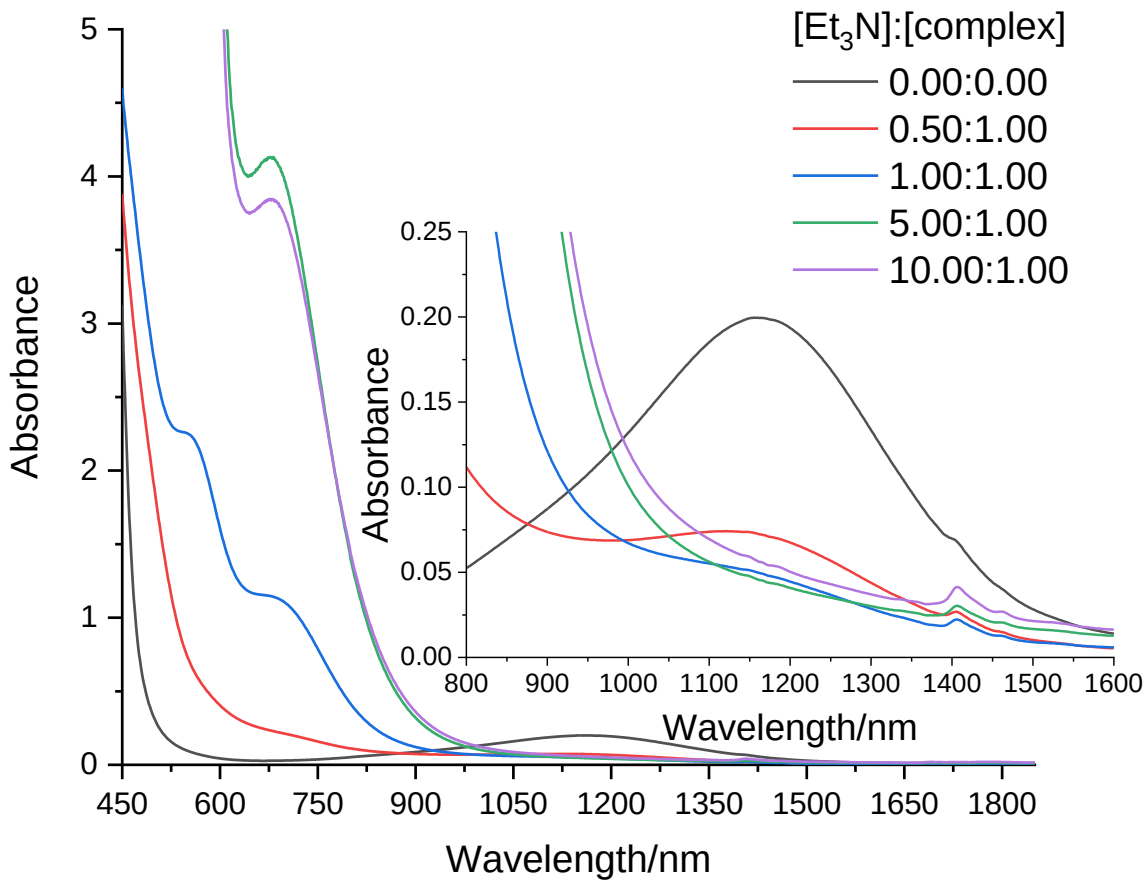

Figure 59. Spectrophotometric titration of Et_3N with $[Co(dmgBF_2)_2(OH_2)_2]$ in acetonitrile after 2 days. $[Co(dmgBF_2)_2(OH_2)_2]$ = 2.00 mM, $[Et_3N]$ = 0.00 < x < 20.0 mM.

As this interaction was very surprising, a study with another aliphatic tertiary amine was also conducted, Figure 60. After 24 hours the sample that was mixed with $(HOEt)_3N$ had minimal changes in its spectrum especially when compared to the complex alone. These minimal changes that were observed are the slight bathochromic shift circa 325 nm and hypochromic shift circa 425 nm. After allowing the solution to sit for 2 weeks, the peak that was originally observed circa 425 nm was transformed into a shoulder and had disappeared after one month. Likewise, the solution with Et_3N which had two prominent peaks between 500 to 900 nm after 24 hours slowly faded away overtime.

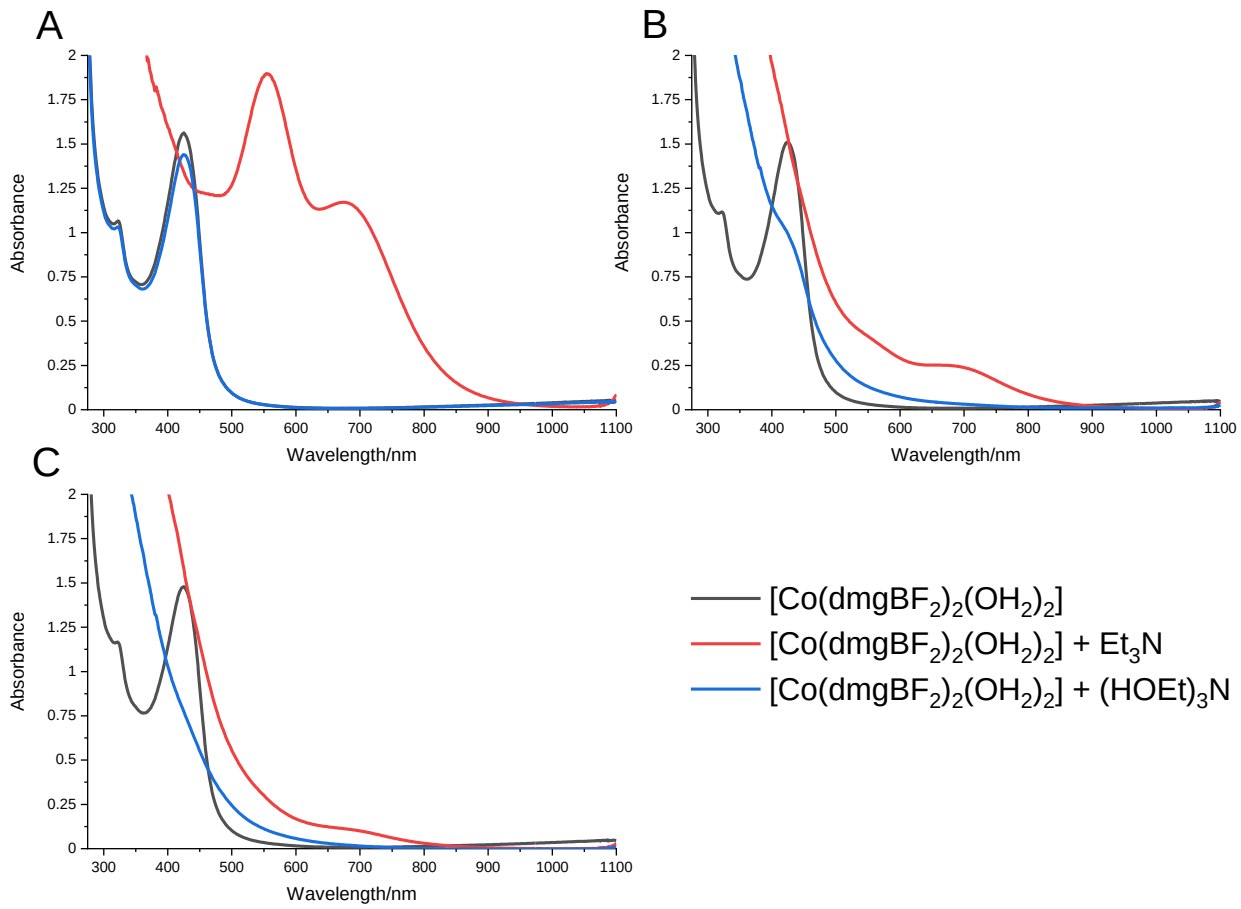

Figure 60. UV-visible spectra of $[Co(dmgBF_2)_2(OH_2)_2]$ with(out) Et_3N or $(HOEt)_3N$ in acetonitrile. [complex] = 0.5 mM, $[R_3N]$ = 5.0 mM, (A) 24 hours, (B) 2 weeks, and (C) 1 month after mixing.

Repeating the study with Et_3N, the spectral changes of the complex with Et_3N was monitored daily for 5 days before it was switched over to a weekly monitoring, Figure 61. Within the first 24 hours the absorbance at 554 and 680 nm is observed to grow from 0 to about 1.4 and 0.9, respectively. However, that absorbance growth was short lived as by the second day a decrease was observed which began to level off circa the second week. This was repeated with Et_3N•HCl, Figure 62, the growth in the absorbance between 500 to 900 nm was a lot slower which spans three to four days with a decrease in the absorbance following suit.

When Et_3N•HCl is used in place of Et_3N, Figure 62, after 24 hours the peak at 450 nm becomes a shoulder with the two peaks observed between 500 to 800 nm being slightly visible. However, as time progresses, an increase is observed within this region, leading to the probability of either the proton or chloride anion retarding the overall reaction speed, with leveling off of the absorbance being observed between 72 and 96 hours with the absorbance decreasing after 96

hours. Whereas when a mixture of $Et_3N/Et_3N•HCl$ was used, the suppression of the peak circa 700 nm is observed, and the violet color that was originally observed is replaced with an equally dark blue one. After the initial increase in absorbance within the first 24 hours, the absorbance then begins to decrease in a linear fashion which begins to slow after the first five days. Also, the suppressed peak circa 700 nm becomes more apparent as the peak circa 600 nm decreases in intensity. Interestingly enough when we compare the Et_3N at the two-week mark to the other two spectra the peak circa 600 nm has disappeared completely whereas in the presence of $Et_3N•HCl$ that peak is still present, however they are all similar with the peak circa 700 nm decaying a lot slower.

To further understand if it is indeed the chloride anion that is retarding the reaction, $[^nBu_4N]Cl$ was also used. When 5 mM $[^nBu_4N]Cl$ was used, Figure 64, the growth in absorbance lasted about 48 hours before the decay was observed.

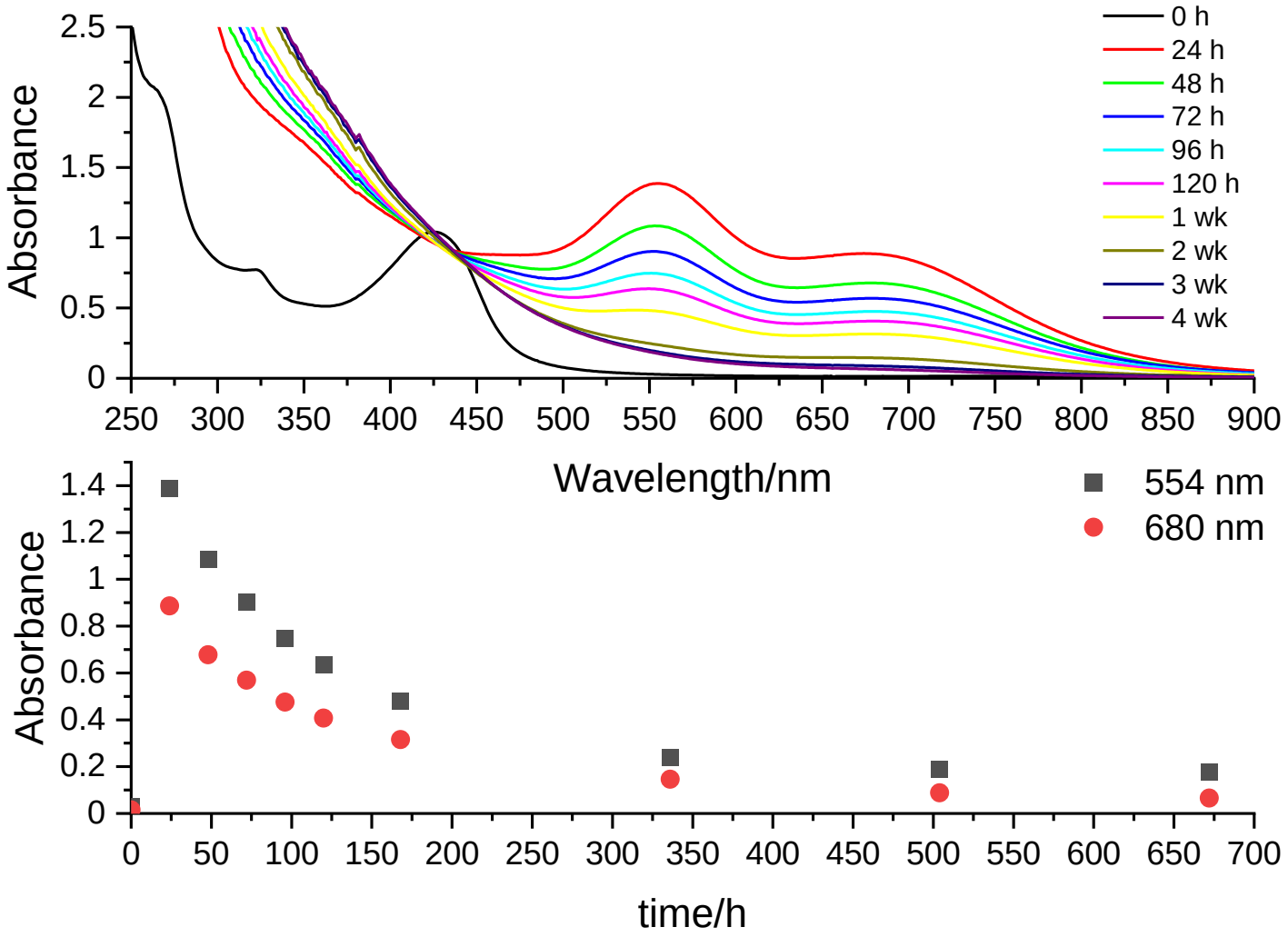

Figure 61. UV-visible spectra of $[Co(dmgBF_2)_2(OH_2)_2]$ with Et_3N in acetonitrile (**top**), and absorbance versus time (**bottom**). [complex] = 0.5 mM and $[Et_3N]$ = 5 mM.

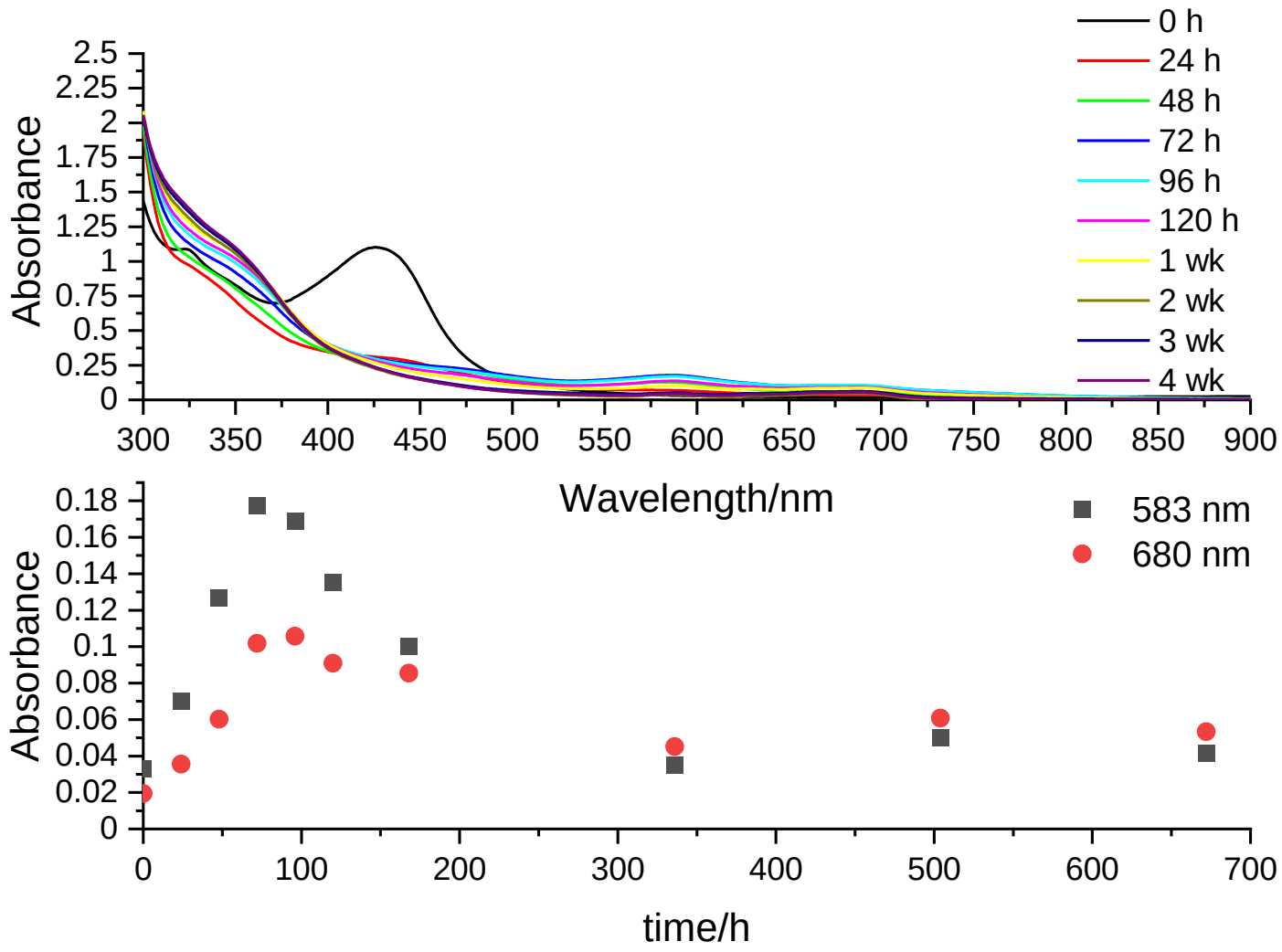

Figure 62. UV-visible spectra of $[Co(dmgBF_2)_2(OH_2)_2]$ with Et_3N•HCl in acetonitrile (**top**), and absorbance versus time (**bottom**). [complex] = 0.5 mM and $[Et_3N]$ = 5 mM.

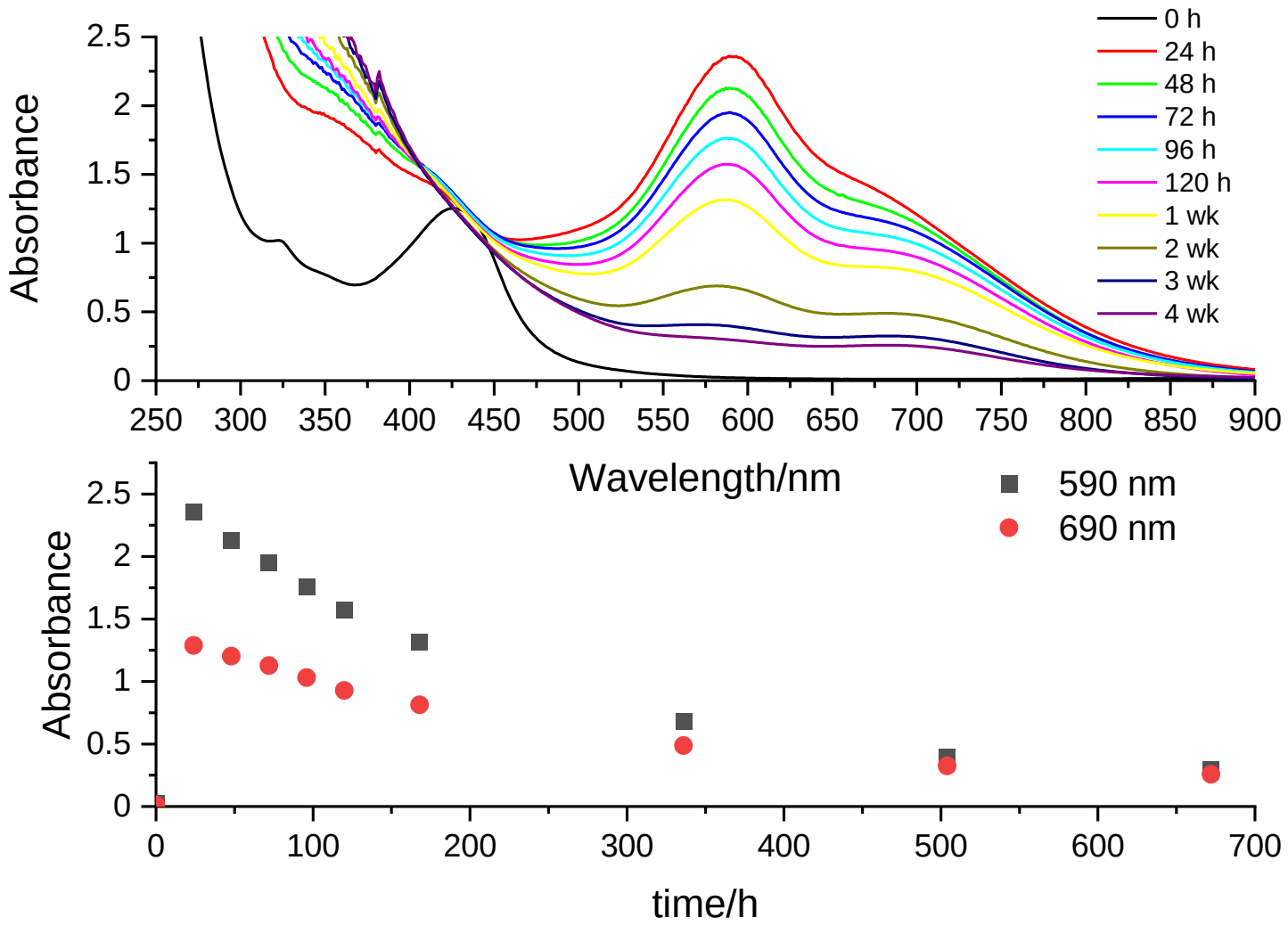

Figure 63. UV-visible spectra of $[Co(dmgBF_2)_2(OH_2)_2]$ with $Et_3N/Et_3N{\bullet}HCl$ in acetonitrile (**top**), and absorbance versus time (**bottom**). [complex] = 0.5 mM, $[Et_3N]$ = 2.86 mM, and $[Et_3N{\bullet}HCl]$ = 2.18 mM.

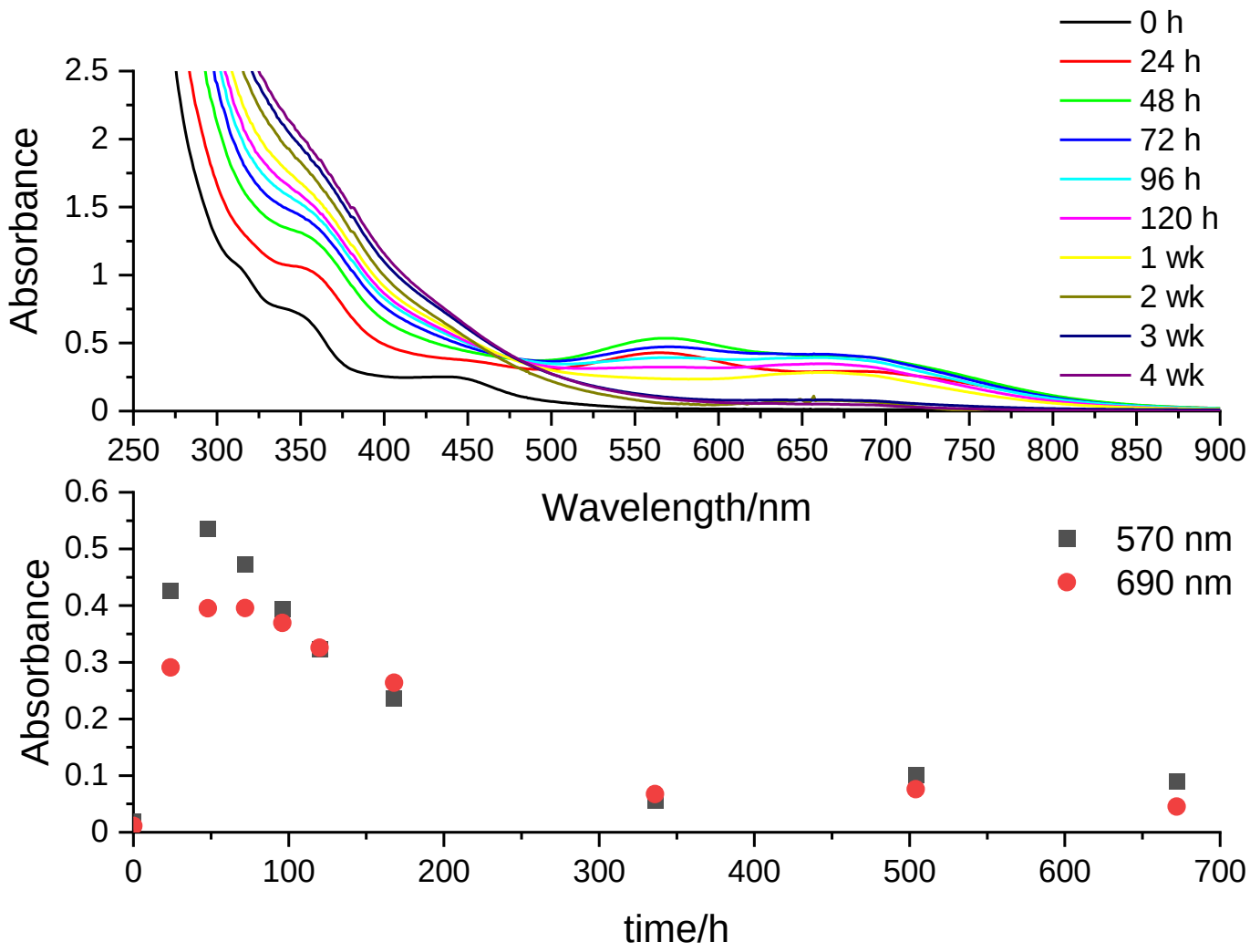

Figure 64. UV-visible spectra of $[Co(dmgBF_2)_2(OH_2)_2]$ with Et_3N and $[^nBu_4N]Cl$ in acetonitrile (**top**), and absorbance versus time (**bottom**). [complex] = 0.5 mM, $[Et_3N]$ = 5.0 mM, and $[^nBu_4N]Cl$ = 5.0 mM.

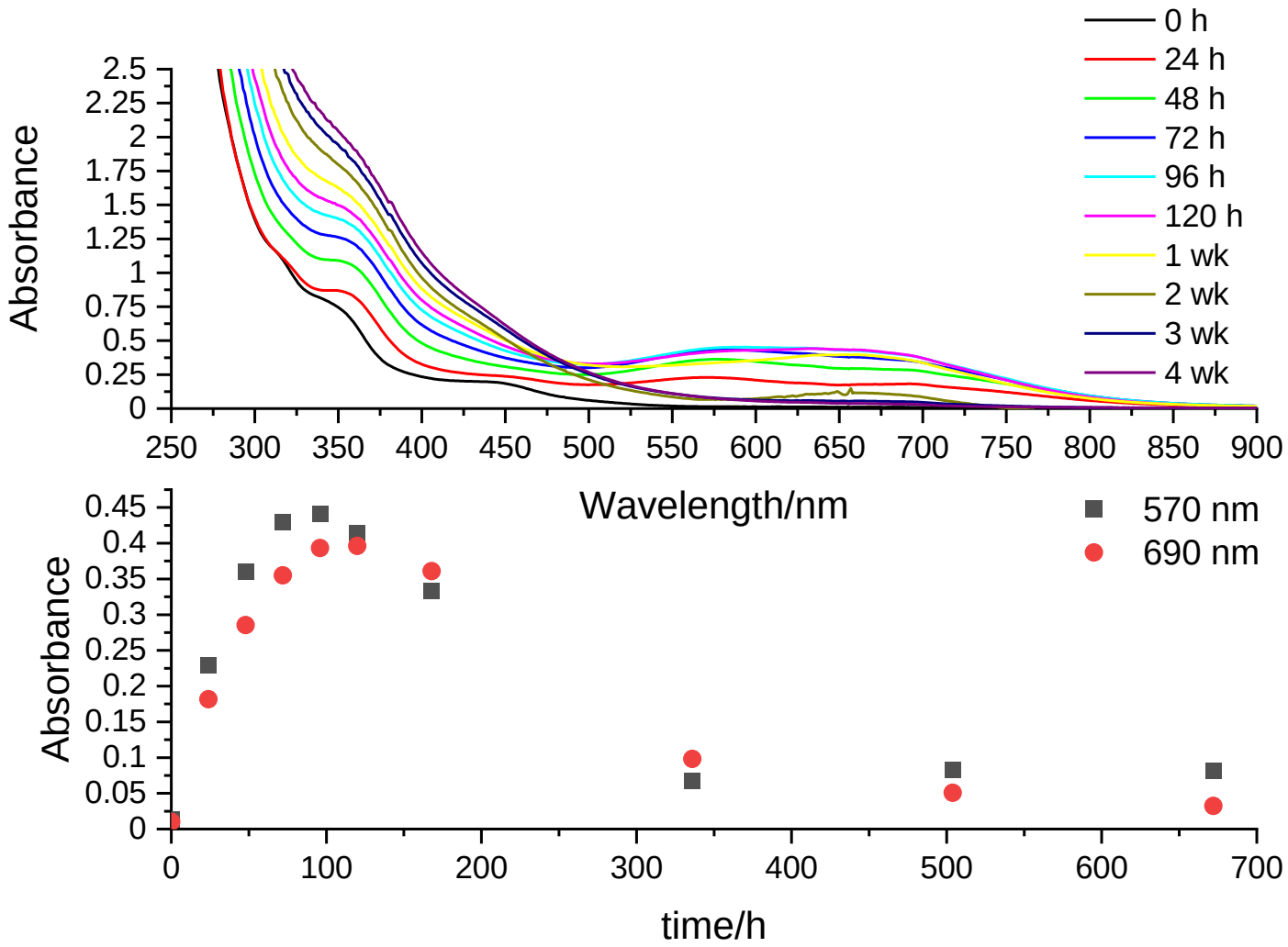

Figure 65. UV-visible spectra of $[Co(dmgBF_2)_2(OH_2)_2]$ with Et_3N and $[^nBu_4N]Cl$ in acetonitrile (**top**), and absorbance versus time (**bottom**). [complex] = 0.5 mM, $[Et_3N]$ = 5.0 mM, and $[^nBu_4N]Cl$ = 10 mM.

For the kinetic experiments, there are several factors that can influence the rate of the reaction. These include but not limited to: (i) temperature, (ii) ionic strength of the medium, (iii) concentration and (iv) solvent. It is therefore imperative to keep as many variables as possible constant in the experiments. Previously there have been observations that the complex can react with many species such as buffers and supporting electrolyte. The possibility of a reaction between the cobalt complex and the medium (i.e. solvent and supporting electrolyte) was investigated (Figure 66). From this we found that there was very small change in the absorbance of the mixture of the complex and the supporting electrolyte over five hours.

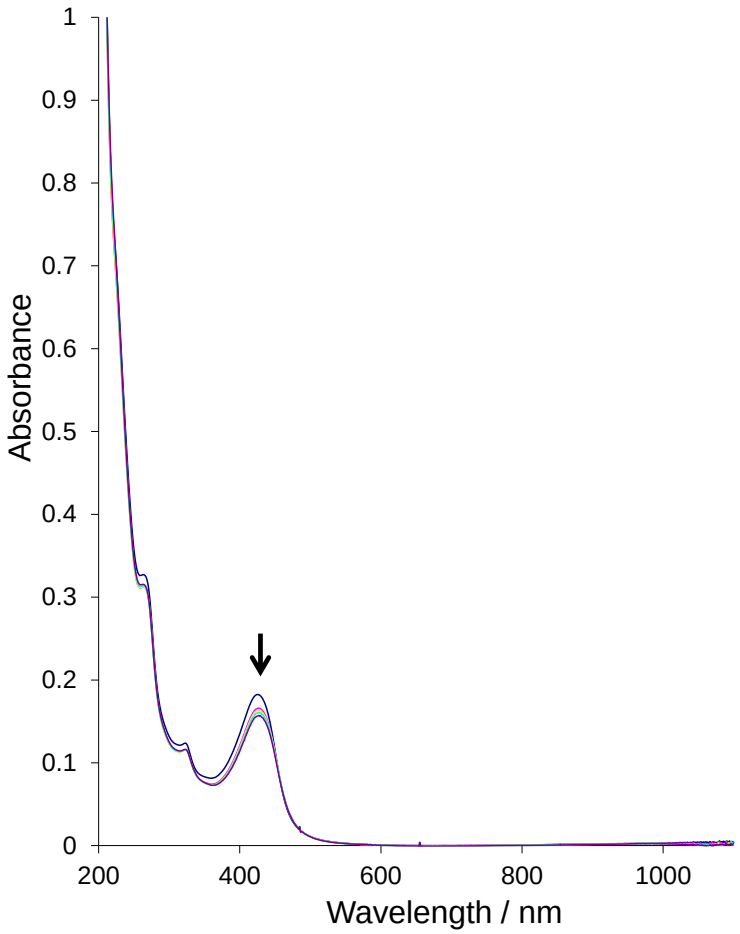

Figure 66. Repetitive scan spectra of an acetonitrile mixture of 0.5 mM ($[Co(dmgBF_2)_2(OH_2)_2]$) in 0.05 M Me_4NBF_4 at 20 °C (one hour intervals shown for five hours).

In the presence of Et_3N, two new bands in the visible region developed with time as shown in Figure 67. The reaction between the complex and Et_3N appears to be complex in nature. At lower concentrations, there is a rapid increase in the absorbance in the UV portion of the spectrum which was monitored at 326 nm and subsequently the bands with λ_{max} ~560 and 650 nm emerges and this species also contributes to the absorbance in the UV region of the spectrum (Figure 68 and Figure 69). However, at higher concentrations of the Et_3N these bands at 560 and 650 nm formed rapidly and continued to increase over several hours (Figure 70). Interestingly their absorbances appeared to level off within 2000 s (Figure 71) and then continued to increase over several hours. These absorptions bands are typically associated with Co(I) (see Figure 116). It therefore appears as if the Co(II) complex ($[Co(dmgBF_2)_2(H_2O)_2]$) is reduced by the Et_3N in acetonitrile.

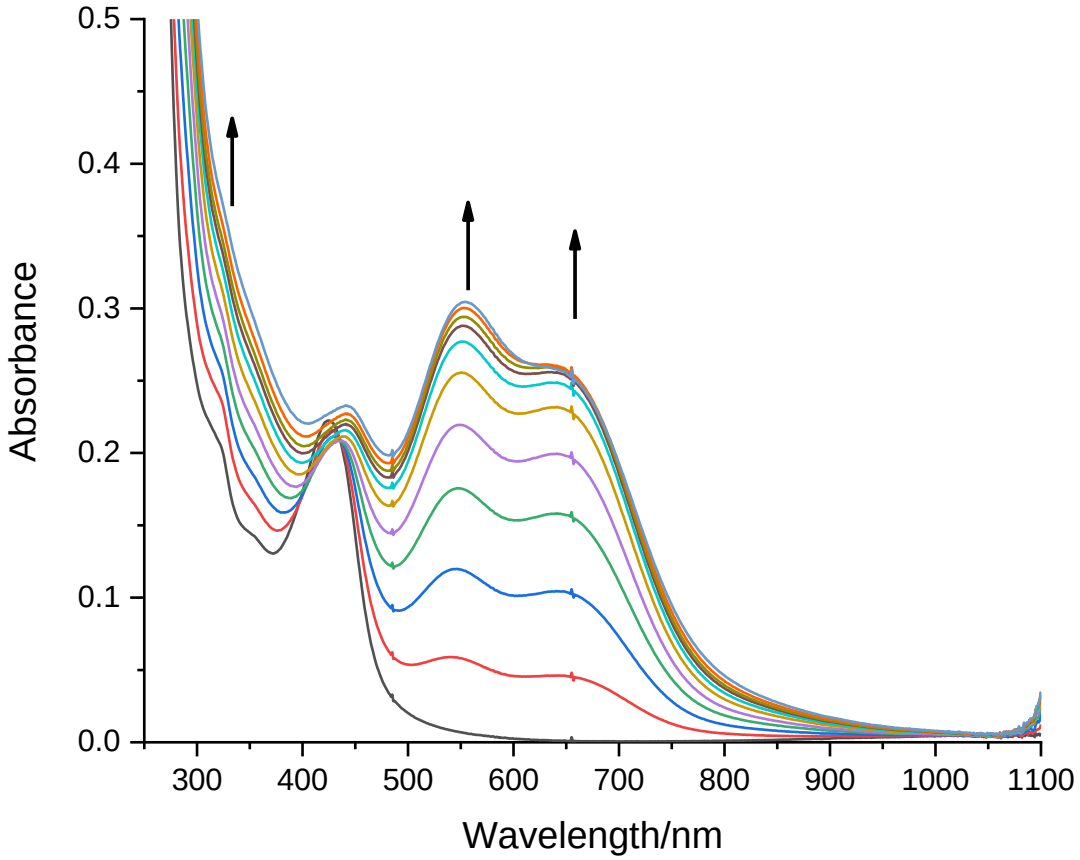

Figure 67. Repetitive scan spectra (180 s intervals shown for 1800 s) of the reaction mixture containing [Et3N] = 0.25 M and $[Co(dmgBF_2)_2(OH_2)_2]$ = 0.05 mM in CH_3CN at 20 °C, I = 0.05 M ($[Me_4N]BF_4$).

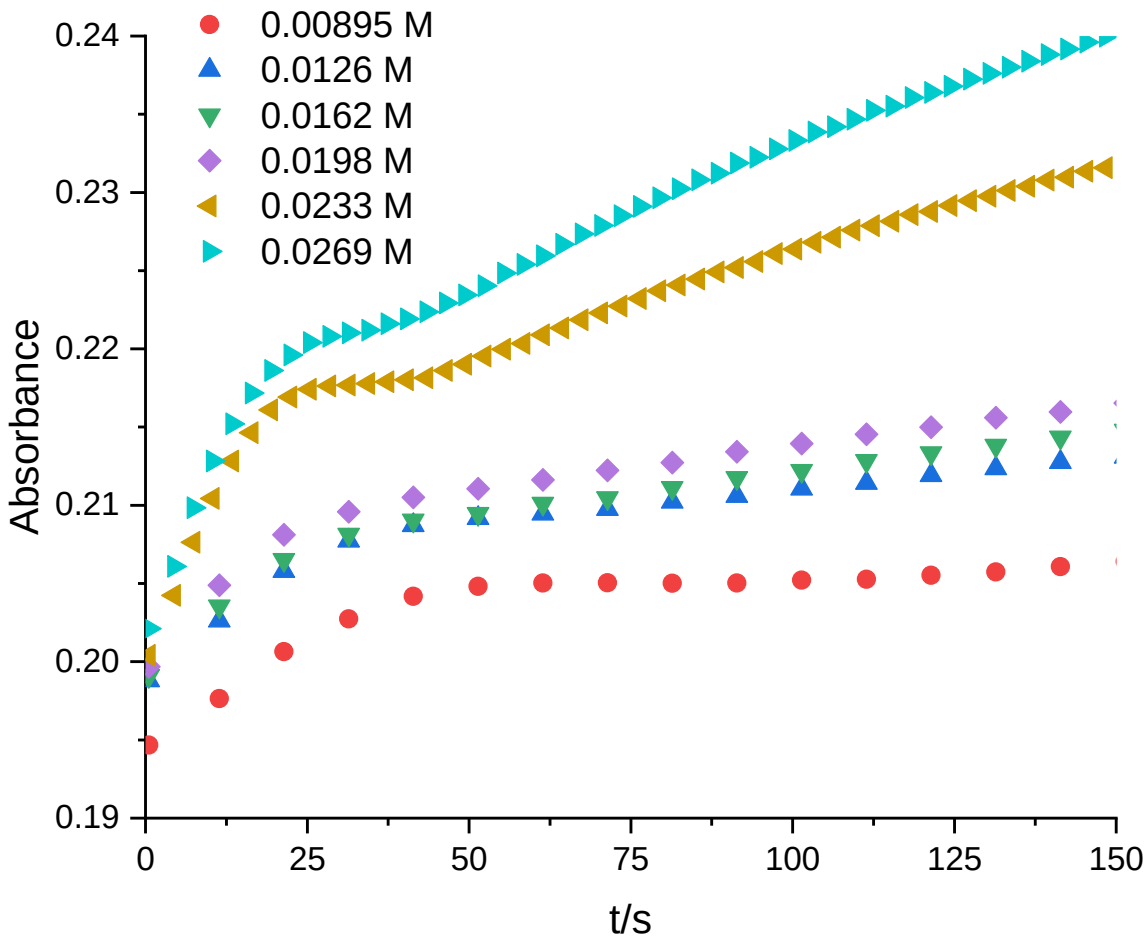

Figure 68. Absorbance time plots at 326 nm of the reaction mixtures containing $0.0054 \leq [Et_3N] \leq 0.0269$ M and $[Co(dmgBF_2)_2(OH_2)_2] = 0.05$ mM in CH_3CN at 20 °C, $I = 0.05$ M ($[Me_4N]BF_4$).

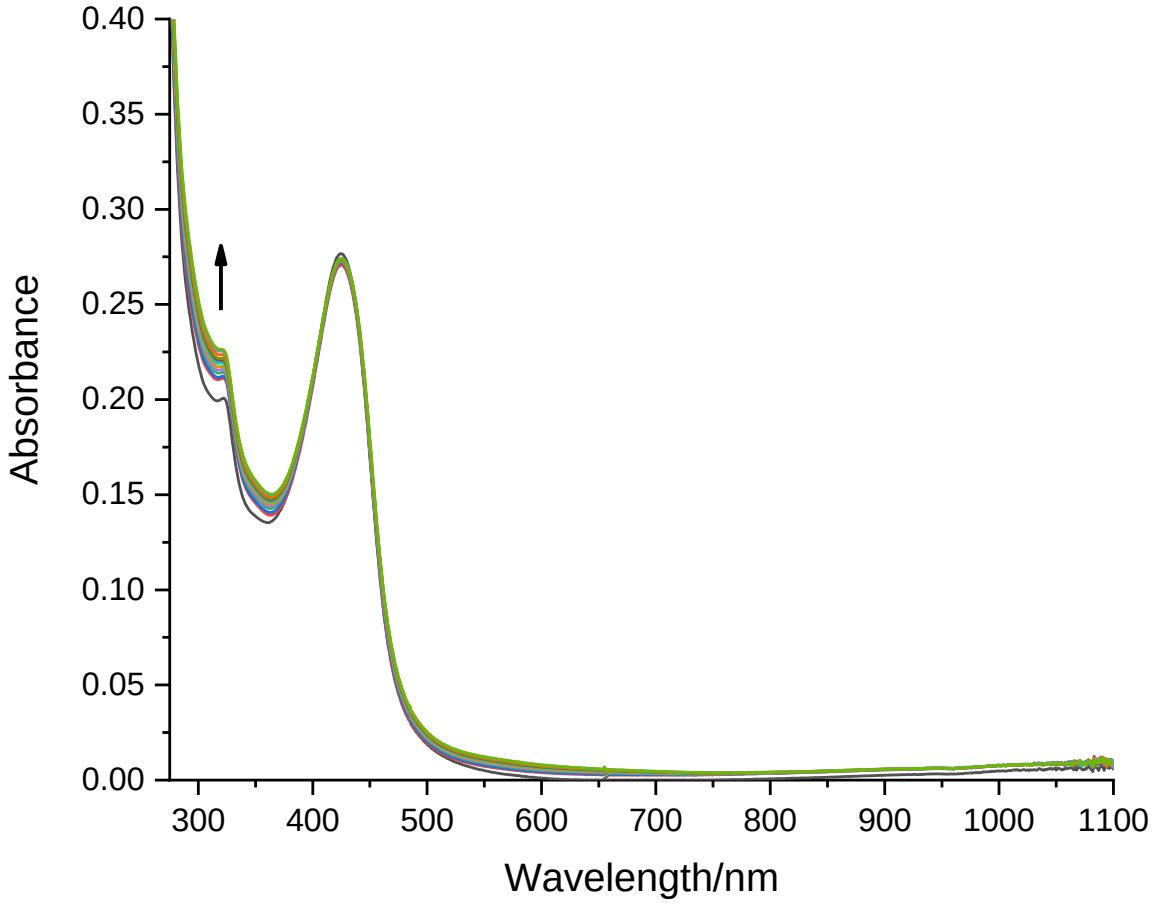

Figure 69. Repetitive scan spectra (50 s intervals shown for 550 s) of the reaction mixture containing [Et_3N] = 8.95 mM and [$Co(dmgBF_2)_2(OH_2)_2$] = 0.05 mM in CH_3CN at 20 °C, I = 0.05 M ([Me_4N]BF_4).

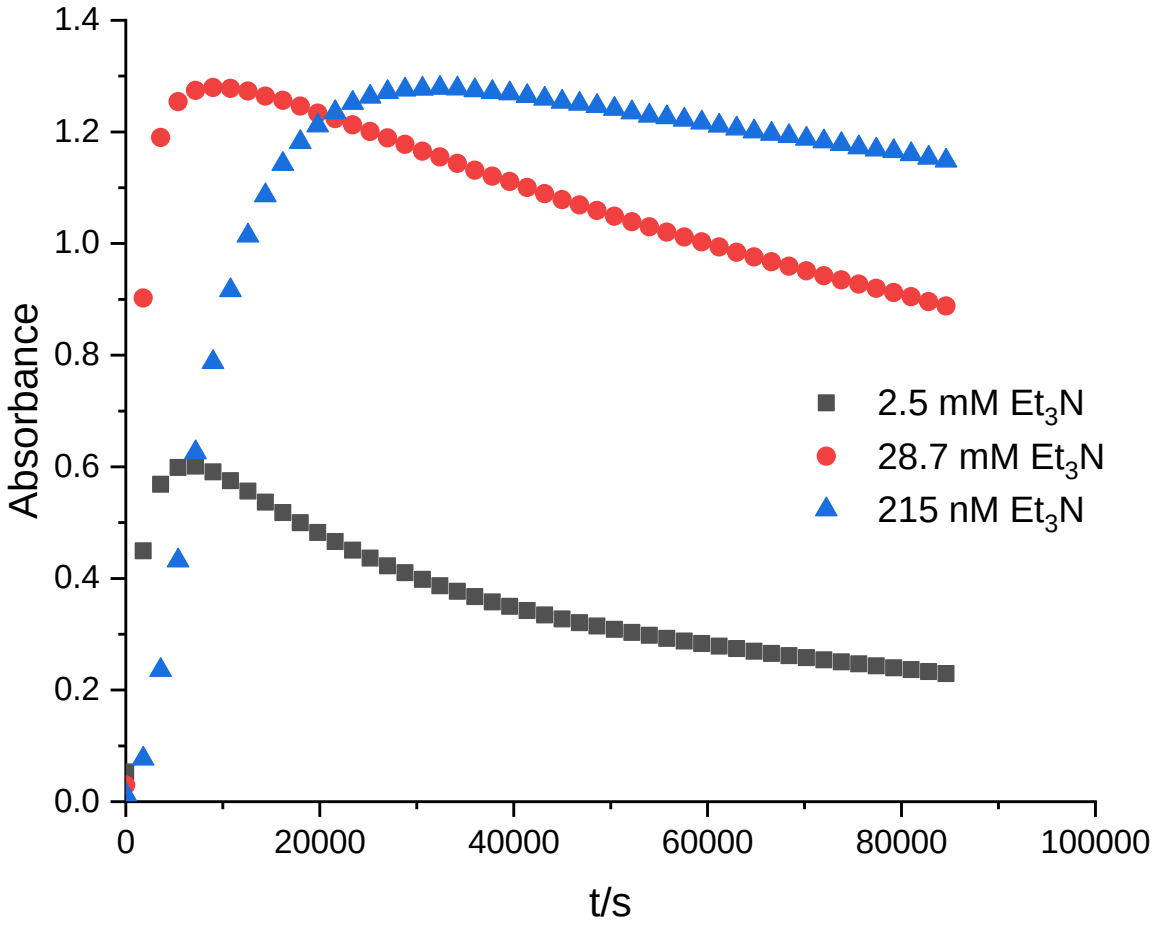

Figure 70. Absorbance-time plots at 560 nm of some reaction mixtures containing 0.25 mM $[Co(dmgBF_2)_2(OH_2)_2]$ and Et_3N over a 24 hour period.

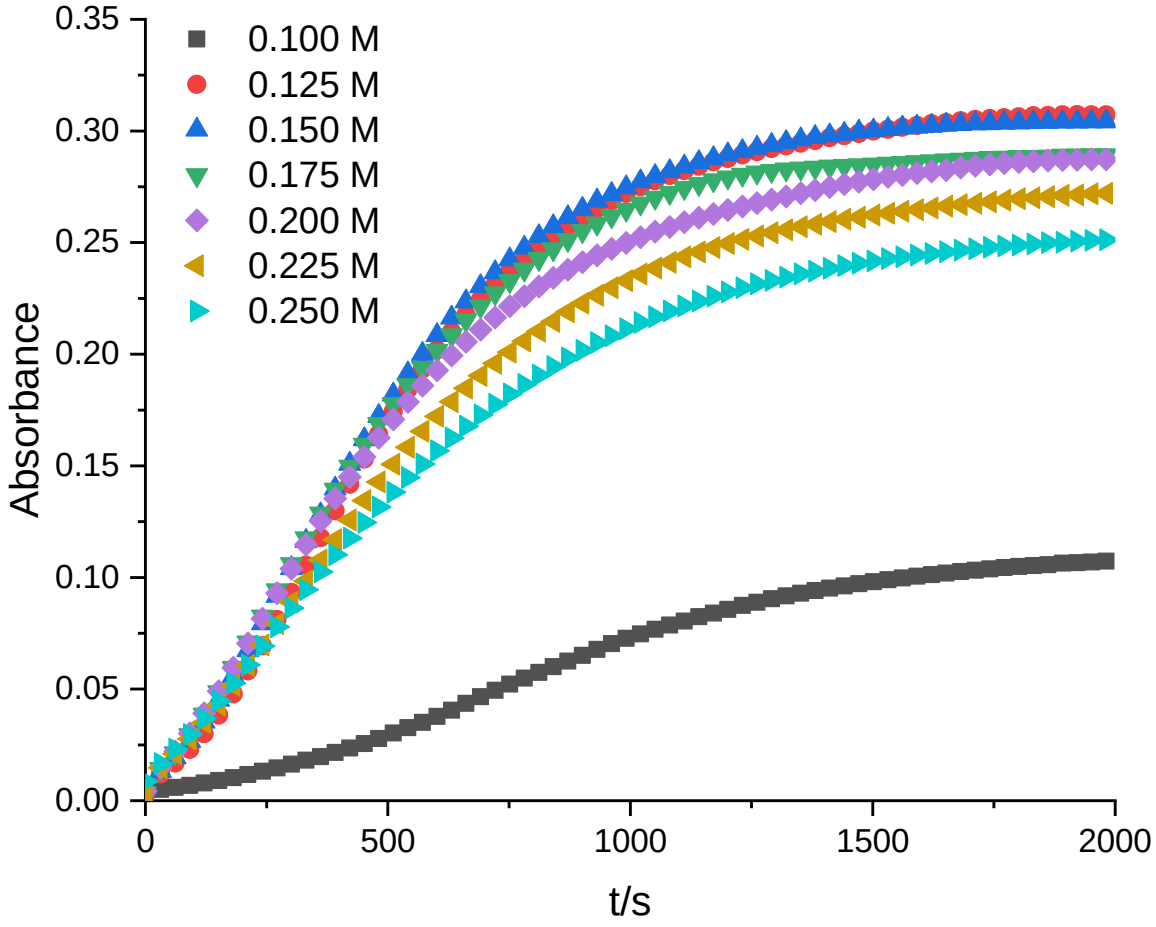

Figure 71. Absorbance-time plots at 560 nm of the reaction mixtures containing $0.10 \leq [Et_3N] \leq 0.25$ M and $[Co(dmgBF_2)_2(OH_2)_2] = 0.05$ mM in CH_3CN at 20 °C, $I = 0.05$ M ($[Me_4N]BF_4$).

The overall reaction can be represented as:

$$\text{rate} = k[Co(dmgBF_2)_2(OH_2)_2]^a[Et_3N]^b \qquad (2)$$

where a and b are the orders of the reaction with respect to each reactant.

We attempted to investigate the reaction under pseudo-first-order conditions of $[Et_3N]$. Under these conditions, the rate law can be written as:

$$\text{rate} = k'[Co(dmgBF_2)_2(OH_2)_2]$$

where k' is the pseudo-first-order rate constant = $k[Et_3N]$

At the lower $[Et_3N]$ at 326 nm. The pseudo-first order rate constants (rate/$[Co(dmgBF_2)_2(H_2O)_2]$) are given in Table 17. A plot of the observed rate constants vs $[Et_3N]$

over this concentration range gave a linear plot with positive slope and intercept (Figure 72). Such a plot can be interpreted to have two plausible meanings. The first is that the slope gives the second order rate constant k and the intercept would be related to a reaction that is independent of the [Et_3N] for example a solvent pathway. The second interpretation could be that this represents and equilibrium in which the slope gives the forward rate constant k_f and the intercept gives the reverse rate constant k_r and the ratio of which is the equilibrium constant K.

Table 17. A table of pseudo-first order rate constants for the variation in Et_3N concentration for its interaction with [$Co(dmgBF_2)_2(OH_2)_2$]. [$Co(dmgBF_2)_2(OH_2)_2$] = 0.05 mM in CH_3CN at 20 °C, I = 0.05 M ([Me_4N]BF_4).

[Et_3N]/mM	**10^2 k_{obs}/s^{-1}**
5.38	2.06
8.95	2.95
12.6	3.74
16.2	4.48
19.8	5.12
23.3	5.94
26.9	6.52

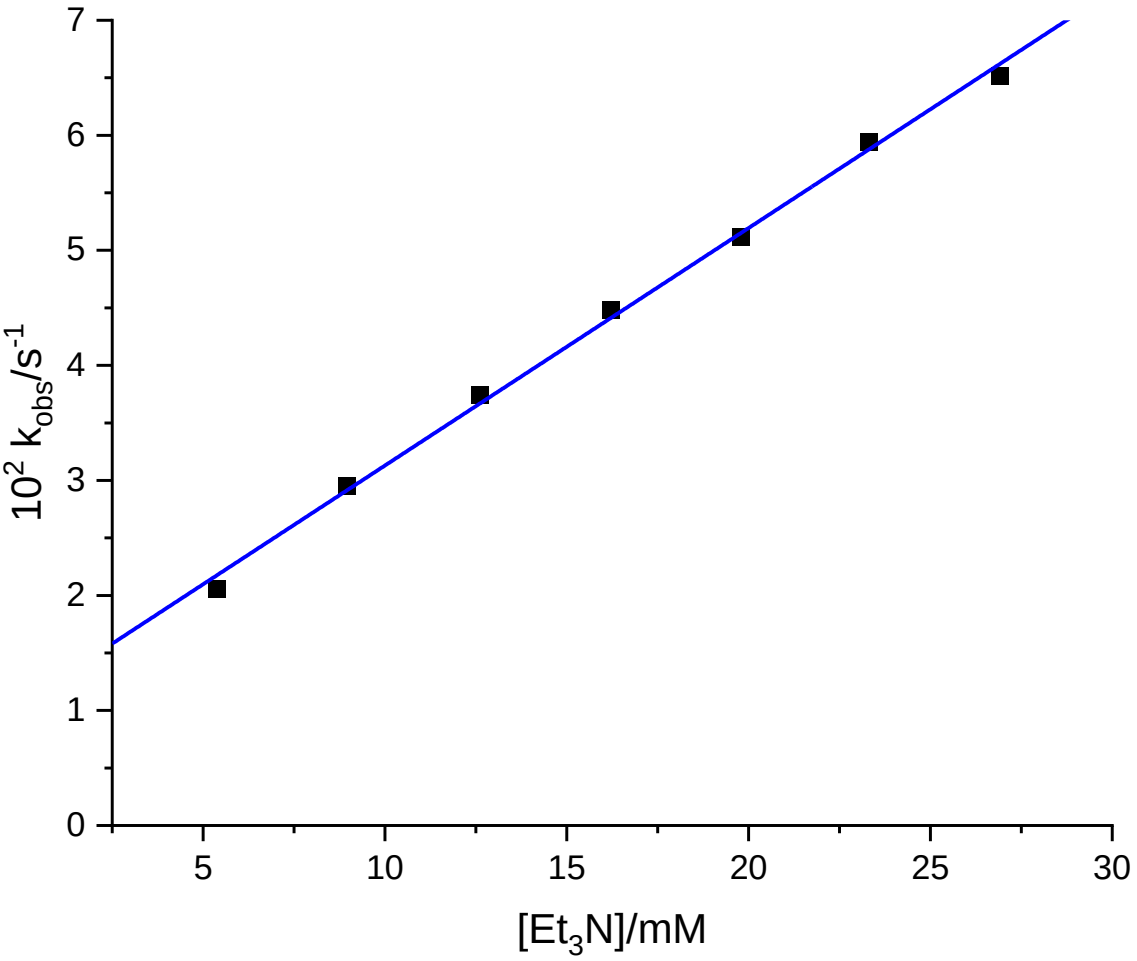

Figure 72. A plot of $k_{obs,\,1}$ vs [Et_3N], [$Co(dmgBF_2)_2(OH_2)_2$] = 0.05 mM in CH_3CN at 20 °C, I = 0.05 M ([Me_4N]BF_4).

3.2.8 Electrochemical studies

In cyclic voltammogram of the complex, see Figure 73, the redox couples for the cobalt(II/I) redox couple ($E_{½}$ = -0.481 V) and the cobalt(I/0) redox couple ($E_{½}$ = -1.58 V) are very visible. After Et_3N was added to the mixture a cyclic voltammogram was taken every 10 minutes. Within the new voltammograms that were acquired, a decrease in the current associated with the cobalt(II/I) redox couple is observed, and new current is observed anodic to the reduction peak at -0.418 V. With the peak at -0.418 V, no return wave was observed

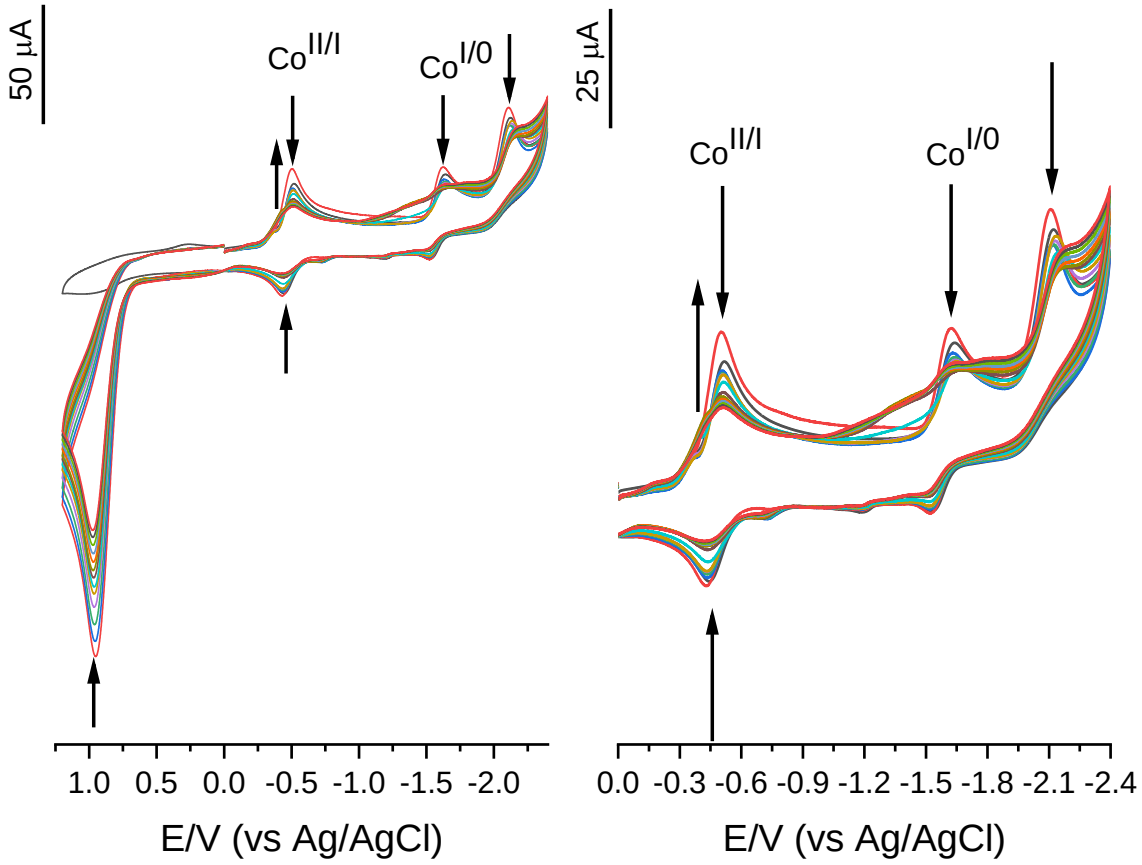

Figure 73. Time resolved cyclic voltammograms of $[Co(dmgBF_2)_2(OH_2)_2]$ in the presence of Et_3N in acetonitrile. Run time = 2 hours, cycle time = 10 minutes, $[Co(dmgBF_2)_2(OH_2)_2]_i$ = 1.0 mM, $[Et_3N]_i$ = 5 mM, and I = 0.1 M ($[^nBu_4N]ClO_4$)

Based on the spectroscopic results and known reactions of Et_3N, the following mechanism was proposed, Figure 74. Upon dissolving the complex in MeCN, the aquo ligands were displaced by the solvent. At one point as observed within the mass spectra, Et_3N displaces one of the solvent molecules. Just like with Tollin, Weiss, and Yoke's works[97-98] with their copper salts, the Et_3N transfers and electron to the metal center and the resulting radical cation reacts with the solution and other Et_3N molecules in solution to initially produce diethylvinylamine, Figure 75. As the cobalt(I) species is very reactive, it would be oxidized by the oxygen is the system reforming the cobalt(II) species. The process is then repeated with diethylvinylamine, and subsequent ethyldivinylamine resulting in the formation of trivinylamine.

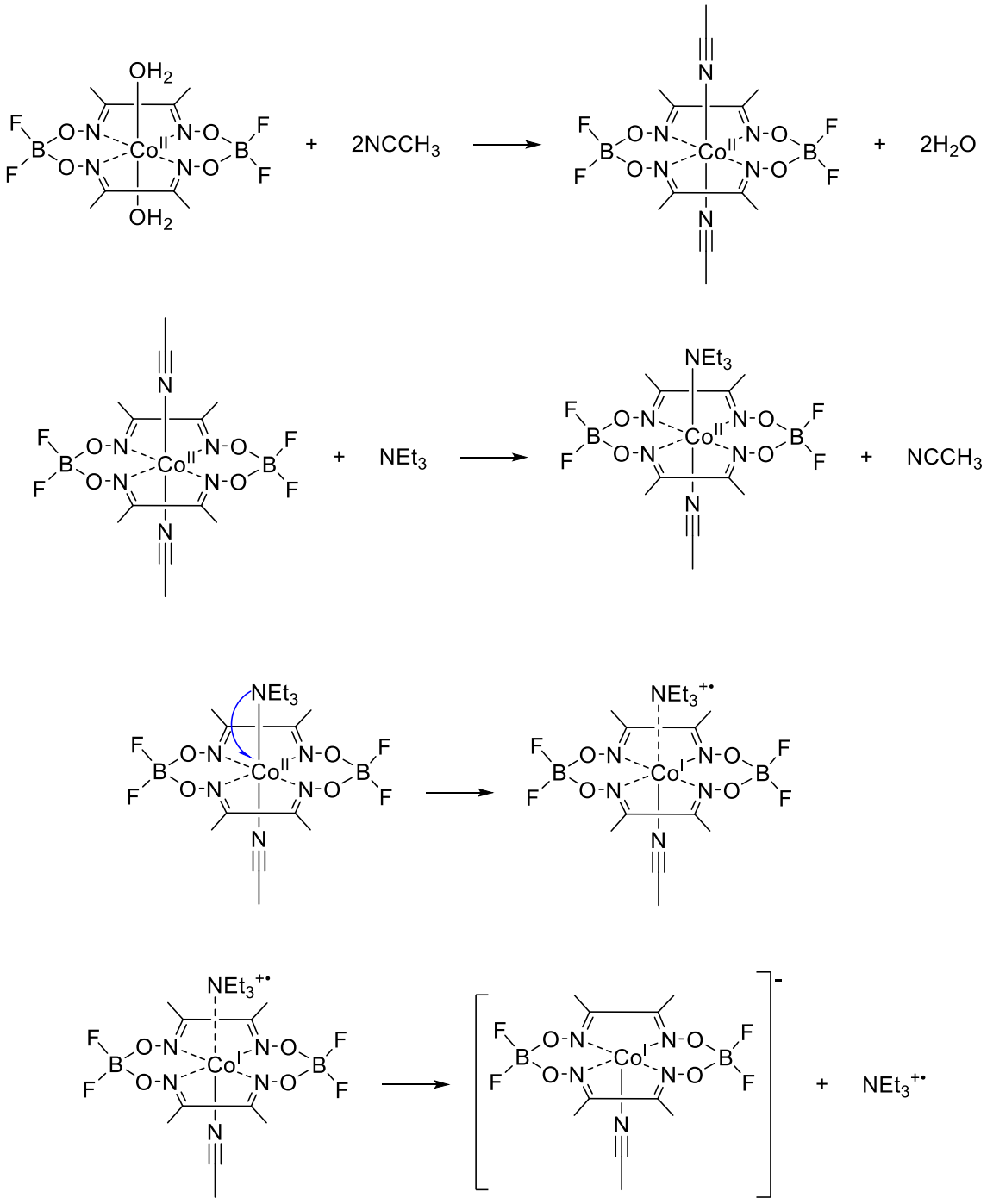

Figure 74. Proposed mechanism for the interaction of $[Co(dmgBF_2)_2(OH_2)_2]$ with Et_3N in acetonitrile.

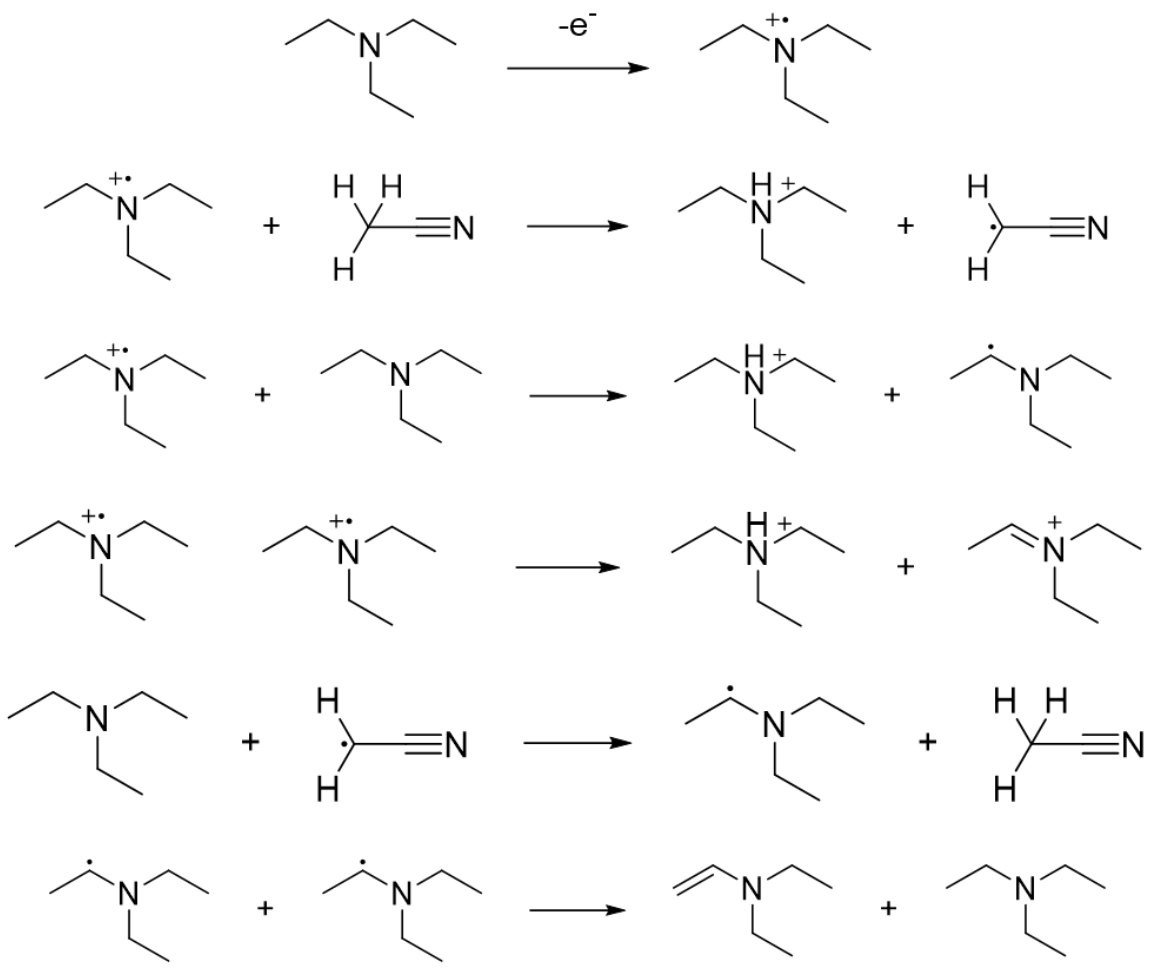

Figure 75. Radical mechanism for Et_3N.[95, 163].

3.2.9 High Field EPR studies

Thus if we take into the account the two studies above, then if the product produced is a cobalt(II) complex, then it should still be EMR (electron magnetic resonance) active, whereas if it is a low-spin cobalt(III) complex then it should be EMR silent. When the X-band study was conducted on $[Co(dmgBF_2)_2(OH_2)_2]$ by Cropek *et al*.[73] their spectra had large g tensor anisotropy with three g features that were observed. They also observed hyperfine interactions caused by the cobalt-59 metal center and the nitriogen-14 center. With High Field EMR measurements hyperfine interactions are lost,[164] but the g value features were a lot more define than when you compare it to the Cropek *et al*. study mentioned above. In Figure 76, the first thing that is observable is that

at the EPR (electron paramagnetic resonance) spectra is dependent on the frequency used. As the increases, so does where the spectra will appear versus the magnetic field. However, the magnetic field values can be converted to g-values which would allow the data to be comparable no matter what frequency is used. Thus, Figure 77 reveals that at the three frequencies used and no matter how different they looked in Figure 76 are exactly the same.

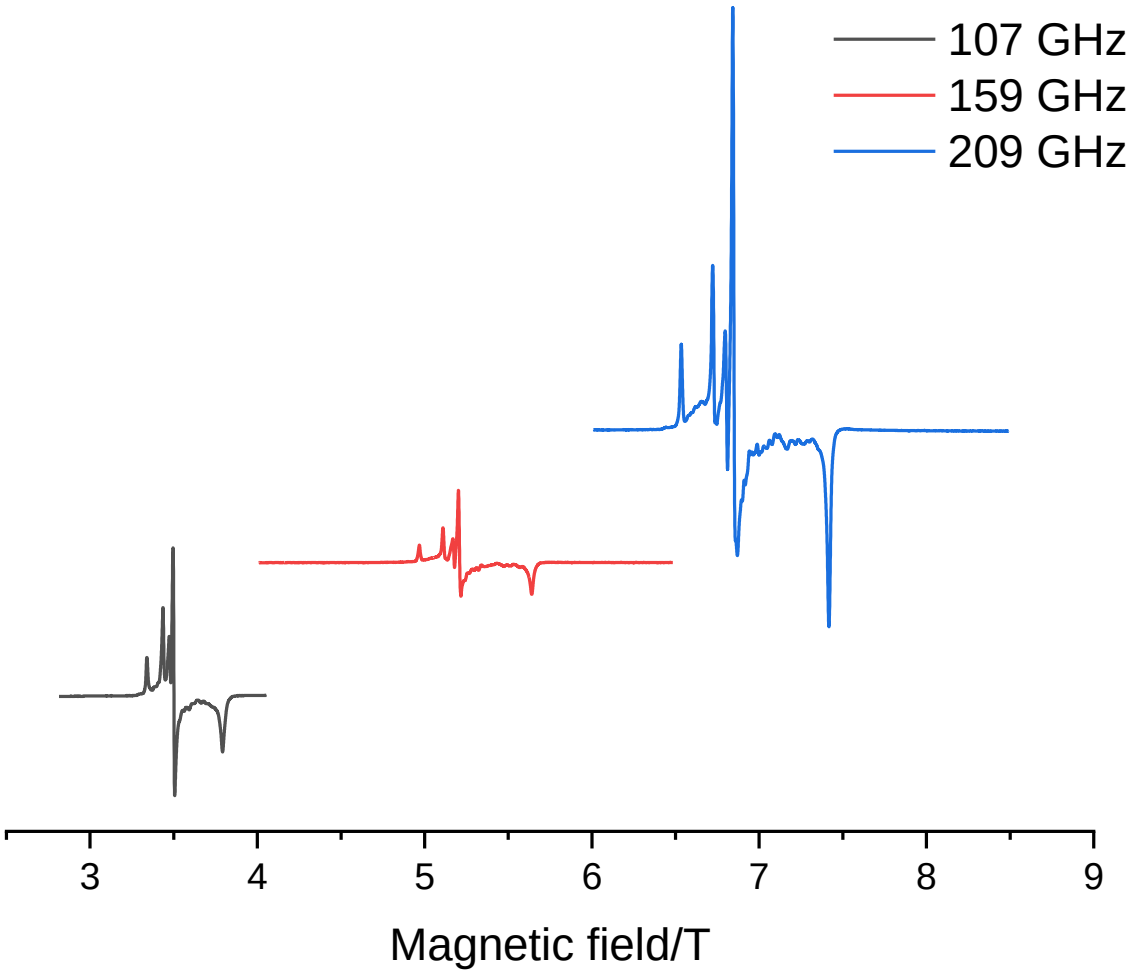

Figure 76. High field EPR spectra of $[Co(dmgBF_2)_2(OH_2)_2]$ as a pellet. 16 mg of complex + 79 mg n-eicosane, θ = 10 K

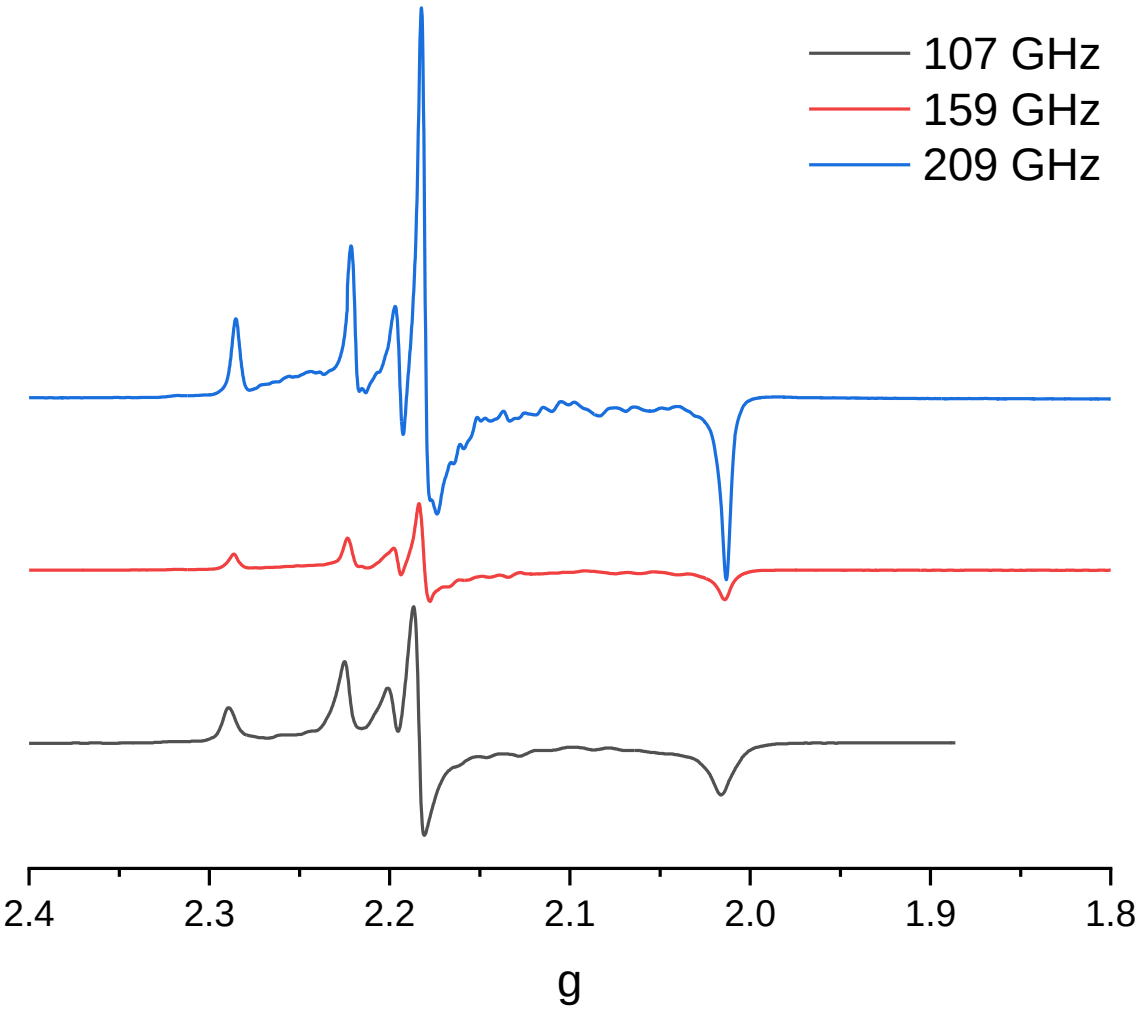

Figure 77. High field EPR spectra of $[Co(dmgBF_2)_2(OH_2)_2]$ as a pellet. 16 mg of complex + 79 mg n-eicosane, θ = 10 K

When the EPR spectra were acquired for $[Co(dmgBF_2)_2(OH_2)(N(C_2H_3)_3)]$, Figure 78, it was observed to have similar g-values to that of the parent complex, Figure 77. From this we know that the anisotropic characteristics of the complexes is rhombic in nature. The observed g-values for the g_x, g_y, and g_z were 2.25, 2.15, and 2.01, respectively. The values have been summarized in the table below, Table 18. When $[Co(dmgBF_2)_2(OH_2)_2]$ was reacted with Et_3N, Figure 80, the spectrum no longer resembled that of the starting complex (solid: Figure 77 and when frozen in MeCN: Figure 79) or of the isolated product. At a radiating frequency of 106 GHz the once rhombic nature is now shifted to an axial ($g_x = g_y < g_z$) or isotropic nature ($g_x = g_y = g_z$) with it favoring the axial nature.

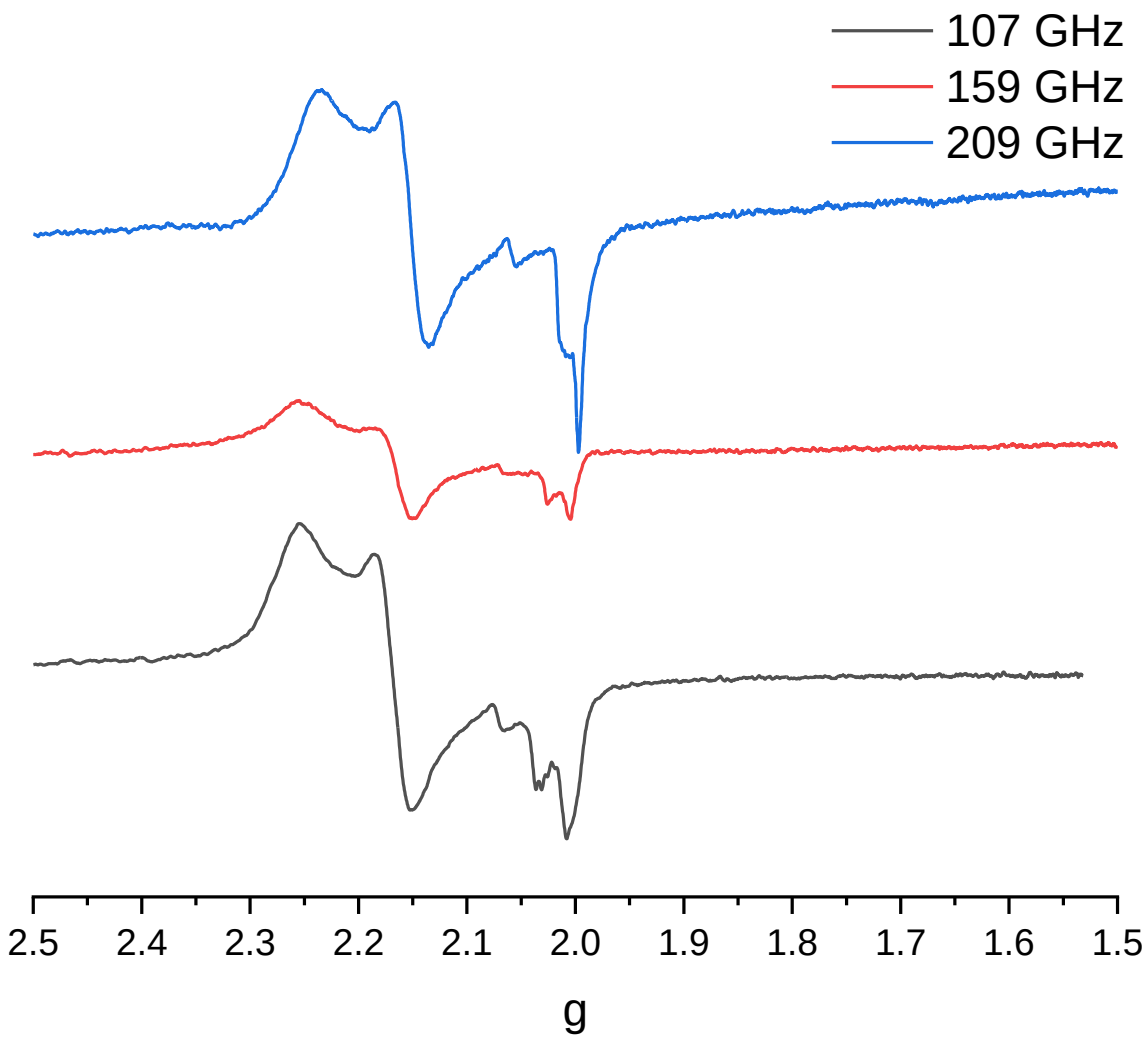

Figure 78. High field EPR spectra of $[Co(dmgBF_2)_2(OH_2)(N(C_2H_3)_3)]$ as a pellet. 83 mg of complex + 120 mg n-eicosane, θ = 10 K

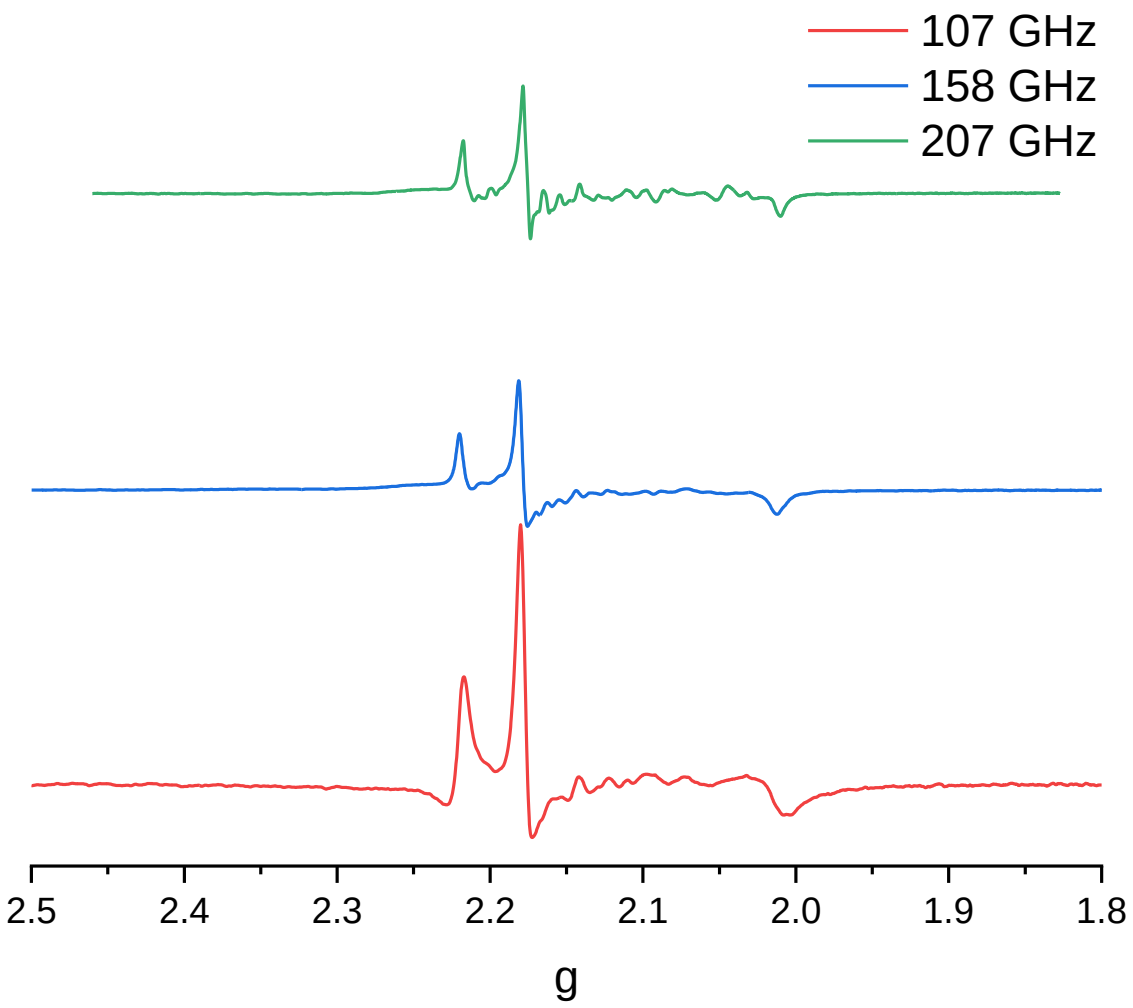

Figure 79. High field EPR spectra of $[Co^{II}(dmgBF_2)_2(OH_2)_2]$. 21 mg of complex in 1 ml of CH_3CN (sat.), θ = 10 K

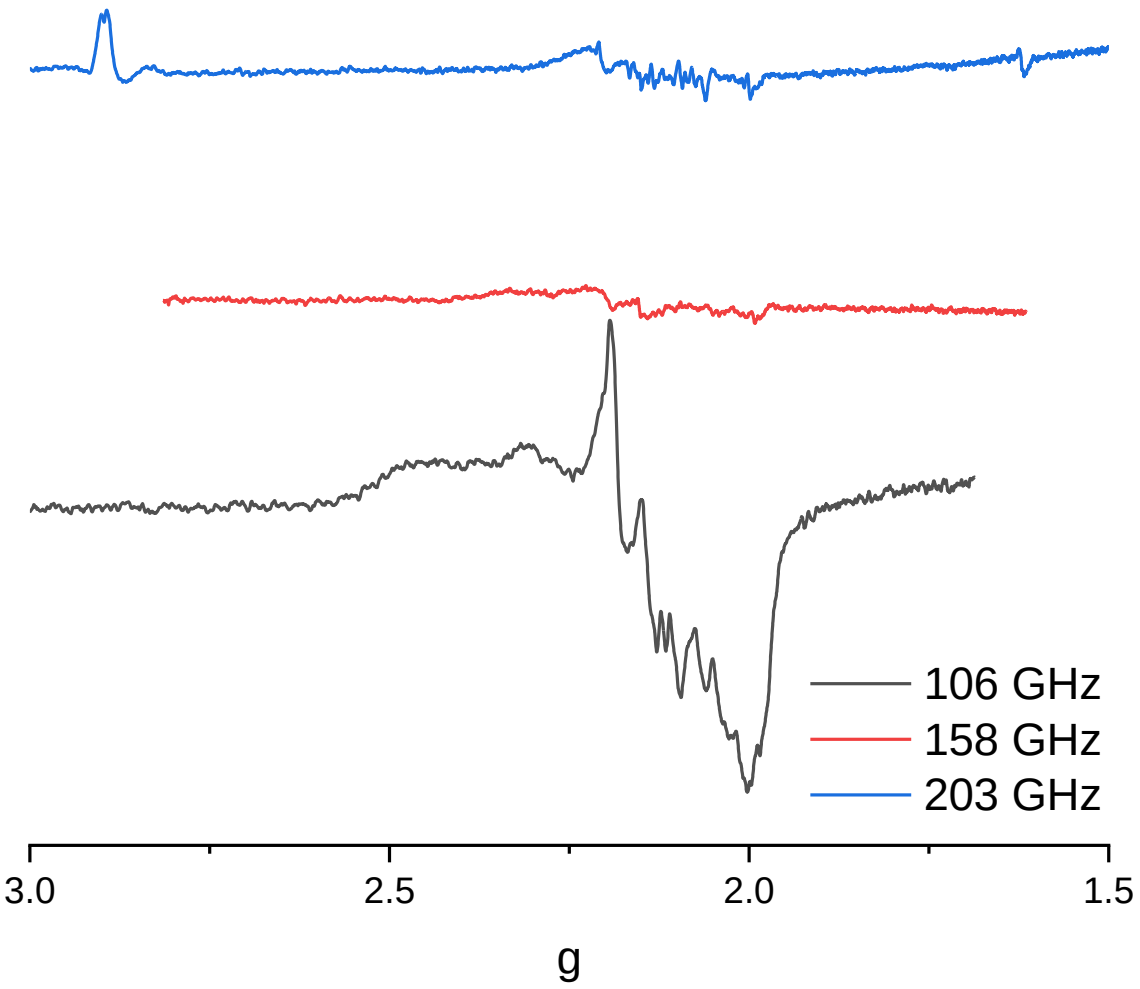

Figure 80. High field EPR spectra of $[Co^{II}(dmgBF_2)_2(OH_2)_2]$ + Et_3N. 50 mM complex in CH_3CN with 500 mM $[^nBu_4N]BH_4$ and 700 mM NEt_3, θ = 10 K

The data of the complex acquired at 209 GHz was used to produce a simulated spectrum utilizing the observed g-values, Figure 81. The A-strain was calculated as 20, 20, and 200 cm^{-1} for A_1, A_2, and A_3, respectively, with linewidths of 900, 400, 300 for linewidth x, linewidth y, and linewidth z from the simulation that fit the data the best.

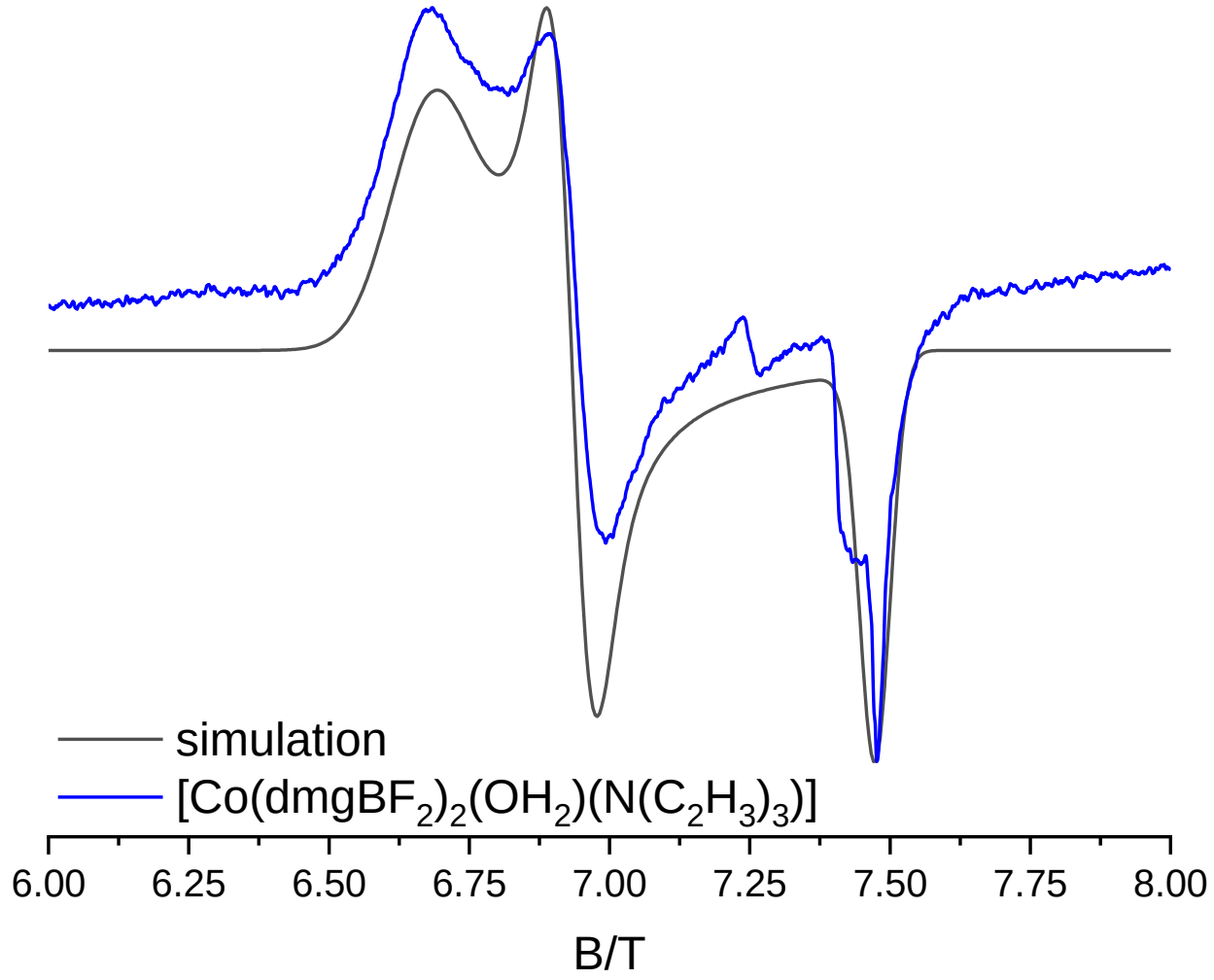

Figure 81. High field EPR spectrum at 209 GHz and simulated spectrum of $[Co(dmgBF_2)_2(OH_2)(N(C_2H_3)_3)]$ as a pellet. 83 mg of complex + 120 mg n-eicosane, θ = 10 K.

This was different for the cobalt(I) samples, which were EPR silent, Figure 82 and Figure 83. The only signals that were observed were from oxygen or from the sample's surface that was oxidized back to the cobalt(II) complex. To understand what is happening we first must understand the effects that the geometry would have on the EPR spectrum. The cobalt(II) complex starts begins as an octahedral complex, but upon reduction there is a geometry change to that of square planar. The next step is identifying where the added electron goes, this is illustrated in Figure 84. As we know cobalt normally holds seven electrons in its d-orbital, and with the cobalt(I) metal center when the electron is added to the d-orbital, there are two possible states where the first one has no unpaired electrons and the second having two with spins of 0 and 1, respectively. The EPR

silence that was observed from the studies where the cobalt(I) species was formed hints to the electron being added to the d-orbital with the complex remaining in the low-spin configuration. The other explanation would be that the Zeeman Field Splitting (ZFS) energy for the two high-spin configurations are large enough that range of the magnetic field used was too narrow to view. From literature it is known that when the cobalt metal center of the cobaloxime complex is in the +1 state that it has the square pyramidal geometry which is tends to be diamagnetic and thus EPR silent.[111, 165-167]

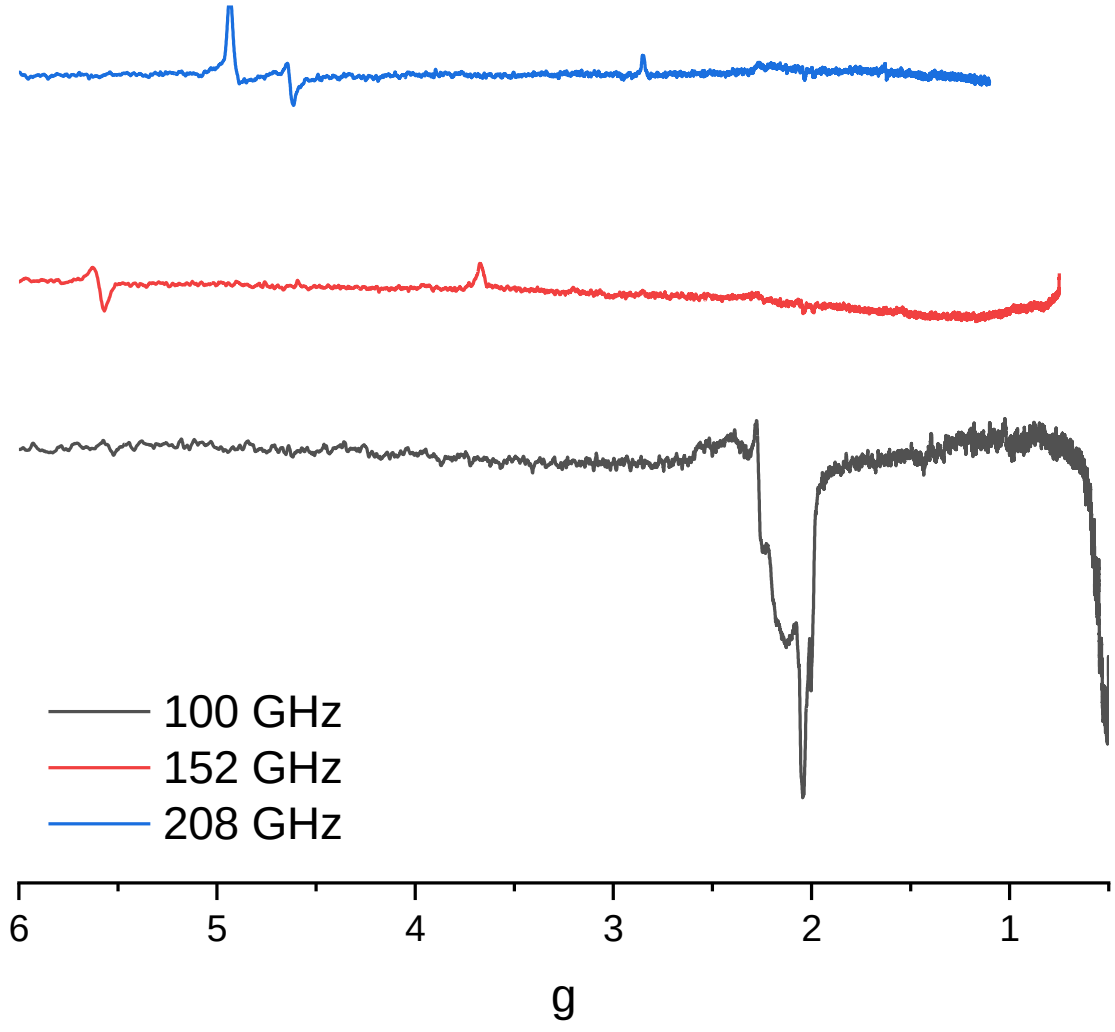

Figure 82. High field EPR spectra of $[Co^{I}(dmgBF_2)_2(OH_2)_2]$. 50 mM complex in CH_3CN with 500 mM $[^{n}Bu_4N]BH_4$, θ = 5 K (100 and 152 GHz); 10 K (208 GHz).

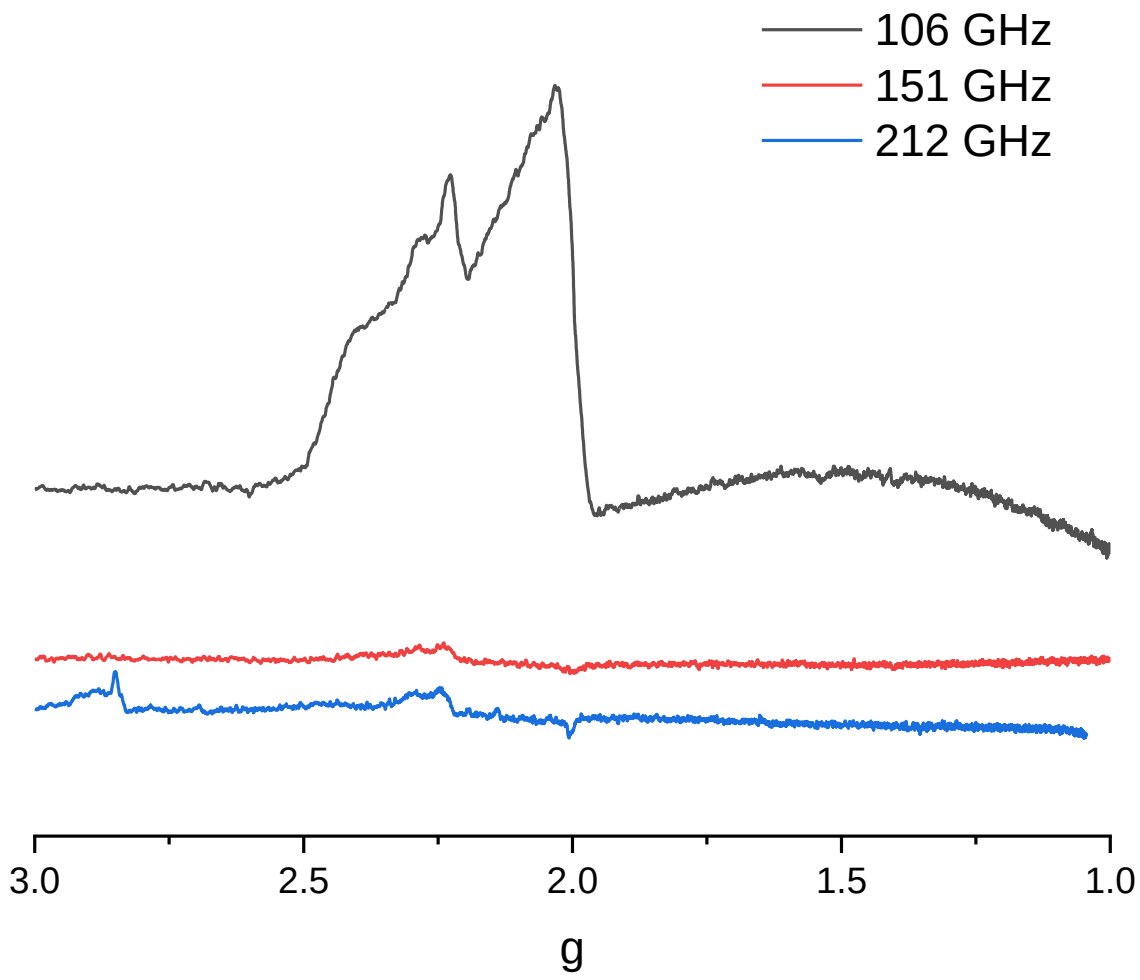

Figure 83. High field EPR spectra of $[Co^{I}(dmgBF_2)_2(OH_2)_2]$ + NEt_3. 50 mM complex in CH_3CN with 500 mM $[^nBu_4N]BH_4$ and 700 mM NEt_3, θ = 5 K.

Table 18. List of the observed g-values from the EPR spectroscopic studies.

Complex	Sample	g_x	g_y	g_z
$[Co(dmgBF_2)_2(OH_2)_2]$[73]	FS	2.26	2.16	2.01
$[Co(dmgBF_2)_2(OH_2)_2]$	P	2.24	2.15	2.00
$[Co(dmgBF_2)_2(OH_2)_2]$	FS	2.24	2.15	2.00
$[Co(dmgBF_2)_2(OH_2)(N(C_2H_3)_3)]$	P	2.24-2.25	2.15-2.16	2.00-2.01
$[Co(dmgBF_2)_2(OH_2)_2]$ + NEt_3	FS	2.19		2.00
$[Co(dmgBF_2)_2(OH_2)_2]$ + $[^nBu_4N]BH_4$	FS	--	--	--
$[Co(dmgBF_2)_2(OH_2)_2]$ + $[^nBu_4N]BH_4$ + NEt_3	FS	--	--	--

[73] samples were dissolved in DMSO

FS = Frozen sample

P = Pellet

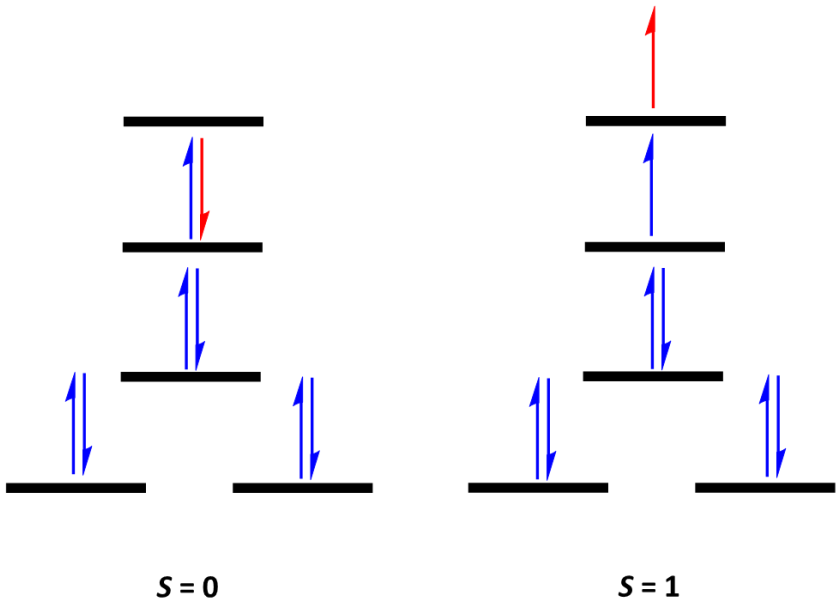

Figure 84. Electron diagram for low- and high-spin square planar complexes.

Lastly, the spectra were simulated using XSophe for the cobalt(II) complex as well as for oxygen, Figure 85. The g value parameters used for the g values were obtained from the acquired spectra of the complex, the Anisotropic values were obtained from Cropek *et al*.[73], and line width used were 900, 400, and 150 for l_x, l_y, and l_z, respectively. This gave the best fit to the data that it was modeled after. Likewise, oxygen was also simulated using the values provided by Dr. J. Krystek, with all three g values being 2 with the ZFS energy being about 38500.. The g value parameters used for the g values were obtained from the acquired spectra of the complex, the Anisotropic values were obtained from Cropek *et al*.[73], and line width used were 900, 400, and 150 for l_x, l_y, and l_z, respectively. [73], and line width used were 900, 400, and 150 for l_x, l_y, and l_z, respectively. This gave the best fit to the data that it was modeled after. Likewise, oxygen was also simulated using the values provided by Dr. J. Krystek, with all three g values being 2 with the ZFS energy being about 38500.

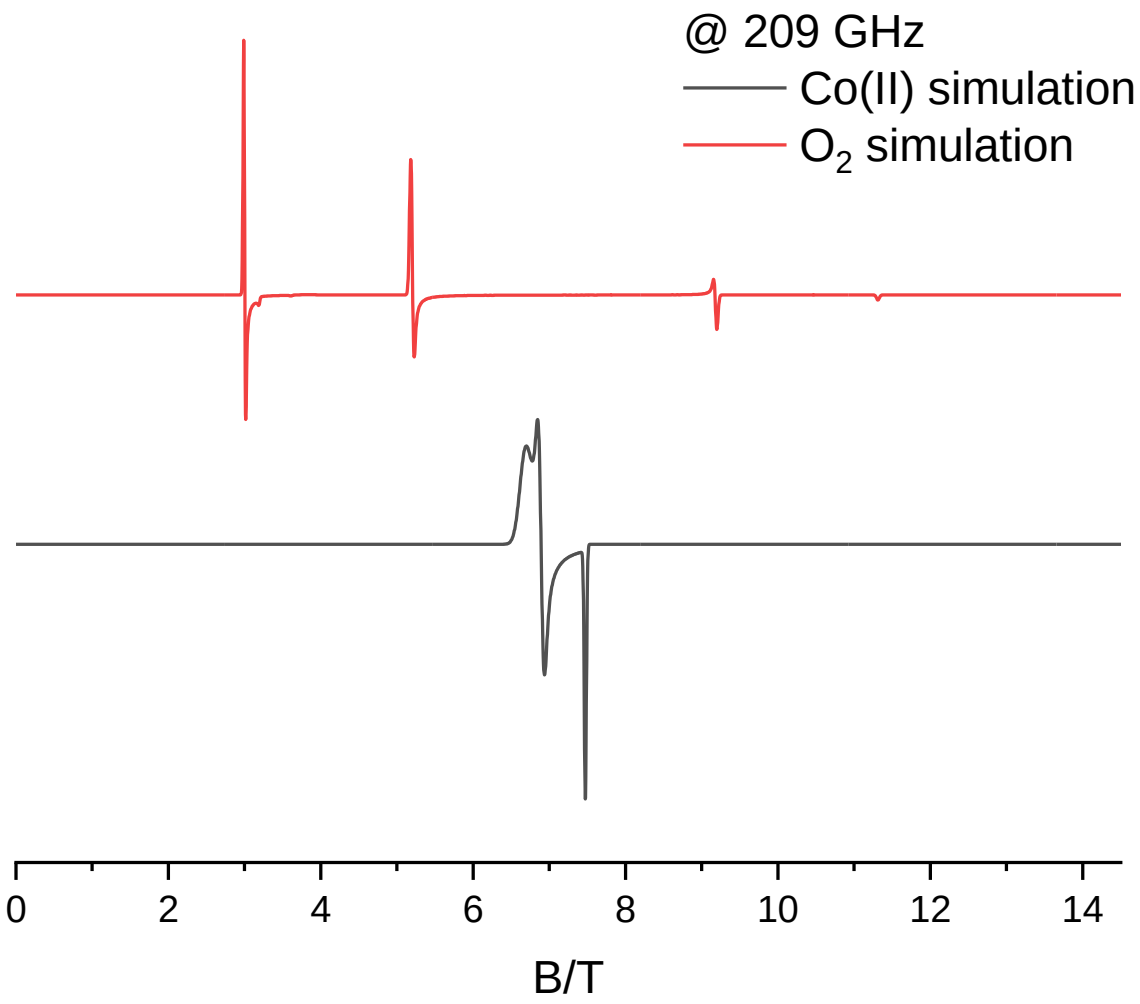

Figure 85. Simulated HFEPR spectra of $[Co(dmgBF_2)_2(OH_2)(N(C_2H_3)_3)]$ and O_2 at 209 GHz.

3.2.10 Conclusions

In conclusion, the product isolated from the reaction of $[Co(dmgBF_2)_2(OH_2)_2]$ with Et_3N was indeed a cobalt(II) complex, which produced a similar EPR spectrum to its parent complex. An interesting study that could be done in the future would be to monitor the change in the EPR spectra overtime for this interaction. And finally, not much can be said for the studies where the complex was reduced to the cobalt(I) species as they appeared to be EPR silent. The time course mass spectral study shows the oxidized Et_3N species coordinated to the cobalt metal center, which was further confirmed by its elemental analysis and mass spectrum of the isolated product.

Chapter 4: *N*-substituted 2-pyridinecarbothioamides and Polypyridyl Mixed-ligand Cobalt(III)-Containing Complexes for Photocatalytic Hydrogen Generation

4.0 Materials and physical measurements

All the chemicals including solvents were obtained from Sigma-Aldrich (St. Louis, MO, U.S.A), Fisher Scientific, VWR, or other commercial vendors, and used as received.

Microanalyses (C, H, and N) were performed by Intertek Pharmaceutical Services, P.O. Box 470, Salem Industrial Park, Building #5, Whitehouse, NJ 08888, U.S.A. FTIR and ATR data were acquired on a Nicolet AVATAR 370 DTGS spectrometer. ^{1}H, ^{13}C, and ^{19}F spectra were acquired on a Bruker 400 MHz NMR spectrometer in the respective solvent and were referenced internally to the residual protons of the incompletely deuterated solvent; except where all ^{19}F NMR spectra which were acquired in DMSO-d_6. Here CF_3CO_2H (δ = –76.55 ppm) was used as an external reference at room temperature. All NMR spectra were processed with the ACD Spectrus Processor 2012 software.†

High resolution ESI MS spectra were acquired via positive electrospray ionization on a Bruker 12 Tesla APEX –Qe FTICR-MS with an Apollo II ion source at the College of Sciences Major Instrument Cluster (COSMIC), Old Dominion University. Samples were dissolved in methanol before being introduced by direct injection using a syringe pump with a flow rate of 2 $\mu L\ s^{-1}$. The data was processed using Bruker Daltonics Data Analysis Version 3.4.

Voltammograms were acquired on a Bioanalytical Systems Inc. Epsilon workstation on a C3 cell stand at room temperature in acetontrile containing 0.10 M tetra-*n*-butylammonium perchlorate (TBAP) as supporting electrolyte, using a three electrode system consisting of a glassy carbon working electrode, a platinum wire auxiliary electrode, and a Ag/AgCl reference electrode, against which ferrocene shows a reversible wave at +0.43 V. Solutions were saturated with argon for 15 minutes prior to each acquisition, and a blanket of argon gas was

† Available from Advanced Chemistry Development (ACD, Inc.), 8 King Street East, Suite 107, Toronto, Ontario M5C 1B5, Canada).

maintained throughout the measurements.

All UV-visible spectra were acquired on an Agilent 8453 diode array spectrophotometer using a quartz cuvette with a path length of 1.0 cm for standard measurements, and a quartz cuvette with a path length of 0.1 cm for the spectroelectrochemical measurements.

4.0.1 DFT calculations

Geometries were optimized in the gas- and solvent-phase using the mPW1PW91 exchange correlation functional and Gaussian 09. Implicit solvation in acetonitrile was modeled with the integral equation formalism variant of the polarizable continuum model (IEF-PCM) [168]. Cobalt was represented by the Wachters-Hay all-electron basis set [169-170]. The Dunning triple-ξ basis was used for all other atoms [171]. Diffuse functions were added to N, O, F, and S. Optimized structures were confirmed as minima on the potential energy surface by vibrational analysis. Vertical electronic excitations were calculated using time-dependent DFT (TD-DFT) from the optimized structures. Geometries were optimized in the gas- and solvent-phase using the mPW1PW91 exchange correlation functional and Gaussian 09. Implicit solvation in acetonitrile was modeled with the integral equation formalism variant of the polarizable continuum model (IEF-PCM) [168]. Cobalt was represented by the Wachters-Hay all-electron basis set [169-170]. The Dunning triple-ξ basis was used for all other atoms [171]. Diffuse functions were added to N, O, F, and S. Optimized structures were confirmed as minima on the potential energy surface by vibrational analysis. Vertical electronic excitations were calculated using time-dependent DFT (TD-DFT) from the optimized structures.Geometries were optimized in the gas- and solvent-phase using the mPW1PW91 exchange correlation functional and Gaussian 09. Implicit solvation in acetonitrile was modeled with the integral equation formalism variant of the polarizable continuum model (IEF-PCM) [168]. Cobalt was represented by the Wachters-Hay all-electron basis set [169-170]. The Dunning triple-ξ basis was used for all other atoms [171]. Diffuse functions were added to N, O, F, and S. Optimized structures were confirmed as minima on the potential energy surface by vibrational analysis. Vertical electronic excitations were calculated using time-dependent DFT (TD-DFT) from the optimized structures.

4.0.2 Photocatalytic measurements

Hydrogen evolution was measured using a Perkin Elmer Clarus-580 gas chromatograph (GC) with a thermal conductivity detector, argon as carrier and eluent gas, a 7' HayeSep N 60/80 pre-column, a 9' molecular sieve 13 × 45 /60 column and a 1 mL injection loop. Three distinct solutions were prepared for the photosensitizer $[Ru(bpy)_3](PF_6)_2$, the respective catalyst, and last, the sacrificial electron donor and the acid source (HBF_4, 48% water): the three solutions were mixed together to obtain 5 mL of sample solutions in standard 20 mL headspace vials.

In DMF, the resulting molar concentrations of photocatalytic components were: 1 M for triethanolamine (TEOA), 0.1 M for (HBF_4), 0.56 M for water, 0.1 mM for $[Ru(bpy)_3](PF_6)_2$, 0.01 mM for $[Co(N\text{-}N)_2(PCA\text{-}(CF_3)_2)](PF_6)_2$ or $[Co(dmgH)_2Cl(py)]$ (apparent pH = 8.9). Those vials were placed on a LED panel in a thermostatic bath set at 20 °C. They were sealed with a rubber septum pierced with two stainless steel tubes. The first tube carried an argon flow pre-bubbled in spectroscopic grade solvent. The flow was set to 5 mL min^{-1} (adjusted with a manual flow controller (Porter, 1000) and referenced with a digital flowmeter (Perkin Elmer FlowMark). The second tube leads the flow to the GC sample loop through a 2 mL overflow protection vial, then through an 8-port stream select valve (VICCI) and finally to the GC sample loop. A microprocessor (Arduino Uno) coupled with a custom PC interface allows for timed injections.

For general calibration, stock cylinders of known concentration of H_2 in nitrogen replaced the nitrogen flow (inserted at the pre-bubbler, to keep the vapor matrix consistent). The measured results, independent of flow rate (under same pressure) can be easily converted into a rate of hydrogen following equation **1** in the supporting information. For calibration of H_2 production, a nitrogen bottle of certified 100 ppm hydrogen was set to deliver a specific flow. H_2 production rate at a specific nitrogen flow, a syringe pump (New Era Pump) equipped with a gas-tight syringe (SGE) and a 26s gauge needle (Hamilton) was used to bubble different rates of pure hydrogen gas into the sample, to a minimum of 0.5 μL min^{-1} (see supporting information for additional details).

4.1 Synthesis of the ligand and the cobalt(III) complexes

4.1.1 *N*-(3,5-bis(trifluoromethyl)phenyl)pyridine-2-carbothioamide (PCA-$(CF_3)_2$)

A mixture of 3,5-bis(trifluoromethyl)aniline (3.41 mL, 21.6 mmol), sulfur (2.01 g, 65.4 mol) and sodium sulfide nonahydrate (0.24 g, 2 mol %) in 2-methylpyridine (30 mL) was refluxed for 48 h. After cooling and removal of all volatiles *in vacuo*, the dark brown oil residue was taken up in $CHCl_3$/MeOH (20:1) and was purified using column chromatography on silica gel. Fractions containing the desired product were combined and the filtrate was evaporated under reduced pressure to yield a yellow solid. A single crystal suitable for X-ray analysis was grown via the slow evaporation technique from chloroform. Yield = 5.90 g (77%). FTIR (ν/cm^{-1}): 3170 (NH, m); 1380 (C=S, s); 1278 (C-F, vs). ^{1}H NMR (400 MHz, $CDCl_3$, δ/ppm): 12.38-12.28 (m, 1H), 8.76 (d, J = 7.8 Hz, 1H), 8.67 (s, 2H), 8.61-8.54 (m, 1H), 7.93 (dt, J = 1.6, 7.8 Hz, 1H), 7.77 (s, 1H), 7.54 (ddd, J = 1.2, 4.7, 7.4 Hz, 1H). ^{13}C NMR (101MHz, $CDCl_3$, δ/ppm): 189.4, 150.7, 146.6, 140.0, 137.8, 132.4, 132.1, 126.7, 124.9, 122.2, 121.7, 119.5. ^{19}F NMR (376 MHz, $CDCl_3$, δ/ppm): -62.94 (s, 6F)

4.1.2 General procedure for the preparation of $[Co(N\text{-}N)_2Cl_2)]Cl$ (where N-N = bpy (complex 1) or phen (complex 2))

$[Co(bpy)_2Cl_2)]Cl$ **1** and $[Co(phen)_2Cl_2)]Cl$ **2** were synthesized via the procedure as by Ghosh *et al*.[172]

4.1.3 Synthesis of $[Co(bpy)_2(PCA\text{-}(CF_3)_2)](PF_6)_2 \bullet H_2O$ 3

$[Co(bpy)_2Cl_2)]Cl$, **1** (0.175 g, 0.366 mmol) and PCA-$(CF_3)_2$ (0.256 g, 0.733 mmol) were mixed in ethanol (50 mL) and stirred at room temperature for 4 hours. The solvent was then removed via rotary evaporation (note that the water bath temperature should **NOT** exceed 50 °C); then H_2O (10 mL) was added and the mixture was filtered. The residue was washed with H_2O (~20 ml). The filtrate was then collected to which NH_4PF_6 (0.597 g, 3.66 mmol) was added and the resulting mixture was then placed in an ice bath. The mixture was then filtered, and the residue was washed with cold H_2O, followed by Et_2O, and air dried. Yield = 0.389 g (92%). Found C, 39.70; H, 2.38; and N 8.05%, Anal. Calc. for $C_{34}H_{25}CoF_{18}N_6OP_2S$: C, 39.70; H, 2.45; and N, 8.17%. ESI MS (positive mode, CH_3CN): $[M\text{-}2PF_6^-]^{2+}$ 360 (360.05). ^{1}H NMR (400 MHz, DMSO-

d_6, δ/ppm) 9.43 (d), 9.04 (dd), 8.99 (d), 8.92 (d), 8.75 (d), 8.56 (m), 8.33 (dtd), 8.01 (m), 7.91 (m), 7.86 (s), 7.81 (qd), 7.73 (m), 7.68 (m), 7.50 (m), 7.44 (d), 7.16 (d). ^{13}C NMR (101 MHz, DMSO-d_6, δ/ppm) 170.9, 159.4, 156.3, 156.0, 155.4, 155.3, 152.9, 152.3, 151.2, 151.0, 149.9, 142.7, 142.5, 142.2, 142.0, 131.5, 131.2, 131.2, 130.7, 130.3, 130.1, 129.9, 127.0, 126.7, 126.3, 126.2, 125.4, 124.4, 121.7, 121.2. ^{19}F NMR (376 MHz, DMSO-d_6, δ/ppm) -61.02, -68.94, and -70.83.

4.1.4 Synthesis of [Co(phen)$_2$(PCA-(CF$_3$)$_2$)](PF$_6$)$_2$•1.25H$_2$O 4

[Co(phen)$_2$Cl$_2$)]Cl, **2** (0.175 g, 0.333 mmol) and PCA-(CF$_3$)$_2$ (0.233 g, 0.666 mmol) were mixed in ethanol (50 mL) and stirred at room temperature for 4 hours. The solvent was then removed via rotary evaporation; then H_2O (10 ml) was added and the mixture was then filtered. The residue was washed with H_2O (~20 ml). The filtrate was then collected to which NH_4PF_6 (0.543 g, 3.33 mmol) was added and the resulting mixture was placed in an ice bath. The mixture was then filtered, and the residue was washed with cold H_2O followed by Et_2O, and air dried. Yield: 0.288 g (72%). Found C, 42.03; H, 2.17; and N 7.74%, Anal. Calc. for $C_{38}H_{25.5}CoF_{18}N_6O_{1.25}P_2S$: C, 42.22; H, 2.38; and N, 7.77%. ESI MS (positive mode, MeCN): [M-2PF_6^-]$^{2+}$ 384.1 (384.05). ^{1}H NMR (400 MHz, DMSO-d_6, δ/ppm) 9.79 (m), 9.18 (m), 8.83 (d), 8.54 (m), 8.32 (m), 7.94 (m), 7.81 (s), 7.73 (m), 7.60 (m), 7.25 (d). ^{13}C NMR (101 MHz, DMSO-d_6, δ/ppm) 171.2, 159.7, 154.7, 153.5, 152.8, 152.5, 151.6, 151.2, 146.4, 146.0, 145.6, 145.1, 141.9, 141.5, 141.1, 140.5, 131.9, 131.7, 131.6, 131.5, 131.2, 131.1, 130.7, 129.2, 128.8, 128.7, 128.5, 128.4, 128.4, 128.2, 128.0, 126.5, 124.4, 121.6, 121.1 . ^{19}F NMR (376 MHz, DMSO-d_6), δ/ppm) -60.97, -68.94, and -70.83

4.1.5 Synthesis of [Co(N-N)$_3$](PF$_6$)$_3$ where N-N = bpy (complex 5) or phen (complex 6)

[Co(bpy)$_3$](PF$_6$)$_3$ **5** was synthesized following the procedure as by Kim [173]. [Co(phen)$_3$](PF$_6$)$_3$ **6** was synthesized from [Co(phen)$_2$Cl$_2$]Cl **2** using stoichiometric quantities of complex **2** and 1,10-phenanthroline (see supporting information).[Co(bpy)$_3$](PF$_6$)$_3$ **5** was synthesized following the procedure as by Kim [173]. [Co(phen)$_3$](PF$_6$)$_3$ **6** was synthesized from [Co(phen)$_2$Cl$_2$]Cl **2** using stoichiometric quantities of complex **2** and 1,10-phenanthroline (see supporting information).[Co(bpy)$_3$](PF$_6$)$_3$ **5** was synthesized following the procedure as by Kim

[173]. $[Co(phen)_3](PF_6)_3$ **6** was synthesized from $[Co(phen)_2Cl_2]Cl$ **2** using stoichiometric quantities of complex **2** and 1,10-phenanthroline (see supporting information).

4.2 Results and discussion

4.2.1 Synthesis and characterization

4.2.1.1 *N*-(3,5-bis(trifluoromethyl)phenyl)pyridine-2-carbothioamide (PCA-$(CF_3)_2$)

The synthesis of *N*-(3,5-bis(trifluoromethyl)phenyl)pyridine-2-carbothioamide (PCA-$(CF_3)_2$) followed a one-pot protocol as reported by Klingele and Brooker [174] under aerobic conditions (see Scheme 10). The synthesis of *N*-(3,5-bis(trifluoromethyl)phenyl)pyridine-2-carbothioamide (PCA-$(CF_3)_2$) followed a one-pot protocol as reported by Klingele and Brooker [174] under aerobic conditions (see Scheme 10). The synthesis of *N*-(3,5-bis(trifluoromethyl)phenyl)pyridine-2-carbothioamide (PCA-$(CF_3)_2$) followed a one-pot protocol as reported by Klingele and Brooker [174] under aerobic conditions (see Scheme 10).

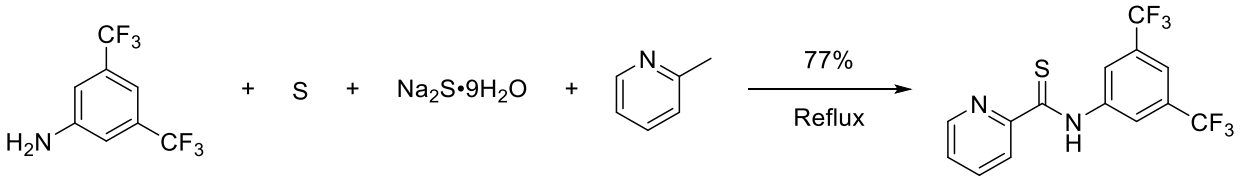

Scheme 10. Synthesis of *N*-(3,5-bis(trifluoromethyl)phenyl)pyridine-2-carbothioamide (PCA-$(CF_3)_2$).

In the FTIR spectrum (Figure 86), the diagnostic stretching frequency of the ν(N-H) of the thioamide was observed at 3200 cm^{-1} and the corresponding bend (amide II) at 1550 cm^{-1}. These values are comparable to those of other thioamide systems.[175-176] In the ^1H NMR spectrum (Figure 87), the NH proton is observed resonating circa 12.33 ppm, integrating for a single proton, and the aryl region integrated for a total of seven protons, all consistent with the desired product PCA-$(CF_3)_2$. In the ^{13}C NMR spectrum, the thioamide resonance was observed at 189.4 ppm along with the aryl resonances and a single resonance at -62.94 ppm for the trifluoromethyl carbons, indicating their equivalence in the molecule.

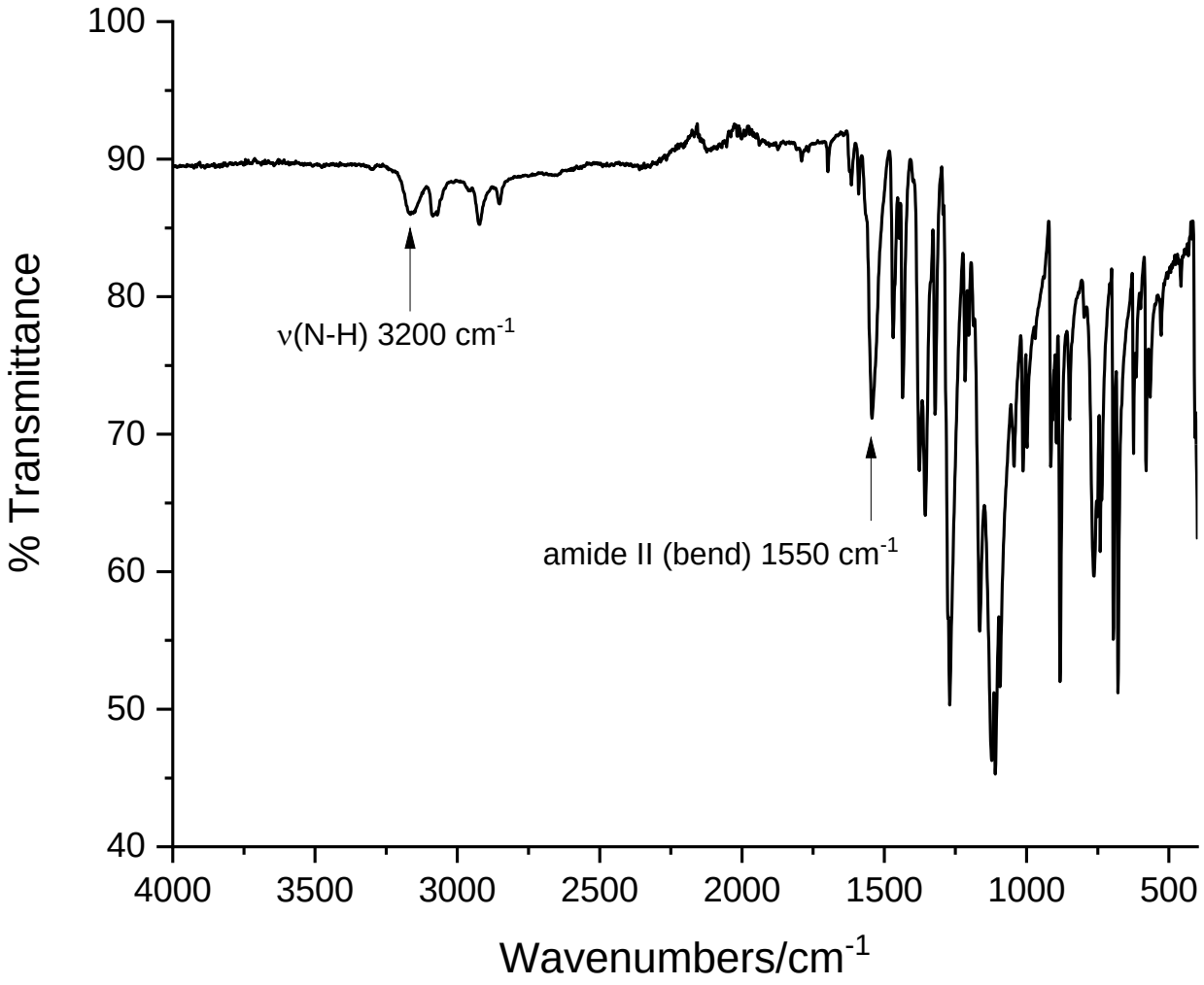

Figure 86. FTIR spectrum of PCA-$(CF_3)_2$.

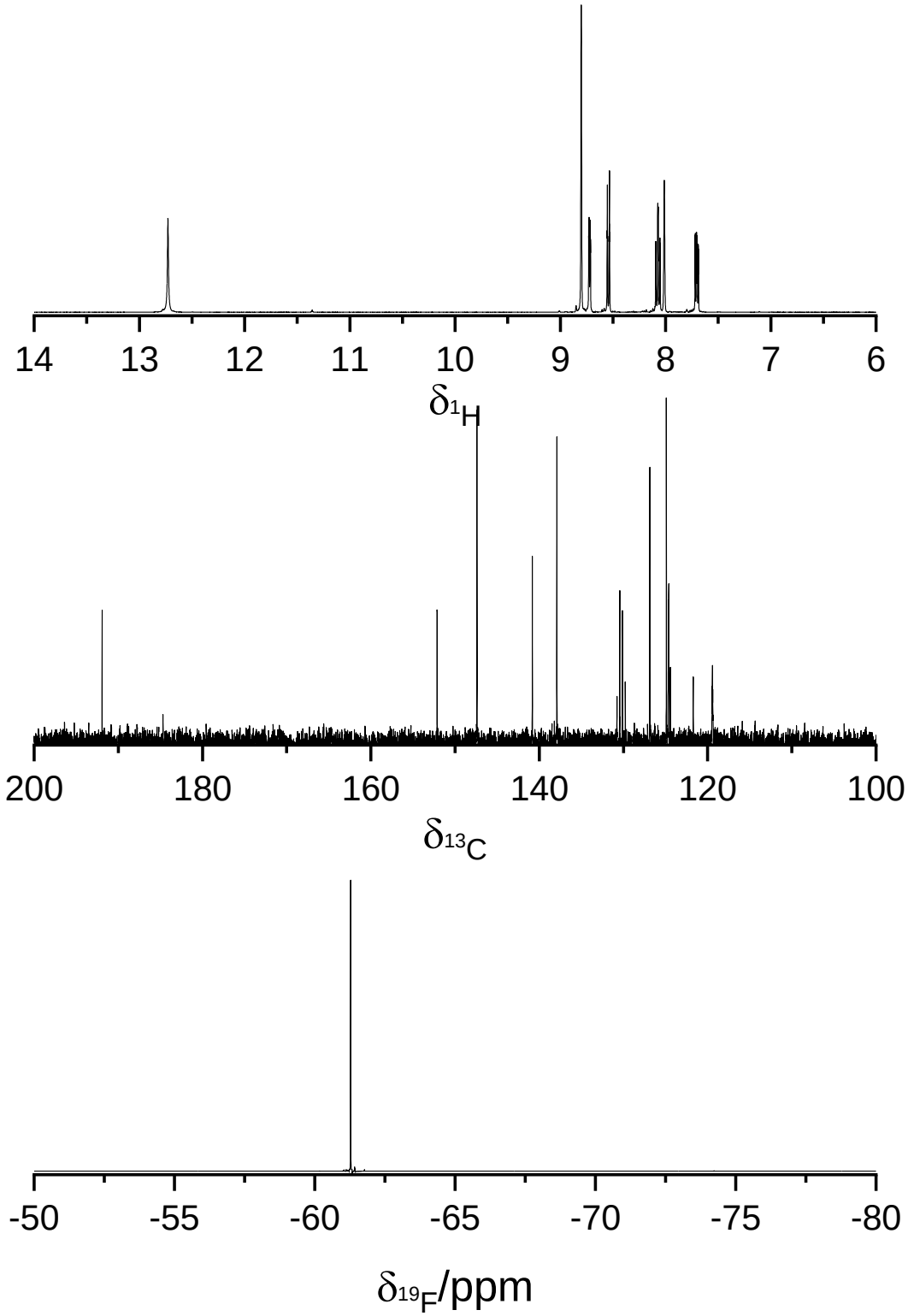

Figure 87. ^{1}H, ^{13}C, and ^{19}F NMR spectra of PCA-$(CF_3)_2$ in DMSO-d_6.

The DFT optimized structures of PCA-$(CF_3)_2$ is near planar with a short NH···N distance of 1.917 Å, consistent with the X-ray structure.[177] The amide NH bending mode is found at 1607 cm^{-1} and the overall spectrum in agreement with experiment (Figure 88). Calculated structures of complex **3** are similar in the gas phase and the solvent phase. The Co-N bond distances for the bpy ligand *trans* to the Co-S bond to PCA-$(CF_3)_2$ are slightly longer than for the bpy *trans* to the pyridyl ring of PCA. The imine C=N stretching frequency mixes with the C-C stretch for two bands at 1657 and 1678 cm^{-1}.

4.2.1.2 [Co(N-N)$_2$(PCA-(CF$_3$)$_2$)](PF$_6$)$_2$ • xH$_2$O (where N-N = bpy (x = 1) or phen (x = 1.25)

The syntheses of the complexes **3** and **4** were achieved via a two-step protocol, from complexes **1** and **2** ([Co(N-N)Cl_2]Cl species) which were prepared by a literature method [172].[172].[172]. Complexes **1** and **2** were then reacted with two equivalences of the PCA-$(CF_3)_2$ in ethanol (Scheme 11). [Co(N-N)$_2$(PCA-(CF$_3$)$_2$)](PF$_6$)$_2$•*x*H$_2$O (complexes **3** and **4**) were isolated in good to excellent yields as red-brown (complex **3**) or green-brown (complex **4**) colored solids using this simple protocol. The identities of complexes **3** and **4** were confirmed form their elemental analyses and a series of spectroscopic measurements. In the infrared spectra of complexes **3** and **4**, a key feature is the disappearance of the ν(N-H) stretch and bend, in going from the free PCA-CF_3 ligand, signaling coordination via thioamide sulfur with concomitant tautomerization to the imino thiolate.[175-176, 178] A second feature is the appearance of a broad ν(O-H) frequency signaling the presence of water in the solids (Figure 88).

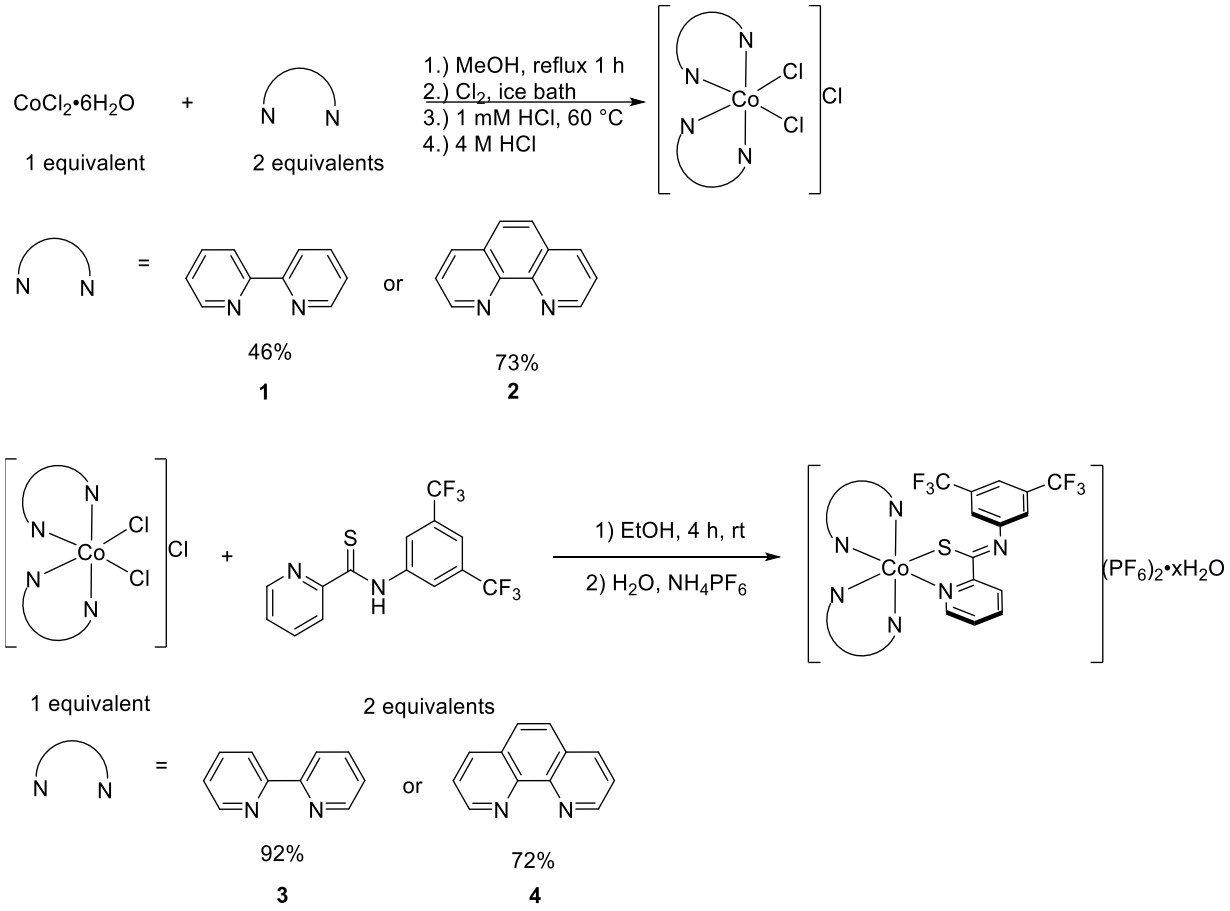

Scheme 11. Synthesis of complexes **1**-**4**.

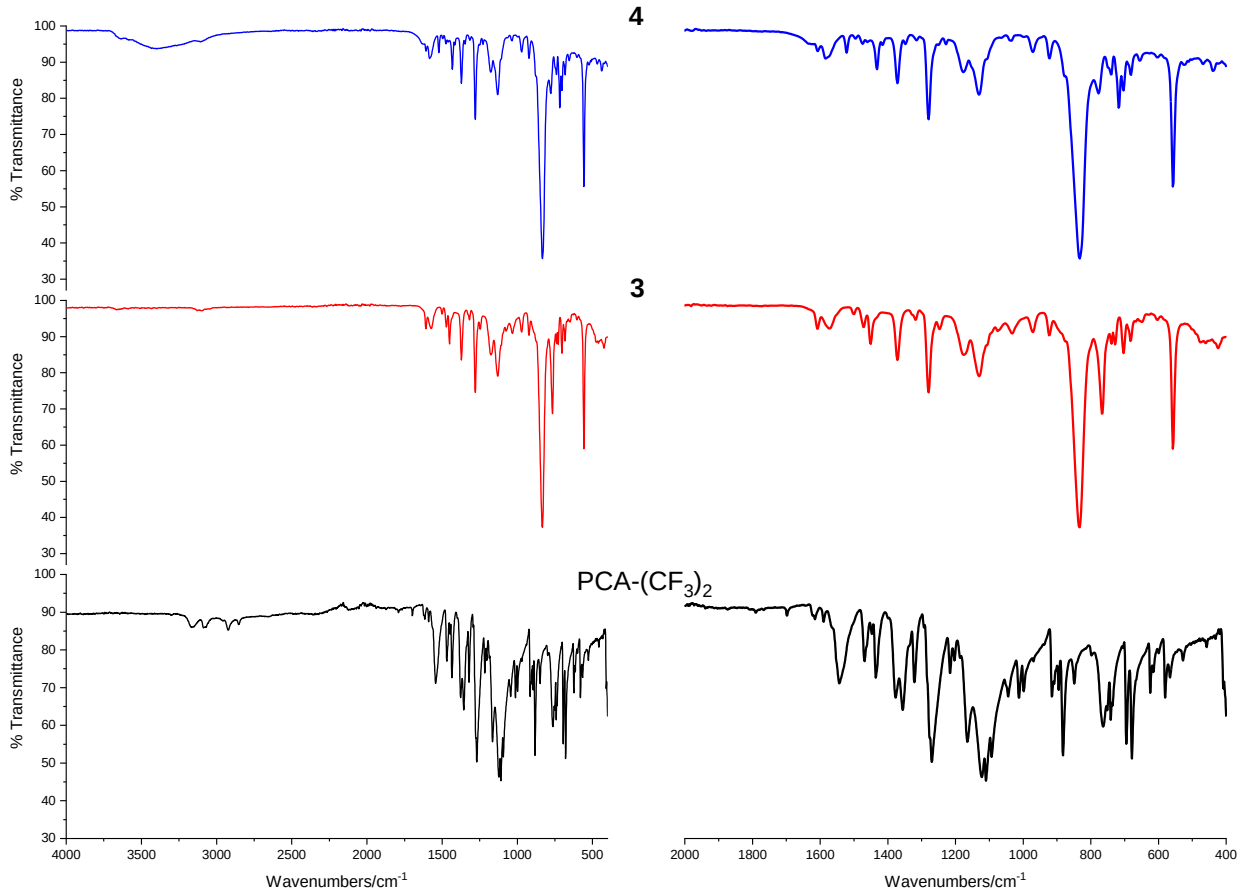

Figure 88. FT IR spectra of PCA-$(CF_3)_2$ and complexes **3** and **4**.

In the ^{1}H NMR spectra of complexes **3** and **4** (Figure 89), the NH resonance observed in the PCA-$(CF_3)_2$ ligand is absent in both complexes, which is consistent with the FTIR spectra. Similarly, in the ^{13}C NMR spectra of complexes **3** and **4**, Figure 90, the thioamide resonance at 189.4 ppm, which is observed in the "free" PCA-$(CF_3)_2$ is absent. These data are consistent with coordination by the thiolate's sulfur as a result of tautomerization of PCA-$(CF_3)_2$ to the imino thiolate. In the ^{19}F NMR spectra of the complexes (Figure 91), the formation of the PF_6^- salt is evident from the appearance of two new peaks due to P-F coupling. ESI MS of the complexes in acetonitrile (Figure 92) revealed an intense molecular ion for the $[M\text{-}H\text{-}2PF_6^-]^{2+}$. All of the spectroscopic data support the proposed formulations of coordination through the thiolate.

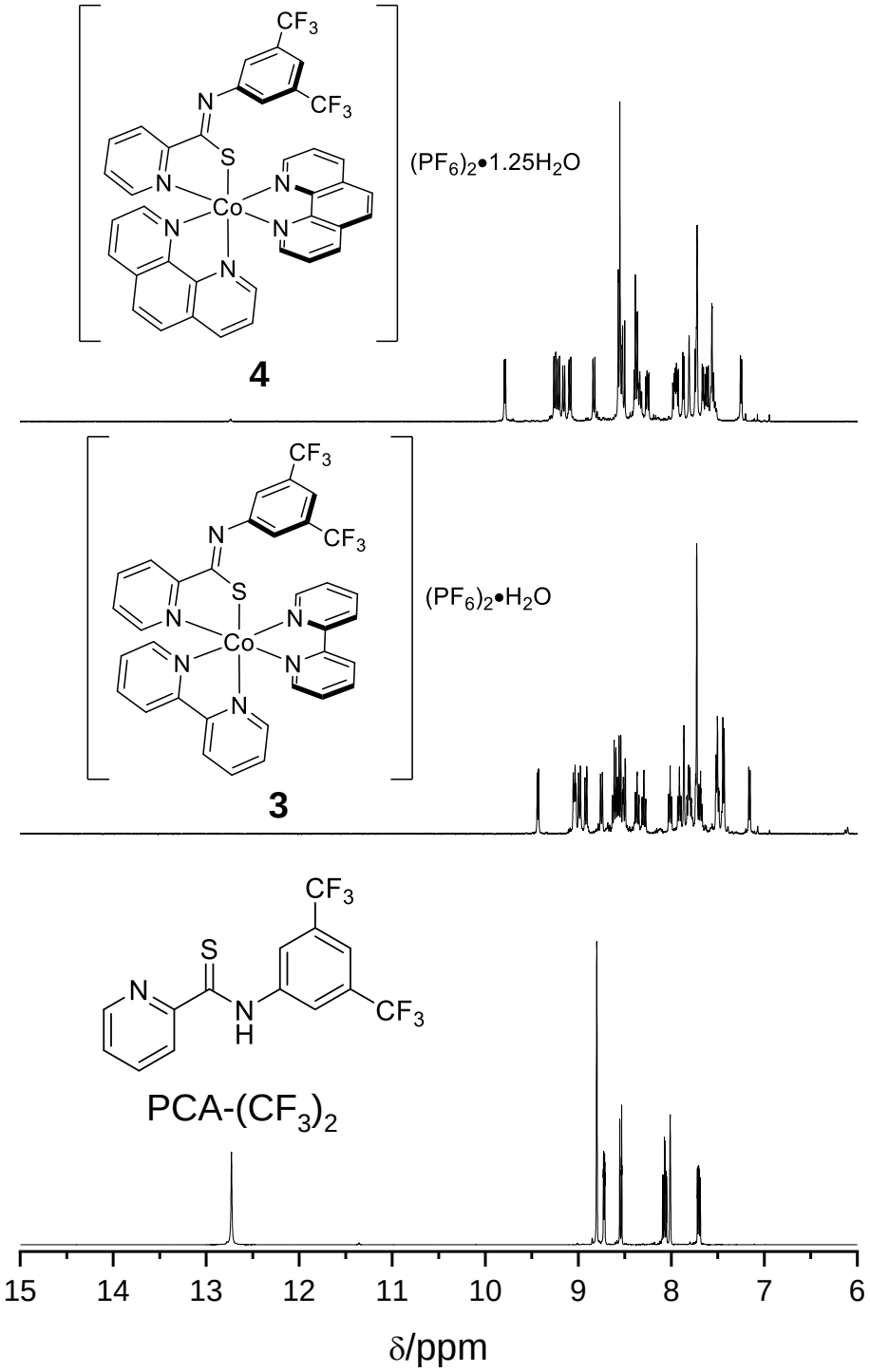

Figure 89. ^{1}H NMR spectra of PCA-$(CF_3)_2$ and complexes **3** and **4** in DMSO-d_6.

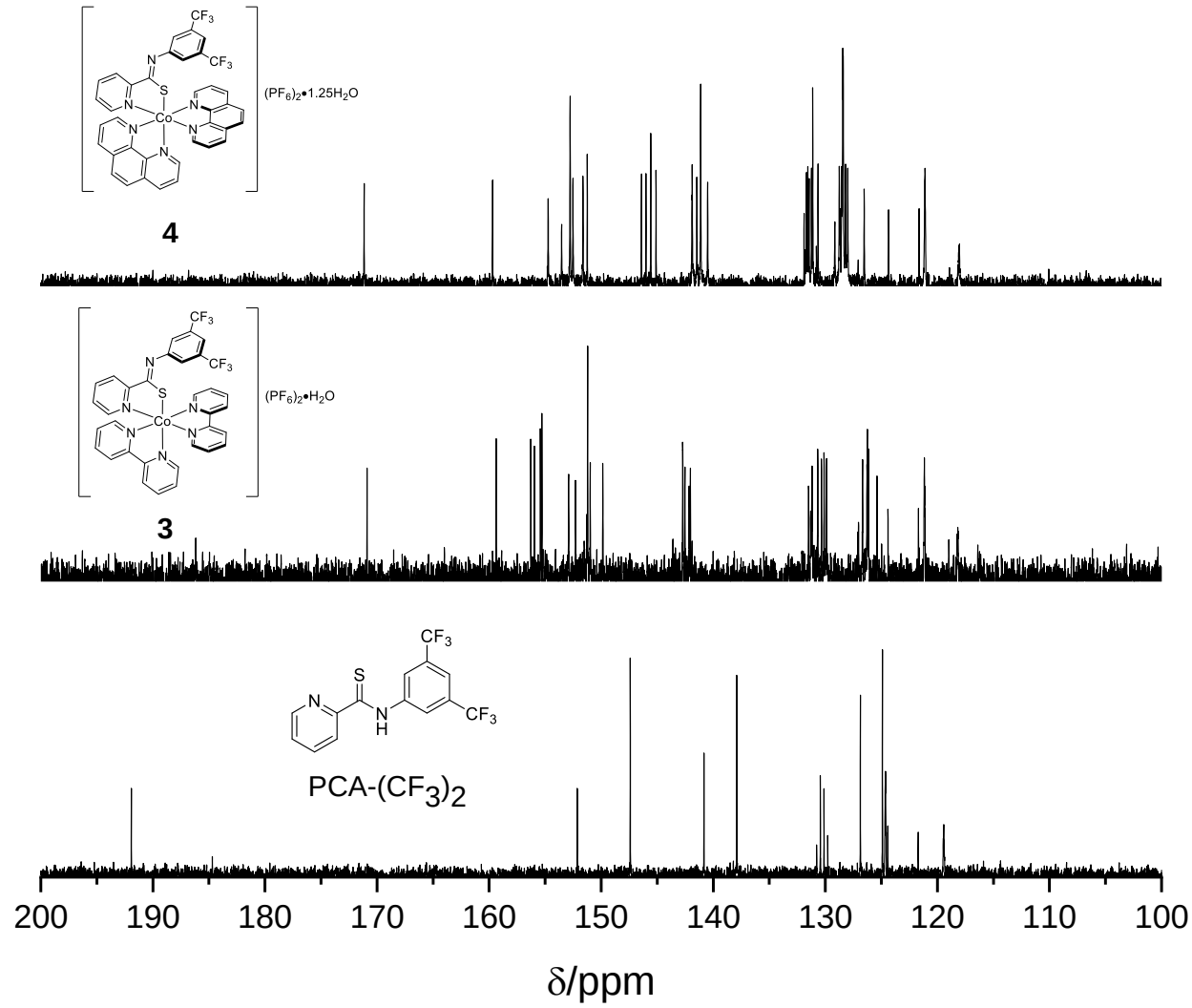

Figure 90. ^{13}C NMR spectra of PCA-$(CF_3)_2$ and complexes **3** and **4** in DMSO-d_6.

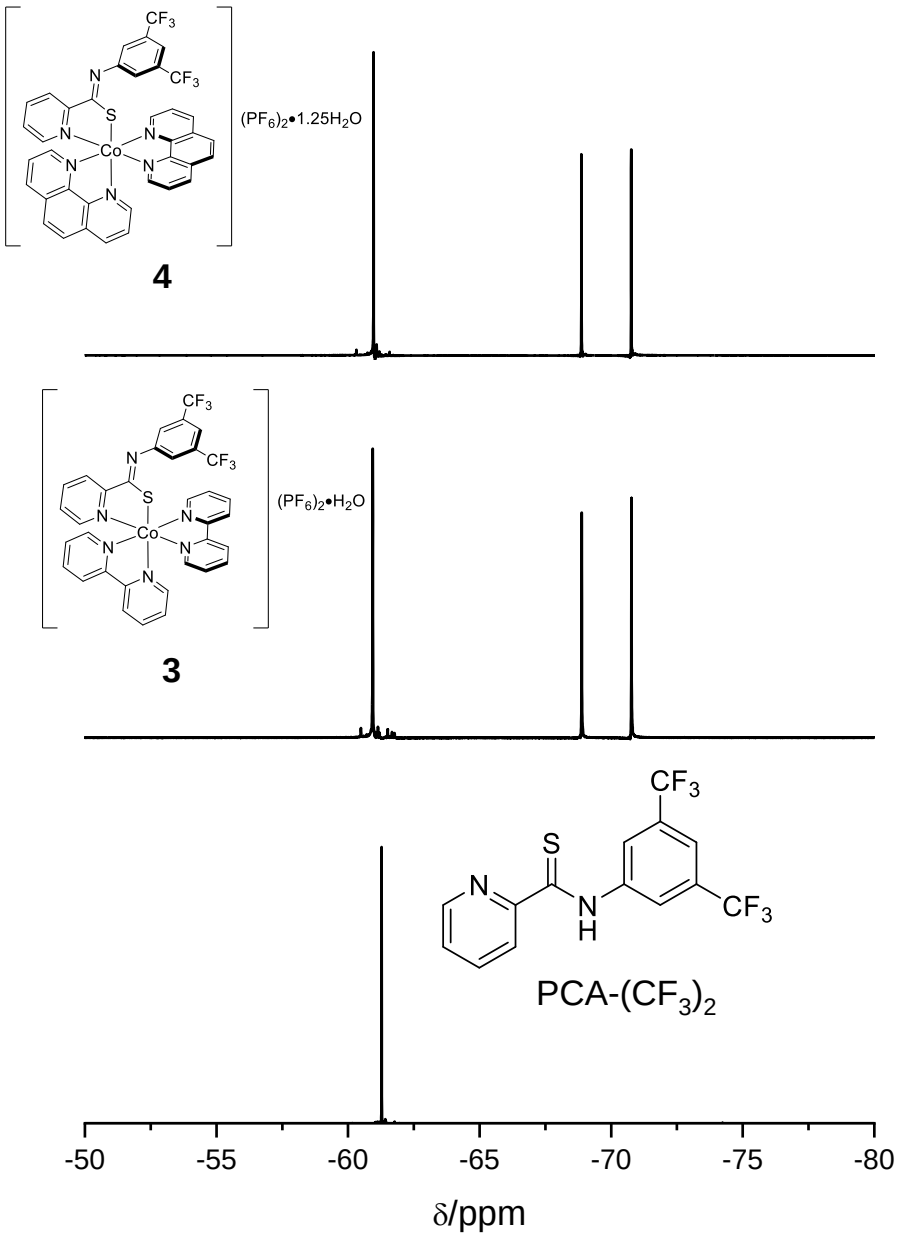

Figure 91. ^{19}F NMR spectra of PCA-$(CF_3)_2$ and complexes **3** and **4** in DMSO-d_6.

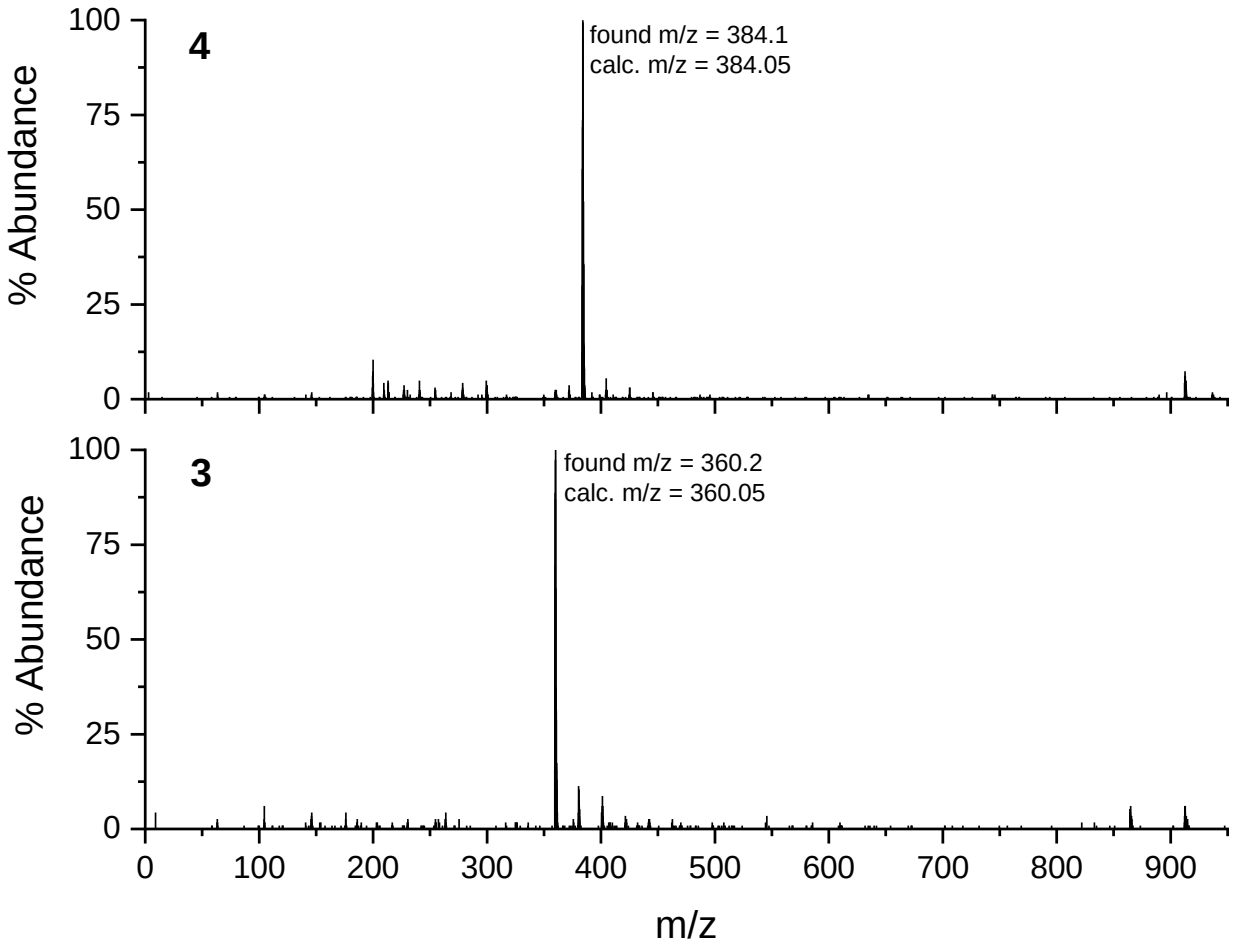

Figure 92. ESI MS of complexes **3** and **4** in CH_3CN

The UV-visible spectra of complexes **3** and **4** (Figure 93) revealed d-d transitions of the Co(III) mixed with n→π* and π→π* electronic transitions of the ligand between 450 to 330 nm. This is accompanied by intense metal-to-ligand charge transfer (MLCT), ligand-to-metal charge transfer (LMCT) and mixed with intra-ligand charge transfer (ILCT) bands between 330 to 190 nm, as revealed by the large molar extinction coefficient values. TD-DFT calculations in acetontirile are consistent with the experimental assignment of the UV-visible spectrum. Three transitions with significant intensity occur at 375 (f = 0.0170), 367 (f = 0.0875), and 357 (f = 0.0407) nm. These transitions consist of excitations from the HOMO to the LUMO (375 nm) and linear combinations of LUMO+1 and LUMO+3 orbitals (367 and 357 nm), see Figure 94. The

HOMO is localized on the imine-thiolate of PCA-$(CF_3)_2$ with an anti-bonding interaction to a Co t_{2g}-type acceptor orbital (AO). The LUMO and LUMO+1 are the combinations of the bpy π* and LUMO+3 consists of π*-character on the pyridine ring of PCA-$(CF_3)_2$. These three excitations are consistent with the assignment of the absorption between 450 to 330 nm as n→π* and π→π*. An additional set of closely spaced excitations between 320 and 275 nm involve excitations from HOMO-1 through HOMO-3 (occupied ligand π and metal t_{2g}-type orbitals) to the π* LUMOs, consistent with the experimental assignment of absorptions a wavelengths less than 330 as LMCT and ILCT excitations.

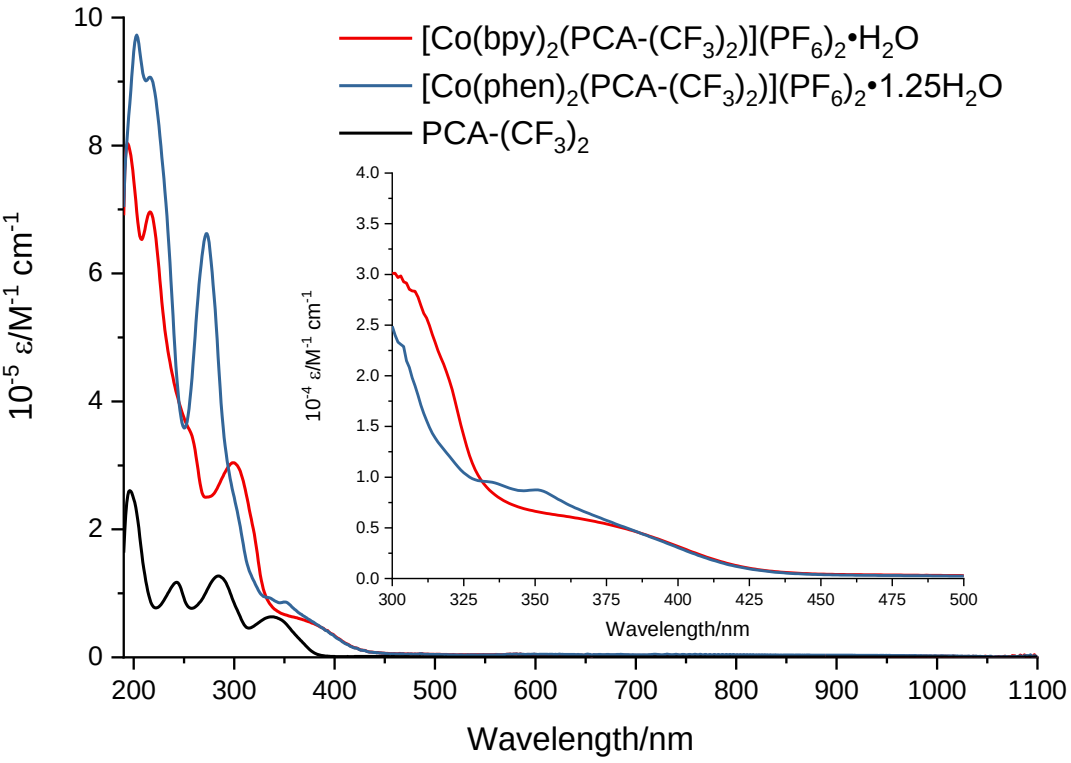

Figure 93. UV-visible spectra of PCA-$(CF_3)_2$ and complexes **3** and **4** in CH_3CN (inset: 300-500 nm expanded view).

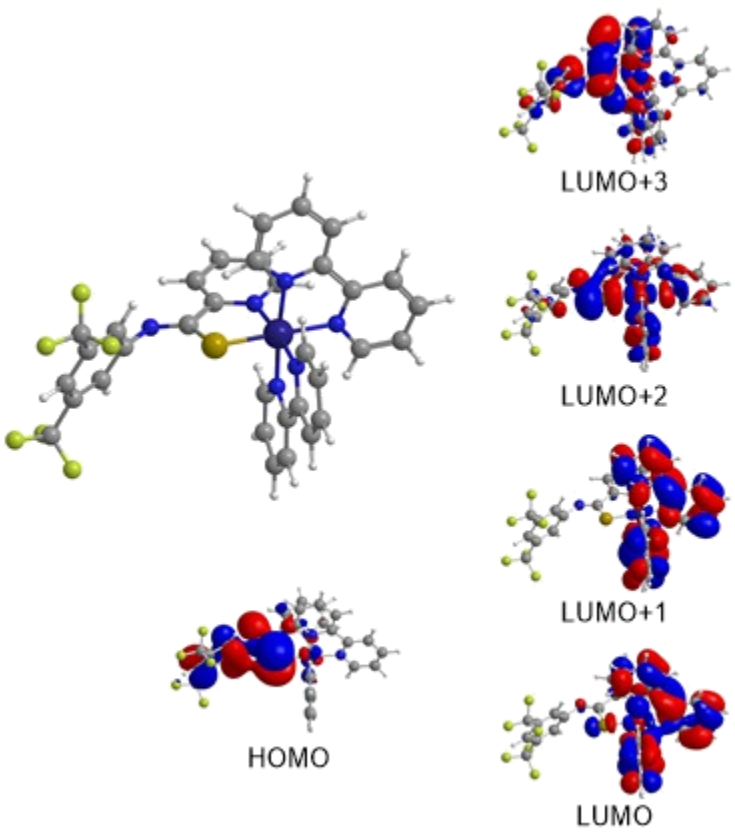

Figure 94. HOMO-LUMO plots for complex **3**.

4.3.0 Electrochemical studies

Voltammograms of PCA-$(CF_3)_2$ measured between +2.0 and –2.5 V in CH_3CN revealed a reversible one electron reduction of the thioamide moiety at $E_{1/2}$ = –1.40 V vs Ag/AgCl, and the thioamide moiety is oxidized via an irreversibe two electron process at E_{pa} = +1.50 V vs Ag/AgCl (Figure 95). In the voltamograms of complexes **3** and **4**, there are a series of one electron quasi-reversible electron transfers (Figure 95). There was no anodic current at potentials more positive than +0.20 V indicating the absence of the thioamide moiety in complexes **3** and **4**. The coordination of PCA-$(CF_3)_2$ to $[Co(N\text{-}N)Cl_2]^+$, in general, resulted in the reduction potentials of the cobalt shifting to more negative values (Table 19 and Figure 96), whilst maintaining their quasi-reversible characteristics. Of note, the coordination of PCA-$(CF_3)_2$ had a pronounced effect on the $Co^{III/II}$ and $Co^{II/I}$ redox couples, shifting the potential more negative by 100-200 mV. Secondly, ΔE_p for the $Co^{III/II}$ redox couple is less in the $[Co(N\text{-}N)_2(PCA\text{-}(CF_3)_2)](PF_6)_2$ (complexes

3 and **4**) in comparison to the $[Co(N\text{-}N)_2Cl_2)]PF_6$ (complexes **1** and **2**) species, making the redox process more Nernstian in its nature. This behavior is similar to that observed in the $[Co(N\text{-}N)_3)]PF_6$ (complexes **5** and **6**) species when compared to the $[Co(N\text{-}N)_2Cl_2)]PF_6$ species (Figure 96), and is thus related to the enhanced stability introduced by the third bidentate ligand, which is more resistant to dissociation in the +2 oxidation state. This is also consistent with the κ^2-S,N coordination of the PCA-$(CF_3)_2$ ligand. Additionally, the potential shifts of the cobalt redox couples to more negative values in complexes **3** and **4** when compared to complexes **1** and **2**, are consistent with coordination of the soft base, sulfur in which dπ-pπ backdonation can occur. The seemingly haphazard and large ΔE_p values associated with the $Co^{III/II}$ couples can be attributed to the reorganization energy associated with the $Co^{III/II}$ conversion. In complexes **1** and **2**, these reorganization effects coupled with the loss of chloro ligands result in intermediate values relative to complexes **3**-**6**. The similarity in the $Co^{II/I}$ reduction potentials of complexes **1**-**4** are likely due to the partial dissociation of the ligand(s) in the +2 oxidation state.

Table 19. Redox potentials of the cobalt couples of $[Co(N\text{-}N)_2Cl_2)]PF_6$ and $[Co(N\text{-}N)_2(PCA\text{-}(CF_3)_2)](PF_6)_2 \bullet xH_2O$ in CH_3CN at a glassy carbon working electrode *vs* Ag/AgCl in CH_3CN.

Complex	**$Co^{III/II}$/V (ΔE_p/mV)**	**$Co^{II/I}$/V (ΔE_p/mV)**	**$L^{0/\bullet-}$/V (ΔE_p/mV)**
1	+0.24 (178)	–0.92 (66)	–1.50 (71)
2	+0.13 (376)	–1.08 (144)	–1.56 (124)
3	+0.04 (78)	–1.05 (86)	--
4	+0.05 (120)	–1.07 (71)	–1.64 (109)
5	+0.39 (180)	–0.89 (66)	–1.50 (70)
6	+0.44 (140)	–0.88 (68)	–1.58 (64)

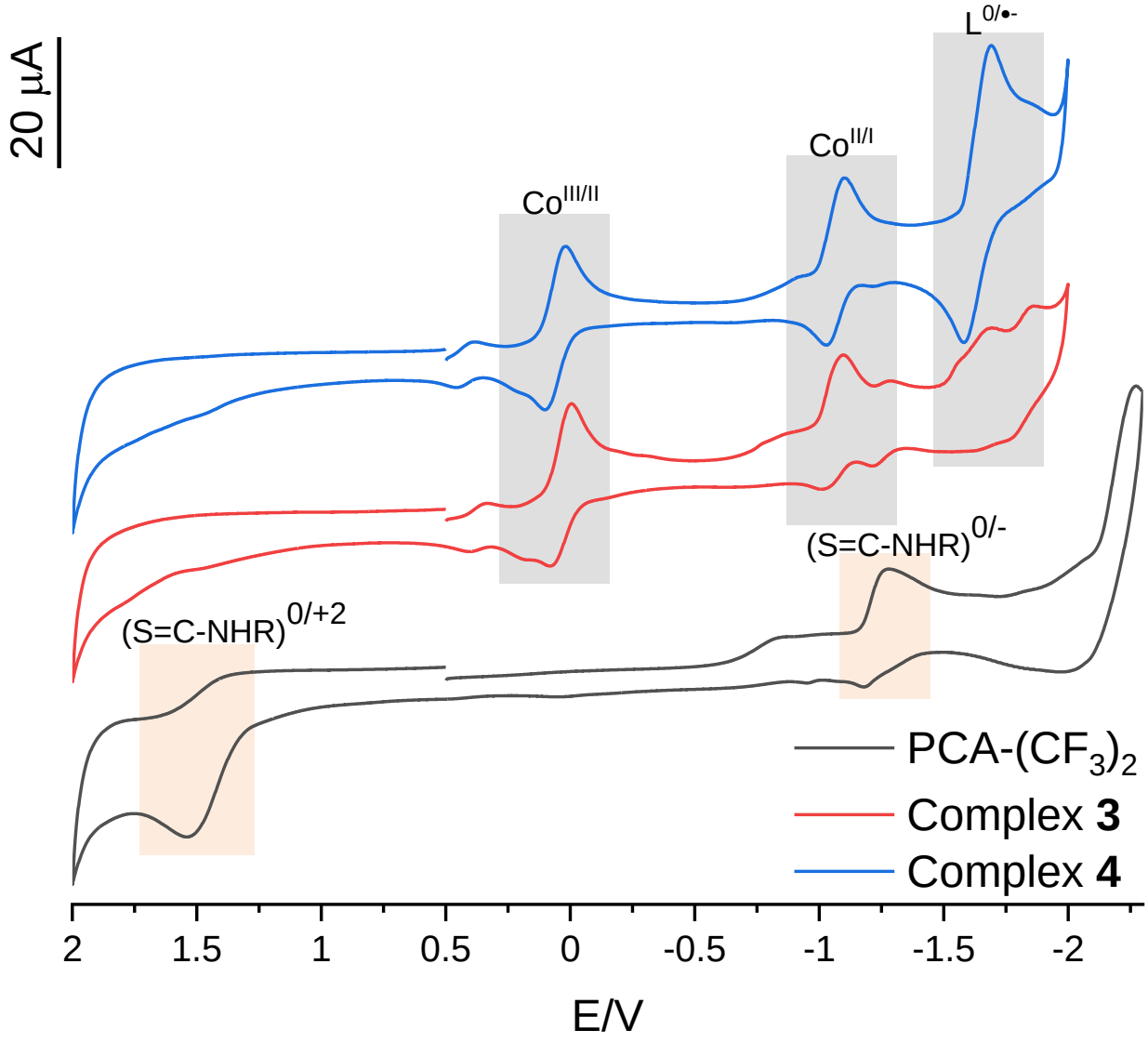

Figure 95. Cyclic voltammograms of PCA-$(CF_3)_2$, complexes **3** and **4** in CH_3CN. [complex] = 1.0 mM, supporting electrolyte = 0.1 M ($[^nBu_4N]ClO_4$), and scan rate = 100 mV s^{-1}.

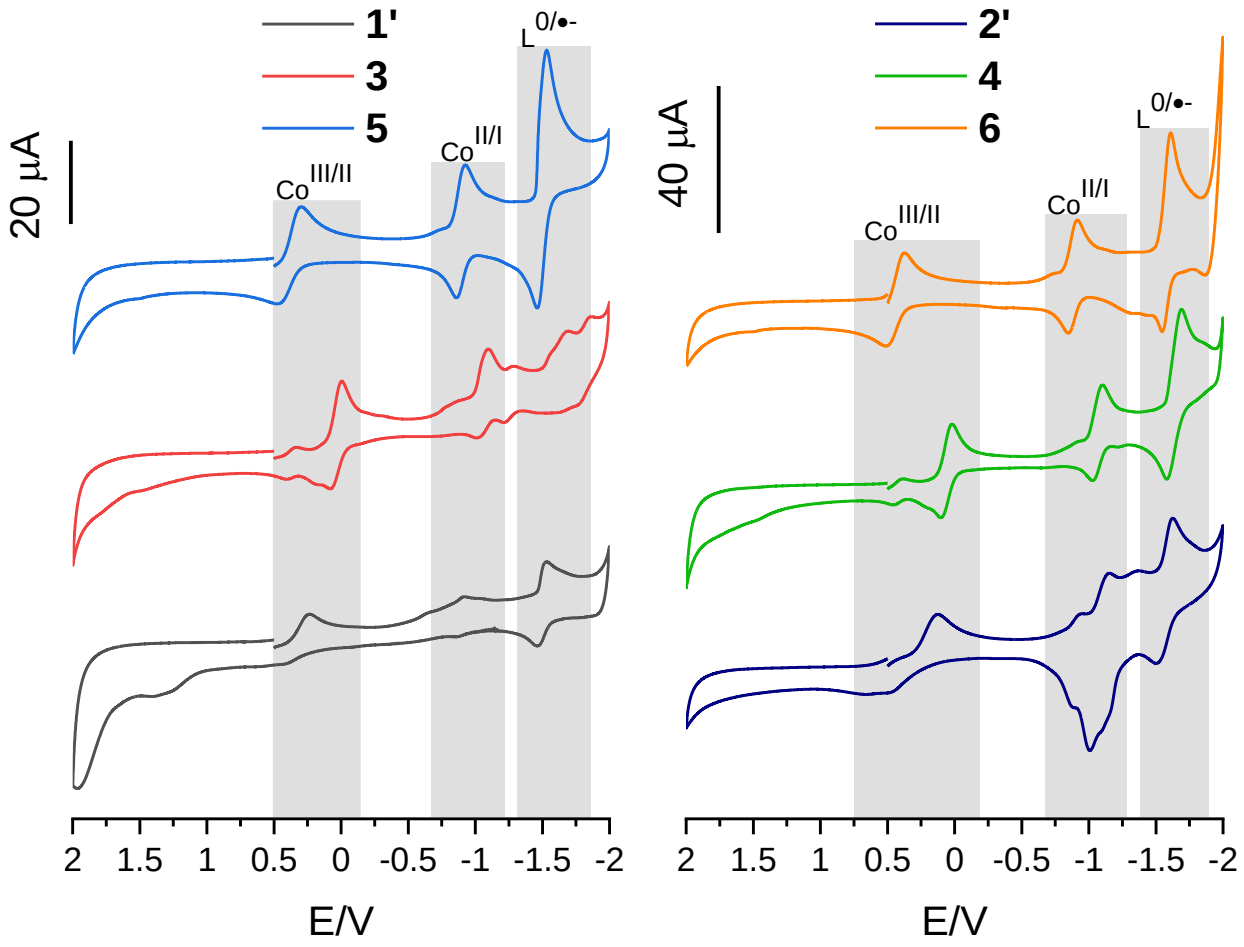

Figure 96. Cyclic voltammograms of complexes **1** – **6** in CH_3CN. [complex] = 1.0 mM, supporting electrolyte = 0.1 M ($[^nBu_4N]ClO_4$), and scan rate = 100 mV s^{-1}.

4.3.1 Electrocatalytic behavior of $[Co(N\text{-}N)_2(PCA\text{-}(CF_3)_2)](PF_6)_2 \bullet xH_2O$ in the presence of *p*-cyanoanilinium tetrafluoroborate in CH_3CN

The addition of *p*-cyanoanilinium tetrafluoroborate to acetonitrile solutions of complexes **1**-**6**, resulted in the appearance of a new cathodic wave in the vicinity of the $Co^{II/I}$ redox couple. In complexes **3** and **4**, the new cathodic wave is observed at ca –0.9 V of which the peak current increases with a simultaneous peak potential shift to increasingly negative values with increasing [*p*-cyanoanilinium tetrafluoroborate] (Figure 97). In addition to the cathodic wave at –0.9 V, a pre-wave is observed at ca –0.6 V. This pre-wave or "adsorption wave" is postulated to be the result of protonation of the nitrogen of the imino thiol, and may also include hydrogenation of the bond

[179-180].[179-180].[179-180]. This can be inferred from the initial increase in the current of the pre-wave with the [*p*-cyanoanilinium tetrafluoroborate], however, the peak current quickly plateau at a ratio of ca 1:4, [Co(III) complex]/[proton source], suggesting a slow reaction compared to proton transfer from the *p*-cyanoanilinium tetrafluoroborate in the electrocatalytic process. This 4-H process as suggested by the saturation ratio at –0.6 V would be consistent with the 3H proton coupled reduction required to convert the -C=N- to -H_2CNH- followed by protonation to $H_2CNH_2^+$.

This protonated complex may also present (a minor) alternative pathway to the formation of hydrogen from the Co^{III}-H via intra-molecular electron. The peak current observed at –0.9 V did not display any apparent saturation within the concentration range explored, and on the return scan, no stripping wave was observed, suggesting cobalt was not deposited at the electrode, to facilitate heterogeneous catalysis. Nevertheless, such a possibility cannot be excluded without further analysis of the electrode following electro-catalytic experiments [180].Nevertheless, such a possibility cannot be excluded without further analysis of the electrode following electro-catalytic experiments [180].Nevertheless, such a possibility cannot be excluded without further analysis of the electrode following electro-catalytic experiments [180]. The production of hydrogen was confirmed from the analysis of the head space of a controlled potential electrolysis experiment involving the complex in the presence of *p*-cyanoanilinium tetrafluoroborate. In light of nature of the voltammograms, a mechanism involving the Co(I) species produced upon electro-reduction is proposed (Scheme 12) and also suggest overpotentials for the HER of 730 and 630 mV for complex **3** and **4**, respectively. The magnitude of the Gibbs free energy for the homolytic and heterolytic H_2 evolution from *p*-cyanoanilinium tetrafluoroborate (HA) in CH_3CN can be determined using the methodology suggested by Kellett and Spiro [181], on the basis of the values for the potentials of the cobalt and HA/H_2 couples versus the $Fc^{+/0}$ couple [18]The magnitude of the Gibbs free energy for the homolytic and heterolytic H_2 evolution from *p*-cyanoanilinium tetrafluoroborate (HA) in CH_3CN can be determined using the methodology suggested by Kellett and Spiro [181], on the basis of the values for the potentials of the cobalt and HA/H_2 couples versus the $Fc^{+/0}$ couple [18]The magnitude of the Gibbs free energy for the homolytic and heterolytic H_2 evolution from *p*-cyanoanilinium tetrafluoroborate (HA) in CH_3CN can be determined using the methodology

suggested by Kellett and Spiro [181], on the basis of the values for the potentials of the cobalt and HA/H_2 couples versus the $Fc^{+/0}$ couple [18]. The heterolytic pathways are calculated at –83 and –86 kJ mol^{-1}, and the homolytic pathways at –120 and –123 kJ mol^{-1} for complexes **3** and **4**, respectively. From the analyses, it is evident that the thermodynamics of the hydrogen evolution tends to favour the homolytic pathway by about 40 kJ mol^{-1}. This preference for the homolytic pathway is consistent with the deduction made for some cobaloximes [18, 182]. This preference for the homolytic pathway is consistent with the deduction made for some cobaloximes [18, 182]. This preference for the homolytic pathway is consistent with the deduction made for some cobaloximes [18, 182].

$$[Co^{3+}(N\text{-}N)_2(L)] + H^+ \leftrightarrow [Co^{3+}(N\text{-}N)_2(L\text{-}H^+)] \quad \text{protonation}$$

$$\left.\begin{array}{l}[Co^{3+}(N\text{-}N)_2(L\text{-}H^+)] + e^- \leftrightarrow [Co^{2+}(N\text{-}N)_2(L\text{-}H^+)] \\ [Co^{2+}(N\text{-}N)_2(L\text{-}H^+)] + e^- \leftrightarrow [Co^{+}(N\text{-}N)_2(L\text{-}H^+)]\end{array}\right\} \text{electon transfer}$$

$$[Co^{+}(N\text{-}N)_2(L\text{-}H^+)] + H^+ \leftrightarrow [Co^{III}\text{-}H(N\text{-}N)_2(L\text{-}H^+)]$$

$$[Co^{III}\text{-}H(N\text{-}N)_2(L\text{-}H^+)] \rightarrow [Co^{3+}(N\text{-}N)_2(L)] + H_2 \quad (k_1, \text{intra-molecular})$$

$$2[Co^{III}\text{-}H(N\text{-}N)_2(L\text{-}H^+)] \rightarrow 2[Co^{II}(N\text{-}N)_2(L\text{-}H^+)] + H_2 \quad (k_2, \text{homolytic})$$

$$[Co^{III}\text{-}H(N\text{-}N)_2(L\text{-}H^+)] + H^+ \rightarrow [Co^{3+}(N\text{-}N)_2(L\text{-}H^+)] + H_2 \quad (k_3, \text{heterolytic})$$

Scheme 12. Mechanism for protonation, electron transfer, and hydrogen evolution.

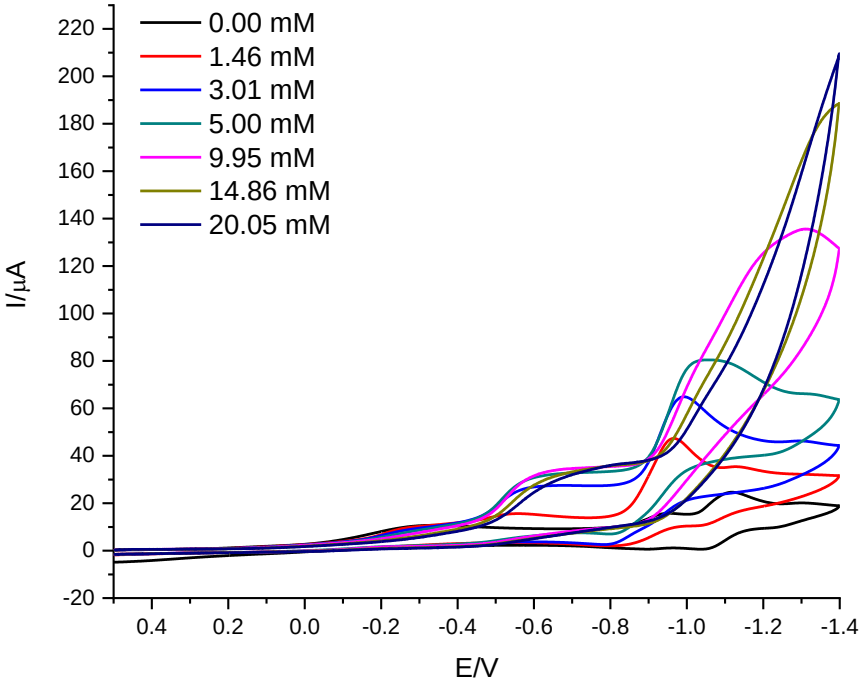
0.00 mM
1.46 mM
3.01 mM
5.00 mM
9.95 mM
14.86 mM
20.05 mM
I/μA
E/V

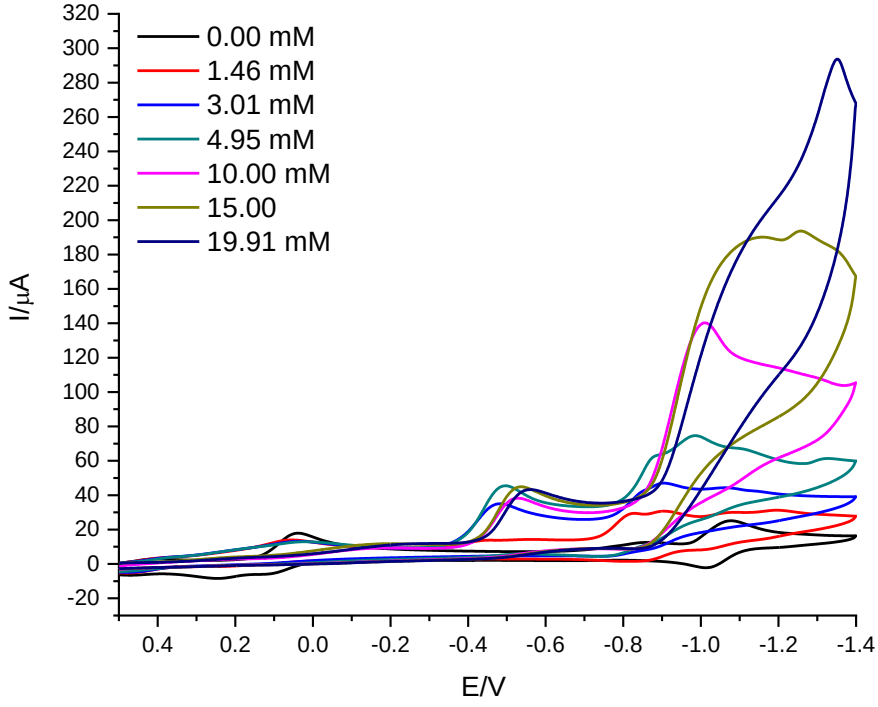
0.00 mM
1.46 mM
3.01 mM
4.95 mM
10.00 mM
15.00
19.91 mM
I/μA
E/V

Figure 97 Cyclic voltammograms of complexes **3** (top) and **4** (bottom) in CH_3CN with increasing [*p*-cyanoanilinium tetrafluoroborate]. [complex] = 1.1 mM, supporting electrolyte = 0.1 M tetrabutylammonium perchlorate ($[^nBu_4N]ClO_4$). Scan rate = 100 mV s^{-1}.

4.4 Photocatalytic hydrogen production

The photosensitizer (PS) $[Ru(bpy)_3](PF_6)_2$ [183-187] was chosen to photo-reduce the Co HER catalysts.[183-187] was chosen to photo-reduce the Co HER catalysts.[183-187] was chosen to photo-reduce the Co HER catalysts. Complex **3**, complex **4**, and the reference catalyst $[Co(dmgH)_2(Py)Cl]$ were tested under the same photoreaction conditions (Figure 98). The samples were irradiated with blue LEDs centered at 445 nm, in dimethylformamide as solvent, 1 M of triethanolamine as the sacrificial electron donor and 0.1 M aqueous tetrafluoroboric acid as the proton source, 0.1 mM of $[Ru(bpy)_3](PF_6)_2$, and the respective cobalt catalysts at 0.01 mM. The $[Ru(bpy)_3](PF_6)_2$ is fully excited into the ^{1}MLCT band to drive the photo-reactions. The excess of PS permits the evaluation of the maximum TON of HER cobalt-containing catalyst. No hydrogen is detected for the control experiments of the PS in the presence of sacrificial electron donor and HBF_4. A peak of activity occurred for all the systems when the light is turned on. The cobaloxime reaches a rate of 4500 $mmolH_2.mol^{-1}{}_{CAT}.min^{-1}$, complex **3** and complex **4** attain 2700 $mmolH_2.mol^{-1}{}_{CAT}.min^{-1}$ and 2600 $mmolH_2.mol^{-1}{}_{CAT}.min^{-1}$, respectively. The 2,2'-bipyridine and 1,10-phenanthroline systems react more slowly than the cobaloxime standard and their lower activity is aligned with the loss of ligand on going from Co(III) to Co(I) (d^6 to d^8, respectively) whereas the dmg in the cobaloxime complex are stable anionic ligands. The activities of all the systems decrease slowly to end after almost three hours, with the 1,10-phenanthroline system decreasing more slowly than the 2,2'-bipyridine system. We observed a TON of 140 for the cobaloxime, and 140 for complex **4** and 91 for complex **3** over a 2.5 h period. Aliquots of fresh photosensitizer and catalyst were added at the end of the photoreactions. For the three catalysts, the activity starts again with addition of photosensitizer and no revival is observed in the case of catalyst addition indicating that the photosensitizer decomposes first.

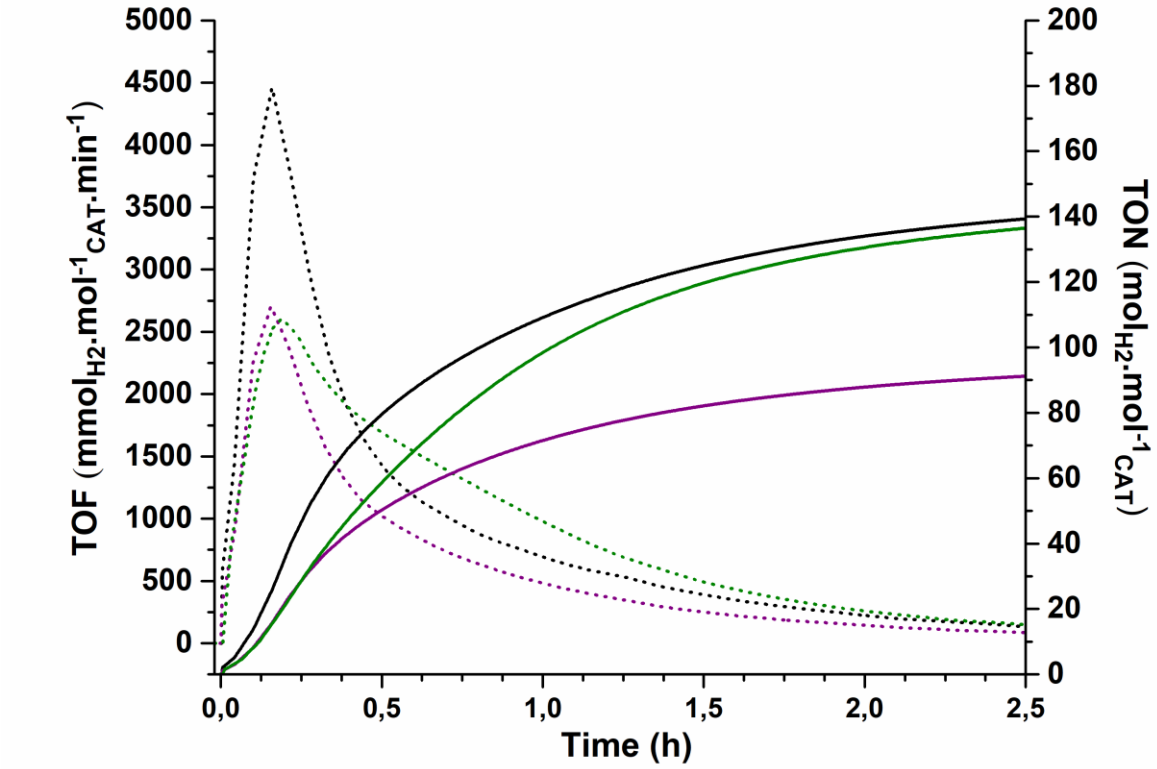

Figure 98. Hydrogen evolution with [Co(dmgH)$_2$(py)Cl] (black), complex **3** (purple), and complex **4** (green). TOF: dotted line. TON: solid line.

4.5 Conclusions

Two new Co(III) complexes (complexes **3** and **4**) bearing a *N*-substituted 2-pyridinecarbothioamide (PCA-(CF$_3$)$_2$) and either bpy or phen ligands were synthesized, and isolated in high purity. Both complexes demonstrated reversible metal-based redox processes in CH$_3$CN, and yielded a Co$^{II/I}$ redox couple more positive than the polypyridyl analogues [Co(N-N)$_2$Cl$_2$)]PF$_6$ or [Co(N-N)$_3$](PF$_6$)$_3$ (where (N-N) = bpy or phen). Both complexes showed electrocatalytic hydrogen evolution at moderate overpotential in the presence of the acid source, *p*-cyanoanilinium tetrafluoroborate in CH$_3$CN, and photocatalytic hydrogen evolution in the

presence of $[Ru(bpy)_3](PF_6)_2$ as a photosensitizer and triethanolamine as a sacrificial reductant in DMF.

Chapter 5. Synthesis and characterization of $[Co(tpy)(phen)Cl](PF_6)_3$ for H_2 production

5.0 Materials and physical measurements

5.0.1 Materials

All chemicals and reagents were purchased from commercial sources and were used without further purification.

5.0.2 Physical measurements

^{59}Co NMR spectra were acquired on a Bruker 400 MHz spectrometer with $K_3[Co(CN)_6]$ as an external reference in either DMSO-d_6 (δ = 289 ppm[188]) or CH_3CN-d_3 (δ = 293 ppm [188]) at room temperature.^{59}Co NMR spectra were acquired on a Bruker 400 MHz spectrometer with $K_3[Co(CN)_6]$ as an external reference in either DMSO-d_6 (δ = 289 ppm[188]) or CH_3CN-d_3 (δ = 293 ppm [188]) at room temperature.^{59}Co NMR spectra were acquired on a Bruker 400 MHz spectrometer with $K_3[Co(CN)_6]$ as an external reference in either DMSO-d_6 (δ = 289 ppm[188]) or CH_3CN-d_3 (δ = 293 ppm [188]) at room temperature. ^{1}H NMR spectra were acquired on a Bruker AVANCE III 400 MHz spectrometer with DMSO-d_6 as solvent. All NMR spectra were processed with the ACD/NMR Processor Academic Edition software which was available from Advanced Chemistry Development (ACD, Inc., 8 King Street East, Suite 107, Toronto, Ontario M5C 1B5, Canada).

Microanalyses (C, H, and N) were performed by Intertek Chemical and Pharmaceuticals, 291 Route 22 East, Salem Industrial Park, Building #5, Whitehouse, NJ 08888, U.S.A.

HRMS spectra were acquired via positive electrospray ionization on a Bruker 12 Tesla APEX –Qe FTICR-MS with an Apollo II ion source at the College of Sciences Major Instrument Cluster (COSMIC), Old Dominion University, 143 Oceanography & Physical Sciences Building Norfolk, VA 23529, U.S.A. Samples were dissolved in acetonitrile before being introduced by direct injection using a syringe pump with a flow rate of 2 $\mu l\ s^{-1}$. The data was processed using Bruker Daltonics Data Analysis Version 3.4.

All electrochemical experiments were performed on a BAS Epsilon C3 under an argon atmosphere in CH_3CN at room temperature (ca 20 ^oC). A standard three electrode configuration was employed consisting of a glassy carbon working electrode (3 mm diameter) and a Pt wire as auxiliary electrode. For the reference electrode, AgCl/Ag (BASi, 3.0 M NaCl) was employed,

which was separated from the analytical solution by a Vicor® frit, against which ferrocene shows a reversible wave at +0.43 V. The ionic strength was maintained at 0.1 M using [^{n}Bu$_4$N]ClO$_4$.

Spectroelectrochemical measurements were regulated at 20 ^{o}C with a thermostatic water bath/circulator (Thermo Scientific®). Absorbance measurements were performed on an Agilent® 8453A diode array spectrophotometer. A Pt gauze and Pt wire were employed as working and auxiliary electrodes, respectively, and AgCl/Ag (BASi, 3.0 M NaCl) reference electrode. The ionic strength was maintained at 0.10 M as stated above. Each solution was purged with Ar for at least two minutes in the spectroelectrochemical cuvette (1 mm path length) prior to the measurement.

5.1 Synthesis and physical measurements of the cobalt(III) complex

5.1.1 Synthesis of [Co(tpy)(phen)Cl](PF$_6$)$_2$•0.25CH$_3$CN 7

2,2':6',2"-Terpyridine (0.98 g, 4.2 mmol), 1,10-phenanthroline (0.76 g, 4.2 mmol), and CoCl$_2$•6H$_2$O (1.00 g, 4.2 mmol) were stirred in ethanol (320 ml) for 3 hours. Iodine (1.31 g, 5.2 mmol) in ethanol (60 ml) was added dropwise to the stirring solution. The filtrate was collected and NH$_4$PF$_6$ (6.86 g, 42 mmol) in methanol (60 ml) was added. The resulting precipitate was then filtered and the residue air dried. The crude product was then dissolved in acetonitrile and filtered before it was purified three times by chromatography on a Sephadex LH-20 stationary phase with acetonitrile as eluent. Yield = 1.17 g (34%); calculated for $C_{27.5}H_{19.75}N_{5.25}ClP_2F_{12}$: C 40.88, H 2.46, N 9.10, Cl 4.39%. Found C 40.85, H 2.51, N 9.17, Cl 4.21%. HRMS (positive mode, found (calc.): M-1PF$_6^-$ = 652.0247 (652.0247). ^{1}H NMR (400 MHz, CD$_3$CN, δ/ppm) 10.21 (d, J = 5.06 Hz, 1 H, phen-j'), 9.30 (d, J = 8.14 Hz, 1 H, phen-h'), 8.89 (d, J = 6.82 Hz, 1 H, tpy-h), 8.80 - 8.86 (m, 2 H, tpy-g), 8.67 (d, J = 8.14 Hz, 1 H, phen-a'), 8.61 (dd, J = 7.92, 5.94 Hz, 1 H, phen-i'), 8.48 - 8.57 (m, 3 H, tpy-a and phen-e'), 8.29 (d, J = 9.02 Hz, 1 H, phen-f'), 8.18 (t, J = 7.59 Hz, 2 H, tpy-b), 7.64 (dd, J = 7.59, 5.83 Hz, 1 H, phen-b'), 7.43 (d, J = 4.84 Hz, 1 H, phen -c'), 7.33 (t, J = 6.38 Hz, 2 H, tpy-c), 7.18 (d, J = 5.50 Hz, 2 H, tpy-d). ^{1}H NMR (400 MHz, DMSO-d_6, δ/ppm) 10.12 (d, *J* = 5.06 Hz) 9.51 (d, *J* = 8.14 Hz) 9.38 (d, *J* = 7.92 Hz) 9.23 (m) 9.10 (m) 8.93 (m) 8.86 (d, *J* = 7.92 Hz) 8.75 (dd, *J* = 8.14, 5.50 Hz) 8.66 (d, *J* = 8.80 Hz) 8.43 (d, *J* = 8.80 Hz) 8.34 (q, *J* = 7.92 Hz) 7.72 (m) 7.46 (m) 7.35 (d, *J* = 5.50 Hz); ^{59}Co NMR (95 MHz, CD$_3$CN, δ/ppm) 7148;

^{59}Co NMR (95 MHz, DMSO-d_6, δ/ppm) 7177; UV-visible (CH_3CN, λ/nm (10^{-4} ε/M^{-1} cm^{-1})): 203 (78), 222 (75), 275 (39), 322 (12), and 487 (0.27).

5.1.2 X-ray crystallography

Single crystal X-ray diffraction was carried out at 150 K using a Bruker D8 Quest diffractometer with Mo Kα radiation and a Photon 100 detector. Data were collected using phi and omega scans in 0.5 degree oscillations. The structure was solved and refined using the Bruker SHELXTL[189] Software Package.The structure was solved and refined using the Bruker SHELXTL[189] Software Package.The structure was solved and refined using the Bruker SHELXTL[189] Software Package. All non-hydrogen atoms were refined anisotropically, and hydrogen atoms were placed in calculated positions using riding models. The crystal was found to be the acetonitrile solvate of the target cobalt complex. The acetonitrile solvent molecule was found to be disordered and partially occupied, having 1/2 occupancy per formula unit of the cobalt(III) complex. Details of data collection and structural solution for $[Co(tpy)(phen)Cl](PF_6)_2 \bullet 0.5C_2H_3N$ are provided in the supporting crystallographic files (CIF).

5.1.3 Photocatalytic measurements

Hydrogen evolution was monitored using a Perkin Elmer Clarus-580 gas chromatograph (GC) with a thermal conductivity detector, argon as carrier and eluent gas, a 7' HayeSep N 60/80 pre-column, a 9' molecular sieve 13 x 45/60 column and a 1 mL injection loop.

Three distinct solutions for photosensitizer $[Ru(bpy)_3](PF_6)_2$, for catalyst and last for sacrificial electron donor and acid source (HBF_4, 48% water) were prepared: the three solutions were mixed together to obtain 5 mL of sample solutions in standard 20 mL headspace vials. In DMF, the resulting molar concentrations of photocatalytic components were as follows: 1 M for triethanolamine (TEOA), 0.1 M for (HBF_4), 0.56 M for water, 0.1 mM for $[Ru(bpy)_3](PF_6)_2$, 0.01 mM for complex **1** or $[Co(dmgH)_2Cl(py)]$ (apparent pH = 8.9). Those vials were placed on a LED panel in a thermostatic bath set at 20 °C. They were sealed with a rubber septum pierced with two stainless steel tubes. The first tube carried an argon flow pre-bubbled in spectroscopic grade solvent. The flow rate was set to 5 mL min^{-1} (adjusted with a manual flow controller (Porter, 1000) and referenced with a digital flowmeter (Perkin Elmer FlowMark).

The second tube leads the flow to the GC sample loop through a 2 mL overflow protection vial, then through an 8-port stream select valve (VICCI) and finally to the GC sample loop. A microprocessor (Arduino Uno) coupled with a custom PC interface allows for timed injections. For general calibration, stock cylinders of known concentration of H_2 in nitrogen replaced the nitrogen flow (inserted at the pre-bubbler, to keep the vapor matrix consistent). The measured results, independent of flow rate (under same pressure) can be easily converted into a rate of hydrogen following equation 1. For calibration of H_2 production, a nitrogen bottle of certified 100 ppm hydrogen was set to deliver a specific flow. H_2 production rate at a specific nitrogen flow, a syringe pump (New Era Pump) equipped with a gas-tight syringe (SGE) and a 26s gauge needle (Hamilton) was used to bubble different rates of pure hydrogen gas into the sample, to a minimum of 0.5 μL min^{-1}. This gave a linear fit for peak area for H_2 versus the flow rates of H_2 (Eq. 1). All experiments were carried out in duplicate to verify the reproducibility of results, and an average for the TOF and TON curves was calculated with Origin software. The error associated with the TOF and TON values is estimated to be 10%.[186]The error associated with the TOF and TON values is estimated to be 10%.[186]The error associated with the TOF and TON values is estimated to be 10%.[186]

$$H_2 \text{ rate } (\mu L\ min^{-1}) = [H_2 \text{ standard}]\ (ppm) \times N_2 \text{ flow rate } (L\ min^{-1}) \quad 1$$

CCDC no. 1953060 contains the supplementary crystallographic data for $[Co(tpy)(phen)Cl](PF_6)_2 \bullet 0.5C_2H_3N$. These data can be obtained free of charge from The Cambridge Crystallographic Data Center via www.ccdc.cam.ac.uk/data_request/cif. Supporting information containing additional spectral and voltammetric characterizations are also provided.

5.2 Results and discussion

5.2.1 Synthesis

Complex **7** was synthesized (Scheme 13) using stoichiometric quantities in one pot, and was purified three times on a Sephadex LH-20 column to separate the main by-products $[Co(tpy)_2](PF_6)_3$ and $[Co(phen)_2(solv)](PF_6)_3$ from **7**. Complex **7** was characterized by elemental analysis, HRMS, UV-visible, ^1H and ^{59}Co NMR spectroscopies, X-ray crystallography, and cyclic voltammetry.

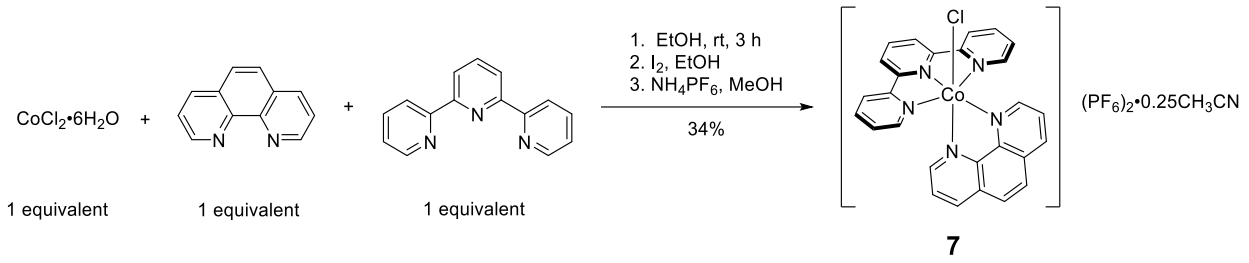

7

Scheme 13. Synthesis of complex **7**.

5.2.2 HRMS analysis

HRMS data were acquired for **7** in CH_3CN (Figure 99). In the HRMS, the most intense peak is observed at m/z = 652.0247, which corresponded to the loss of one of the PF_6^- counter ions to produce ({[Co^{III}(tpy)(phen)Cl](PF_6)}$^+$). The HRMS data do complement the elemental analysis and the other spectroscopic characterizations.

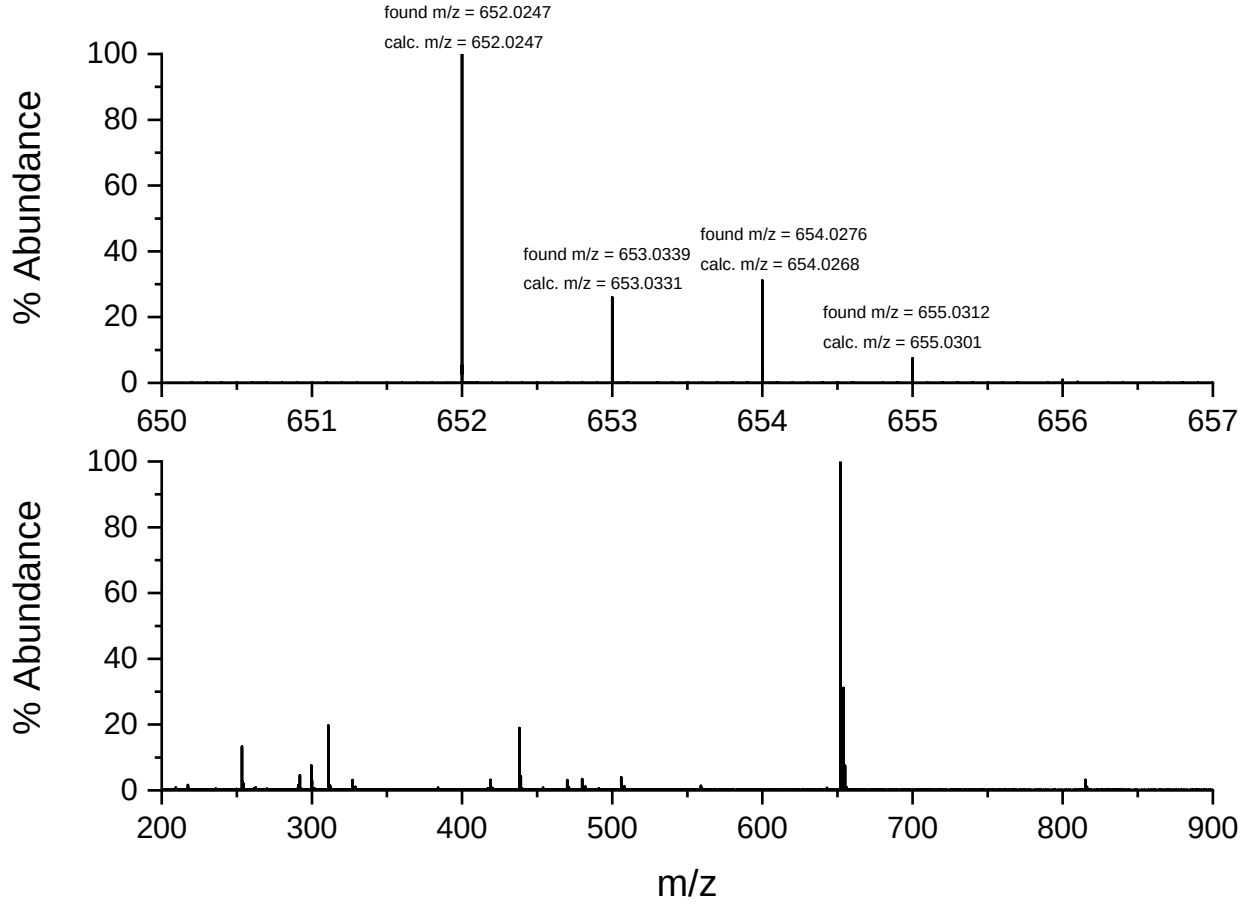

Figure 99. HRMS of complex **7** in CH_3CN

5.2.3 ^{1}H and ^{59}Co NMR spectroscopic studies

In an NMR spectroscopic study, ^{1}H and ^{59}Co NMR spectra were acquired for complex **7** in CD_3CN or DMSO-d_6 at ambient temperature. The ^{1}H NMR spectrum acquired in either DMSO-d_6 or CD_3CN (Figure 100), revealed solvent peaks and aryl resonances.

In the solvent region, the presence of acetonitrile in the isolated product was confirmed (δ = 2.07 ppm in DMSO-d_6). In the aromatic region of the ^{1}H NMR spectrum, there is a significant overlap of the resonances of the tpy and phen ligands. The assignment of these peaks was guided by ^{1}H-^{1}H the COSY NMR spectrum (Figure 101); and coordinated tpy protons are assigned to resonances at 7.18, 7.33, 8.18, 8.54, 8.83, and 8.89 ppm. Paramagnetic ^{1}H NMR spectra of polypyridyl cobalt(II) complexes are observed to have chemical shifts between 10 to 120 ppm,[190] however paramagnetic ^{1}H NMR measurements on **7** suggested the absence of analogous cobalt(II) species in the isolated solid (see Figure S4). Paramagnetic ^{1}H NMR spectra of polypyridyl cobalt(II) complexes are observed to have chemical shifts between 10 to 120 ppm,[190] however paramagnetic ^{1}H NMR measurements on **7** suggested the absence of analogous cobalt(II) species in the isolated solid (see Figure 102)

^{59}Co NMR spectroscopic measurements (Figure 100), revealed one chemical shift at 7148 ppm in CH_3CN-d_3 and at 7177 ppm in DMSO-d_6. A comparison with other Co(III) complexes such as $[Co(phen)_3](PF_6)_3$ (δ = 7000 ppm in DMSO-d_6,[191] 7080 ppm[192]) or $[Co(phen)_2(bpy)](PF_6)_3 \cdot 0.5(C_2H_5)_2O$ (δ = -6900 ppm in DMSO-d_6)[191] revealed that the chemical shift of **7** is in a similar region to other cobalt(III)-containing polypyridyl complexes. The ^{59}Co NMR spectroscopic chemical shift of cobalt-containing complexes is very sensitive to the type(s) of ligand in the coordination sphere, as well as the oxidation state of a cobalt metal center. The ^{59}Co NMR spectroscopic data (in conjunction with the ESI-MS data) strongly suggest that cobalt(II) impurities and by-products are absent from the isolated product, complex **7**.^{59}Co NMR spectroscopic measurements (Figure 100), revealed one chemical shift at 7148 ppm in CH_3CN-d_3 and at 7177 ppm in DMSO-d_6. A comparison with other Co(III) complexes such as $[Co(phen)_3](PF_6)_3$ (δ = 7000 ppm in DMSO-d_6,[191] 7080 ppm[192]) or

$[Co(phen)_2(bpy)](PF_6)_3 \cdot 0.5(C_2H_5)_2O$ (δ = -6900 ppm in DMSO-d_6)[191] revealed that the chemical shift of **7** is in a similar region to other cobalt(III)-containing polypyridyl complexes. The ^{59}Co NMR spectroscopic chemical shift of cobalt-containing complexes is very sensitive to the type(s) of ligand in the coordination sphere, as well as the oxidation state of a cobalt metal center. The ^{59}Co NMR spectroscopic data (in conjunction with the ESIMS data) strongly suggest that cobalt(II) impurities and by-products are absent from the isolated product, complex **7**.^{59}Co NMR spectroscopic measurements (Figure 2), revealed one chemical shift at 7148 ppm in CH_3CN-d_3 and at 7177 ppm in DMSO-d_6. A comparison with other Co(III) complexes such as $[Co(phen)_3](PF_6)_3$ (δ = 7000 ppm in DMSO-d_6,[191] 7080 ppm[192]) or $[Co(phen)_2(bpy)](PF_6)_3 \cdot 0.5(C_2H_5)_2O$ (δ = -6900 ppm in DMSO-d_6)[191] revealed that the chemical shift of **7** is in a similar region to other cobalt(III)-containing polypyridyl complexes. The ^{59}Co NMR spectroscopic chemical shift of cobalt-containing complexes is very sensitive to the type(s) of ligand in the coordination sphere, as well as the oxidation state of a cobalt metal center. The ^{59}Co NMR spectroscopic data (in conjunction with the ESI-MS data) strongly suggest that cobalt(II) impurities and by-products are absent from the isolated product, complex **7**.

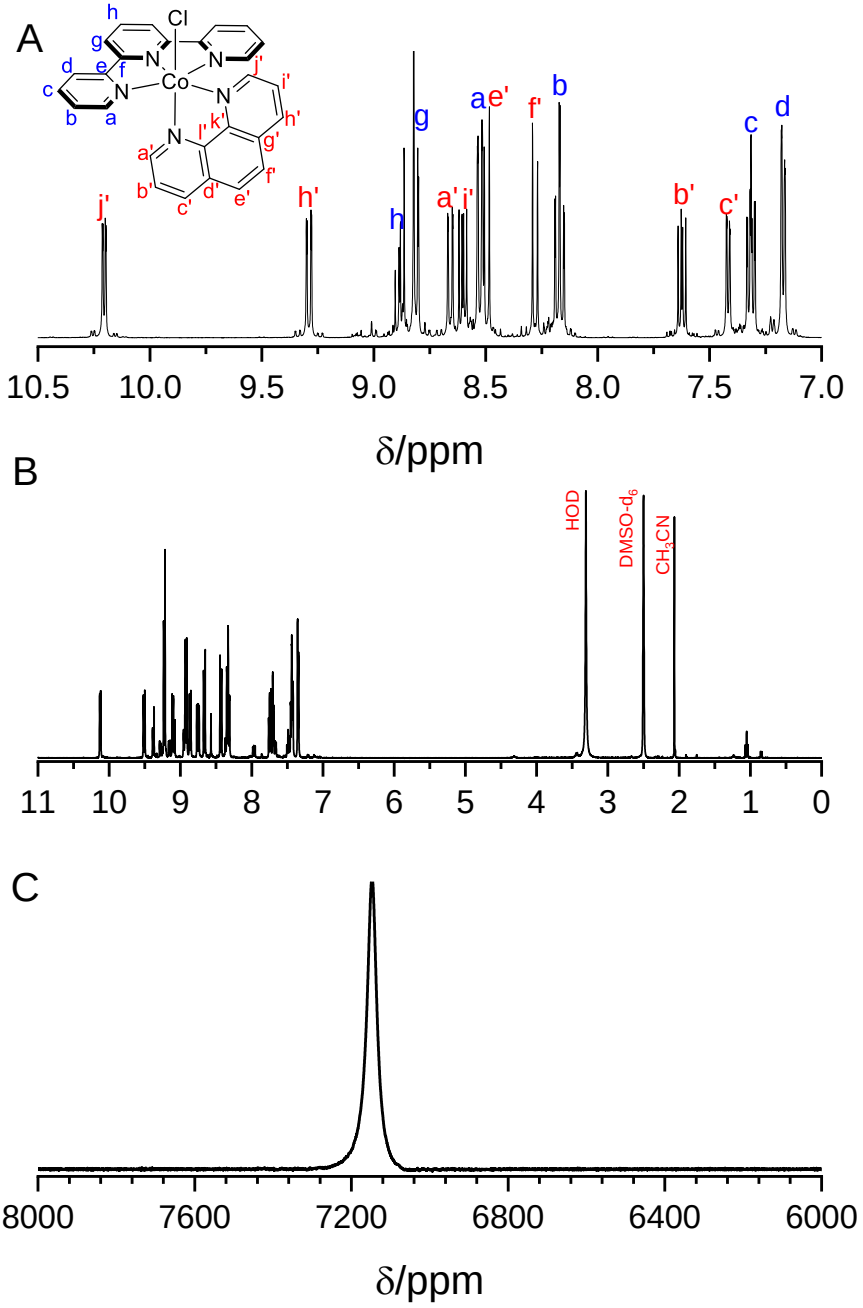

Figure 100. ^{1}H NMR spectra of complex **7** in CD_3CN (A) and DMSO-d_6 (B), and ^{59}Co NMR spectrum of 40 mM complex **7** in CD_3CN (C).

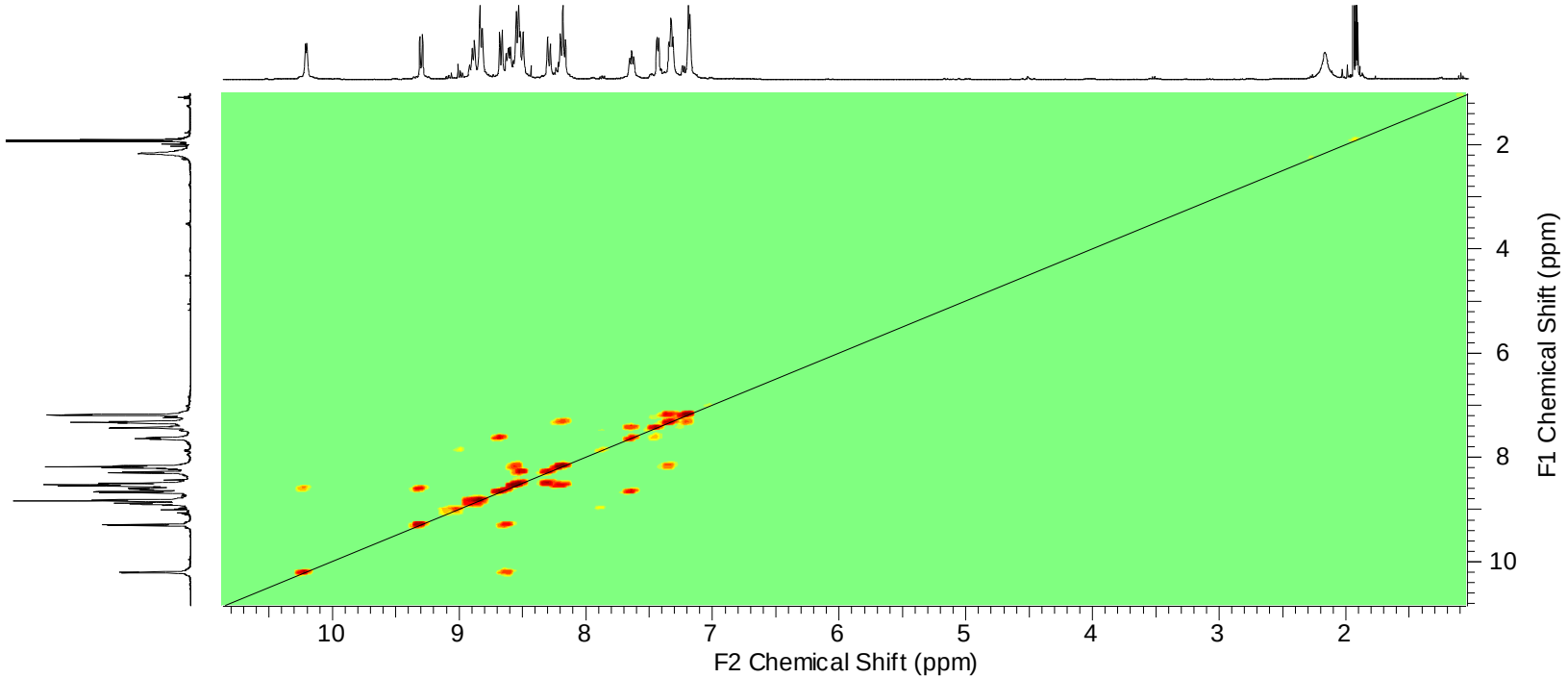

Figure 101. ^{1}H-^{1}H COSY NMR spectrum of complex **7** in CD_3CN.

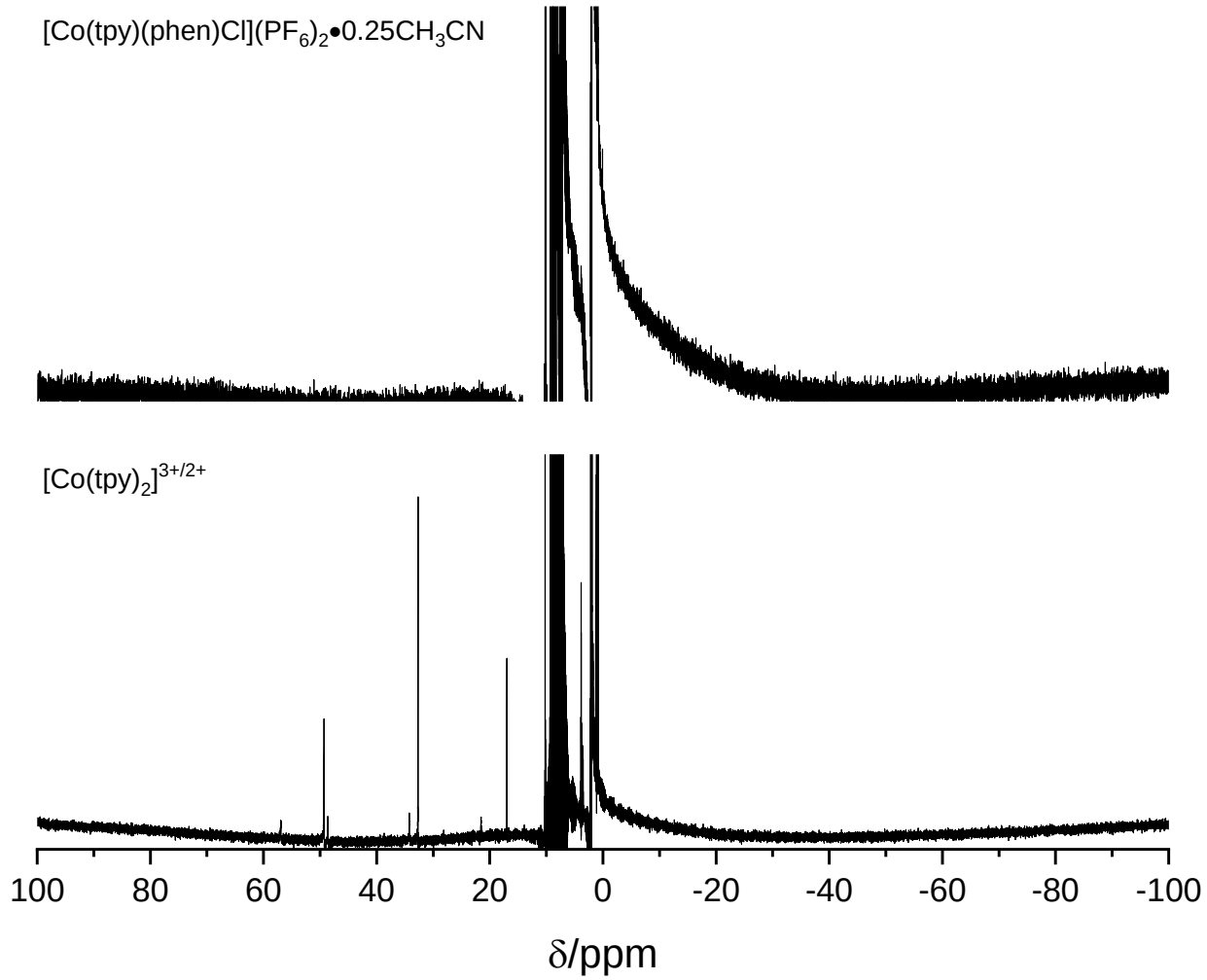

Figure 102. ^{1}H NMR spectra of $[Co(tpy)_2](PF_6)_{2/3}$ and $[Co(tpy)(phen)Cl](PF_6)_2 \bullet 0.25CH_3CN$ in CD_3CN.

5.2.4 UV-visible spectroscopic studies

The UV-visible spectra of complex **7** in acetonitrile which are shown in Figure 103 show transitions that are consistent with d-d transitions (dual bands) at 487 nm, $\pi \rightarrow \pi^*$, intra-ligand, and metal-to-ligand charge transfer bands in the UV region. The molar extinction coefficients are 78 $\times 10^4$, 75 $\times 10^4$, 29 $\times 10^4$, 13 $\times 10^4$, and 0.27 $\times 10^4$ M^{-1} cm^{-1} at 203, 222, 275, 322, and 487 nm, respectively. In H_2O/CH_3CN (1:1 v/v) a dual band at 487 nm in CH_3CN is observed at λ_{max} = 460 nm and 491 nm.

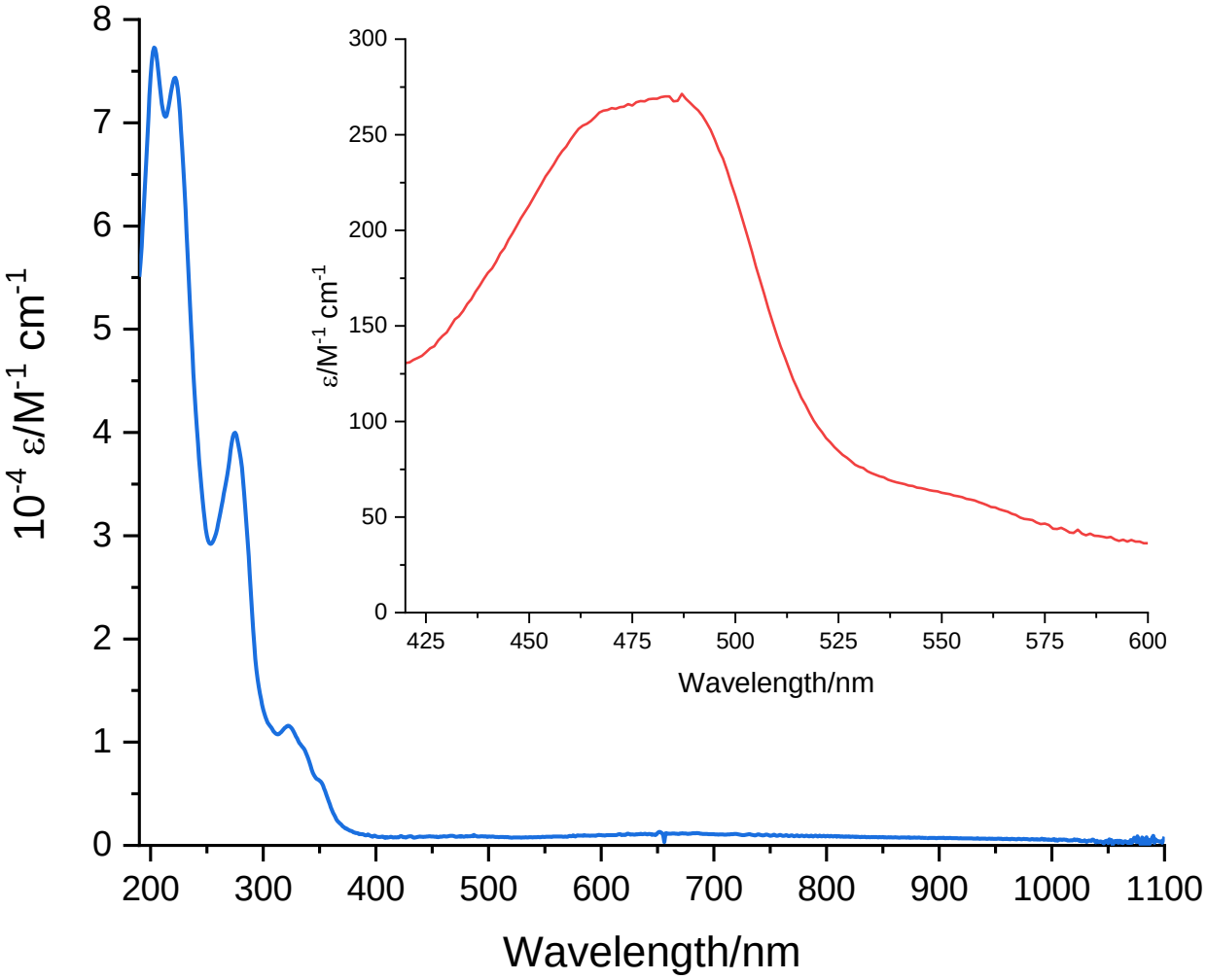

Figure 103. UV-visible spectra of complex **7** in acetonitrile.

5.2.5 **X-ray** crystallography

A single crystal of complex **7** was grown as an acetonitrile solvate by slow evaporation at first in acetonitrile solution; followed by the addition of acetone. The X-ray crystal structure for the dication of **7** is shown in Figure 104, with selected structure refinement parameters given in Table 20.

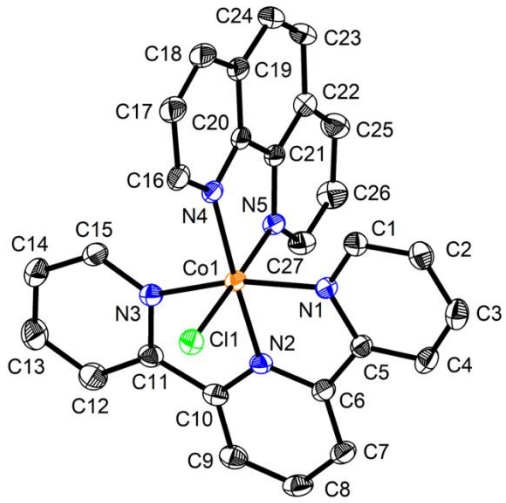

Figure 104. Structure for the *mer*-$[Co(tpy)(phen)Cl]^{2+}$ complex as shown at 50% probability ellipsoids.

Selected bond lengths and angles are shown in Table 21. The structural analysis revealed a distorted octahedral arrangement about to the cobalt(III) metal center. The tpy ligand is coordinated in a tridentate fashion and is meridionally arranged about the cobalt(III) core with resulting tpy and phen ligands lying in perpendicular coordination planes to each other, with the chloride ligand completing the octahedron. This coordination behaviour, bond lengths, and angles observed here are similar to the analogous $[Rh(tpy)(Z)Cl]^{2+}$ (where Z = bpy or phen) species.[193] In particular, the Co-N bond to the central nitrogen atom of the tpy ligand is the shortest of tpy, and all the tpy Co-N bonds are marginally shorter than those to phen ligand, which is consistent with what is observed in the Rh(III) complex. This coordination behaviour, bond lengths, and angles observed here are similar to the analogous $[Rh(tpy)(Z)Cl]^{2+}$ (where Z = bpy or phen) species.[193] In particular, the Co-N bond to the central nitrogen atom of the tpy ligand is the shortest of tpy, and all the tpy Co-N bonds are marginally shorter than those to phen ligand, which is consistent with what is observed in the Rh(III) complex. This coordination behaviour, bond lengths, and angles observed here are similar to the analogous $[Rh(tpy)(Z)Cl]^{2+}$ (where Z = bpy or phen) species.[193] In particular, the Co-N bond to the central nitrogen atom of the tpy ligand is the shortest of tpy, and all the tpy Co-N bonds are marginally shorter than those to phen ligand, which is consistent with

what is observed in the Rh(III) complex. The N5-Co1-Cl1 bond angle is almost 180°, the bond length is normal for Co–Cl bonds.[194] The charge of the complex is counterbalanced by two PF_6^- anions. In the extended structure, these anions, along with acetonitrile solvent molecules, occupy voids between complex **7**.[194] The charge of the complex is counterbalanced by two PF_6^- anions.[194] The charge of the complex is counterbalanced by two PF_6^- anions. In the extended structure, these anions, along with acetonitrile solvent molecules, occupy voids between complex **7**.

Table 20. Crystal data and structure refinement for $[Co(tpy)(phen)Cl](PF_6)_2 \bullet 0.5CH_3CN$.

Identification code	$[Co(tpy)(phen)Cl](PF_6)_2$
Chemical formula	$C_{27}H_{19}ClCoF_{12}N_5P_2 \bullet 0.5C_2H_3N$
Formula weight (g/mol)	818.32
Crystal system, space group	monoclinic, C2/c
Unit cell dimensions (Å, °)	a = 30.0763(13)
	b = 14.5703(6)
	c = 14.9762(6)
	β = 114.3491(13)
Volume ($Å^3$)	5979.1(4)
Z, Calculated density (g cm^{-3})	8, 1.818
Reflections collected/unique	41055/6133
Data/restraints/parameters	6133/0/461
Final R indices [4838 data; I>2σ(I)]	0.0348, 0.0722
R indices (all data)	0.0531, 0.0796
Largest diff. peak and hole	0.362, -0.421
CCDC no.	1953060

Table 21. Selected bond lengths and angles for $[Co(tpy)(phen)Cl](PF_6)_2 \bullet 0.5CH_3CN$.

Bond	Length (Å)	Bond	Length (Å)
Co1-N1	1.945(2)	Co1-N4	1.948(2)
Co1-N2	1.853(2)	Co1-N5	1.953(2)
Co1-N3	1.935(2)	Co1-Cl1	2.2241(8)
Bonds	Bond angle	Bonds	Bond angle
N2–Co1–N1	82.91(9)	N5–Co1–N4	85.04(9)
N2–Co1–N3	83.06(9)	N5–Co1–Cl1	177.80(7)
N1–Co1–N3	165.97(9)	N4–Co1–Cl1	93.86(7)
N2–Co1–N4	177.07(9)	N5–Co1–N3	91.11(9)
N2–Co1–Cl1	88.59(7)	N5–Co1–N1	90.00(9)
N2–Co1–N5	93.49(9)	N3–Co1–N4	98.54(9)
N1–Co1–N4	95.49(9)	N3–Co1–Cl1	89.86(7)
N1–Co1–Cl1	89.54(7)		

5.2.6 Electrochemical studies

The complex, [Co(tpy)(phen)Cl]Cl, as reported by Chen *et al.*[195] showed remarkable activity in HER, especially when grafted (via electrochemical polymerization) on a Cu_2O surface. In their work, the $Co^{IV/III}$ and $Co^{III/II}$ couples showed reversible characteristics, however, the $Co^{II/I}$ redox couple showed little reversibility in acetonitrile. It was intriguing that system was an efficient HER catalyst despite the apparent irreversibility of the $Co^{II/I}$ redox couple. It is therefore of interest to investigate the cyclic voltammetric characteristics of this species, bearing in mind the widely accepted view that a stable Co(I) species capable of undergoing reversible electron transfer is ideal for HER in cobalt-containing systems.

Cyclic and square wave voltammograms of complex **7** in aqueous mixed solvents, and non-aqueous media revealed a series of (quasi-)reversible waves with i_{pa}/i_{pc} = >0.9 (Table 22). The peak potentials are scan rate dependent and showed negligible potential drift with increasing scan rate, consistent with their reversible nature. The $Co^{III/II}$ redox couple is observed between +0.2 and

+0.4 V vs Ag/AgCl, whereas the $Co^{II/I}$ redox couple is observed between –0.8 to –0.9 V depending on the solvent and supporting electrolyte employed (see Figure 105). In aqueous media, cobalt(II)-containing halides are well known to undergo rapid aquation [196], which can only be retarded by the presence of high halide concentration. In water, NaCl supporting electrolyte did not appear to improve the voltammetric reversibility of the electron transfers, and indeed a Co(I) species appears to be more unstable with NaCl compared to $NaClO_4$, resulting in a stripping wave on the return scan, due to the deposition of cobalt metal at the electrode surface (see Figure 106). However, in the H_2O/CH_3CN (1:1, v/v) mixed solvent, improved voltammograms were obtained (see supporting information), and no stripping wave was observed. In the mixed solvent containing NaCl supporting electrolyte, the ΔE_p decreased to 80 mV which is closer to the 57 mV value expected for a one-electron Nernstian process, and was lower than that obtained with the $NaClO_4$ supporting electrolyte.

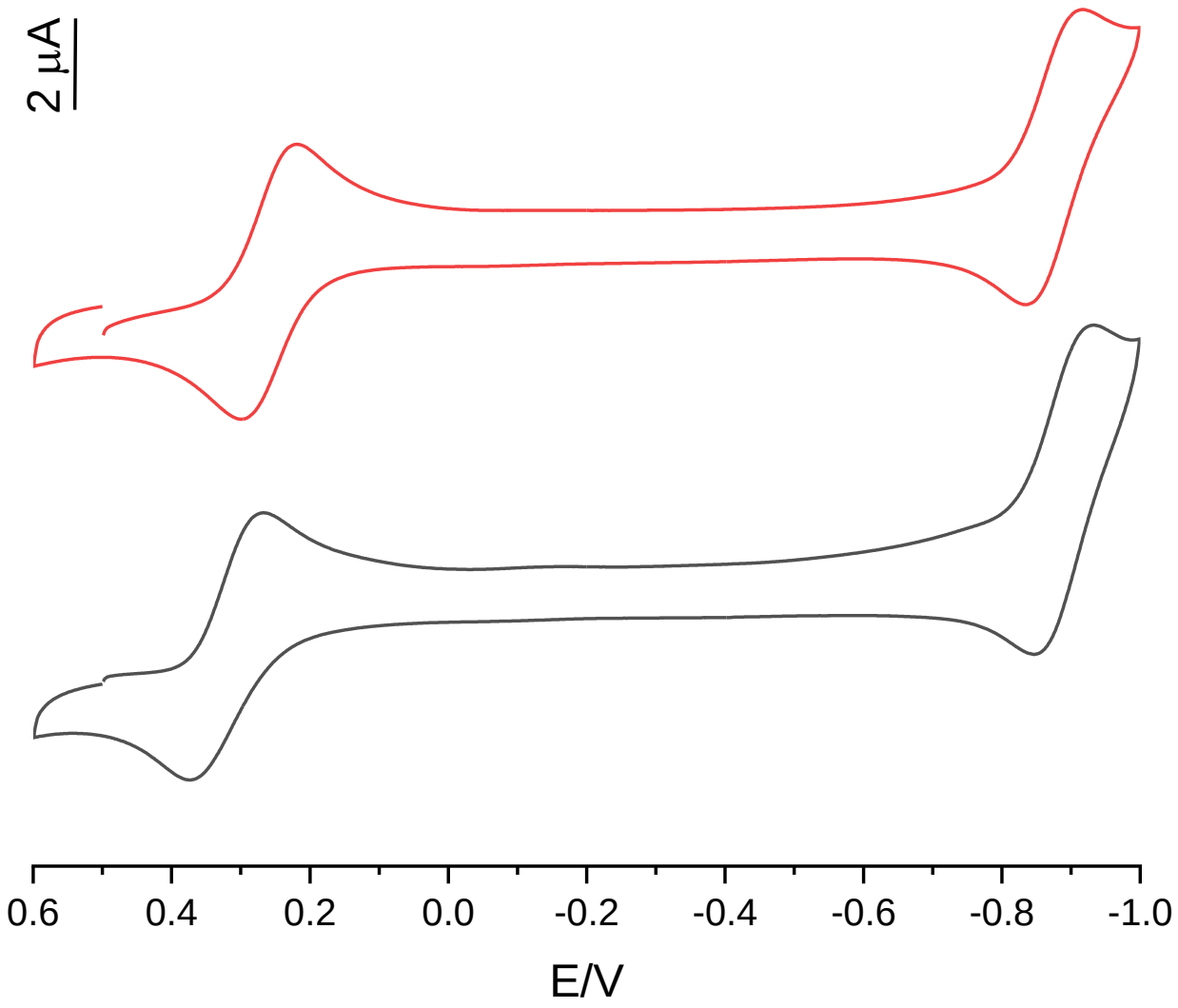

Figure 105**.** Cyclic voltammograms of $[Co(tpy)(phen)Cl]Cl_2$. Solvent = acetonitrile:water (1:1, v/v), [complex] = 1.0 mM, supporting electrolyte = 0.1 M ($NaClO_4$ (**black**) or NaCl (**red**)), working electrode = Pt, auxiliary electrode = Pt wire, reference electrode = Ag/AgCl, and scan rate = 100 mV s^{-1}.

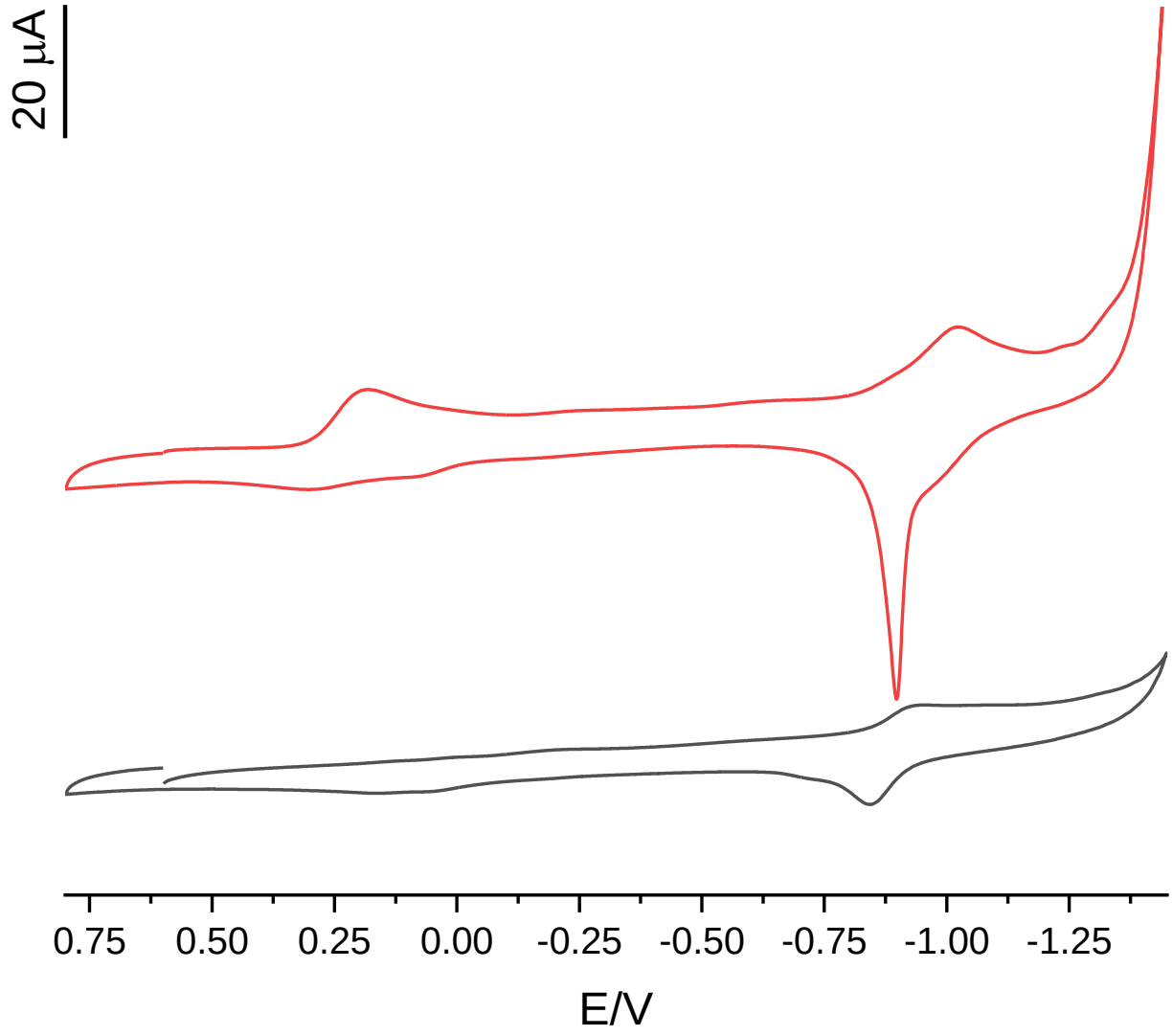

Figure 106**.** Cyclic voltammograms of [Co(tpy)(phen)Cl]Cl_2. Solvent = water, [complex] = 1.0 mM, supporting electrolyte = 0.1 M ($NaClO_4$ (**black**) or NaCl (**red**)), working electrode = Pt, auxiliary electrode = Pt wire, reference electrode = Ag/AgCl, and scan rate = 100 mV s^{-1}.

Table 22. Comparison of the reduction potentials of complex **7** in H_2O and CH_3CN with various supporting electrolytes.

Redox couple	$E_{½}$/V	ΔE_p/mV	solvent	Electrolyte
$Co^{III/II}$	+0.22	320	H_2O	$NaClO_4$
	+0.23	--	H_2O	NaCl
	+0.32	109	H_2O/CH_3CN	$NaClO_4$
	+0.26	80	H_2O/CH_3CN	NaCl
	+0.35	92	CH_3CN	$[^nBu_4N]ClO_4$
$Co^{II/I}$	-0.90	100	H_2O	$NaClO_4$
	-1.00	--	H_2O	NaCl
	-0.89	87	H_2O/CH_3CN	$NaClO_4$
	-0.88	83	H_2O/CH_3CN	NaCl
	-0.81	110	CH_3CN	$[^nBu_4N]ClO_4$

In CH_3CN, (Figure 107 and Figure 125), the voltammograms revealed reversible $Co^{III/II}$ and $Co^{II/I}$ redox couples which are slightly sensitive to the working electrode (by ca 60 mV between the GC and Pt electrodes), and are observed at $E_{½}$ = +0.35 and –0.81 V vs Ag/AgCl, respectively, on a GC working electrode (WE). However, on reductively initiated scans on using Pt WE, a pre-wave is observed before the $Co^{II/I}$ redox couple. This pre-wave is present, albeit somewhat suppressed, on the GC WE and may be related to the enhanced lability of the chloride ligand in the +2 oxidation state, which causes a subtle modification of the layer at the electrode surface. A third reversible wave at $E_{½}$ = –1.37 V is most likely attributed to a one electron redox couple for one of the polypyridyl ligands. On the return scan upon switching the potential at –2 V, the oxidation waves are slightly distorted and are likely related to the partial dissociation of the polypyridyl ligand(s) in the highly reduced state [191]. Additionally, as electrons are injected into the system, ΔE_p increased, indicating a drift from Nernstian behaviour. Nevertheless, the $Co^{II/I}$ redox couple showed reversible characteristics in all but the H_2O/NaCl combination.

The overall nature of the voltammogram in CH_3CN suggests that, on the electrochemical time scale, species with all three oxidation states of the cobalt metal center, viz., +3, +2, and +1,

are fairly stable in nature, where complex **7** may potentially be utilised as an electron shuttle in a reaction such as the hydrogen evolution reaction [195] amongst others. A plausible electron transfer mechanism is shown in Scheme 14.

$$[Co(tpy)(phen)Cl]^{2+} + e^- \leftrightarrow [Co(tpy)(phen)Cl]^+$$
$$[Co(tpy)(phen)Cl]^+ + e^- \leftrightarrow [Co(tpy)(phen)]^+ + Cl^-$$
$$[Co(tpy)(phen)]^+ + e^- \leftrightarrow [Co(tpy)(phen)]^0$$

Scheme 14. A plausible redox behaviour of complex **7** in CH_3CN

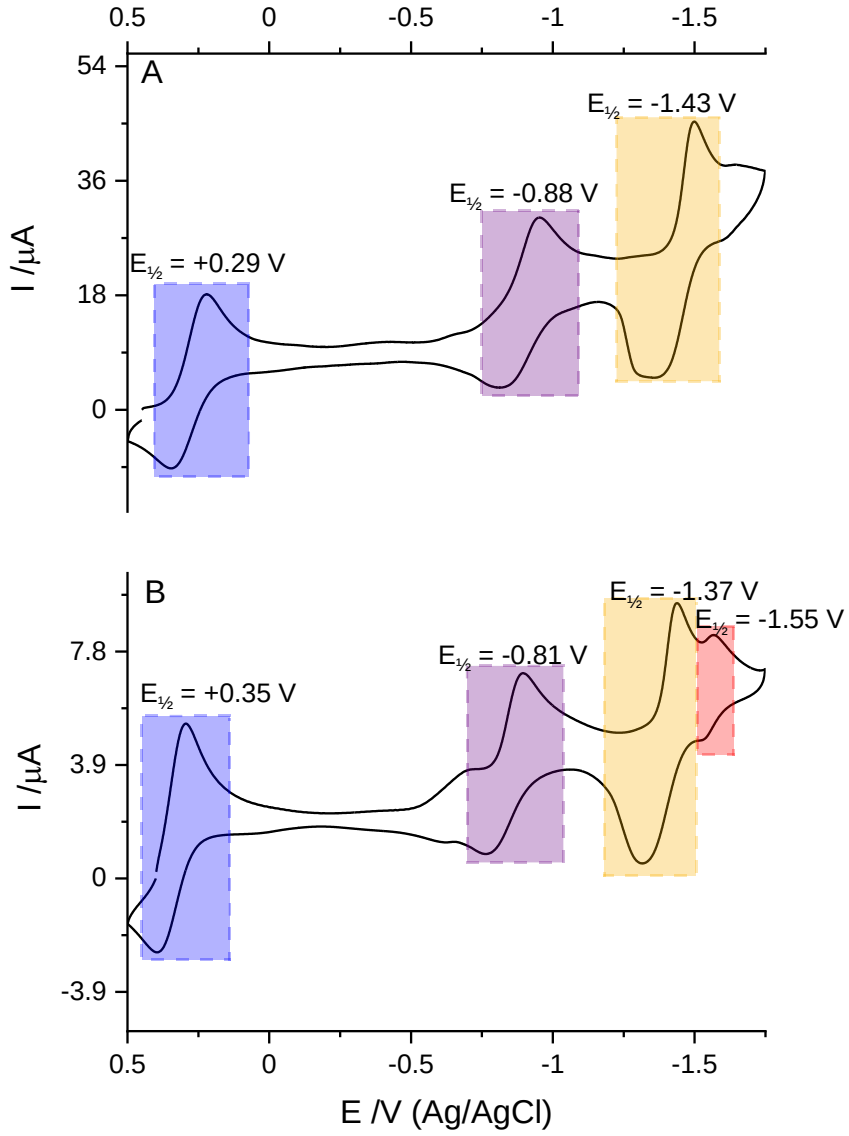

Figure 107. Cyclic voltammogram of complex **7**. Solvent = acetonitrile, [complex] = 1.0 mM, [$^{n}Bu_4N$]ClO_4 = 0.10 M, working electrode = (**A**) glassy carbon or (**B**) Pt, auxiliary electrode = Pt wire, reference electrode = Ag/AgCl, and scan rate = 100 mV s^{-1}.

A series of spectroelectrochemical measurements were made on CH_3CN and H_2O/CH_3CN (1:1 v/v) mixed solvent solutions of complex **1** (Figure 108, Figure 126 and Figure 127). In the H_2O/CH_3CN (1:1 v/v) mixed solvent, Figure S13, the $Co^{3+}\rightarrow Co^{2+}$ reduction resulted in a rapid increase in the absorbance at 460 nm along with a blue shift to 450 nm. This is succeeded by a gradual decrease in the absorbance across the spectrum. In the electrolysis of the solution at a potential sufficient to overcome the overpotential for the $Co^{2+}\rightarrow Co^{+}$ reduction, a similar pattern

is observed at 460 nm, albeit a smaller change in the absorbance. A similar electrolysis in CH_3CN caused the peak that is observed circa 480 nm to first have a blue shift to circa 450 nm, followed by a decrease in the absorbance at this wavelength.

In addition to the blue shift in the d-d transitions, there is an increase in the absorbance across the UV region, suggestive of an increase in the charge transfer characteristics of the system associated with a Co(I) formation. The complex nature of the spectral transformation clearly indicates that the electrolysis did not have a simple A → B transformation. Here again, the exclusion of the chloride ligand from the coordination sphere maybe the cause of the biphasic nature of the spectral transformation. Electrolysis at –1.52 V (vs Ag/AgCl), also presented a biphasic spectrum, in which there is an initial rapid increase in the absorbance which is followed by decay towards a limiting value that is greater than the value prior to the electrolysis experiment. The transformation at this potential did not appear to share the blue shift observed at the more positive potential, and indeed is suggestive that the reduction involves the polypyridyl ligand(s).

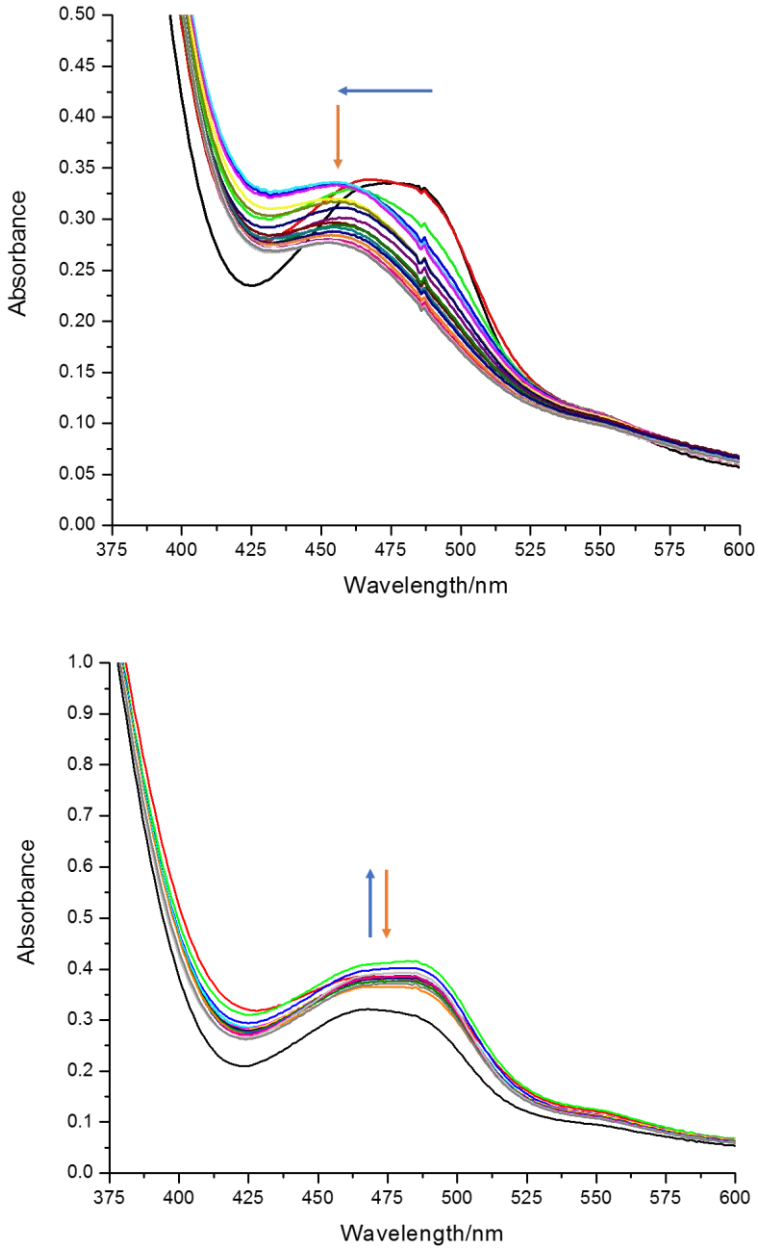

Figure 108. Spectroelectrochemical transformations of complex **7**. Solvent = acetonitrile; [complex] = 14.9 mM, $[^{n}Bu_4N]ClO_4$ = 0.10 M, working electrode = Pt mesh wire, auxiliary electrode = Pt wire, reference electrode = Ag/AgCl, held potential = –1.20 V (top) and –1.52 V (bottom), and path length = 1 mm.

5.2.7 Electrocatalytic studies

The effect of a proton source (*p*-cyanoanilinium tetrafluoroborate) on the voltammograms of complex **7** in CH_3CN was investigated, Figure 109. In the presence of *p*-cyanoanilinium

tetrafluoroborate, a new cathodic wave is observed at ca –0.65 V of which the peak current increases with a simultaneous peak potential shift to increasingly negative values with increasing [*p*-cyanoanilinium tetrafluoroborate]. The electrocatalytic wave was observed to occur ca 300 mV more positive than the $Co^{II/I}$ reduction wave, and displayed what is considered a "normal" catalysis,[197-199] owing the lack of any apparent pre-wave or unexpected diffusional peaks. The production of hydrogen was confirmed from the analysis of the head space of a controlled potential electrolysis experiment involving the complex in the presence of *p*-cyanoanilinium tetrafluoroborate. In CH_3CN, the overpotential[†] associated with the catalyzed proton reduction was determined to be 830 mV. The magnitude of the Gibbs free energy for the homolytic and heterolytic hydrogen evolution from *p*-cyanoanilinium tetrafluoroborate in CH_3CN can be determined using the methodology suggested by Kellett and Spiro [181] on the basis of the values for the potentials of the cobalt and HA/H_2 couples versus $Fc^{+/0}$. The magnitude of the Gibbs free energy for the homolytic and heterolytic hydrogen evolution from *p*-cyanoanilinium tetrafluoroborate in CH_3CN can be determined using the methodology suggested by Kellett and Spiro [181] on the basis of the values for the potentials of the cobalt and HA/H_2 couples versus $Fc^{+/0}$. The magnitude of the Gibbs free energy for the homolytic and heterolytic hydrogen evolution from *p*-cyanoanilinium tetrafluoroborate in CH_3CN can be determined using the methodology suggested by Kellett and Spiro [181] on the basis of the values for the potentials of the cobalt and HA/H_2 couples versus $Fc^{+/0}$. From the thermodynamic analysis of the heterolytic and the homolytic pathways, the free energies of $\Delta G = –15.4$ and –56.9 kJ mol^{-1}, respectively, which suggests that the homolytic pathway is favored thermodynamically.

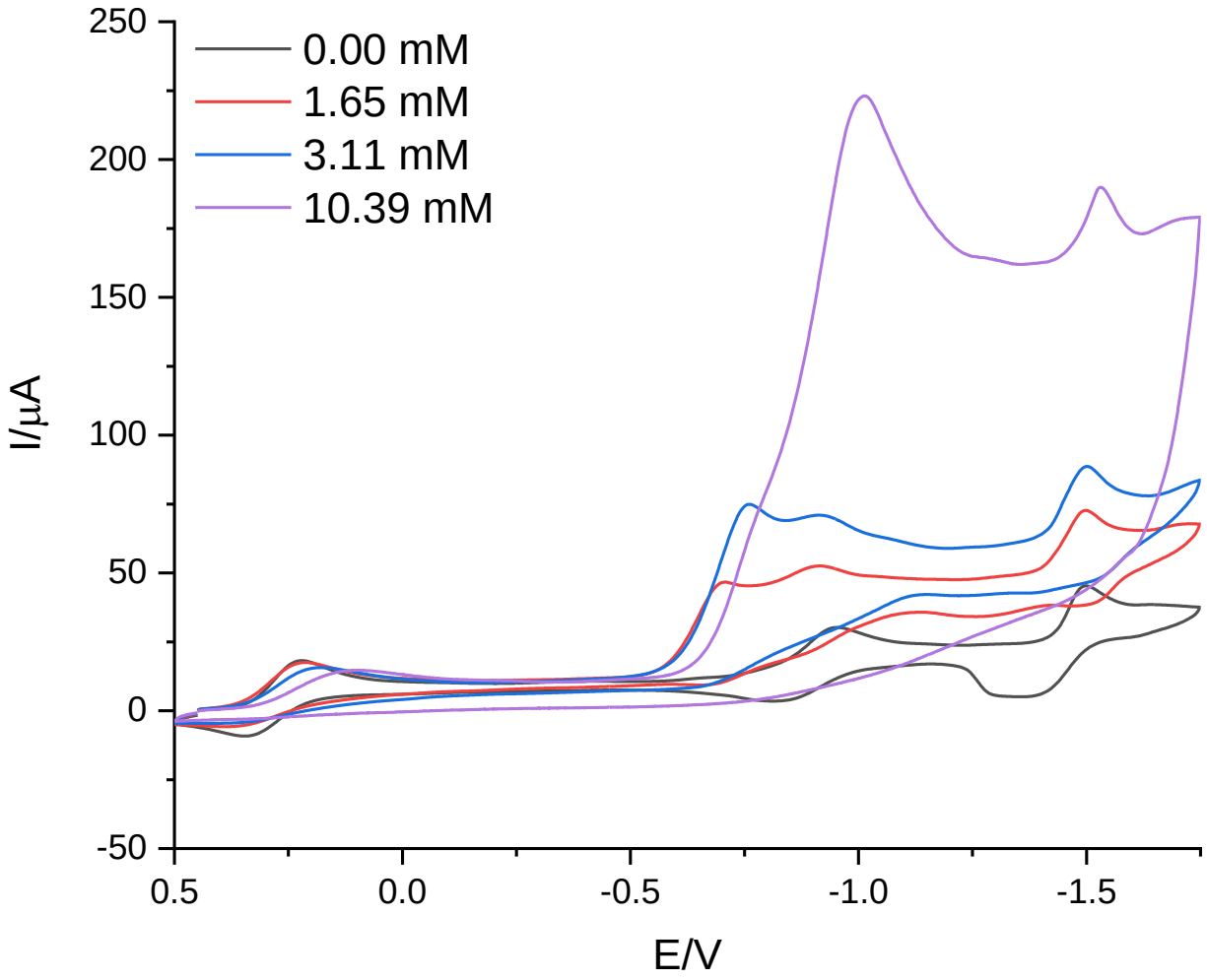

Figure 109. Cyclic voltammograms illustrating the electrocatalytic behaviour of complex **7**. Solvent = acetonitrile; [complex] = 1.0 mM, [$^{n}Bu_4N]ClO_4$ = 0.10 M, [*p*-cyanoanilinium tetrafluoroborate] = varied (from 0.0 mM to 10 mM), working electrode = glassy carbon, auxiliary electrode = Pt wire, reference electrode = Ag/AgCl, and scan rate = 100 mV s^{-1}.

5.2.8 Photocatalytic studies

Based on the electrochemical and spectroscopic results discussed above, the light driven hydrogen evolution reactions (HERs) for complex **7** and the reference cobaloxime $[Co(dmgH)_2Cl(py)]$ were investigated, as polypyridyl and macrocyclic design for cobalt HER catalysts shows promising performances.[186-187, 200-204] The weak molar absorptivity of complex **7** in the visible portion of the spectrum suggests that the complex is unlikely to be an intrinsic photosensitizer, and thus requires external activation. The most studied inorganic photosensitizer

(PS), $[Ru(bpy)_3](PF_6)_2$[183-187] was chosen to photo-reduce the Co HER catalysts.[183-187] was chosen to photo-reduce the Co HER catalysts.[183-187] was chosen to photo-reduce the Co HER catalysts. The samples were irradiated with blue LEDs centered at 445 nm, in dimethylformamide as solvent, 1 M of triethanolamine as the sacrificial electron donor and 0.1 M aqueous tetrafluoroboric acid as the proton source, 0.1 mM of $[Ru(bpy)_3](PF_6)_2$, and the cobalt-containing catalysts at 0.01 mM. The $[Ru(bpy)_3](PF_6)_2$ is fully excited into the ^{1}MLCT band to drive the photoreactions. The excess of PS permits the evaluation of the maximum TON of HER cobalt-containing catalyst. No hydrogen was detected for the control experiments of the PS in the presence of sacrificial electron donor and HBF_4. When the illumination begins, a peak of activity occurred for both systems after a short lag time due to the required reduction of a Co(III) metal center to a Co(I) metal center.[186]When the illumination begins, a peak of activity occurred for both systems after a short lag time due to the required reduction of a Co(III) metal center to a Co(I) metal center.[186] When the illumination begins, a peak of activity occurred for both systems after a short lag time due to the required reduction of a Co(III) metal center to a Co(I) metal center.[186] The cobaloxime reaches a maximum turn over number (TON) of 4500 $mmolH_2\,mol^{-1}{}_{CAT}\,min^{-1}$ and complex **7** attains 3300 $mmolH_2\,mol^{-1}{}_{CAT}\,min^{-1}$ (Figure 110). The activities decrease slowly to end after almost three hours. We observed a TON of 79 for complex **7** and TON of 141 for the cobaloxime in ca 3 h of illumination. Aliquots of fresh photosensitizer and catalyst are added at the end of the photoreactions. For both catalysts, the activity starts again with addition of photosensitizer and no revival is observed in the case of catalyst addition indicating that the photosensitizer decomposes first.

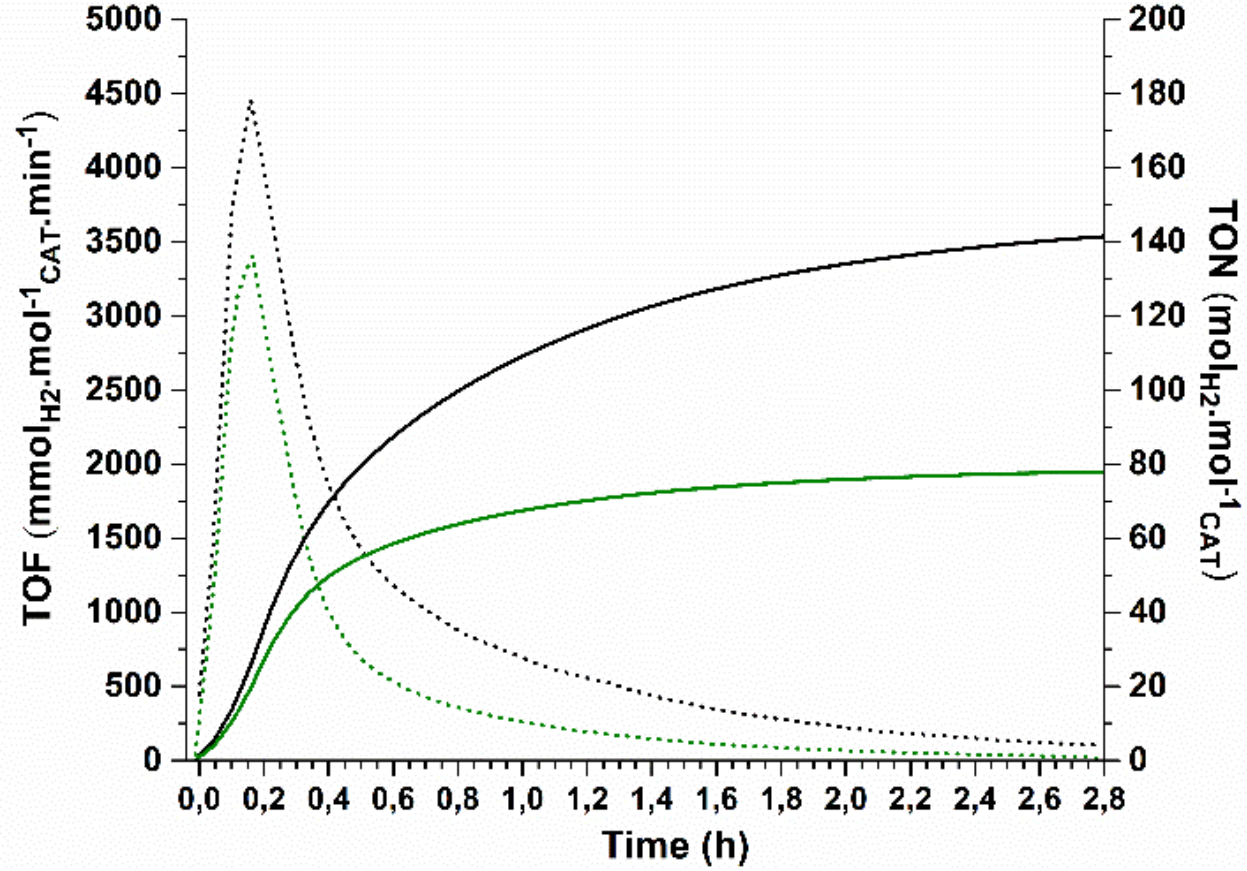

Figure 110. Hydrogen evolution of [Co(dmgH)$_2$Cl(py)] (black) and complex **7** (green). TOF: dotted line. TON: solid line.

5.2.9 Conclusions

The X-ray crystallographic structure of complex **7** presented revealed that the complex was infact octahedral in geometry with the ligands being in the meridional configuration. The biggest downside in this study was the low yield from the one pot synthesis. However, under both electrocatalytic and photocatalytic conditions the complex was observed to be able to produce hydrogen. Complex **7** demonstrated excellent electrocatalytic hydrogen evolution at 830 mV overpotential in CH_3CN, as well as photocatalytic hydrogen evolution with a high turnover number and moderate turnover frequency in DMF over a 3 h period.

REFERENCES

1. Royer, D. L.; Berner, R. A.; Park, J. *Nature* **2007,** *446* (7135), 530-532.
2. Lewis, N. S.; Nocera, D. G. *Proc. Natl. Acad. Sci. U. S. A.* **2006,** *103* (43), 15729-15735.
3. Panwar, N. L.; Kaushik, S. C.; Kothari, S. *Renew. Sust. Energ. Rev.* **2011,** *15* (3), 1513-1524.
4. Ritchie, H.; Roser, M. Energy Production & Changing Energy Sources. https://ourworldindata.org/energy-production-and-changing-energy-sources (accessed November 30).
5. Sims, R. E. *Solar energy* **2004,** *76* (1-3), 9-17.
6. Keeling, C. D.; Piper, S. C.; Bacastow, R. B.; Wahlen, M.; Whorf, T. P.; Heimann, M.; Meijer, H. A., Atmospheric CO 2 and 13 CO 2 exchange with the terrestrial biosphere and oceans from 1978 to 2000: Observations and carbon cycle implications. In *A history of atmospheric CO2 and its effects on plants, animals, and ecosystems*, Springer: 2005; pp 83-113.
7. Macfarling Meure, C.; Etheridge, D.; Trudinger, C.; Steele, P.; Langenfelds, R.; Van Ommen, T.; Smith, A.; Elkins, J. *Geophysical Research Letters* **2006,** *33* (14).
8. Armaroli, N.; Balzani, V. *Angew. Chem. Int. Ed.* **2007,** *46* (1+2), 52-66.
9. Eisenberg, R.; Nocera, D. G. *Inorg. Chem.* **2005,** *44* (20), 6799-6801.
10. Hoffert, M. I.; Caldeira, K.; Jain, A. K.; Haites, E. F.; Harvey, L. D. D.; Potter, S. D.; Schlesinger, M. E.; Schneider, S. H.; Watts, R. G.; Wigley, T. M. L.; Wuebbles, D. J. *Nature* **1998,** *395* (6705), 881-884.
11. Gray, H. B. *Nature Chemistry* **2009,** *1* (2), 112.
12. Lubitz, W.; Tumas, W. *Chem. Rev.* **2007,** *107* (10), 3900-3903.
13. Service, R. F. *Science* **2005,** *309* (5734), 548-551.
14. Zee, D. Z.; Chantarojsiri, T.; Long, J. R.; Chang, C. J. *Acc. Chem. Res.* **2015,** *48* (7), 2027-2036.
15. Gordon, R. B.; Bertram, M.; Graedel, T. E. *Proc. Natl. Acad. Sci. U.S.A* **2006,** *103* (5), 1209-1214.
16. Gordon, R. B.; Bertram, M.; Graedel, T. E. *Proc. Natl. Acad. Sci. USA* **2006,** *103* (5), 1209-1214.
17. Esswein, A. J.; Nocera, D. G. *Chem. Rev.* **2007,** *107* (10), 4022-4047.
18. Dempsey, J. L.; Brunschwig, B. S.; Winkler, J. R.; Gray, H. B. *Acc. Chem. Res.* **2009,** *42* (12), 1995-2004.
19. Fihri, A.; Artero, V.; Razavet, M.; Baffert, C.; Leibl, W.; Fontecave, M. *Angew. Chem. Int. Ed.* **2008,** *47* (3), 564-567.
20. Fihri, A.; Artero, V.; Pereira, A.; Fontecave, M. *Dalton Trans.* **2008,** (41), 5567-5569.
21. Du, P.; Knowles, K.; Eisenberg, R. *J. Am. Chem. Soc.* **2008,** *130* (38), 12576-12577.
22. Goldsmith, J. I.; Hudson, W. R.; Lowry, M. S.; Anderson, T. H.; Bernhard, S. *J. Am. Chem. Soc.* **2005,** *127* (20), 7502-7510.
23. Li, X.; Wang, M.; Zhang, S.; Pan, J.; Na, Y.; Liu, J.; Aakermark, B.; Sun, L. *J. Phys. Chem. B* **2008,** *112* (27), 8198-8202.
24. Na, Y.; Pan, J.; Wang, M.; Sun, L. *Inorg. Chem.* **2007,** *46* (10), 3813-3815.

25. Na, Y.; Wang, M.; Pan, J.; Zhang, P.; Akermark, B.; Sun, L. *Inorg. Chem.* **2008,** *47* (7), 2805-2810.
26. Elvington, M.; Brown, J.; Arachchige, S. M.; Brewer, K. J. *J. Am. Chem. Soc.* **2007,** *129* (35), 10644-10645.
27. Kaeffer, N.; Chavarot-Kerlidou, M.; Artero, V. *Acc. Chem. Res.* **2015,** *48* (5), 1286-1295.
28. Zadvornyy, O.; Lucon, J.; Gerlach, R.; Zorin, N.; Douglas, T.; Elgren, T.; Peters, J. *J. Inorg. Biochem.* **2012,** *106* (1), 151-155.
29. Reisner, E.; Powell, D.; Cavazza, C.; Fontecilla-Camps, J.; Armstrong, F. *J. Am. Chem. Soc.* **2009,** *131* (51), 18457-18466.
30. Brown, G. M.; Brunschwig, B. S.; Creutz, C.; Endicott, J. F.; Sutin, N. *J. Am. Chem. Soc.* **1979,** *101* (5), 1298-300.
31. Fisher, J. R.; Cole-Hamilton, D. J. *J. Chem. Soc., Dalton Trans.* **1984,** (5), 809-813.
32. Hawecker, J.; Lehn, J. M.; Ziessel, R. *Nouveau J. Chimie* **1983,** *7* (5), 271-277.
33. Krishnan, C. V.; Brunschwig, B. S.; Creutz, C.; Sutin, N. *J. Am. Chem. Soc.* **1985,** *107* (7), 2005-15.
34. Krishnan, C. V.; Sutin, N. *J. Am. Chem. Soc.* **1981,** *103* (8), 2141-2.
35. Kuhn, A. T. *J. Power Sources* **1984,** *11* (1), 63-67.
36. Halka, M.; Nordstrom, B., *Transition Metals*. Facts on File: 2011.
37. Cotton, F. A.; Wilkinson, G.; Murillo, C. A.; Bochmann, M.; Grimes, R., *Advanced inorganic chemistry*. Wiley New York: 1999; Vol. 5.
38. Rayner-Canham, G.; Overton, T., *Descriptive inorganic chemistry*. Macmillan: 2003.
39. Nicholls, D., *The Chemistry of Iron, Cobalt and Nickel*. Pergamon Press: 1973.
40. Constable, E. C.; Housecroft, C. E. *Chem. Soc. Rev.* **2013,** *42* (4), 1429-1439.
41. Dereven'kov, I. A.; Salnikov, D. S.; Silaghi-Dumitrescu, R.; Makarov, S. V.; Koifman, O. I. *Coord. Chem. Rev.* **2016,** *309*, 68-83.
42. Mishra, A. K.; Mishra, L., *Ruthenium Chemistry*. Jenny Stanford Publishing: 2018.
43. Livingstone, S. E., *The Chemistry of Ruthenium, Rhodium, Palladium, Osmium, Iridium and Platinum: Pergamon Texts in Inorganic Chemistry, Volume 25*. Elsevier Science: 2017.
44. Seddon, E. A.; Seddon, K. R., *The Chemistry of Ruthenium*. Elsevier: 1984.
45. Sutin, N.; Creutz, C., Properties and Reactivities of the Luminescent Excited States of Polypyridine Complexes of Ruthenium(II) and Osmium(II). In *Inorganic and Organometallic Photochemistry*, AMERICAN CHEMICAL SOCIETY: 1978; Vol. 168, pp 1-27.
46. Fujita, I.; Kobayashi, H. *J. Chem. Phys.* **1970,** *52* (9), 4904-4905.
47. Lv, H.; Guo, W.; Wu, K.; Chen, Z.; Bacsa, J.; Musaev, D. G.; Geletii, Y. V.; Lauinger, S. M.; Lian, T.; Hill, C. L. *J. Am. Chem. Soc.* **2014,** *136* (40), 14015-14018.
48. Zheng, M.; Ding, Y.; Yu, L.; Du, X.; Zhao, Y. *Adv. Funct. Mater.* **2017,** *27* (11), n/a.
49. Lazarides, T.; McCormick, T.; Du, P.; Luo, G.; Lindley, B.; Eisenberg, R. *J. Am. Chem. Soc.* **2009,** *131* (26), 9192-9194.
50. Chen, L.; Wang, Z.; Kang, P. *Chin. J. Catal.* **2018,** *39* (3), 413-420.
51. Fihri, A.; Artero, V.; Pereira, A.; Fontecave, M. *Dalton Trans.* **2008,** (41), 5567-5569.
52. Lubitz, W.; Reijerse, E. J.; Messinger, J. *Energy Environ. Sci.* **2008,** *1* (1), 15-31.
53. Dempsey, J. L. Hydrogen evolution catalyzed by cobaloximes. 2011.

54. Kaerkaes, M. D.; Verho, O.; Johnston, E. V.; Aakermark, B. *Chem. Rev. (Washington, DC, U. S.)* **2014,** *114* (24), 11863-12001.
55. Nocera, D. G. *Acc. Chem. Res.* **2012,** *45* (5), 767-776.
56. Mase, K.; Yoneda, M.; Yamada, Y.; Fukuzumi, S. *ACS Energy Lett.* **2016,** *1* (5), 913-919.
57. Sherman, B. D.; Sheridan, M. V.; Wee, K.-R.; Marquard, S. L.; Wang, D.; Alibabaei, L.; Ashford, D. L.; Meyer, T. J. *J. Am. Chem. Soc.* **2016,** *138* (51), 16745-16753.
58. Miseki, Y.; Fujiyoshi, S.; Gunji, T.; Sayama, K. *The Journal of Physical Chemistry C* **2017,** *121* (18), 9691-9697.
59. Rodenberg, A.; Orazietti, M.; Probst, B.; Bachmann, C.; Alberto, R.; Baldridge, K. K.; Hamm, P. *Inorg. Chem.* **2015,** *54* (2), 646-657.
60. Fujishima, A.; Honda, K. *nature* **1972,** *238* (5358), 37-38.
61. Wang, M.; Shen, S.; Li, L.; Tang, Z.; Yang, J. *J. Mater. Sci.* **2017,** *52* (9), 5155-5164.
62. Troppmann, S.; Brandes, E.; Motschmann, H.; Li, F.; Wang, M.; Sun, L.; Koenig, B. *Eur. J. Inorg. Chem.* **2016,** *2016* (4), 554-560.
63. Hartley, C. L.; DiRisio, R. J.; Screen, M. E.; Mayer, K. J.; McNamara, W. R. *Inorg. Chem.* **2016,** *55* (17), 8865-8870.
64. Han, Z.; McNamara, W. R.; Eum, M.-S.; Holland, P. L.; Eisenberg, R. *Angew. Chem., Int. Ed.* **2012,** *51* (7), 1667-1670, S1667/1-S1667/14.
65. Zou, X.; Zhang, Y. *Chem. Soc. Rev.* **2015,** *44* (15), 5148-5180.
66. Ensafi, A. A.; Heydari-Soureshjani, E.; Rezaei, B. *Int. J. Hydrogen Energy* **2017,** *42* (8), 5026-5034.
67. Liu, X.; Li, Y.; Peng, S.; Lu, G.; Li, S. *Int. J. Hydrogen Energy* **2012,** *37* (17), 12150-12157.
68. Gueret, R.; Poulard, L.; Oshinowo, M.; Chauvin, J.; Dahmane, M.; Dupeyre, G.; Laine, P. P.; Fortage, J.; Collomb, M.-N. *ACS Catal.* **2018,** *8* (5), 3792-3802.
69. Losse, S.; Vos, J. G.; Rau, S. *Coord. Chem. Rev.* **2010,** *254* (21-22), 2492-2504.
70. Fisher, B. J.; Eisenberg, R. *J. Am. Chem. Soc.* **1980,** *102* (24), 7361-3.
71. Wang, M.; Na, Y.; Gorlov, M.; Sun, L. *Dalton Trans.* **2009,** (33), 6458-6467.
72. Fihri, A.; Artero, V.; Razavet, M.; Baffert, C.; Leibl, W.; Fontecave, M. *Angew. Chem., Int. Ed.* **2008,** *47* (3), 564-567.
73. Cropek, D. M.; Metz, A.; Muller, A. M.; Gray, H. B.; Horne, T.; Horton, D. C.; Poluektov, O.; Tiede, D. M.; Weber, R. T.; Jarrett, W. L.; Phillips, J. D.; Holder, A. A. *Dalton Trans.* **2012,** *41* (42), 13060-13073.
74. Rau, S.; Schaefer, B.; Gleich, D.; Anders, E.; Rudolph, M.; Friedrich, M.; Goerls, H.; Henry, W.; Vos, J. G. *Angew. Chem., Int. Ed.* **2006,** *45* (37), 6215-6218.
75. Ozawa, H.; Haga, M.; Sakai, K. *J. Am. Chem. Soc.* **2006,** *128* (15), 4926-4927.
76. Greenwood, N. N.; Earnshaw, A., *Chemistry of the Elements*. Elsevier: 2012.
77. Krishnan, C.; Brunschwig, B. S.; Creutz, C.; Sutin, N. *J. Am. Chem. Soc.* **1985,** *107* (7), 2005-2015.
78. Liu, J.; Hill, C. M.; Pan, S.; Liu, H. *Phys. Chem. Chem. Phys.* **2014,** *16* (42), 23150-23156.
79. England, J.; Bill, E.; Weyhermueller, T.; Neese, F.; Atanasov, M.; Wieghardt, K. *Inorg. Chem.* **2015,** *54* (24), 12002-12018.
80. Schwarz, H. A.; Creutz, C.; Sutin, N. *Inorg. Chem.* **1985,** *24* (3), 433-9.

81. Creutz, C.; Schwarz, H. A.; Sutin, N. *J. Am. Chem. Soc.* **1984,** *106* (10), 3036-7.
82. Chae, S. Y.; Park, S. J.; Joo, O.-S.; Min, B. K.; Hwang, Y. J. *Sol. Energy* **2016,** *135*, 821-826.
83. Teets, T. S.; Nocera, D. G. *Chem. Commun. (Cambridge, U. K.)* **2011,** *47* (33), 9268-9274.
84. Balzani, V.; Juris, A. *Coord. Chem. Rev.* **2001,** *211* (1), 97-115.
85. Kalyanasundaram, K. *Coord. Chem. Rev.* **1982,** *46*, 159-244.
86. Natali, M.; Badetti, E.; Deponti, E.; Gamberoni, M.; Scaramuzzo, F. A.; Sartorel, A.; Zonta, C. *Dalton Trans.* **2016,** *45* (37), 14764-14773.
87. Soltau, S. R.; Dahlberg, P. D.; Niklas, J.; Poluektov, O. G.; Mulfort, K. L.; Utschig, L. M. *Chemical Science* **2016,** *7* (12), 7068-7078.
88. Gueret, R.; Poulard, L.; Oshinowo, M.; Chauvin, J.; Dahmane, M.; Dupeyre, G.; Laine, P. P.; Fortage, J.; Collomb, M.-N. *ACS Catal.* **2018**, Ahead of Print.
89. Bartelmess, J.; Francis, A. J.; El Roz, K. A.; Castellano, F. N.; Weare, W. W.; Sommer, R. D. *Inorg. Chem.* **2014,** *53* (9), 4527-4534.
90. Peng, Q.-X.; Xue, D.; Yang, L.-F.; Zhan, S.-Z. *Int. J. Hydrogen Energy* **2017,** *42* (26), 16428-16435.
91. Guo, S.; Chen, K.-K.; Dong, R.; Zhang, Z.-M.; Zhao, J.; Lu, T.-B. *ACS Catalysis* **2018,** *8* (9), 8659-8670.
92. Natali, M. *ACS Catal.* **2017,** *7* (2), 1330-1339.
93. Reynal, A.; Pastor, E.; Gross, M. A.; Selim, S.; Reisner, E.; Durrant, J. R. *Chemical Science* **2015,** *6* (8), 4855-4859.
94. Graetzel, M. *Acc. Chem. Res.* **1981,** *14* (12), 376-384.
95. Pellegrin, Y.; Odobel, F. *Comptes Rendus Chimie* **2017,** *20* (3), 283-295.
96. Arneson, R. L. The oxidation of triethylamine by thallium (III) chloride. Masters Thesis, Oregon State University, Oregon State University, 1973.
97. Yoke, J. T.; Weiss, J. F.; Tollin, G. *Inorg. Chem.* **1963,** *2* (6), 1210-1216.
98. Weiss, J. F.; Tollin, G.; Yoke III, J. T. *Inorg. Chem.* **1964,** *3* (10), 1344-1348.
99. Fowles, G. W. A.; Pleass, C. M. *J. Chem. Soc.* **1957**, 1674-81.
100. Fowles, G. W. A.; Pleass, C. M. *J. Chem. Soc.* **1957**, 2078-80.
101. Fowles, G. W. A.; Hoodless, R. A. *J. Chem. Soc.* **1963**, 33-8.
102. Cowdell, R. T.; Fowles, G. W. A.; Walton, R. A. *J. Less-Common Met.* **1963,** *5* (5), 386-96.
103. Hatfield, W. E.; Yoke, J. T. *Inorg. Chem.* **1962,** *1* (3), 463-470.
104. Sizeneva, I. P.; Kondrashova, N. B.; Val'tsifer, V. A. *Russ. J. Appl. Chem.* **2005,** *78* (4), 541-545.
105. Gray, E. T.; Taylor, R. W.; Margerum, D. W. *Inorg. Chem.* **1977,** *16* (12), 3047-3055.
106. Weil, J. A.; Bolton, J. R., *Electron paramagnetic resonance: elementary theory and practical applications*. John Wiley & Sons: 2007.
107. Eaton, G. R.; Eaton, S. S.; Barr, D. P.; Weber, R. T., *Quantitative Epr*. Springer Science & Business Media: 2010.
108. Brustolon, M.; Giamello, E., *Electron Paramagnetic Resonance: A Practitioners Toolkit*. John Wiley & Sons: 2009.
109. Savitsky, A.; Möbius, K. *Photosynth. Res.* **2009,** *102* (2-3), 311-333.

110. Krzystek, J.; Ozarowski, A.; Telser, J. *Coord. Chem. Rev.* **2006,** *250* (17), 2308-2324.
111. Krzystek, J.; Ozarowski, A.; Zvyagin, S. A.; Telser, J. *Inorg. Chem.* **2012,** *51* (9), 4954-64.
112. Horton, D. C.; VanDerveer, D.; Krzystek, J.; Telser, J.; Pittman, T.; Crans, D. C.; Holder, A. A. *Inorg. Chim. Acta* **2014,** *420*, 112-119.
113. Holder, A. A.; Dasgupta, T. P. *Inorg. Chim. Acta* **2002,** *331* (1), 279-289.
114. Holder, A. A.; Dasgupta, T. P.; Im, S.-C. *Transition Met. Chem.* **1997,** *22* (2), 135-140.
115. Holder, A. A.; Dasgupta, T. P. *J. Chem. Soc. Dalton Trans.* **1996,** (13), 2637-2643.
116. Holder, A. A.; Dasgupta, T. P.; McFarlane, W.; Rees, N. H.; Enemark, J. H.; Pacheco, A.; Christensen, K. *Inorg. Chim. Acta* **1997,** *260* (2), 225-228.
117. Moody, L. M.; Balof, S.; Smith, S.; Rambaran, V. H.; VanDerveer, D.; Holder, A. A. *Acta Crystallogr. Sect. E: Struct. Rep. Online* **2008,** *E64*, m262-m263.
118. Rambaran, V. H.; Erves, T. R.; Grover, K.; Balof, S.; Moody, L. V.; Ramsdale, S. E.; Seymour, L. A.; VanDerveer, D.; Cropek, D. M.; Weber, R. T.; Holder, A. A. *J. Chem. Crystallogr.* **2013,** *43* (10), 509-516.
119. Yuan, H.; Newton, D. A. L.; Seymour, L. A.; Metz, A.; Cropek, D.; Holder, A. A.; Ofoli, R. Y. *Catal. Commun.* **2014,** *56*, 76-80.
120. Varey, J. E.; Lamprecht, G. J.; Fedin, V. P.; Holder, A.; Clegg, W.; Elsegood, M. R. J.; Sykes, A. G. *Inorg. Chem.* **1996,** *35* (19), 5525-5530.
121. Holder, A. A.; Brown, R. F. G.; Marshall, S. C.; Payne, V. C. R.; Cozier, M. D.; Alleyne, W. A.; Bovell, C. O. *Transition Met. Chem.* **2000,** *25* (5), 605-611.
122. Jeffery, G.; Bassett, J.; Mendham, J.; Denney, R., *Vogel's text book of quantitative inorganic analysis*. 1989; Vol. 10158.
123. Taura, T. *Bull. Chem. Soc. Jpn.* **1990,** *63*, 1105-1110.
124. Bakac, A.; Brynildson, M. E.; Espenson, J. H. *Inorg. Chem.* **1986,** *25* (23), 4108-4114.
125. Halmos, Z.; Wendlandt, W. W. *Thermochim. Acta* **1972,** *5* (2), 165-171.
126. Dwyer, F. P.; Gyarfas, E. C.; Mellor, D. P. *J. Phys. Chem.* **1955,** *59* (4), 296-297.
127. Nakamoto, K., *Infrared and Raman spectra of inorganic and coordination compounds*. Wiley Online Library: 1986.
128. Hedberg, K.; Badger, R. M. *J. Chem. Phys.* **1951,** *19* (4), 508-509.
129. Chen, T. K.; Thornton, D.; Ho, M. Y. *Int. J. Pharm.* **1990,** *59* (3), 211-216.
130. López, N. I.; Duarte, C. M. *J. Sea Res.* **2004,** *51* (1), 11-20.
131. Kharasch, N.; Thyagarajan, B. *Ann. N.Y. Acad. Sci.* **1983,** *411* (1), 391-402.
132. Beilke, M. A.; Collins-Lech, C.; Sohnle, P. G. *J. Lab. Clin. Med.* **1987,** *110* (1), 91-6.
133. Sharon, D.; Afri, M.; Noked, M.; Garsuch, A.; Frimer, A. A.; Aurbach, D. *J. Phys. Chem. Lett.* **2013,** *4* (18), 3115-3119.
134. Wang, K.; Jordan, R. B. *Can. J. Chem.* **1996,** *74* (5), 658-665.
135. Rayner-Canham, G.; Overton, T., The Group 17 Elements: The Halogens. In *Descriptive inorganic chemistry*, Macmillan: 2003; pp 4421-472.
136. Bronsted, J. N. *Z. physik. Chem.* **1922,** *102*, 169-207.
137. Holder, A. A.; Brown, R. F.; Marshall, S. C.; Payne, V. C.; Cozier, M. D.; Alleyne, W. A.; Bovell, C. O. *Transition Met. Chem.* **2000,** *25* (5), 605-611.

138. Manov, G. G.; Bates, R. G.; Hamer, W. J.; Acree, S. F. *J. Am. Chem. Soc.* **1943,** *65* (9), 1765-1767.
139. Soulard, M.; Bloc, F.; Hatterer, A. *J. Chem. Soc., Dalton Trans.* **1981,** (12), 2300-2310.
140. Gazda, M.; Margerum, D. W. *Inorg. Chem.* **1994,** *33* (1), 118-123.
141. Wangila, G. W.; Jordan, R. B. *Inorg. Chim. Acta* **2005,** *358* (9), 2804-2812.
142. Wangila, G. W.; Jordan, R. B. *Inorg. Chim. Acta* **2005,** *358* (13), 3753-3760.
143. Marcus, R. *Disc. Faraday Soc.* **1960,** *29*, 21-31.
144. Marcus, R. A. *Can. J. Chem.* **1959,** *37* (1), 155-163.
145. Marcus, R. *J. Phys. Chem.* **1963,** *67* (4), 853-857.
146. Lawrence, M. A.; Celestine, M. J.; Artis, E. T.; Joseph, L. S.; Esquivel, D. L.; Ledbetter, A. J.; Cropek, D. M.; Jarrett, W. L.; Bayse, C. A.; Brewer, M. I.; Holder, A. A. *Dalton Trans.* **2016,** *45* (25), 10326-42.
147. Hu, X. L.; Brunschwig, B. S.; Peters, J. C. *J. Am. Chem. Soc.* **2007,** *129* (29), 8988-8998.
148. Baffert, C.; Artero, V.; Fontecave, M. *Inorg. Chem.* **2007,** *46* (5), 1817-1824.
149. Harrison, R., Standard Electrode Potentials. In *Nuffield Advanced Science Book of Data*, Longman, London: 1972; pp 116-118.
150. Silverman, J.; Dodson, R. W. *J. Phys. Chem.* **1952,** *56* (7), 846-852.
151. Hupp, J. T.; Weaver, M. J. *Inorg. Chem.* **1983,** *22* (18), 2557-2564.
152. Pujari, M. P.; Banerjee, P. *J. Chem. Soc., Dalton Trans.* **1983,** (5), 1015-1016.
153. Birk, J. P.; Kozub, S. G. *Inorg. Chem.* **1973,** *12* (10), 2460-2464.
154. Kamble, D. L.; Nandibewoor, S. T. *Int. J. Chem. Kinet.* **1996,** *28* (9), 673-679.
155. Summer, S.; Naqvi, I. I.; Khattak, R.; Gulzar, S.; Reyaz, F. *J. Chem. Soc. Pak.* **2016,** *38* (3), 384-389.
156. Iyun, J. F.; Ayoko, G. A.; Lohdip, Y. N. *Polyhedron* **1992,** *11* (18), 2389-94.
157. Jhanji, A. K.; Gould, E. S. *Inorg. Chem.* **1990,** *29* (19), 3890-2.
158. Linn, D. E., Jr.; Ghosh, S. K.; Gould, E. S. *Inorg. Chem.* **1989,** *28* (16), 3225-8.
159. Balasubramanian, P. N.; Reed, J. W.; Gould, E. S. *Inorg. Chem.* **1985,** *24* (12), 1794-7.
160. Hassan, A.; Pardi, L.; Krzystek, J.; Sienkiewicz, A.; Goy, P.; Rohrer, M.; Brunel, L.-C. *Journal of Magnetic Resonance* **2000,** *142* (2), 300-312.
161. Michaely, W. J.; Schrauzer, G. *J. Am. Chem. Soc.* **1973,** *95* (17), 5771-5772.
162. Silverman, R. B.; Dolphin, D. *J. Am. Chem. Soc.* **1974,** *96* (22), 7094-7096.
163. Cline, E. D.; Adamson, S. E.; Bernhard, S. *Inorg. Chem.* **2008,** *47* (22), 10378-10388.
164. Reijerse, E. J. *Appl. Magn. Reson.* **2010,** *37* (1-4), 795.
165. Schrauzer, G. N.; Windgassen, R. J. *J. Am. Chem. Soc.* **1966,** *88* (16), 3738-3743.
166. Shi, S.; Daniels, L. M.; Espenson, J. H. *Inorg. Chem.* **1991,** *30* (18), 3407-3410.
167. Williams, O. M.; Cowley, A. H.; Rose, M. J. *Dalton Trans.* **2015,** *44* (29), 13017-13029.
168. Tomasi, J.; Mennucci, B.; Cammi, R. *Chem. Rev.* **2005,** *105* (8), 2999–3094.
169. Hay, P. J. *J. Chem. Phys.* **1977,** *66* (10), 4377-4384.
170. Wachters, A. J. H. *J. Chem. Phys.* **1970,** *52* (3), 1033-1036.
171. Dunning, T. H. *J. Chem. Phys.* **1971,** *55* (2), 716-723.
172. Ghosh, S.; Barve, A. C.; Kumbhar, A. A.; Kumbhar, A. S.; Puranik, V. G.; Datar, P. A.; Sonawane, U. B.; Joshi, R. R. *J. Inorg. Biochem.* **2006,** *100* (3), 331-343.

173. Kim, H.-S.; Ko, S.-B.; Jang, I.-H.; Park, N.-G. *Chem. Commun.* **2011,** *47* (47), 12637-12639.
174. Klingele, M. H.; Brooker, S. *Eur. J. Org. Chem.* **2004,** *2004* (16), 3422-3434.
175. Lawrence, M. A. W.; Jackson, Y. A.; Mulder, W. H.; Björemark, P. M.; Håkansson, M. *Aust. J. Chem.* **2015,** *68* (5), 731-741.
176. Lawrence, M. A. W.; Mulder, W. H. *ChemistrySelect* **2018,** *3* (28), 8387-8394.
177. Celestine, M. J.; Lawrence, M. A. W.; Evaristo, N. K.; Legere, B. W.; Knarr, J. K.; Schott, O.; Picard, V.; Bullock, J. L.; Hanan, G. S.; McMillen, C. D.; Bayse, C. A.; Holder, A. A. *Inorg. Chim. Acta* **2020,** *510*, 119726.
178. Bakir, M.; Lawrence, M. A. W.; Ferhat, M.; Conry, R. R. *J. Coord. Chem.* **2017,** *70* (17), 3048-3064.
179. Pantani, O.; Naskar, S.; Guillot, R.; Millet, P.; Anxolabehere-Mallart, E.; Aukauloo, A. *Angew. Chem., Int. Ed.* **2008,** *47* (51), 9948-9950.
180. Lee, K. J.; McCarthy, B. D.; Dempsey, J. L. *Chem. Soc. Rev.* **2019,** *48* (11), 2927-2945.
181. Kellett, R. M.; Spiro, T. G. *Inorg. Chem.* **1985,** *24* (15), 2373-2377.
182. Dempsey, J. L.; Winkler, J. R.; Gray, H. B. *J. Am. Chem. Soc.* **2010,** *132*, 1060–1065.
183. Dongare, P.; Myron, B. D. B.; Wang, L.; Thompson, D. W.; Meyer, T. J. *Coord. Chem. Rev.* **2017,** *345*, 86-107.
184. Rousset, E.; Chartrand, D.; Ciofini, I.; Marvaud, V.; Hanan, G. S. *Chem Commun (Camb)* **2015,** *51* (45), 9261-4.
185. Rousset, E.; Ciofini, I.; Marvaud, V.; Hanan, G. S. *Inorg Chem* **2017,** *56* (16), 9515-9524.
186. Schott, O.; Pal, A. K.; Chartrand, D.; Hanan, G. S. *Chemsuschem* **2017,** *10* (22), 4436-4441.
187. Hogue, R. W.; Schott, O.; Hanan, G. S.; Brooker, S. *Chemistry* **2018,** *24* (39), 9820-9832.
188. Taura, T. *Bull. Chem. Soc. Jpn.* **1990,** *63*, 1105-1110.
189. Sheldrick, G. M. *SHELXL 2014/7*, University of Gottngen, Germany, 2014.
190. Brisig, B.; Constable, E. C.; Housecroft, C. E. *New J. Chem.* **2007,** *31* (8), 1437-1447.
191. Lawrence, M. A. W.; McMillen, C. D.; Gurung, R. K.; Celestine, M. J.; Arca, J. F.; Holder, A. A. *J. Chem. Crystallogr.* **2015,** *45* (8-9), 427-433.
192. Yamasaki, A.; Yajima, F.; Fujiwara, S. *Inorg. Chim. Acta* **1968,** *2*, 39-42.
193. Kim, M. Y.; Seok, W. K.; Dong, Y.; Yun, H. *Inorg. Chim. Acta* **2001,** *319* (1), 194-198.
194. House, D. A. *Comments Inorg. Chem.* **1997,** *19* (6), 327-350.
195. Chen, X.; Ren, H.; Peng, W.; Zhang, H.; Lu, J.; Zhuang, L. *J. Phys. Chem. C* **2014,** *118* (36), 20791-20798.
196. Rotzinger, F. P. *Inorg. Chem.* **1999,** *38* (25), 5730-5733.
197. Lee, K. J.; McCarthy, B. D.; Dempsey, J. L. *Chem. Soc. Rev.* **2019,** *48* (11), 2927-2945.
198. Costentin, C.; Savéant, J.-M. *ChemElectroChem* **2014,** *1* (7), 1226-1236.
199. Costentin, C.; Dridi, H.; Savéant, J.-M. *J. Am. Chem. Soc.* **2014,** *136* (39), 13727-13734.
200. Queyriaux, N.; Jane, R. T.; Massin, J.; Artero, V.; Chavarot-Kerlidou, M. *Coord Chem Rev* **2015,** *304-305*, 3-19.
201. Rajak, S.; Schott, O.; Kaur, P.; Maris, T.; Hanan, G. S.; Duong, A. *RSC Advances* **2019,** *9* (48), 28153-28164.

202. Khnayzer, R. S.; Thoi, V. S.; Nippe, M.; King, A. E.; Jurss, J. W.; El Roz, K. A.; Long, J. R.; Chang, C. J.; Castellano, F. N. *Energ Environ Sci* **2014,** *7* (4), 1477-1488.
203. Zee, D. Z.; Chantarojsiri, T.; Long, J. R.; Chang, C. J. *Acc Chem Res* **2015,** *48* (7), 2027-36.
204. Lo, W. K.; Castillo, C. E.; Gueret, R.; Fortage, J.; Rebarz, M.; Sliwa, M.; Thomas, F.; McAdam, C. J.; Jameson, G. B.; McMorran, D. A.; Crowley, J. D.; Collomb, M. N.; Blackman, A. G. *Inorg Chem* **2016,** *55* (9), 4564-81.

APPENDIX 1

Copyright Permissions

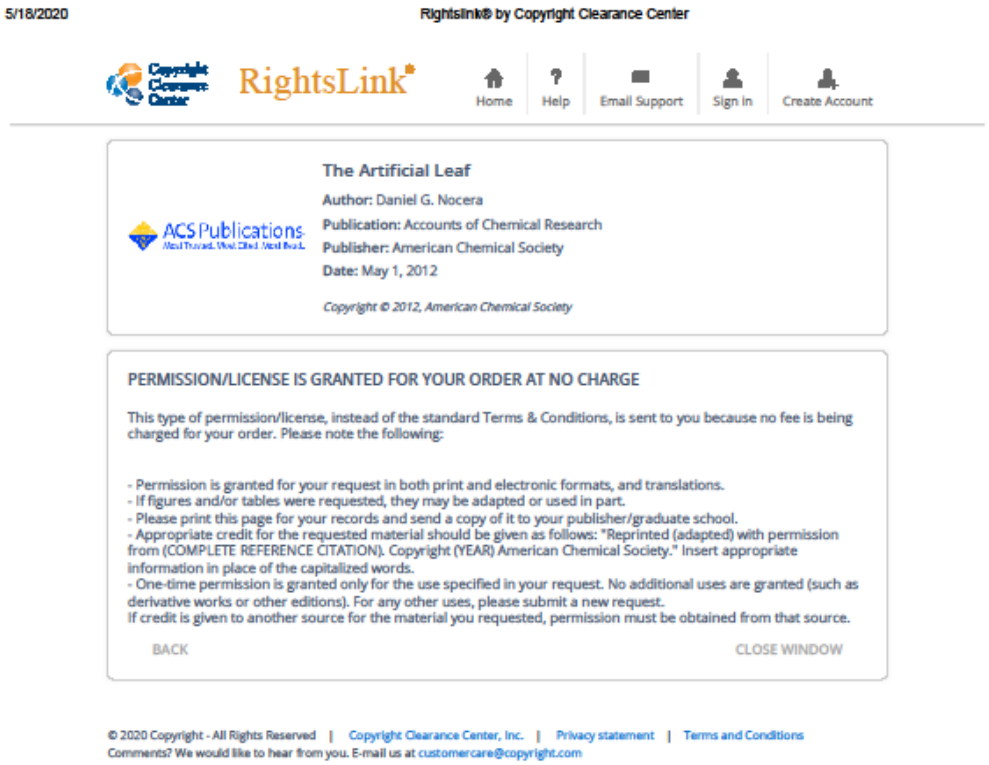

5/18/2020 Rightslink® by Copyright Clearance Center

RightsLink

Home | Help | Email Support | Sign In | Create Account

The Artificial Leaf

Author: Daniel G. Nocera

Publication: Accounts of Chemical Research

Publisher: American Chemical Society

Date: May 1, 2012

Copyright © 2012, American Chemical Society

PERMISSION/LICENSE IS GRANTED FOR YOUR ORDER AT NO CHARGE

This type of permission/license, instead of the standard Terms & Conditions, is sent to you because no fee is being charged for your order. Please note the following:

- Permission is granted for your request in both print and electronic formats, and translations.
- If figures and/or tables were requested, they may be adapted or used in part.
- Please print this page for your records and send a copy of it to your publisher/graduate school.
- Appropriate credit for the requested material should be given as follows: "Reprinted (adapted) with permission from (COMPLETE REFERENCE CITATION). Copyright (YEAR) American Chemical Society." Insert appropriate information in place of the capitalized words.
- One-time permission is granted only for the use specified in your request. No additional uses are granted (such as derivative works or other editions). For any other uses, please submit a new request.

If credit is given to another source for the material you requested, permission must be obtained from that source.

BACK CLOSE WINDOW

© 2020 Copyright - All Rights Reserved | Copyright Clearance Center, Inc. | Privacy statement | Terms and Conditions

Comments? We would like to hear from you. E-mail us at customercare@copyright.com

https://s100.copyright.com/AppDispatchServlet#formTop 1/1

RightsLink

Home | Help | Email Support | Sign In | Create Account

Photocatalytic Z-Scheme Water Splitting for Independent H2/O2 Production via a Stepwise Operation Employing a Vanadate Redox Mediator under Visible Light

Author: Yugo Miseki, Satoshi Fujiyoshi, Takahiro Gunji, et al
Publication: The Journal of Physical Chemistry C
Publisher: American Chemical Society
Date: May 1, 2017

PERMISSION/LICENSE IS GRANTED FOR YOUR ORDER AT NO CHARGE

This type of permission/license, instead of the standard Terms & Conditions, is sent to you because no fee is being charged for your order. Please note the following:

- Permission is granted for your request in both print and electronic formats, and translations.
- If figures and/or tables were requested, they may be adapted or used in part.
- Please print this page for your records and send a copy of it to your publisher/graduate school.
- Appropriate credit for the requested material should be given as follows: "Reprinted (adapted) with permission from (COMPLETE REFERENCE CITATION). Copyright (YEAR) American Chemical Society." Insert appropriate information in place of the capitalized words.
- One-time permission is granted only for the use specified in your request. No additional uses are granted (such as derivative works or other editions). For any other uses, please submit a new request.

If credit is given to another source for the material you requested, permission must be obtained from that source.

BACK CLOSE WINDOW

ELSEVIER LICENSE
TERMS AND CONDITIONS

May 18, 2020

This Agreement between Michael J Celestine ("You") and Elsevier ("Elsevier") consists of your license details and the terms and conditions provided by Elsevier and Copyright Clearance Center.

License Number	4832050664174
License date	May 18, 2020
Licensed Content Publisher	Elsevier
Licensed Content Publication	Solar Energy
Licensed Content Title	Spontaneous solar water splitting by DSSC/CIGS tandem solar cells
Licensed Content Author	Sang Youn Chae,Se Jin Park,Oh-Shim Joo,Byoung Koun Min,Yun Jeong Hwang
Licensed Content Date	Oct 1, 2016
Licensed Content Volume	135
Licensed Content Issue	n/a
Licensed Content Pages	6
Start Page	821
End Page	826

JOHN WILEY AND SONS LICENSE
TERMS AND CONDITIONS

Jul 31, 2020

This Agreement between Michael J Celestine ("You") and John Wiley and Sons ("John Wiley and Sons") consists of your license details and the terms and conditions provided by John Wiley and Sons and Copyright Clearance Center.

License Number	4879470074510
License date	Jul 31, 2020
Licensed Content Publisher	John Wiley and Sons
Licensed Content Publication	Angewandte Chemie International Edition
Licensed Content Title	A Nickel Thiolate Catalyst for the Long-Lived Photocatalytic Production of Hydrogen in a Noble-Metal-Free System
Licensed Content Author	Zhiji Han, William R. McNamara, Min-Sik Eum, et al
Licensed Content Date	Jan 11, 2012
Licensed Content Volume	51
Licensed Content Issue	7
Licensed Content Pages	4

Type of use	Dissertation/Thesis
Requestor type	University/Academic
Format	Print and electronic
Portion	Figure/table
Number of figures/tables	1
Will you be translating?	No
Title	Synthesis, characterization, and kinetics studies of new cobalt(II/III) complexes for the production of H2
Institution name	Old Dominion University
Expected presentation date	Aug 2020
Portions	Figure 1
Requestor Location	Michael J Celestine 4541 Hampton Blvd. Department of Chemistry and Biochemistry Old Dominion University NORFOLK, VA 23529 United States Attn: Michael J Celestine
Publisher Tax ID	EU826007151
Total	0.00 USD

Terms and Conditions

TERMS AND CONDITIONS

APPENDIX 2

Chapter 3: Supplementary Figures

Mass Spectra

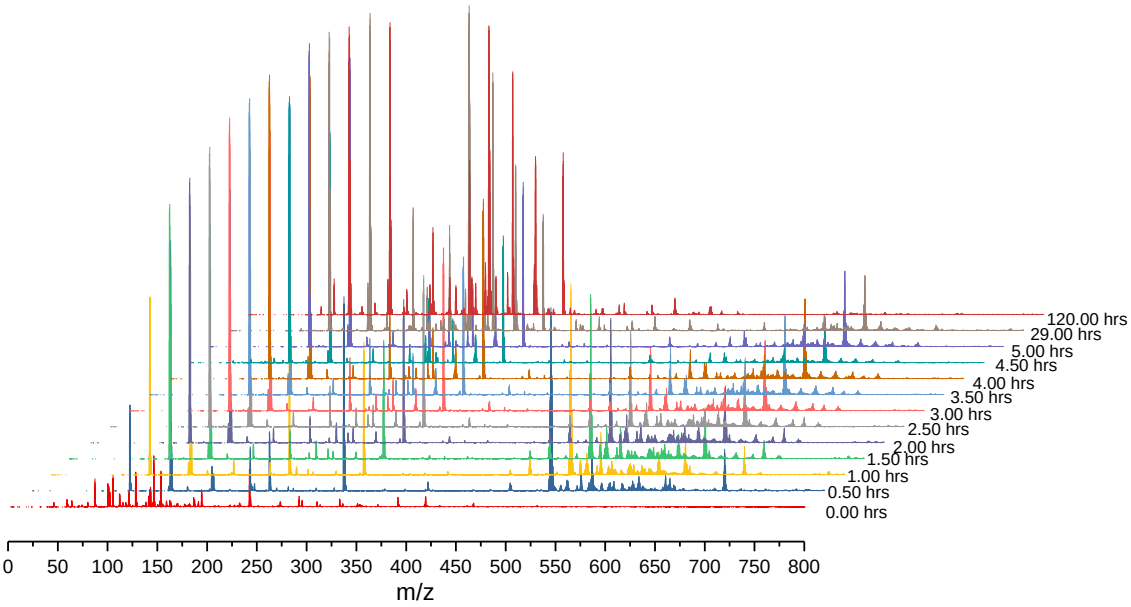

Figure 111. ESI MS of $[Co(dmgBF_2)_2(OH_2)_2]$ with Et_3N in acetonitrile. $[Co(dmgBF_2)_2(OH_2)_2]$ = 1.0 mM, $[Et_3N]$ = 30.0 mM, positive mode.

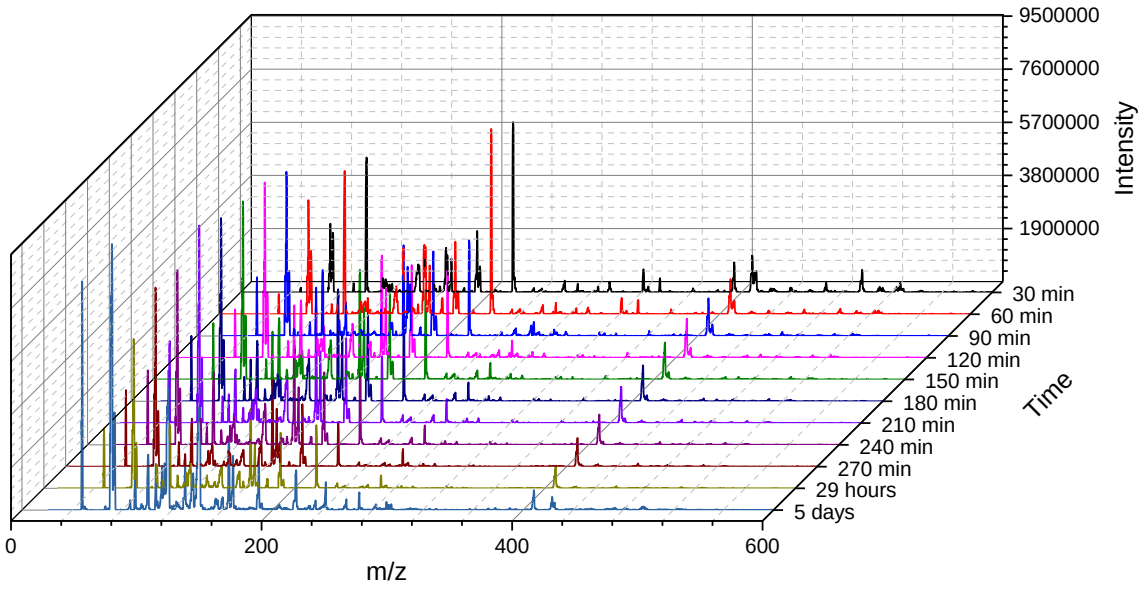

Figure 112. ESI MS of $[Co(dmgBF_2)_2(OH_2)_2]$ with Et_3N in acetonitrile. $[Co(dmgBF_2)_2(OH_2)_2]$ = 1.0 mM, $[Et_3N]$ = 30.0 mM, negative mode.

NMR spectra

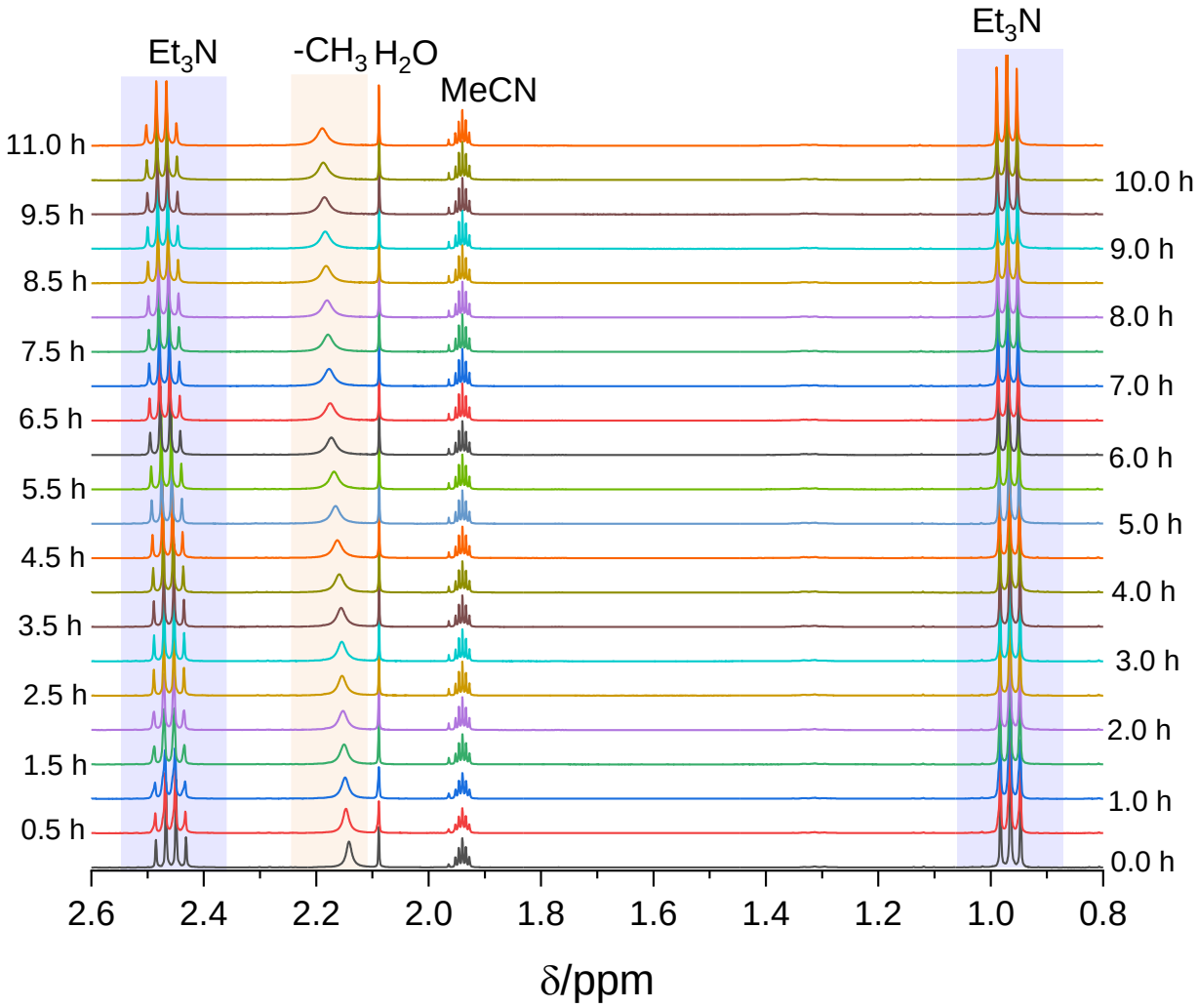

Figure 113. ^{1}H NMR spectra of $[Co(dmgBF_2)_2(OH_2)_2]$ with Et_3N in CD_3CN. $[Co(dmgBF_2)_2(OH_2)_2]$ = 2.38 mM and $[Et_3N]$ = 33.32 mM.

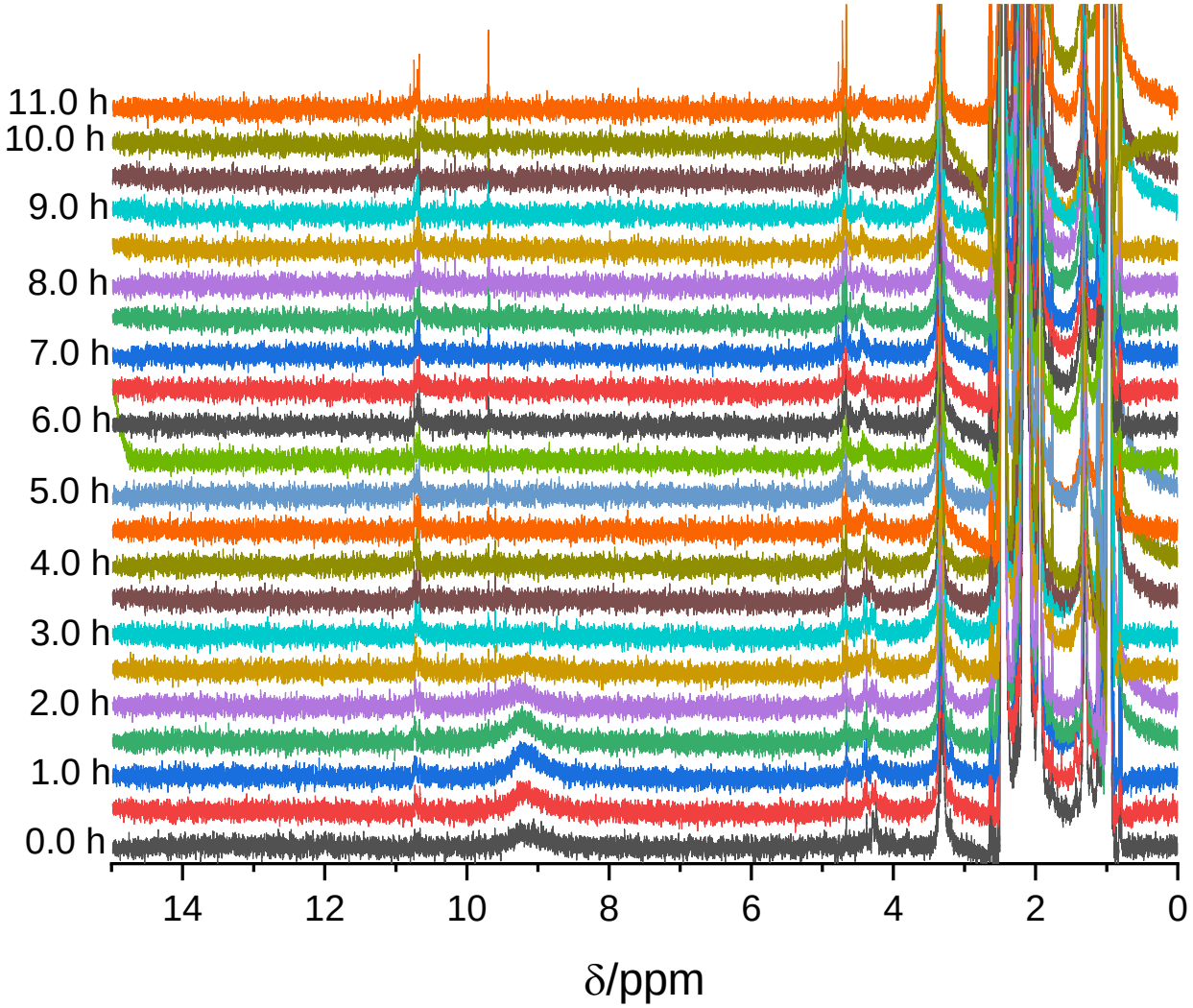

Figure 114. ^{1}H NMR spectra of $[Co(dmgBF_2)_2(OH_2)_2]$ with Et_3N in CD_3CN. $[Co(dmgBF_2)_2(OH_2)_2]$ = 2.38 mM and $[Et_3N]$ = 33.32 mM.

UV-visible spectra

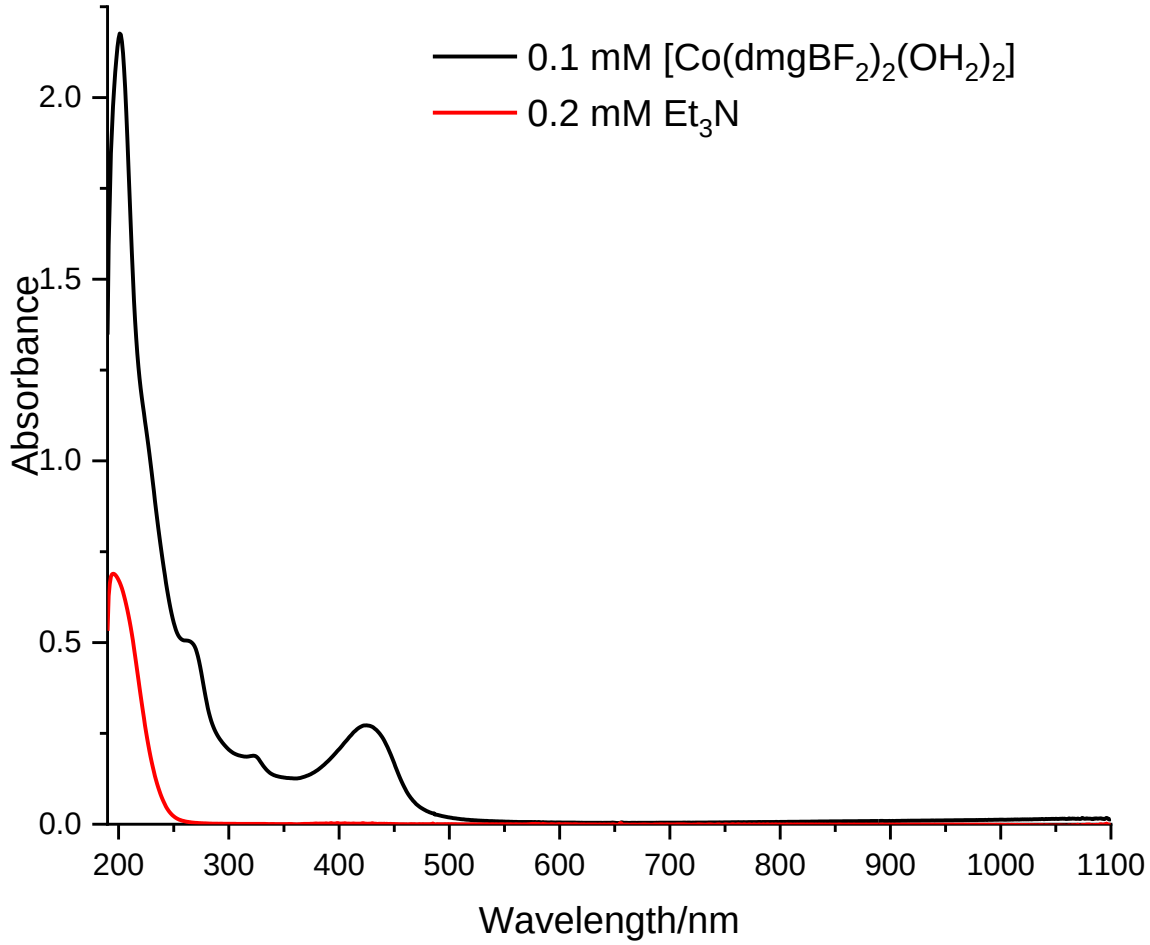

Figure 115. UV-visible spectra of $[Co(dmgBF_2)_2(OH)_2]$ and Et_3N in MeCN.

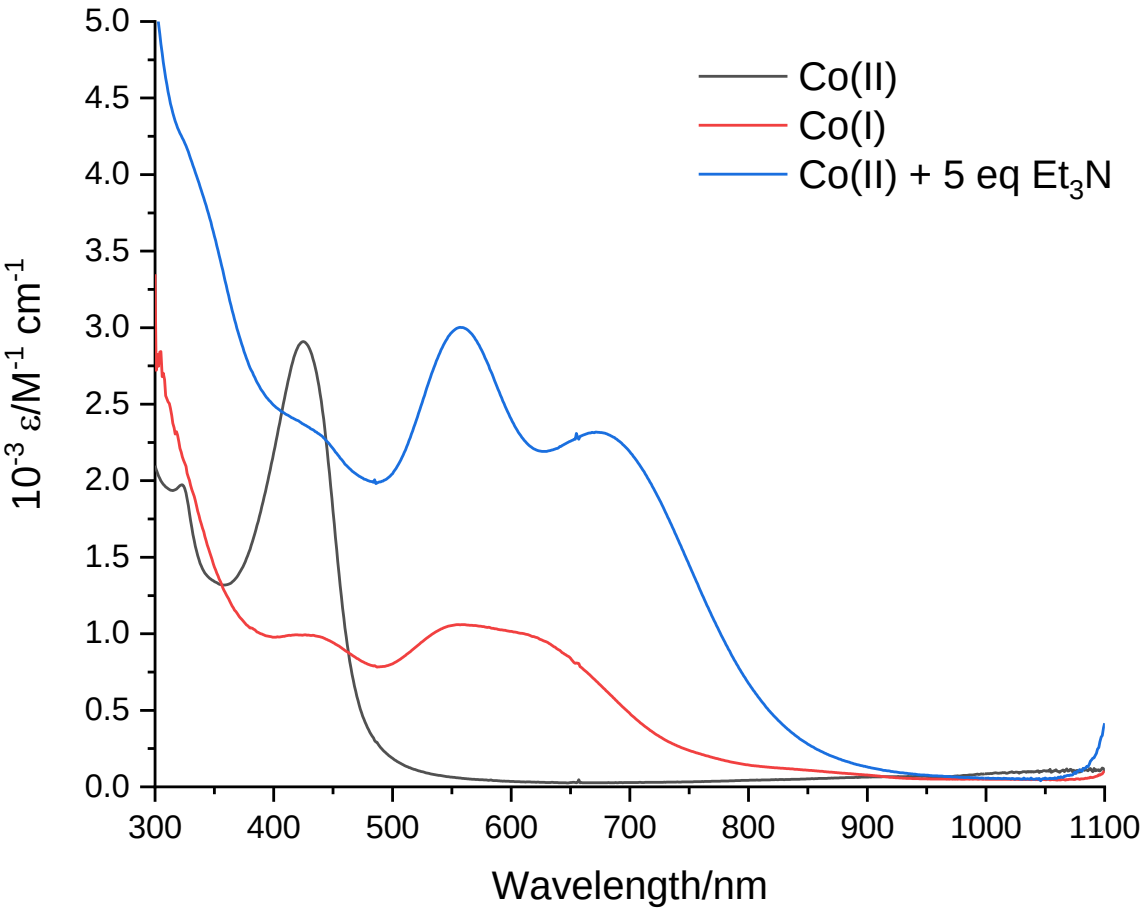

Figure 116. UV-visible spectra of $[Co(dmgBF_2)_2(OH_2)_2]$ in MeCN. (black) Co(II) species, (red) Co(II) species with 5 equivalents $[^nBu_4N]BH_4$, (blue) Co(II) species with 5 equivalents Et_3N.

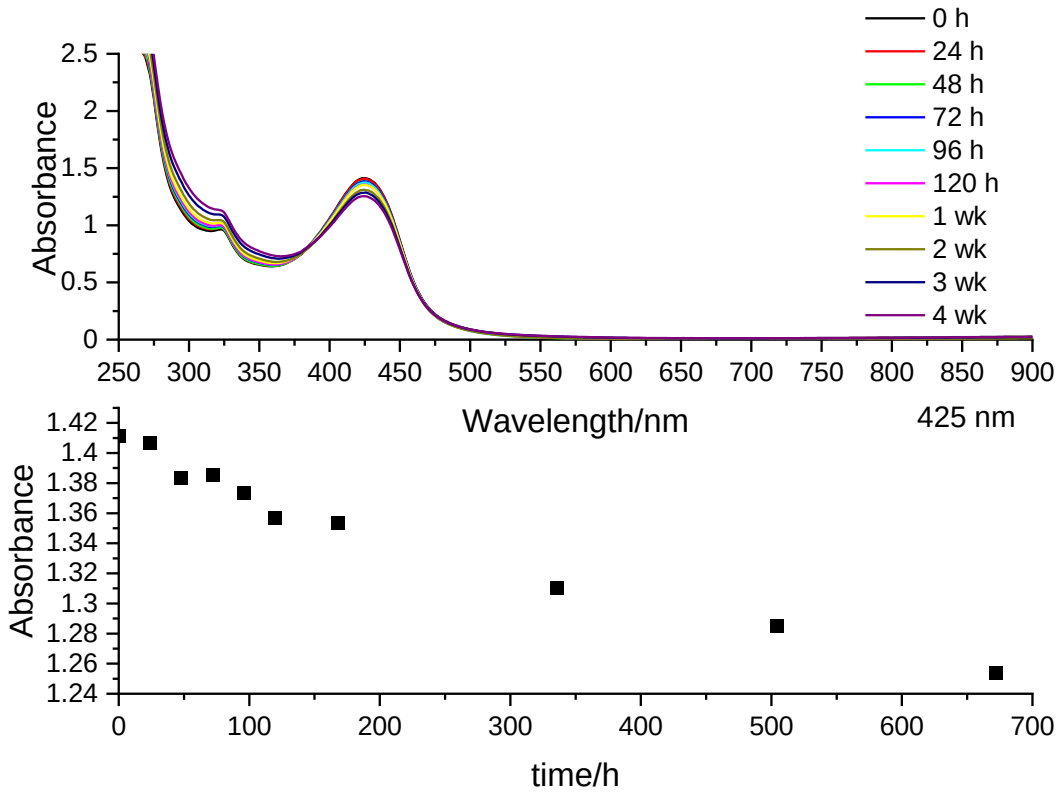

Figure 117. UV-visible spectra of $[Co(dmgBF_2)_2(OH_2)_2]$ in acetonitrile over a four-week period. [complex] = 0.5 mM.

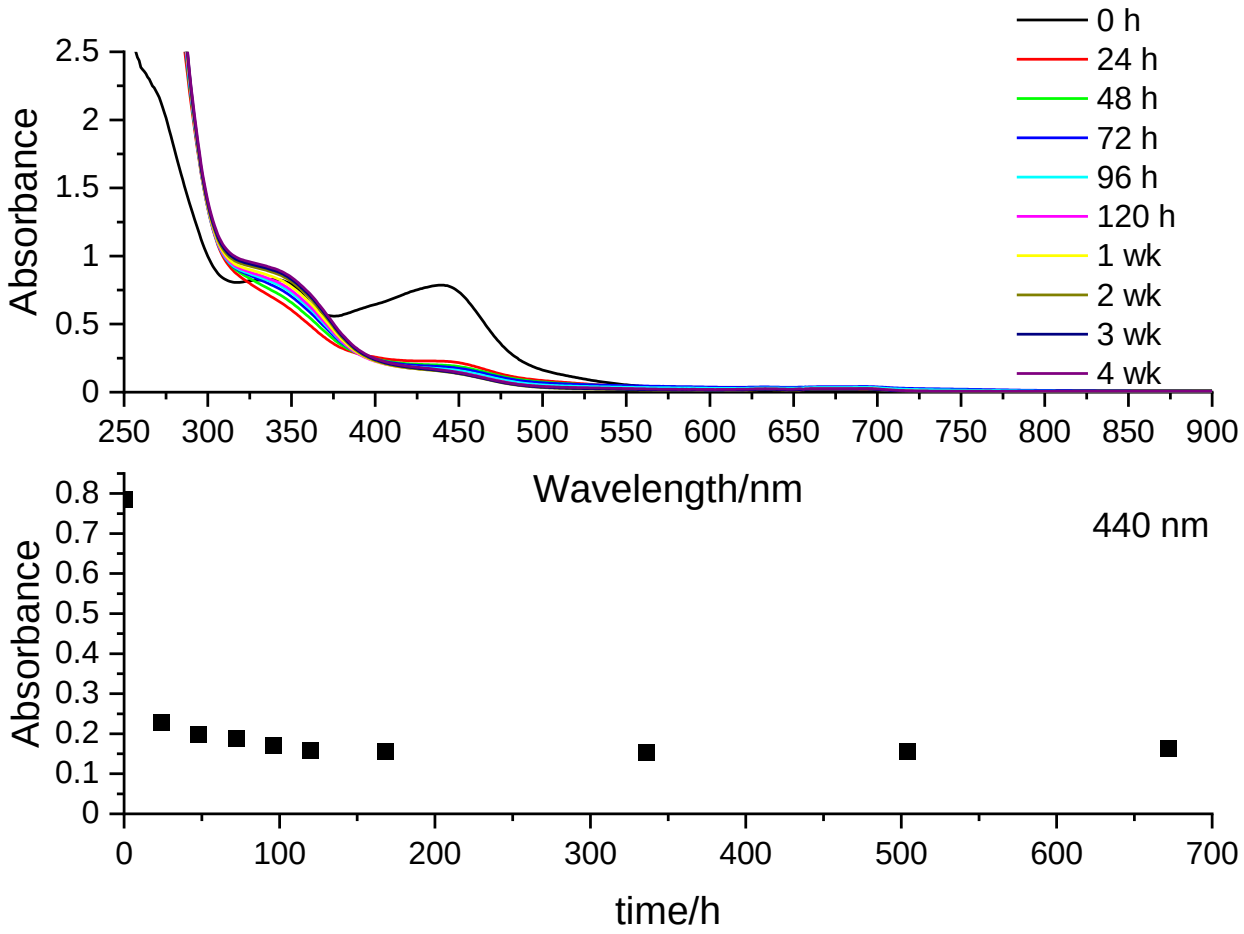

Figure 118. UV-visible spectra of $[Co(dmgBF_2)_2(OH_2)_2]$ and $[^nBu_4N]Cl$ in acetonitrile over a four-week period. [complex] = 0.5 mM and $[^nBu_4N]Cl$ = 5.0 mM.

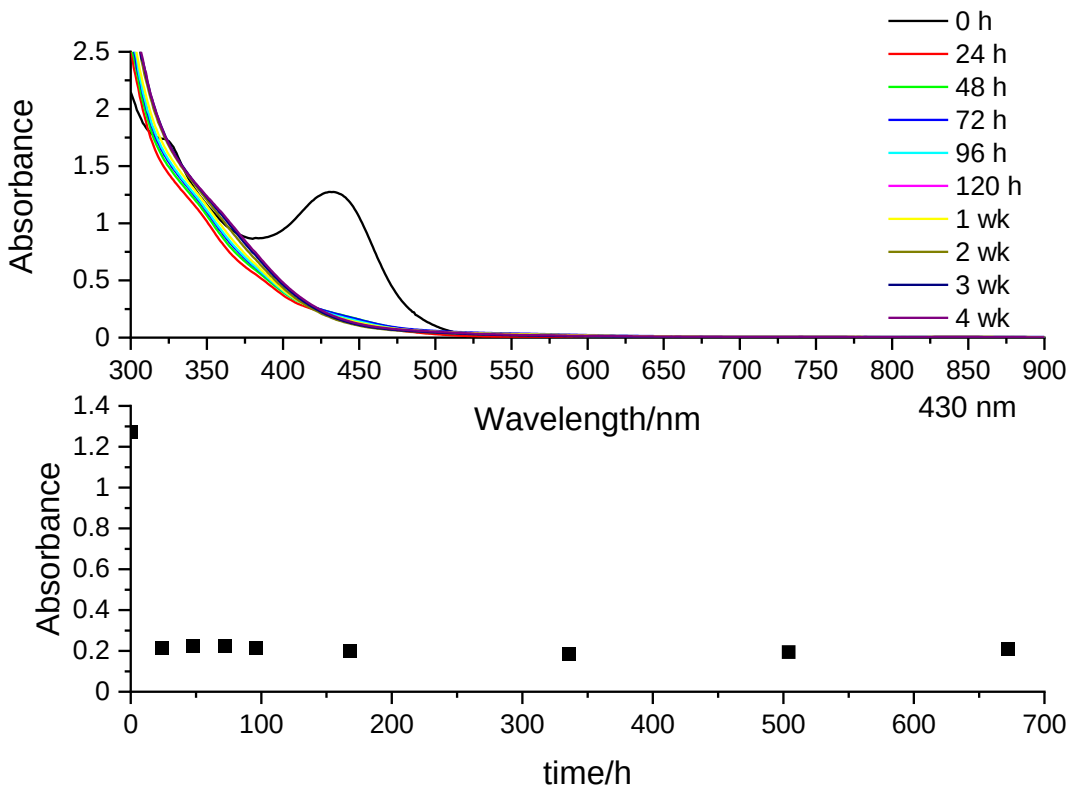

Figure 119. UV-visible spectra of $[Co(dmgBF_2)_2(OH_2)_2]$ and HCl in acetonitrile over a four-week period. [complex] = 0.5 mM and [HCl] = 5.0 mM.

Table 23. List of absorbance and rate of decay for 0.5 mM $[Co(dmgBF_2)_2(OH_2)_2]$ in acetonitrile.

Additions	**λ_1/nm (10^3 rate/h^{-1})**	**λ_2/nm (10^3 rate/h^{-1})**
Nothing	425 (2.01)	--
5 mM Et_3N	554 (10.2)	680 (9.12)
5 mM Et_3N•HCl	583 (9.18)	680 (7.33)
2.86 mM Et_3N + 2.18 mM Et_3N•HCl	590 (4.57)	690 (3.93)
5 mM Et_3N + 5 mM $[^nBu_4N]Cl$	570 (9.15)	690 (4.67)
5 mM Et_3N + 10 mM $[^nBu_4N]Cl$	570 (5.48)	690 (4.29)
5 mM $[^nBu_4N]Cl$	440 (92.9)	--
5 mM HCl	430 (205)	--

EPR Spectra

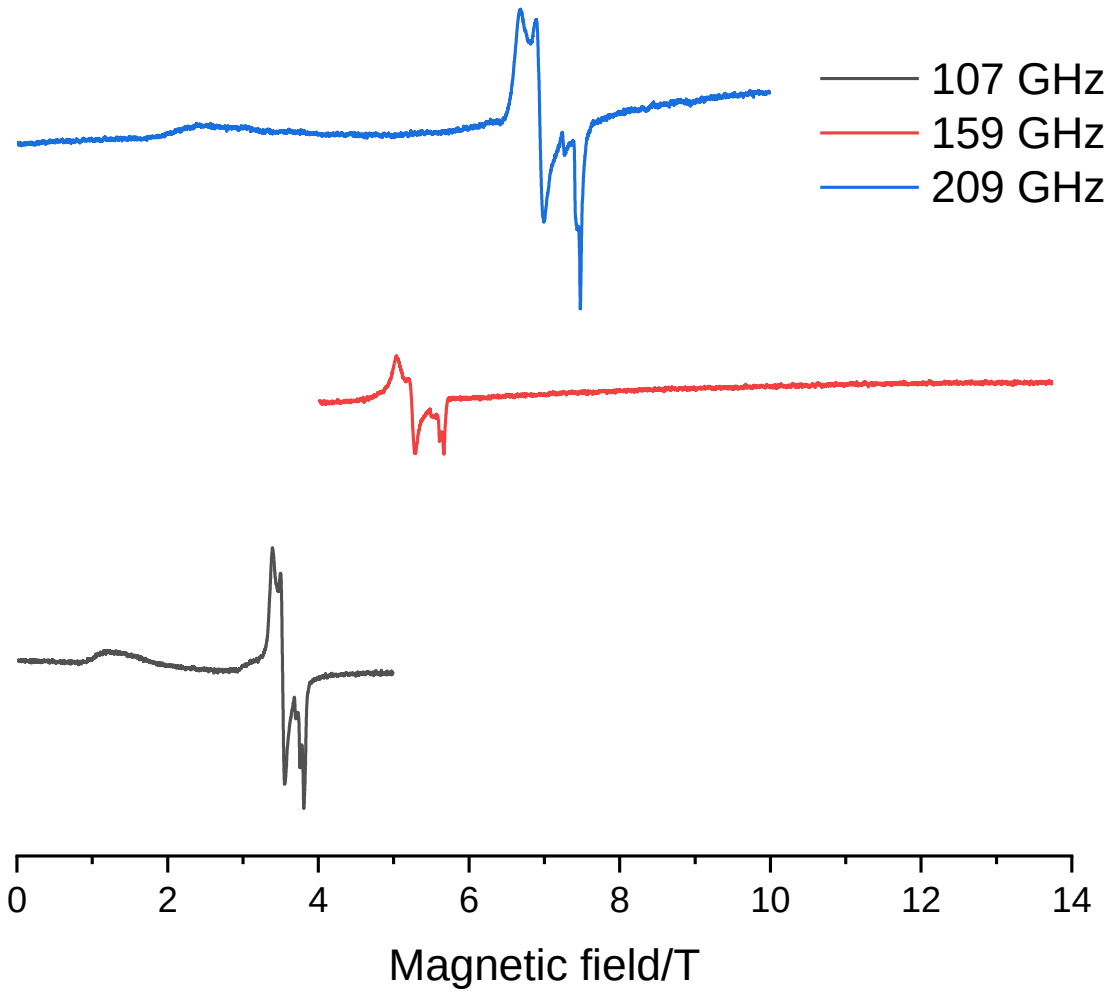

Figure 120. High field EPR spectra of $[Co(dmgBF_2)_2(OH_2)(N(C_2H_3)_3)]$ as a pellet. 83 mg of complex + 120 mg n-eicosane, T = 10 K

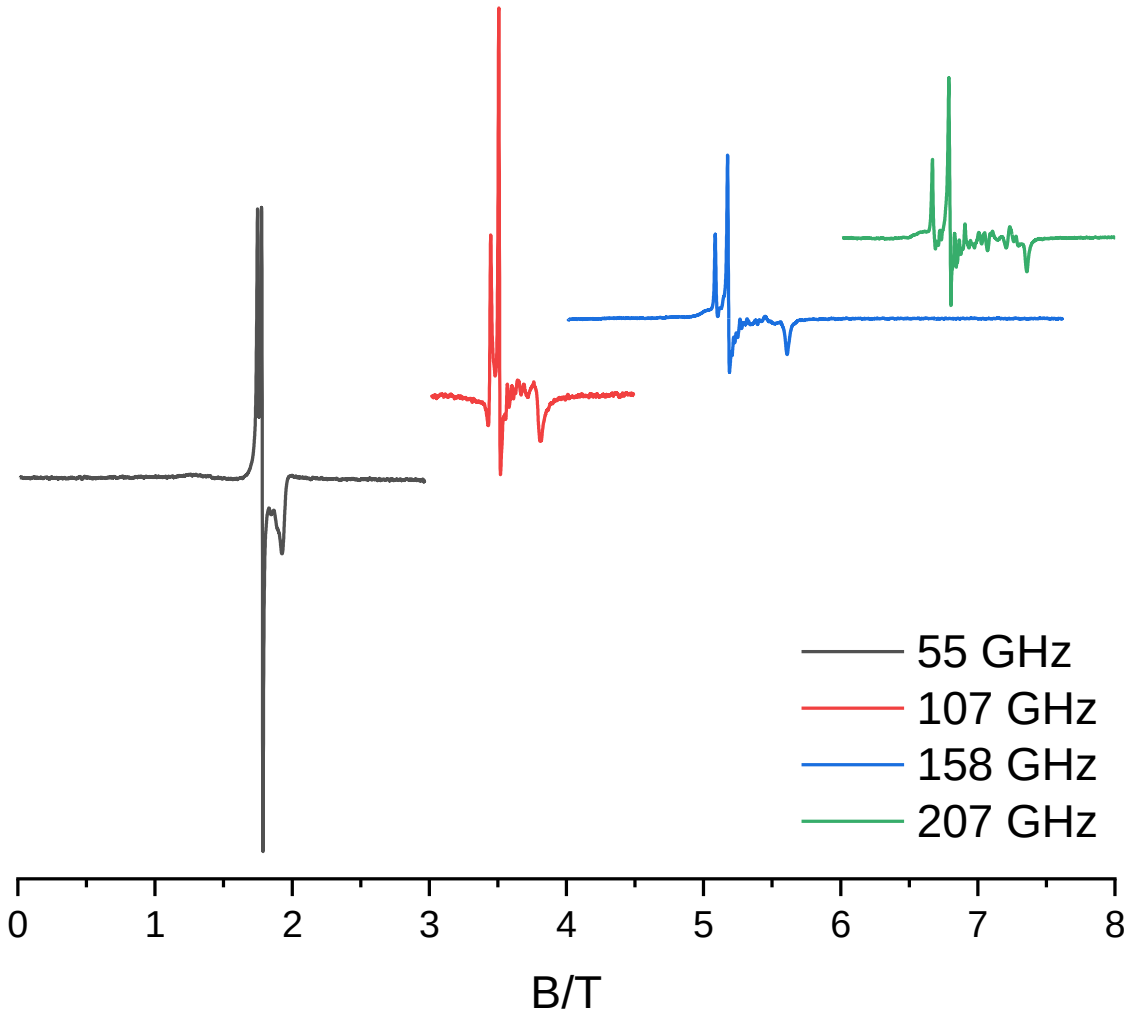

Figure 121. High field EPR spectra of $[Co^{II}(dmgBF_2)_2(OH_2)_2]$. 21 mg of complex in 1 ml of CH_3CN (sat.), T = 10 K

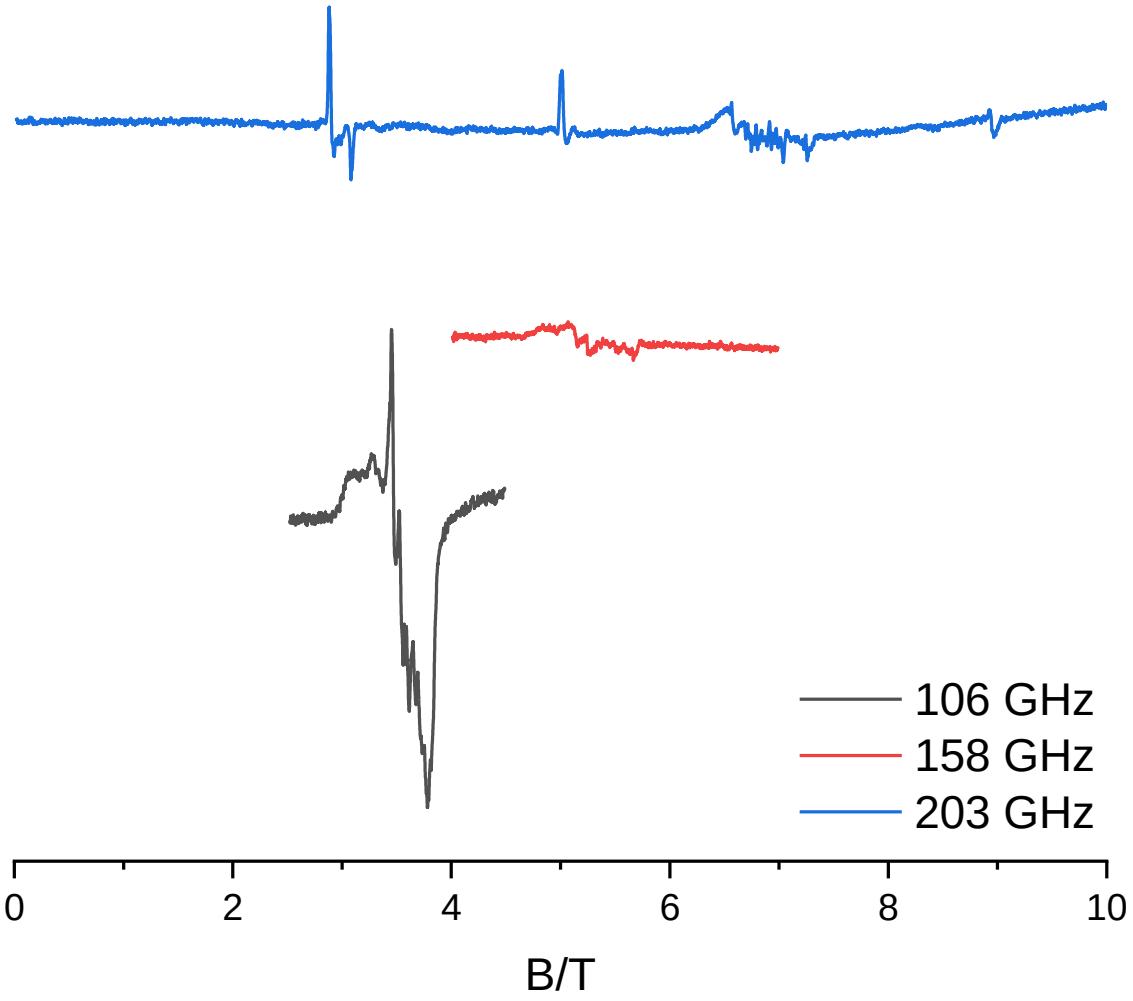

Figure 122. High field EPR spectra of $[Co^{II}(dmgBF_2)_2(OH_2)_2]$ + NEt_3.. 50 mM complex in CH_3CN with 500 mM $[^nBu_4N]BH_4$ and 700 mM $[^nBu_4N]BH_4$, T = 10 K

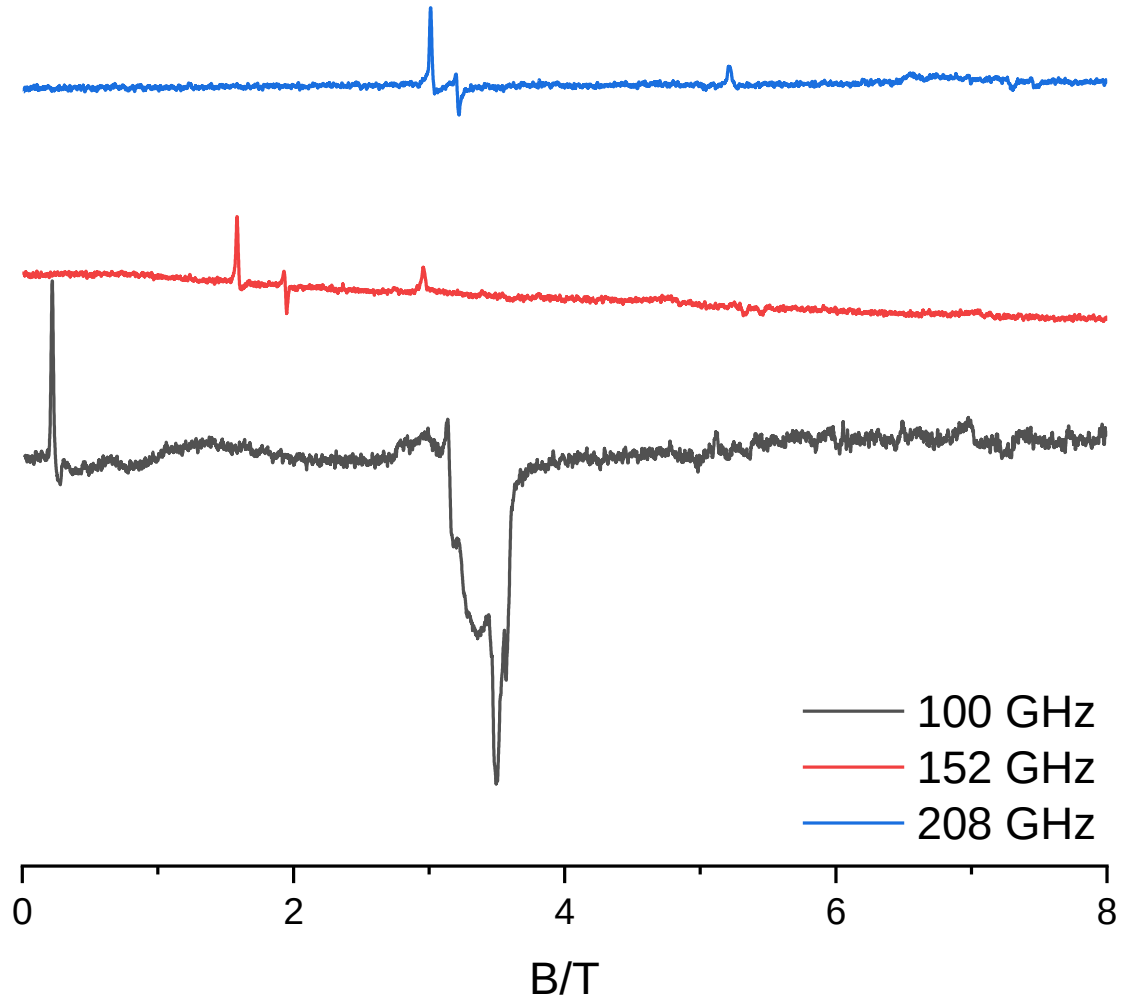

Figure 123. High field EPR spectra of $[Co^{I}(dmgBF_2)_2(OH_2)_2]$. 50 mM complex in CH_3CN with 500 mM $[^{n}Bu_4N]BH_4$, T = 5 K (100 and 152 GHz); 10 K (208 GHz).

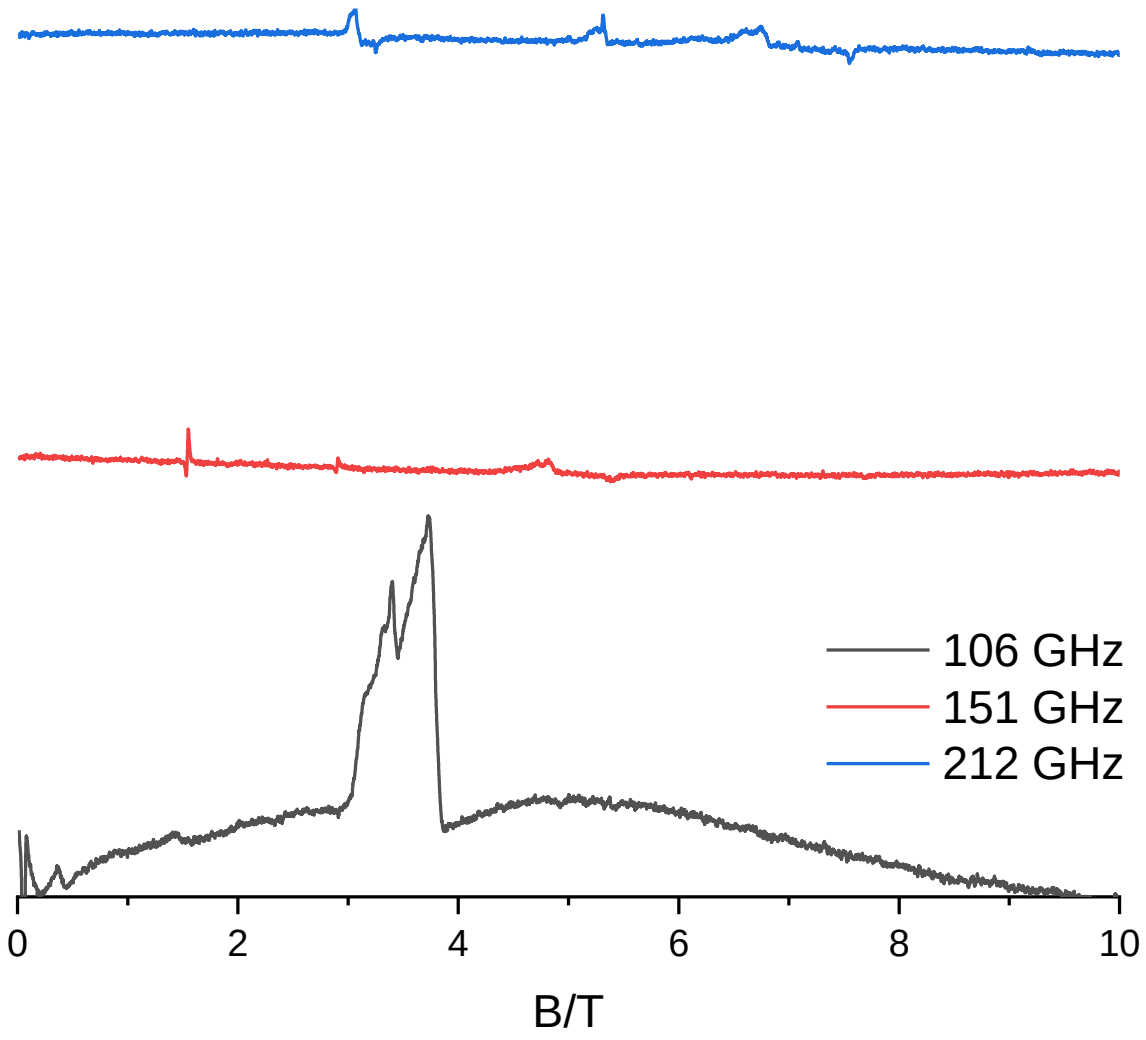

Figure 124. High field EPR spectra of $[Co^{I}(dmgBF_2)_2(OH_2)_2]$ + NEt_3. 50 mM complex in CH_3CN with 500 mM $[^nBu_4N]BH_4$ and 700 mM NEt_3, T = 5 K.

APPENDIX 3

Chapter 5: Supplementary Figures

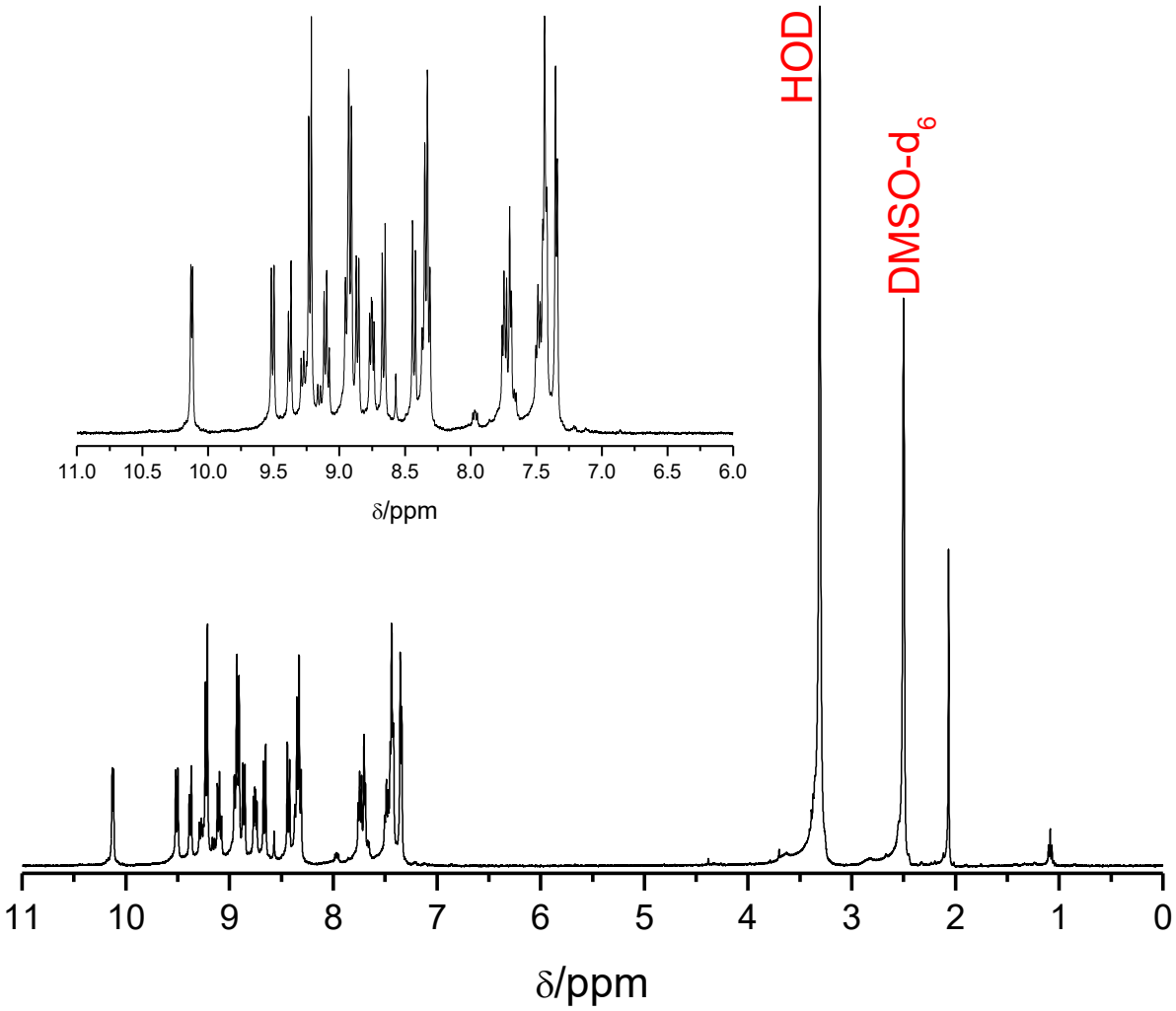

Figure S6. ^{1}H NMR spectra of complex **1** in DMSO-d_6.

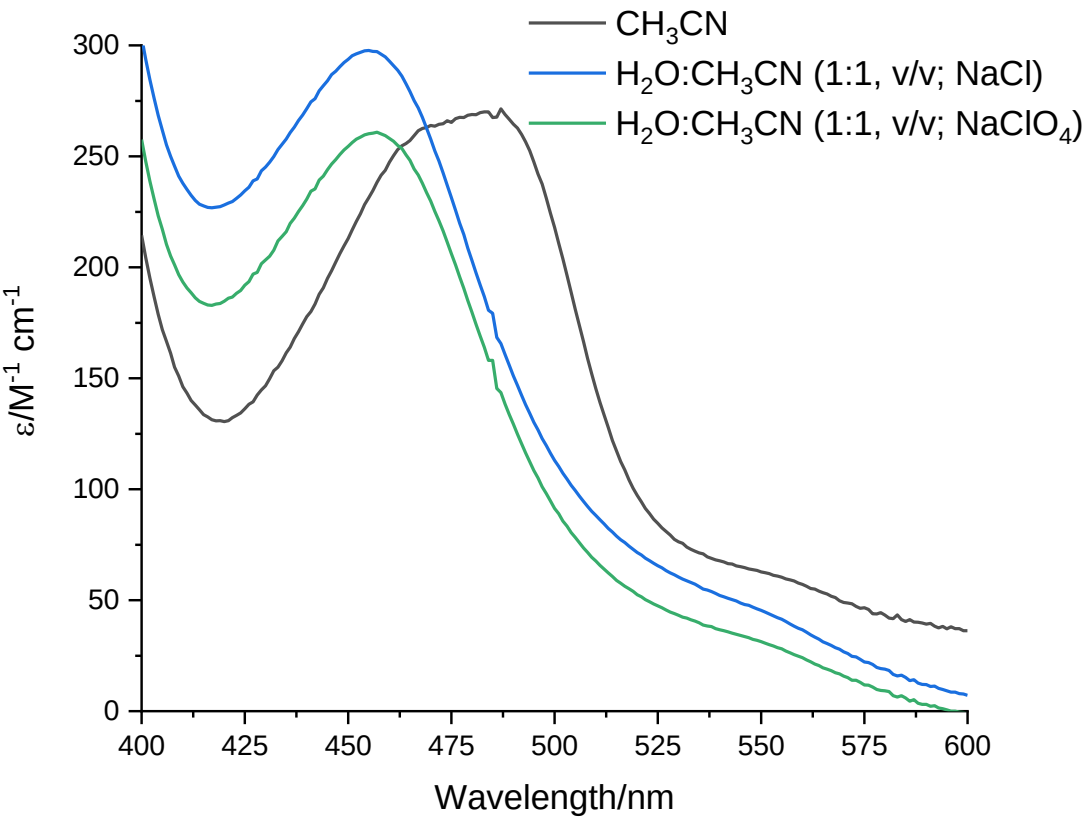

Figure S8. UV-visible spectra of complex **7** in acetonitrile or a mixture of water:acetonitrile (1:1, v/v) with different sodium salts.

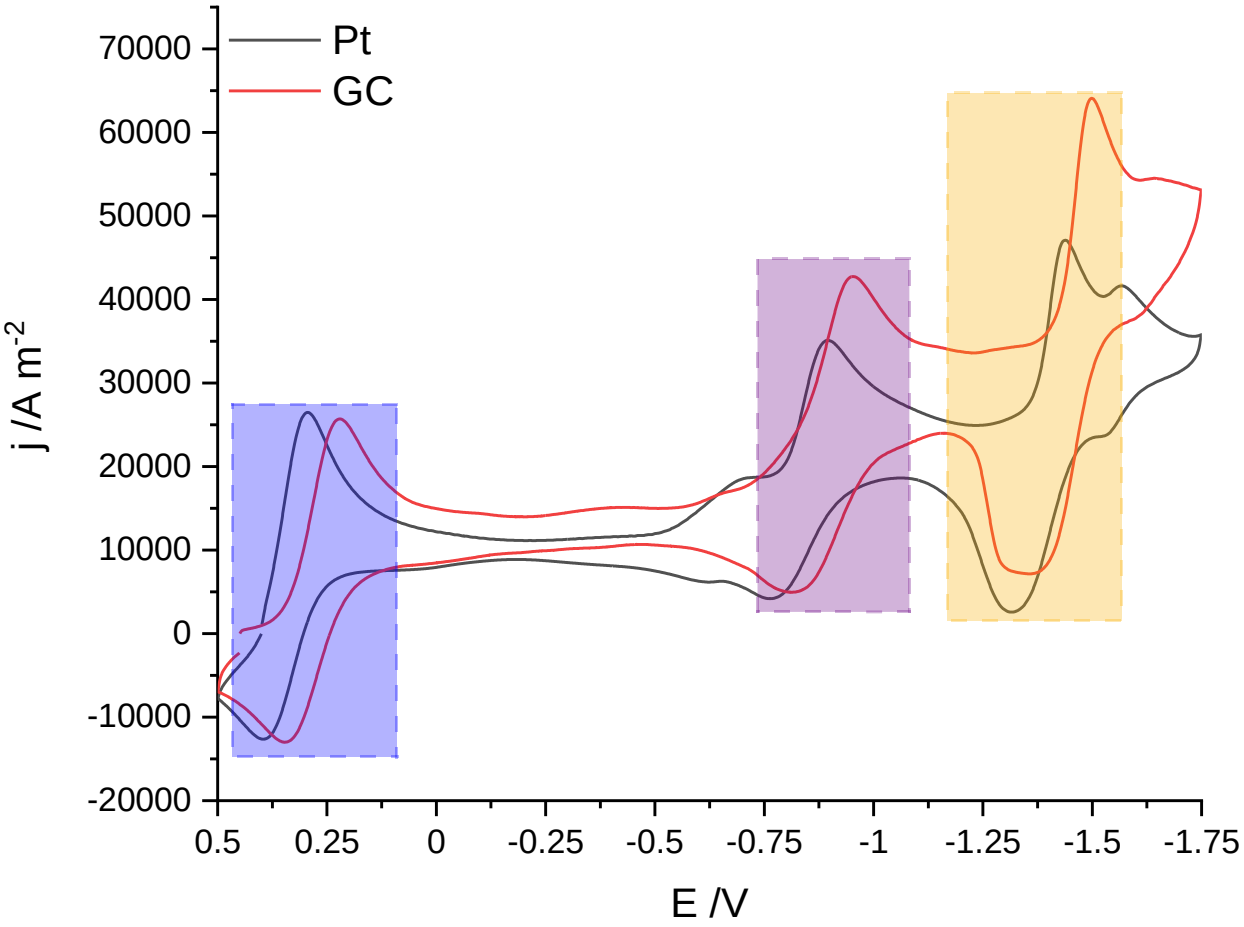

Figure 125. Cyclic voltammogram of complex **7**. Solvent = acetonitrile, [complex] = 1.0 mM, [$^{n}Bu_4N$]ClO_4 = 0.10 M, working electrode = either Pt or glassy carbon, auxiliary electrode = Pt wire, reference electrode = Ag/AgCl, and scan rate = 100 mV s^{-1}.

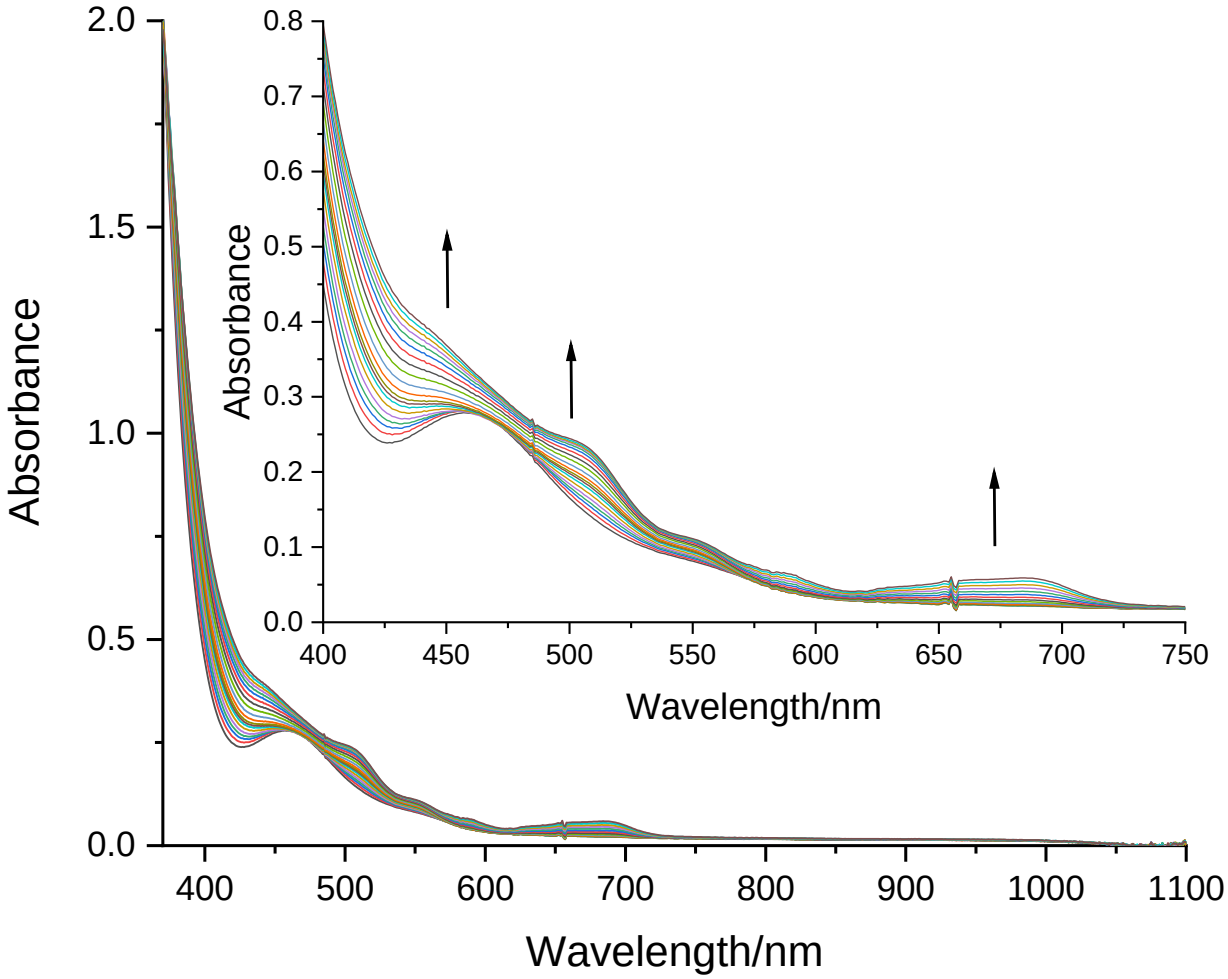

Figure 126. Spectroelectrochemical spectra of $[Co(tpy)(phen)Cl](PF_6)_2 \bullet 0.25CH_3CN$. Solvent = acetonitrile, [complex] = 13.3 mM, $[^nBu_4N]ClO_4$ = 0.10 mM, working electrode = Pt mesh wire, auxiliary electrode = Pt wire, reference electrode = Ag/AgCl, and held potential = 0.50 V.

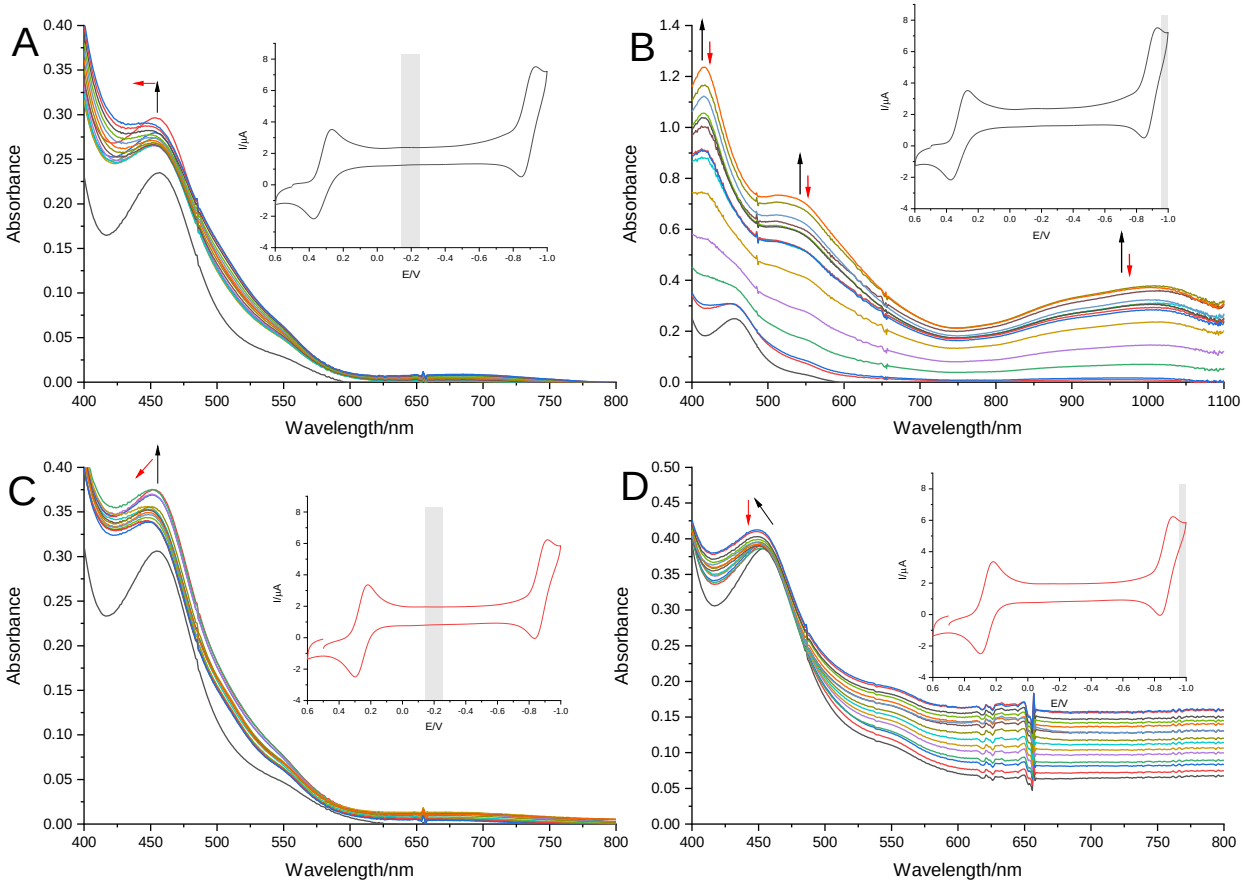

Figure 127. Spectroelectrochemical spectra of $[Co(tpy)(phen)Cl](PF_6)_2 \bullet 0.25CH_3CN$ with the supporting electrolyte $NaClO_4$ (**A** and **B**) or NaCl (**C** and **D**) in H_2O:CH_3CN (1:1, v/v). [complex] = 0.9 – 10.3 mM, [supporting electrolyte] = 0.1 M, working electrode = Pt, auxiliary electrode = Pt wire, and reference electrode = Ag/AgCl.

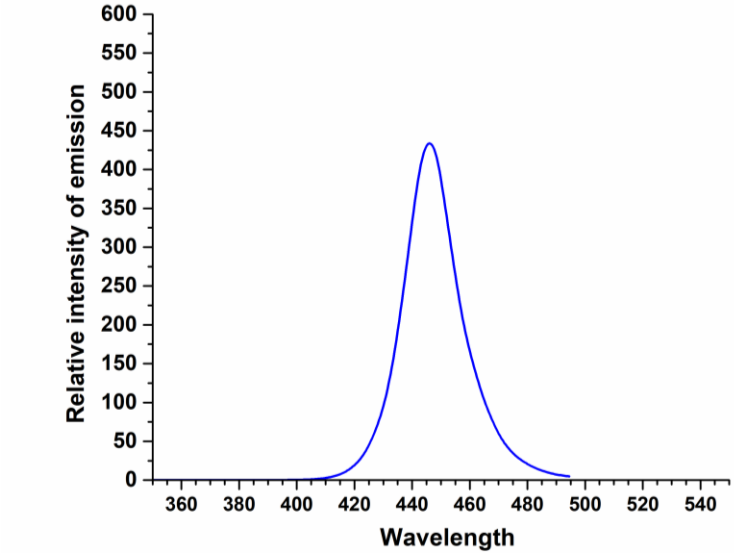

Figure S11. Emission spectrum of blue LED.

Table S2: Emission maxima and amplitude of LED light.

Light source[a]	**Blue**
$\lambda_{max,em}$ (nm)	445
$\Delta\lambda$ (nm)	90
Photon flux in $\mu mol_{photons}\, min^{-1}\, cm^{-2}$ [b]	20

[a] blue LED 445 nm.

[b] an analog power-meter PM100A (THORLABS) associated with a compact photodiode power head with silicon detector S120C was used to evaluate the photon flux for the LEDs. Photodiode detector was placed at the same distance from the LED surface as the bottom of the illuminated vial.

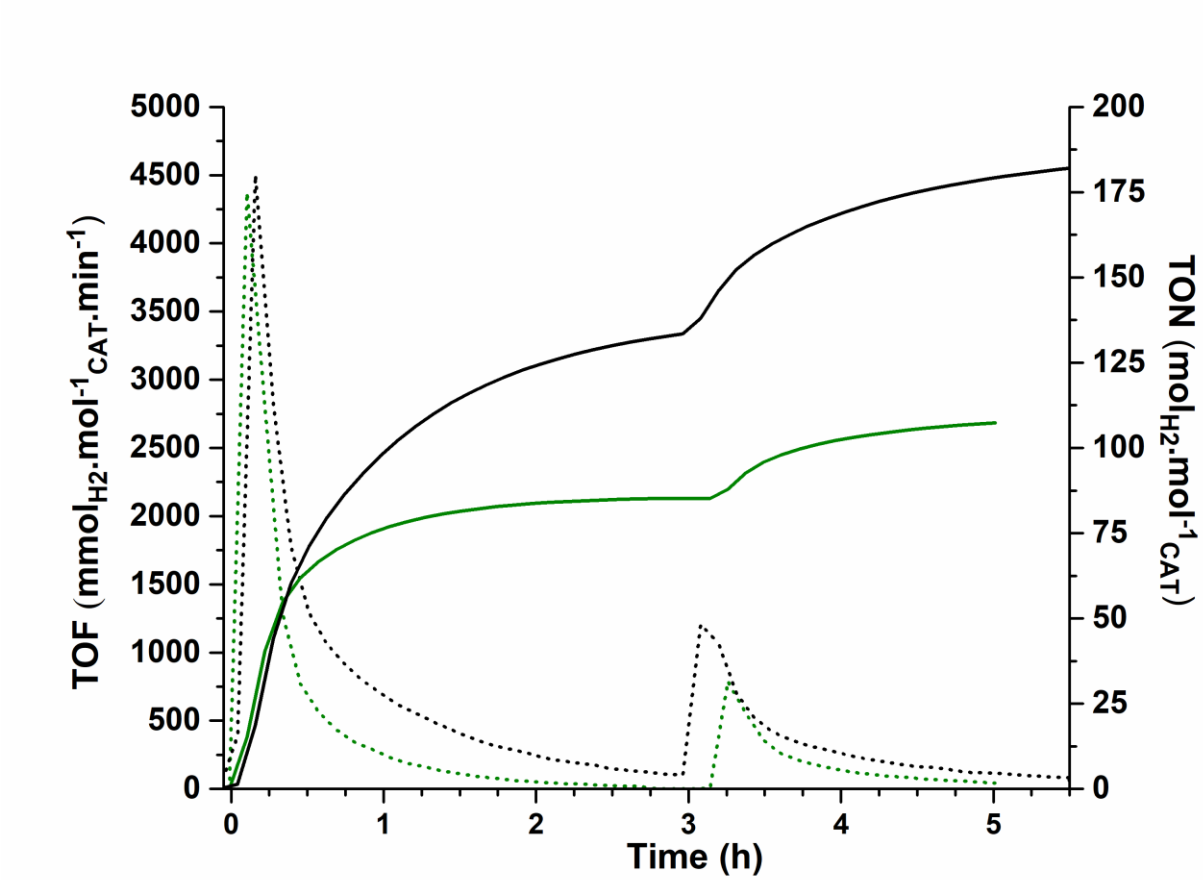

Figure S12. Restart of hydrogen evolution of [Co(dmgH)$_2$Cl(py)] (black) and complex **1** (olive) by the addition of fresh photosensitizer (1.25 ml of 0.4 mM [Ru(bpy)$_3$](PF$_6$)$_2$) at the end of activity. TOF: dotted line. TON: solid line.

VITA

Michael John Celestine

Department of Chemistry and Biochemistry mcele002@odu.edu
Old Dominion Univeristy
Norfolk, VA 23529

Education

May 2012 ……**B.S. Chemistry**, University of the Virgin Islands, Charlotte Amalie, St. Thomas, U.S. Virgin Islands

December 2015……**M.S. Chemistry**, Old Dominion University, Norfolk, Virginia, U.S.A.

December 2020……**Ph.D. Chemistry**, Old Dominion University Norfolk, Virginia, U.S.A.

Publication

Lawrence, M. A. W.; McMillen, C. D.; Gurung, R. K.; Celestine, M. J.; Arca, J. F.; Holder, A. A., Synthesis, X-ray Crystallographic, Electrochemical, and Spectroscopic Studies of Bis-(1,10-phenanthroline)(2,2'-bipyridine)cobalt(III) Hexafluorophosphate, *J. Chem. Crystallogr.* **2015,** *45* (8-9), 427-433.

Lawrence, M. A.; Celestine, M. J.; Artis, E. T.; Joseph, L. S.; Esquivel, D. L.; Ledbetter, A. J.; Cropek, D. M.; Jarrett, W. L.; Bayse, C. A.; Brewer, M. I.; Holder, A. A., Computational, electrochemical, and spectroscopic studies of two mononuclear cobaloximes: the influence of an axial pyridine and solvent on the redox behaviour and evidence for pyridine coordination to cobalt(I) and cobalt(II) metal centres, *Dalton Trans.* **2016,** *45* (25), 10326-42.

Celestine, M. J.; Joseph, L. S.; Holder, A. A., Kinetics and mechanism of the oxidation of a cobaloxime by sodium hypochlorite in aqueous solution: Is it an outer-sphere mechanism?, *Inorg. Chim. Acta* **2017,** *454*, 254-265.

Dutta, S.; Celestine, M. J.; Khanal, S.; Huddleston, A.; Simms, C.; Arca, J. F.; Mitra, A.; Heller, L.; Kraj, P. J.; Ledizet, M.; Anderson, J. F.; Neelakanta, G.; Holder, A. A.; Sultana, H., Coordination of different ligands to copper(II) and cobalt(III) metal centers enhances Zika virus and dengue virus loads in both arthropod cells and human keratinocytes, *Biochim. Biophys. Acta, Gen. Subj.* **2018,** *1862* (1), 40-50.

Beebe, S. J.; Celestine, M. J.; Bullock, J. L.; Sandhaus, S.; Arca, J. F.; Cropek, D. M.; Ludvig, T. A.; Foster, S. R.; Clark, J. S.; Beckford, F. A.; Tano, C. M.; Tonsel-White, E. A.; Gurung, R. K.; Stankavich, C. E.; Tse-Dinh, Y.-C.; Jarrett, W. L.; Holder, A. A., Synthesis, characterization, DNA binding, topoisomerase inhibition, and apoptosis induction studies of a novel cobalt(III) complex with a thiosemicarbazone ligand, *J. Inorg. Biochem.* **2020,** *203*, 110907.

Celestine, M. J.; Lawrence, M. A. W.; Evaristo, N. K.; Legere, B. W.; Knarr, J. K.; Schott, O.; Picard, V.; Bullock, J. L.; Hanan, G. S.; McMillen, C. D.; Bayse, C. A.; Holder, A. A., N-substituted 2-pyridinecarbothioamides and polypyridyl mixed-ligand cobalt(III)-containing complexes for photocatalytic hydrogen generation, *Inorg. Chim. Acta* **2020,** *510*, 119726.

Lawrence, M. A. W.; Mulder, W. H.; Celestine, M. J.; McMillen, C. D.; Holder, A. A., Assessment of two cobalt(II) complexes with pincer ligands for the electrocatalytic hydrogen evolution reaction. A comparison of the SNS vs ONS coordination, *Inorg. Chim. Acta* **2020,** *506*, 119497.

Tonsel-White, E. A.; Celestine, M. J.; Tano, C. M.; Nunez, B. S.; Kumar, S.; Holder, A. A., Biochar and kinetics studies on the reduction of sodium bromate by a cobaloxime in an aqueous media: How we can remove a toxic substance from our environment, *Inorg. Chim. Acta* **2020**, 119697.